SYNTHESIS AND APPLICATIONS OF FUNCTIONAL GRAFT COPOLYMERS

Satu Häkkinen

A thesis submitted in partial fulfilment of the requirements for the degree of

Doctor of Philosophy in Chemistry

University of Warwick

Department of Chemistry

December 2021

Contents

Index to Figures

Index to Tables

Index to Schemes

Abbreviations

ACVA	4,4′-Azobis(4-cyanovaleric acid)
AFM	Atomic force microscopy
AIBN	Azobisisobutyronitrile
Bis-MPDTC	Ethane-1,2-diyl bis(2-(((dodecylthio)carbonothioyl)thio)-2-methylpropanoate)
BuA	*n*-Butyl acrylate
CPADTC	4-Cyano-4-(((dodecylthio)carbonothioyl)thio)pentanoic acid
Cryo-SEM	Scanning electron cryomicroscopy
CTA	Chain transfer agent
DALS	Dual-angle light scattering
DCC	*N*,*N*-Dicyclohexylcarbodiimide
DCM	Dichloromethane
DMAP	4-(Dimethylamino)pyridine
DMF	*N*,*N*-Dimethylformamide
DP	Degree of polymerisation
DRI	Differential refractive index
EPHP	1-Ethylpiperidine hypophosphite
HEA	2-Hydroxyethyl acrylate
HEAm	*N*-Hydroxyethyl acrylamide
HEMA	2-Hydroxyethyl methacrylate
HSQC	Heteronuclear single quantum coherence
LAM	Less activated monomer
LC/MS	Liquid chromatography-mass spectrometry
LED	Light-emitting diode
LPO	Lauroyl peroxide
MAM	More activated monomer
MCPDTC	4-Cyano-4-(((dodecylthio)carbonothioyl)thio)pentanoate
MPADTC	2-(((Dodecylthio)carbonothioyl)thio)-2-methylpropanoic acid
MPPATC	3-((((1-Methoxy-1-oxopropan-2-yl)thio)carbonothioyl)thio) propanoic acid
MTM	Mini traction machine
MW	Molecular weight

MWD	Molecular weight distribution
NMR	Nuclear magnetic resonance
PABTC	2-(((Butylthio)carbonothioyl)thio)propanoic acid
pBzMA	Poly(benzyl methacrylate)
pCTA	Poly(chain transfer agent)
pHEA	Poly(2-hydroxyethyl acrylate)
PISA	Polymerisation-induced self-assembly
pLA	Poly(lauryl acrylate)
pLMA	Poly(lauryl methacrylate)
pMMA	Poly(methyl methacrylate)
pNAM	Poly(4-acryloylmorpholine)
PNR	Polarised neutron reflectometry
PTFE	Polytetrafluoroethylene
QCM-D	Quartz crystal microbalance with dissipation
RAFT	Reversible addition-fragmentation chain transfer
RI	Refractive index
RT	Retention time
SAXS	Small-angle X-ray scattering
SEC	Size-exclusion chromatography
SEM	Scanning electron microscopy
SLD	Scattering length density
TEM	Transmission electron microscopy
TEMPO	(2,2,6,6-Tetramethylpiperidin-1-yl)oxyl
THF	Tetrahydrofuran
TMS	Tetramethylsilane
UV	Ultraviolet
UV-Vis	Ultraviolet-visible
V-40	1,1'-Azobis(cyclohexane-1-carbonitrile)
V-601	Dimethyl 2,2'-azobis(2-methylpropionate)
VS	Viscometer

Acknowledgements

My time at Warwick turned out unlike anything I had ever experienced or anticipated, and I am grateful for everything I have learnt during this time. I want to acknowledge the people who made a significant impact on my life during these three-odd years or influenced me in a helpful way.

First and foremost, I want to thank my supervisor Professor Sébastien Perrier who kindly offered me the opportunity to join his group. Thank you for all your support and guidance. I still vividly remember the day you interviewed me for this position over Skype, and your positive, relaxed energy which made me think this right here could be the right supervisor for me. You have a way of finding a solution to every issue with your students' best interest in mind, and I am very grateful to have had such an accommodating supervisor. The fantastic resources available to us and the group's shared excitement about chemistry made your labs feel like a playground where the only limit was our imagination.

I also want to acknowledge Lubrizol for the opportunity to carry out my research. Thank you, Dr Timothy Smith, Dr Paul O'Hora, and Dr Paul Kirkman for your help throughout our collaboration.

The Perrier group quickly started to feel like a second family to me, and I want to thank everyone that I had the pleasure to work with during my time in the group. A warm thanks to all the Haddleton group and Bon lab members I got to know as well; I will miss you all. A special thanks to Professor Dave Haddleton for his help and never-failing chemical inventory; you always seemed to have the most random reagents that were needed to quickly test out a new idea before heading home. And thank you, Professor Stefan Bon, for your advice and inspiring chemistry discussions.

To Dr Andrew Kerr, thank you for all your guidance from my very first day in the group all the way to reviewing my thesis. I appreciate your patience and insightful comments and questions; needless to say, I learnt a great deal from you. I am thankful for the projects we shared and will miss brainstorming new ideas with you.

To my year group – already doctors – Fannie, Tom, and Robert: thanks for all the experiences we shared together. In particular, travelling to San Diego together for the ACS Meeting will always be a fond memory. Thank you, Robert, for sharing the Lubrizol experience and Hazelwood visits. Tom, your grounded character and dark humour always made me feel like I had a fellow Finn working in the lab with me.

Thanks so much for all your support over these years, I already miss working with you! Fannie, I will always cherish the times we still worked in the office and shared a desk, tea breaks, and daily chats. It already seems so long ago, and I wish we could have gone back to the old ways before leaving Warwick. Either way, I am happy to have shared this experience with you.

To whom I consider my mentors: thank you Joji for the countless chemistry discussions, for showing me how exciting chemistry can be, and for teaching me how to embrace creativity in my first year. Julia, thank you for all your help and support. In particular, you taught me the importance of peer support and the value in working towards a group that everyone feels a part of. I hope I can pass this on in the future.

And the ones I had the honour to mentor: Ramón, Vincent, and Billy. Thank you for the opportunity to improve my teaching skills, and for strengthening my knowledge as well. I had so much fun working with each of you, and I hope you equally got to experience and enjoy the fun side of research.

Steve and Qiao, thank you for taking the time to help me with experimental work and writing, as well as the helpful discussions – you taught me a lot.

Maria and Magda, I find your kindness and compassion inspiring, and you will always have a special place in my heart. Thank you for your support.

And of course, thank you Dr Antti Lahdenperä for encouraging me to take the leap and pursue a PhD programme abroad! I would not have ended up at Warwick if it wasn't for us catching up over some after work beers at Oljenkorsi.

Finally, I want to acknowledge the help and support of my family and friends in Finland. Santeri, kiitos tuestasi tänne lähtiessäni ja sen jälkeen. Vaikka tiemme haarautuivatkin, olen kiitollinen että välimme ovat edelleen lämpimät. Kiitos erityisesti kun pidit huolta Tiarasta poissa ollessani, ja että olit pojan vierellä viimeisinä hetkinään.

Kiitos Ossi sekä työhön liittyneistä keskusteluista, että siihen liittymättömistä höpinöistä, jäniksistä ja kissoista jotka muistuttivat maailmasta labran ja Englannin ulkopuolella.

Viimeiseksi, kiitos äiti tuestasi lähteä matkaan vaikka et ajatuksesta pitänytkään. Olit se voima joka auttoi yli vaikeimmista ajoista. Seuraava etappi saattaa olla kaukana, mutta silti vain lentomatkan päässä. Muistan kun aikoinaan ehdotit, että lähtisin opiskelemaan mikrobiologiaa tai kemiaa; minua ei kiinnostanut. No, niin siinä sitten kuitenkin kävi.

To Virpi and Tiara

List of Publications

Following publications have been produced from the work detailed in this thesis:

Chapter 2

Putting the RAFT in GRAFT: Dynamic Intermolecular Graft Exchange Between Bottlebrush Polymers Using Reversible Addition-Fragmentation Chain Transfer

S. Häkkinen, B. Dyer, A. Kerr, and S. Perrier.

Manuscript submitted.

Chapter 3

Polymerisation-Induced Self-Assembly of Graft Copolymers

S. Häkkinen, J. Tanaka, S. C. L. Hall, R. Garcia Maset, Q. Song, J. Y. Rho, S. Huband, and S. Perrier.

Manuscript in preparation.

Chapter 4

Anchor-Group Bottlebrush Polymers as Oil Additive Friction Modifiers

A. Kerr, **S. Häkkinen**, S. C. L. Hall, P. Kirkman, P. O'Hora, T. Smith, C. J. Kinane, A. Caruana, and S. Perrier.

Manuscript in preparation.

Declaration

Experimental work contained in this thesis is original research carried out by the author, unless otherwise stated, in the Department of Chemistry at the University of Warwick between January 2018 and April 2021. No material herein has been submitted for any other degree, or at any other institution. Results from other authors are referenced in the usual manner throughout the text.

The presented work was carried out by the author with the following exceptions:

Chapter 2

Polymers .1, .3, 1, 3, 1a, and 7 were prepared by Dr Andrew Kerr (Department of Chemistry, University of Warwick). Polymers .2 and 2 were prepared by Billy Dyer (Department of Chemistry, University of Warwick). Reaction E4 was conducted by Dr Andrew Kerr.

Chapter 3

SAXS measurements were conducted by Dr Steven Huband (X-ray diffraction RTP, University of Warwick). SAXS data analysis was carried out by Dr Stephen Hall (Department of Chemistry, University of Warwick; ISIS Neutron and Muon Source, Rutherford Appleton Laboratory). Cryo-SEM images were obtained by Steven Hindmarsh (Electron microscopy RTP, University of Warwick).

Chapter 4

MTM testing and QCM-D analysis were performed by Lubrizol. PNR data analysis was carried out by Dr Stephen Hall.

Signed:  Date: 17.12.2021

Satu Häkkinen

Abstract

This thesis investigates new synthetic methods for preparing graft copolymers using reversible addition-fragmentation chain transfer (RAFT) polymerisation, their solution self-assembly, and use as friction modifier additives in oil.

In the first study two new synthetic routes are described, which make use of the dynamic addition and fragmentation of grafts to and from the backbone in the previously reported Z group approach polymerisation mechanism. The first synthetic route involves an interchange of grafts between distinct graft copolymer starting materials, yielding a product with a mixed graft distribution. In the second method linear chains are transferred to a RAFT agent-decorated polymer, giving a graft copolymer product. The unique RAFT process provides a convenient means to prepare heterograft copolymers and extensive graft copolymer libraries by simply adjusting the stoichiometry of each reaction.

The second study investigates the polymerisation-induced self-assembly of sparsely grafted polymers during reactions in which grafts are polymerised in a backbone-selective solvent. The phase separation of grafts is shown to result in the formation of clustered particles and various multicore morphologies due to the ability of the branched architecture to freeze chain entanglements and bridge separate core domains. The graft copolymer architecture offers a straightforward route to less commonly encountered morphologies and gives additional handles for controlling the polymer structure and the properties of the obtained materials.

In the third study, various oil-soluble graft copolymers with a surface active polar segment are assessed for use as friction modifier oil additives. The incorporation of a polar segment into the polymer structure is shown to promote mass deposition onto steel, ideal for forming lubricating boundary films. Macrotribological tests indicate a significant friction reduction efficacy for all tested polymers but no clear distinction between the different architectures.

Chapter 1

Introduction to Graft Copolymers

1.1 Complex Polymer Architectures in Materials Design

Polymeric materials are all around us, ranging from natural polymers such as proteins and carbohydrates responsible for the structure and function of living organisms to synthetic polymers such as vinyl polymers and polyesters used in infrastructure, packaging, and consumer products. The basis of the suitability of each polymer for its function is an appropriate macromolecular structure which includes chemical, sequential, and topological components. Polymer properties may be changed drastically by varying its constituent monomers, their placement along the chain, and the overall molecular architecture (Scheme 1.1).[1]

While the use of linear homopolymers alone has allowed an extensive selection of materials to be utilised in everyday life, the potential benefits of employing copolymers and branched architectures became apparent and a focal point of materials development very early on.[2-4] For example, the preparation of block copolymers, in which two or more chemical components are segregated into their respective segments, can be used to incorporate complementary functionalities or physical properties into a single material. Some uses of block copolymers have included the employment of thermodynamically incompatible components to induce microphase separation in the bulk or in selective solvents to achieve tailored mechanical, optical or other physical properties[5] or to facilitate encapsulation of small molecular weight cargo.[6] Research in this field has resulted in various block copolymers being produced on an industrial scale for use as dispersants, adhesives, energy storage, and in oil recovery, amongst other applications.[7]

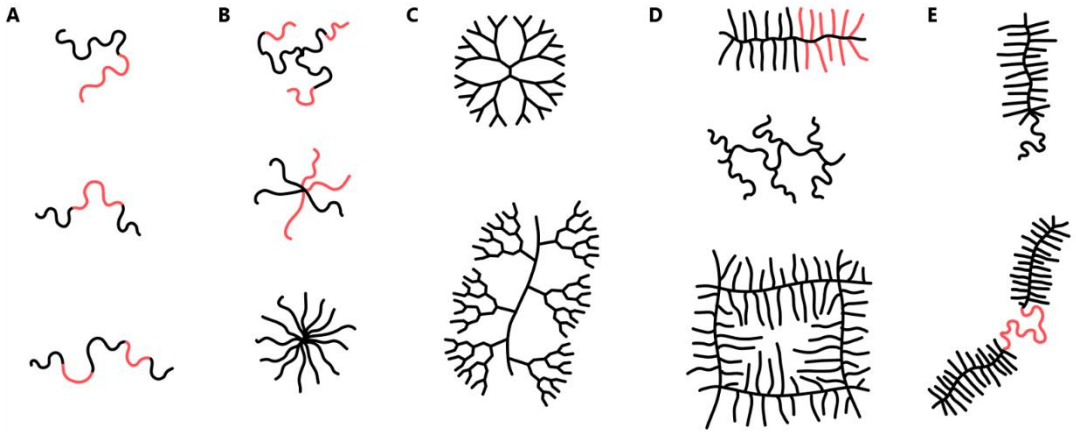

Scheme 1.1 Examples of complex polymer architectures. **A)** Linear di-, tri-, and pentablock copolymers. **B)** Three-arm star polymer with block copolymer arms, a miktoarm star, and a homopolymer star. **C)** A dendrimer and a dendritic polymer. **D)** A densely grafted diblock copolymer, loosely grafted polymer, and a graft copolymer network. **E)** Brush-coil architectures.

Branched architectures have been widely studied and put to use for their properties, which differ from those of linear polymers – and at times defy the general perception of polymer characteristics. For example, star polymers with compact, globular topologies exhibit unique rheological properties,[8] while perfectly branched dendrimers with fractal-like topologies have near-monodisperse structures and well-defined outer surfaces.[9] A key component in the exploration of such complex architectures has been the diligent development of synthetic strategies to continuously improve the level of control that may be achieved over structural detail. The versatile synthetic toolbox available to materials scientists today allows intricate architectures to be employed routinely in polymer research.

Amongst branched architectures, graft copolymers have been of interest for decades due to their unique properties, with some of the earlier studies dating back to the 1980s.[10] Their useful characteristics include and arise from their rigid, cylindrical topology, high chain density, and the various opportunities this architecture offers for tailoring the overall chemical composition. In recent years, graft copolymers have been researched for use in medical applications[11-13] and soft electronics,[14] as well as compatibilizers,[15] emulsifiers,[16] and elastomers,[17] amongst other uses.[18]

1.2 Graft Copolymers

Graft copolymers consist of a number of oligomeric or polymeric side-chains (grafts) attached to a polymeric main chain (backbone). The conformation of such molecules is highly dependent on the number of grafts per backbone repeat unit (the grafting density) and the relative lengths of these two components. Dense grafting of side-chains to a backbone results in steric repulsion between adjacent grafts and consequent extension of the backbone (Figure 1.1A). These interactions give the molecule a cylindrical – or a bottlebrush-like – topology, with flexibility only on the scale of the distance between neighbouring grafts.[19] At length scales longer than the grafts, the molecule behaves like a semiflexible cylinder. Sparse grafting allows the backbone and grafts to exhibit Gaussian behaviour.[20] The topology and conformation of graft copolymers may therefore be described by their backbone length, graft length, and grafting density, as well as their contour length, diameter, and persistence length.[18] The influence of graft length on the persistence length can be visualised in atomic force microscopy images, wherein a gradual extension of the backbone has been observed with increasing graft length (Figure 1.1B).[21, 22]

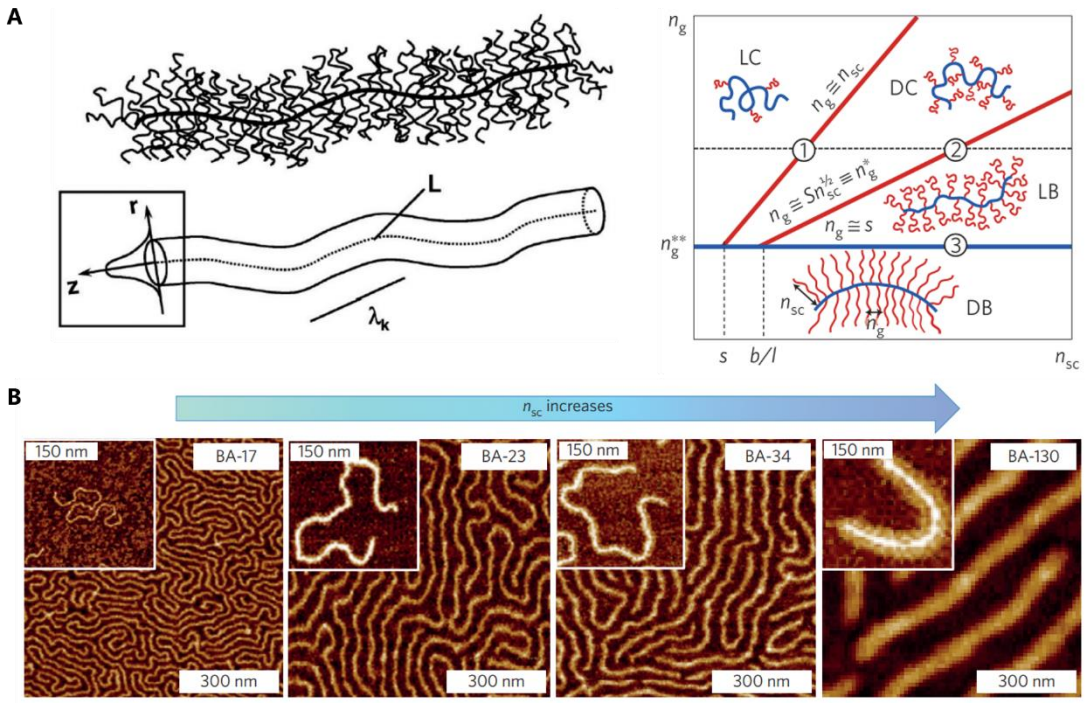

Figure 1.1 A) The cylindrical topology of a densely grafted bottlebrush-like polymer may be described by its contour length (L), Kuhn length (λ_k), and radius (r). The molecular conformation is influenced by the grafting density (n_g^{-1}) and the degree of polymerisation of side-chains (n_{sc}) and transitions from loosely grafted combs (LC) to densely grafted combs (DC) and loosely grafted bottlebrushes (LB) with Gaussian side-chains. Densely grafted bottlebrushes (DB) exhibit extended backbones and side-chains. **B)** AFM height images of bottlebrush polymers with the same backbone but different side-chain lengths. Adapted from refs. 21, 22.

The molecular conformation of graft copolymers is strongly reflected in their physical properties. A notable example is the graft-graft repulsion and backbone rigidity of bottlebrush polymers resulting in reduced chain entanglements, and strongly influencing their mechanical and rheological properties.[23] This feature has been harnessed to produce super-soft elastomers based on bottlebrush-like strands between crosslinks, which exhibit lower moduli than most synthetic polymers in which the lower limit has generally been defined by chain entanglements.[18, 22] The softness and strain stiffening of such materials could be adjusted by tuning chain entanglements and backbone extension, respectively. Rheological studies of graft copolymer melts have sought to understand the relationship between entanglement density and the polymer's structural parameters (i.e., backbone length, graft length, and grafting density).[24-26] The entanglement density is thought to result from an interplay between backbone dilution by grafts (the number and molecular weight of which may be varied), backbone stiffening caused by steric repulsion between the grafts, and an architecture-dependent packing number, defined as the ratio of graft size

to the length of a backbone segment between the grafts.[26] Loosely grafted polymers have been described by reptation theory, which takes into account both backbone and side-chain entanglements, with the latter retarding the reptation of backbone segments due to a strong frictional effect.[27] Densely grafted polymers retain mobility in condensed phases,[28] which combined with large domain sizes up to several hundred nanometers[29, 30] makes them an intriguing subject of study in the field of polymer self-assembly.

1.2.1 Synthetic Strategies

Three synthetic strategies may be used for the preparation of graft copolymers, commonly referred to as the *grafting through*, *grafting to*, and *grafting from* approaches (Scheme 1.2). Each approach offers some practical benefits – such as straightforward isolation of the product or ease of characterisation of the grafts and the backbone – and superior control over certain structural parameters. Most importantly, some polymerisation techniques are better suited for certain approaches than others and care should be taken in selecting a synthetic approach for the desired polymerisation technique. A combination of polymerisation techniques may also be used in conjunction with the selected approach.

Grafting through involves the (co)polymerisation of macromonomers and is arguably the most straightforward approach of the three. The approach is the only one guaranteed to yield a fully grafted backbone if only macromonomers are used in the polymerisation, however statistical copolymerisation of small molecular weight monomers may also be used. The selection of an appropriate polymerisation technique is key to ensure good control over the backbone length. *Grafting through* polymerisations are often conducted using atom-transfer radical polymerisation (ATRP)[31, 32] and has become increasingly popular with the development of ring-

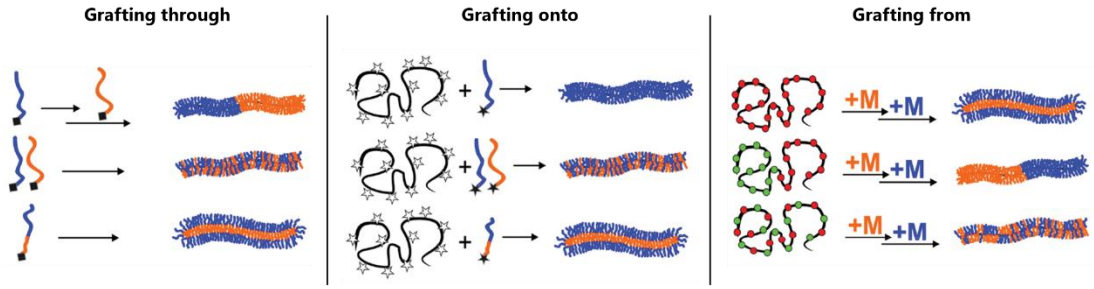

Scheme 1.2 Illustration of the three synthetic strategies used for preparing graft copolymers. Adapted from ref 33.

opening metathesis polymerisation (ROMP),[34, 35] both of which are well-suited to this approach. In contrast, reversible addition-fragmentation chain transfer (RAFT) polymerisation of macromonomers tends to suffer from the sterically hindered chain-end functionality, leading to loss of control even at moderate backbone lengths. The selected polymerisation technique may also impact backbone flexibility and spacing between adjacent grafts. For example, ROMP of norbornene-terminated macromonomers results in a graft copolymer with five C−C bonds across a repeat unit, whereas radical polymerisation of vinyl macromonomers can generate a graft spacing of only two C−C bonds. Regardless of the selected polymerisation technique, the polymerisation of macromonomers is generally challenging due to their low enthalpy and unfavourable entropy of polymerisation, and therefore sensitivity to reaction conditions such as polymerisation temperature.[36, 37] The concentration of the polymerisable functionality is generally limited to moderate to low concentrations due to the large size of the macromonomer, even when conducted as a bulk polymerisation.

The *grafting to* approach involves the preparation of a multifunctional polymer (the backbone precursor) and an end-functional oligomer/polymer (the grafts), followed by a reaction between the two in which the grafts are coupled to the backbone. The modularity of preparing each component individually allows for a good control over their molecular weight and structure, and convenient mixing and matching for preparing multiple products from a selection of starting materials. The polymerisation techniques may be selected to best suit the chemical and structural requirements of the final product. The most significant drawback of the approach is that achievable grafting densities are limited by chain diffusion and steric hindrance near the reactive sites, the latter of which may be generally expected to increase with increasing graft length. These challenges may be reduced by introducing a spacer between the backbone and the coupling site, and by using robust coupling chemistries such as the commonly selected copper-catalysed azide-alkyne cycloaddition.[38-40]

The *grafting from* strategy involves the preparation of a linear polymer with multiple initiating sites along the chain, which are subsequently used to conduct polymerisation of grafts. Examples of commonly selected initiating groups include thiocarbonylthio chain transfer agents used for RAFT polymerisation,[41, 42] alkyl halides used in ATRP,[43, 44] and hydroxy groups used in ring-opening polymerisations.[43, 45] This strategy is well suited for the preparation of large graft copolymers with a long backbone and grafts. However, the polymerisation of grafts

can exhibit reduced control due to steric congestion and close proximity of other initiating groups. The approach is generally deemed suitable for preparing densely or even fully grafted polymers. However, the grafting density depends on the initiation efficiency of the initiating sites and may be challenging to quantify with sufficient accuracy. Termination of grafts may lead to a reduced grafting density, a broad molecular weight distribution, and bimolecular coupling. Careful optimisation of reaction conditions allows the preparation of polymers with astonishing complexity, such as the recently reported bottlebrush copolymer comprising a nonablock copolymer backbone, pentablock copolymer grafts, and 29 separate domains overall across a single molecule.[41]

1.2.2 Prospective Applications

Current literature on graft copolymers presents diverse opportunities for their applications. Motivations for their use include the vast possibilities to tailor their chemical composition and molecular topology. For example, in the field of polymer colloids this creative freedom may be used to fine-tune particle size, structure, and chemistry,[46-48] molecular packing,[43, 49] and solvophobicity.[50] Graft copolymers have also been widely used to prepare hybrid materials of natural and synthetic polymers such as cellulose to achieve materials with improved chemical or physical properties.[51, 52]

Arguably the most evident incentive for employing the graft copolymer architecture is its unique physical properties. For instance, conformational restrictions have been envisioned to be advantageous in materials such as organic electronics, which generally benefit from long-range order.[53] Reduced entanglements have been harnessed to prepare solvent-free polymer networks with reduced physical crosslinks between chemical crosslinking points to yield tissue-mimicking materials with an unprecedented combination of high softness and deformability.[17, 22] Limited chain entanglements have also been reported to result in the formation of highly ordered nano-objects in selective solvents due to increased chain mobility.[28] The energetic penalties of chain bending have also been demonstrated to have an impact on particle morphologies,[45, 54] which could offer an additional handle for directing self-assembly pathways. The large size of the molecules has been used to aid nanoparticle visualisation with microscopic techniques by promoting the formation of larger core domains than those formed by linear polymers.[55]

One of the best known properties of graft copolymers is their extraordinary ability to provide lubrication and wear protection between moving surfaces.[56] Inspired by nature's lubricating biomacromolecule, lubricin, a pursuit to prepare synthetic analogues has given rise to studies involving water-soluble bottlebrush-like polymers attached to surfaces via ionic interactions.[44, 57] While the astounding performance of nature's design has been challenging to replicate, recent literature has shown great success in aqueous systems. In contrast, lubrication in non-polar solvents appears to be unexplored.

1.3 Motivation, Objectives and Outline of This Work

Graft copolymers continue to be of great interest to materials scientists due to their extraordinary physical properties and various real-world applications.[11, 58-60] Their relevance has become increasingly significant with the gradual development of polymerisation techniques and processes, which have made even such complex architectures easily accessible. The work presented in this thesis aims to contribute to the field by developing new methods for graft copolymer synthesis, by investigating their self-assembly behaviour during a polymerisation process in which nanoparticles are formed *in situ*, and by assessing their structure-property relationships and performance as friction modifier additives in oil. In particular, the work will focus on the use of RAFT polymerisation for graft copolymer synthesis due to this technique's versatility[61, 62] and industrial incentives to develop RAFT technologies for commercial use.[7]

The research presented in the first part of this thesis involves the development of new synthetic routes for preparing graft copolymers. Chapter 2 describes two newly developed strategies based on the so-called Z group approach reaction mechanism previously described in the literature,[63] which allows graft radicals to be fragmented off the backbone. These dynamic bonds between the grafts and the backbone may be used to conduct intermolecular graft exchange reactions between graft copolymers with different graft lengths or chemical structures. The work provides a modular approach for preparing heterograft copolymers by simply reinitiating a mixture of graft copolymers or a mixture of graft copolymers and linear polymers capable of forming a chain radical. The second strategy employs the same mechanistic principles to prepare a graft copolymer by transferring linear chains to a RAFT agent-decorated polymer.

The work presented in Chapter 3 explores the self-assembly characteristics of graft copolymers during a process in which grafts are polymerised in a solvent that is selective for the backbone. Specifically, poly(benzyl methacrylate) was *grafted from* a poly(lauryl methacrylate) backbone via RAFT dispersion polymerisation in *n*-dodecane to induce polymer self-assembly during the reaction. The resulting polymer particles and gel-like materials were studied in detail with electron microscopy and scattering techniques to understand underlying phenomena that dictated the fate of the reactions. A clear distinction could be made between the materials obtained in this work, and those reported for linear diblock copolymers using the same approach.

Finally, the concept of graft copolymer lubricants – widely studied in aqueous solvents – was extended to non-polar media to assess their prospective use as friction modifiers in engine oils. Building on previous research conducted in our group, Chapter 4 describes the synthesis, characterisation and preliminary performance tests of oil-soluble graft copolymers designed to adhere to metal surfaces via a polar anchor group. The surface adsorption and lubrication properties were studied in detail to understand key parameters for designing effective lubricants. The architectural intricacies and anchor group placement is shown to strongly influence the formation of lubricating boundary films.

1.4 References

1. Polymeropoulos, G.; Zapsas, G.; Ntetsikas, K.; Bilalis, P.; Gnanou, Y.; Hadjichristidis, N., 50th Anniversary Perspective: Polymers with Complex Architectures. *Macromolecules* **2017,** *50* (4), 1253-1290.
2. Szwarc, M., Living Polymers: Their Significance and Applications. In *Survey of Progress in Chemistry*, Scott, A. F., Ed. Elsevier: 1977; Vol. 8, pp 83-120.
3. Mark, H. F., The Synthesis and Applicability of Block and Graft Copolymers. *Textile Research Journal* **1953,** *23* (5), 294-298.
4. Stockmayer, W. H.; Fixman, M., Dilute Solutions of Branched Polymers. *Annals of the New York Academy of Sciences* **1953,** *57* (4), 334-352.
5. Bates, F. S.; Fredrickson, G. H., Block Copolymers - Designer Soft Materials. *Physics Today* **1999,** *52* (2), 32-38.
6. Phan, H.; Taresco, V.; Penelle, J.; Couturaud, B., Polymerisation-Induced Self-Assembly (PISA) as a Straightforward Formulation Strategy for Stimuli-Responsive Drug Delivery Systems and Biomaterials: Recent Advances. *Biomaterials Science* **2021,** *9* (1), 38-50.
7. Destarac, M., Industrial Development of Reversible-Deactivation Radical Polymerization: Is the Induction Period Over? *Polymer Chemistry* **2018,** *9* (40), 4947-4967.
8. Ren, J. M.; McKenzie, T. G.; Fu, Q.; Wong, E. H.; Xu, J.; An, Z.; Shanmugam, S.; Davis, T. P.; Boyer, C.; Qiao, G. G., Star Polymers. *Chemical Reviews* **2016,** *116* (12), 6743-836.
9. Seo, S. E.; Hawker, C. J., The Beauty of Branching in Polymer Science. *Macromolecules* **2020,** *53* (9), 3257-3261.
10. Ito, K.; Usami, N.; Yamashita, Y., Syntheses of Methyl Methacrylate-Stearyl Methacrylate Graft Copolymers and Characterization by Inverse Gas Chromatography. *Macromolecules* **1980,** *13* (2), 216-221.
11. Banquy, X.; Faivre, J.; Shrestha, B. R.; Matyjaszewski, K.; Burdynska, J.; Moldovan, F. Bottlebrush Polymer Compositions, Lubricating Fluid, Porous Materials Comprising Said Compositions, and Surface Bearing Said Compositions. WO 2017181274A1, 2021.
12. Laroque, S.; Reifarth, M.; Sperling, M.; Kersting, S.; Klöpzig, S.; Budach, P.; Storsberg, J.; Hartlieb, M., Impact of Multivalence and Self-Assembly in the Design of Polymeric Antimicrobial Peptide Mimics. *ACS Applied Materials & Interfaces* **2020,** *12* (27), 30052-30065.
13. Huang, Q.; Xu, Z.; Cai, C.; Lin, J., Micelles with a Loose Core Self-Assembled from Coil-g-Rod Graft Copolymers Displaying High Drug Loading Capacity. *Macromolecular Chemistry and Physics* **2020,** *221* (12), 2000121.
14. Reynolds, V. G.; Mukherjee, S.; Xie, R.; Levi, A. E.; Atassi, A.; Uchiyama, T.; Wang, H.; Chabinyc, M. L.; Bates, C. M., Super-Soft Solvent-Free Bottlebrush Elastomers for Touch Sensing. *Materials Horizons* **2020,** *7* (1), 181-187.
15. Klimovica, K.; Pan, S.; Lin, T.-W.; Peng, X.; Ellison, C. J.; LaPointe, A. M.; Bates, F. S.; Coates, G. W., Compatibilization of iPP/HDPE Blends with PE-g-iPP Graft Copolymers. *ACS Macro Letters* **2020,** *9* (8), 1161-1166.
16. Xie, G.; Krys, P.; Tilton, R. D.; Matyjaszewski, K., Heterografted Molecular Brushes as Stabilizers for Water-in-Oil Emulsions. *Macromolecules* **2017,** *50* (7), 2942-2950.
17. Vatankhah-Varnosfaderani, M.; Keith, A. N.; Cong, Y.; Liang, H.; Rosenthal, M.; Sztucki, M.; Clair, C.; Magonov, S.; Ivanov, D. A.; Dobrynin, A.

V.; Sheiko, S. S., Chameleon-Like Elastomers with Molecularly Encoded Strain-Adaptive Stiffening and Coloration. *Science* **2018,** *359* (6383), 1509-1513.
18. Xie, G.; Martinez, M. R.; Olszewski, M.; Sheiko, S. S.; Matyjaszewski, K., Molecular Bottlebrushes as Novel Materials. *Biomacromolecules* **2019,** *20* (1), 27-54.
19. Saariaho, M.; Ikkala, O.; Szleifer, I.; Erukhimovich, I.; ten Brinke, G., On Lyotropic Behavior of Molecular Bottle-Brushes: A Monte Carlo Computer Simulation Study. *The Journal of Chemical Physics* **1997,** *107* (8), 3267-3276.
20. Nakamura, Y.; Wan, Y.; Mays, J. W.; Iatrou, H.; Hadjichristidis, N., Radius of Gyration of Polystyrene Combs and Centipedes in Solution. *Macromolecules* **2000,** *33* (22), 8323-8328.
21. Rathgeber, S.; Pakula, T.; Wilk, A.; Matyjaszewski, K.; Beers, K. L., On the Shape of Bottle-Brush Macromolecules: Systematic Variation of Architectural Parameters. *The Journal of Chemical Physics* **2005,** *122* (12), 124904.
22. Daniel, W. F. M.; Burdyńska, J.; Vatankhah-Varnoosfaderani, M.; Matyjaszewski, K.; Paturej, J.; Rubinstein, M.; Dobrynin, A. V.; Sheiko, S. S., Solvent-free, supersoft and superelastic bottlebrush melts and networks. *Nature Materials* **2015,** *15*, 183-189.
23. Abbasi, M.; Faust, L.; Wilhelm, M., Comb and Bottlebrush Polymers with Superior Rheological and Mechanical Properties. *Advanced Materials* **2019,** *31* (26), 1806484-1806495.
24. Hu, M.; Xia, Y.; McKenna, G. B.; Kornfield, J. A.; Grubbs, R. H., Linear Rheological Response of a Series of Densely Branched Brush Polymers. *Macromolecules* **2011,** *44* (17), 6935-6943.
25. Liang, H.; Wang, Z.; Sheiko, S. S.; Dobrynin, A. V., Comb and Bottlebrush Graft Copolymers in a Melt. *Macromolecules* **2019,** *52* (10), 3942-3950.
26. Liang, H.; Grest, G. S.; Dobrynin, A. V., Brush-Like Polymers and Entanglements: From Linear Chains to Filaments. *ACS Macro Letters* **2019,** *8* (10), 1328-1333.
27. Inkson, N. J.; Graham, R. S.; McLeish, T. C. B.; Groves, D. J.; Fernyhough, C. M., Viscoelasticity of Monodisperse Comb Polymer Melts. *Macromolecules* **2006,** *39* (12), 4217-4227.
28. Ma, H.; Kim, K. T., Self-Assembly of Bottlebrush Block Copolymers into Triply Periodic Nanostructures in a Dilute Solution. *Macromolecules* **2020,** *53* (2), 711-718.
29. Rzayev, J., Synthesis of Polystyrene−Polylactide Bottlebrush Block Copolymers and Their Melt Self-Assembly into Large Domain Nanostructures. *Macromolecules* **2009,** *42* (6), 2135-2141.
30. Kang, Y.; Walish, J. J.; Gorishnyy, T.; Thomas, E. L., Broad-wavelength-range chemically tunable block-copolymer photonic gels. *Nature Materials* **2007,** *6* (12), 957-960.
31. Cong, Y.; Vatankhah-Varnosfaderani, M.; Karimkhani, V.; Keith, A. N.; Leibfarth, F. A.; Martinez, M. R.; Matyjaszewski, K.; Sheiko, S. S., Understanding the Synthesis of Linear–Bottlebrush–Linear Block Copolymers: Toward Plastomers with Well-Defined Mechanical Properties. *Macromolecules* **2020,** *53* (19), 8324-8332.
32. Martinez, M. R.; Dadashi-Silab, S.; Lorandi, F.; Zhao, Y.; Matyjaszewski, K., Depolymerization of P(PDMS11MA) Bottlebrushes via Atom Transfer Radical Polymerization with Activator Regeneration. *Macromolecules* **2021,** *54* (12), 5526-5538.
33. Müllner, M., Molecular Polymer Brushes in Nanomedicine. *Macromolecular Chemistry and Physics* **2016,** *217* (20), 2209-2222.

34. Levi, A. E.; Lequieu, J.; Horne, J. D.; Bates, M. W.; Ren, J. M.; Delaney, K. T.; Fredrickson, G. H.; Bates, C. M., Miktoarm Stars via Grafting-Through Copolymerization: Self-Assembly and the Star-to-Bottlebrush Transition. *Macromolecules* **2019,** *52* (4), 1794-1802.
35. Radzinski, S. C.; Foster, J. C.; Scannelli, S. J.; Weaver, J. R.; Arrington, K. J.; Matson, J. B., Tapered Bottlebrush Polymers: Cone-Shaped Nanostructures by Sequential Addition of Macromonomers. *ACS Macro Letters* **2017,** *6* (10), 1175-1179.
36. Moad, G.; Solomon, D. H., *The Chemistry of Radical Polymerization*. 2nd Edition ed.; Elsevier: Amsterdam, 2006.
37. Martinez, M. R.; Krys, P.; Sheiko, S. S.; Matyjaszewski, K., Poor Solvents Improve Yield of Grafting-Through Radical Polymerization of OEO19MA. *ACS Macro Letters* **2020,** *9* (5), 674-679.
38. Gan, W.; Shi, Y.; Jing, B.; Cao, X.; Zhu, Y.; Gao, H., Produce Molecular Brushes with Ultrahigh Grafting Density Using Accelerated CuAAC Grafting-Onto Strategy. *Macromolecules* **2017,** *50* (1), 215-222.
39. Long, M.; Shi, Y.; Zhang, K.; Chen, Y., Microphase Separation within Disk Shaped Aggregates of Triblock Bottlebrushes. *Macromolecular Rapid Communications* **2016,** *37* (7), 605-609.
40. Le Fer, G.; Le Cœur, C.; Guigner, J.-M.; Amiel, C.; Volet, G., Biocompatible Soft Nanoparticles with Multiple Morphologies Obtained from Nanoprecipitation of Amphiphilic Graft Copolymers in a Backbone-Selective Solvent. *Langmuir* **2017,** *33* (11), 2849-2860.
41. Kerr, A.; Hartlieb, M.; Sanchis, J.; Smith, T.; Perrier, S., Complex Multiblock Bottle-Brush Architectures by RAFT Polymerization. *Chemical Communications* **2017,** *53* (87), 11901-11904.
42. Radzinski, S. C.; Foster, J. C.; Matson, J. B., Synthesis of Bottlebrush Polymers via Transfer-To and Grafting-Through Approaches Using a RAFT Chain Transfer Agent With a ROMP-Active Z-Group. *Polymer Chemistry* **2015,** *6* (31), 5643-5652.
43. Fenyves, R.; Schmutz, M.; Horner, I. J.; Bright, F. V.; Rzayev, J., Aqueous Self-Assembly of Giant Bottlebrush Block Copolymer Surfactants as Shape-Tunable Building Blocks. *Journal of the American Chemical Society* **2014,** *136* (21), 7762-7770.
44. Faivre, J.; Shrestha, B. R.; Xie, G.; Olszewski, M.; Adibnia, V.; Moldovan, F.; Montembault, A.; Sudre, G.; Delair, T.; David, L.; Matyjaszewski, K.; Banquy, X., Intermolecular Interactions between Bottlebrush Polymers Boost the Protection of Surfaces against Frictional Wear. *Chemistry of Materials* **2018,** *30* (12), 4140-4149.
45. Steinhaus, A.; Pelras, T.; Chakroun, R.; Gröschel, A. H.; Müllner, M., Self-Assembly of Diblock Molecular Polymer Brushes in the Spherical Confinement of Nanoemulsion Droplets. *Macromolecular Rapid Communications* **2018,** *39* (19), 1800177-1800183.
46. Song, J.; Wei, Y.; Hu, J.; Liu, G.; Huang, Z.; Lin, S.; Liu, F.; Mo, Y.; Tu, Y.; Ou, M., pH-Responsive Porous Nanocapsules for Controlled Release. *Chemistry - A European Journal* **2018,** *24* (1), 212-221.
47. Wang, C.; Li, G.; Guo, R., Multiple Morphologies from Amphiphilic Graft Copolymers Based on Chitooligosaccharides as Backbones and Polycaprolactones as Branches. *Chemical Communications* **2005,** (28), 3591-3593.
48. Parry, A. L.; Bomans, P. H. H.; Holder, S. J.; Sommerdijk, N. A. J. M.; Biagini, S. C. G., Cryo Electron Tomography Reveals Confined Complex

Morphologies of Tripeptide-Containing Amphiphilic Double-Comb Diblock Copolymers. *Angewandte Chemie International Edition* **2008,** *47* (46), 8859-8862.
49. Unsal, H.; Onbulak, S.; Calik, F.; Er-Rafik, M.; Schmutz, M.; Sanyal, A.; Rzayev, J., Interplay between Molecular Packing, Drug Loading, and Core Cross-Linking in Bottlebrush Copolymer Micelles. *Macromolecules* **2017,** *50* (4), 1342-1352.
50. Shao, F.; Wang, Y.; Tonge, C. M.; Sauvé, E. R.; Hudson, Z. M., Self-Assembly of Luminescent Triblock Bottlebrush Copolymers in Solution. *Polymer Chemistry* **2020,** *11* (5), 1062-1071.
51. Gürdağ, G.; Sarmad, S., Cellulose Graft Copolymers: Synthesis, Properties, and Applications. In *Polysaccharide Based Graft Copolymers*, Kalia, S.; Sabaa, M. W., Eds. Springer: Berlin, Heidelberg, 2013; pp 15-57.
52. Li, S.; Schroeder, C. M., Synthesis and Direct Observation of Thermoresponsive DNA Copolymers. *ACS Macro Letters* **2018,** *7* (3), 281-286.
53. Ahn, S.-K.; Nam, J.; Zhu, J.; Lee, E.; Michael Kilbey, S., Solution Self-Assembly of Poly(3-Hexylthiophene)–Poly(Lactide) Brush Copolymers: Impact of Side Chain Arrangement. *Polymer Chemistry* **2018,** *9* (23), 3279-3286.
54. Shi, Y.; Zhu, W.; Yao, D.; Long, M.; Peng, B.; Zhang, K.; Chen, Y., Disk-Like Micelles with a Highly Ordered Pattern from Molecular Bottlebrushes. *ACS Macro Letters* **2014,** *3* (1), 70-73.
55. Berlepsch, H. v.; Böttcher, C.; Skrabania, K.; Laschewsky, A., Complex Domain Architecture of Multicompartment Micelles from a Linear ABC Triblock Copolymer Revealed by Cryogenic Electron Tomography. *Chemical Communications* **2009,** (17), 2290-2292.
56. Dėdinaitė, A., Biomimetic Lubrication. *Soft Matter* **2012,** *8* (2), 273-284.
57. Banquy, X.; Burdyńska, J.; Lee, D. W.; Matyjaszewski, K.; Israelachvili, J., Bioinspired Bottle-Brush Polymer Exhibits Low Friction and Amontons-like Behavior. *Journal of the American Chemical Society* **2014,** *136* (17), 6199-6202.
58. Sheiko, S.; Vatankhah-Varnosfaderani, M.; Zhang, D.; Dashtimoghadam, E. Tissue-Adaptive Materials. WO 2019152537A1, 2021.
59. Fouz, M. F.; Matyjaszewski, K.; Armitage, B. A.; Das, S. R.; Averick, S. Nucleic Acid-Polymer Conjugates for Bright Fluorescent Tags. US 10982266B2, 2021.
60. Sheiko, S.; Vatankhah-Varnosfaderani, M. Self-Assembled Elastomers with Molecularly Encoded Tissue-Like Softness, Strain-Adaptive Stiffening and Coloration. WO 2019046840A1, 2020.
61. Perrier, S., 50th Anniversary Perspective: RAFT Polymerization - A User Guide. *Macromolecules* **2017,** *50* (19), 7433-7447.
62. Gregory, A.; Stenzel, M. H., Complex Polymer Architectures via RAFT Polymerization: From Fundamental Process to Extending the Scope Using Click Chemistry and Nature's Building Blocks. *Progress in Polymer Science* **2012,** *37* (1), 38-105.
63. Foster, J. C.; Radzinski, S. C.; Matson, J. B., Graft Polymer Synthesis by RAFT Transfer-To. *Journal of Polymer Science Part A: Polymer Chemistry* **2017,** *55* (18), 2865-2876.

Chapter 2

Dynamic Intermolecular Graft Exchange of Bottlebrush Polymers

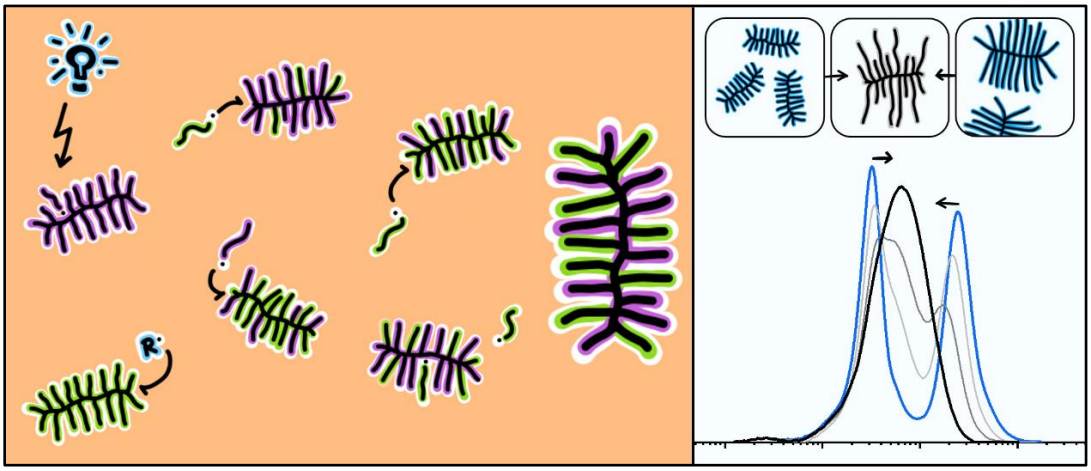

Advances made in controlled polymerisation techniques have given rise to various synthetic strategies for making graft copolymers, each of which have their strengths and limitations. Reversible addition-fragmentation chain transfer (RAFT) polymerisation has been shown to be well-suited for preparing graft copolymers and continues to hold undiscovered possibilities due to the versatile chemistry of RAFT agents. We envisioned the already established Z group grafting from polymerisation mechanism to offer two unexplored routes for graft copolymer synthesis that could find use as a convenient modular strategy for the preparation of extensive polymer libraries. The reactions involved dynamic addition-fragmentation grafting of linear chains between starting materials, which could be graft copolymers, linear polymers, or a mixture thereof. In this study, the new approaches were successfully used to provide a proof of concept for heterograft copolymer synthesis. A critical assessment of the limitations and benefits of the presented synthetic strategies was provided to guide the use and further exploration of similar systems.

2.1 Introduction

The discovery and continuous development of controlled polymerisation techniques have allowed the construction of macromolecules with intricate architectures and topologies. Amongst the architectures of interest, graft copolymers hold promise and have to some extent already been commercialised as viscosity modifiers, emulsifiers, defoamers, lubricants, tissue mimetic materials, and drug delivery vehicles.[1-3] There are three synthetic strategies for their preparation – the *grafting through*, *grafting to*, and *grafting from* approaches – which may be used in conjunction with one or more polymerisation techniques.[4] Further exploration of new synthetic routes is needed to expand the horizons of functional materials to gain access to well-defined materials, to reveal new opportunities in structure-property design, and to make complex architectures more accessible through industrial processes. The use of RAFT polymerisation is well suited for this purpose due to its versatility and applicability for industrial-scale processes.

2.1.1 Preparation of Graft Copolymers Using RAFT Polymerisation

Even two decades after its invention,[5-7] the development of new RAFT polymerisation methods continues to attract attention due to this technique's adaptability and nondemanding reaction conditions.[8, 9] The RAFT process allows the preparation of polymers with predictable molecular weights, reduced dispersities, active end-groups to facilitate further propagation, and complex architectures. One of the most notable benefits is that RAFT polymerisations are akin to conventional free radical polymerisations conducted in the presence of a chain transfer agent, thus making them easy to carry out from an industrial standpoint.[10] The controlling species used in RAFT polymerisations are typically thiocarbonylthio compounds that contain a reactive C=S double bond for radical addition, a Z-substituent to adjust the C=S bond reactivity and intermediate radical stability to suit the monomer of interest, and an R-substituent selected for efficient radical fragmentation and reinitiation (Scheme 2.1A). Numerous RAFT agents have been described in the literature,[8, 11] and suitable R and Z groups have been identified for "more activated monomers" (MAMs) with a vinyl group conjugated to a double bond, an aromatic ring, a carbonyl group, or a nitrile group (e.g., isoprene,[12] methacrylates,[5] styrene,[5] acrylamides[13], and acrylonitrile[14])

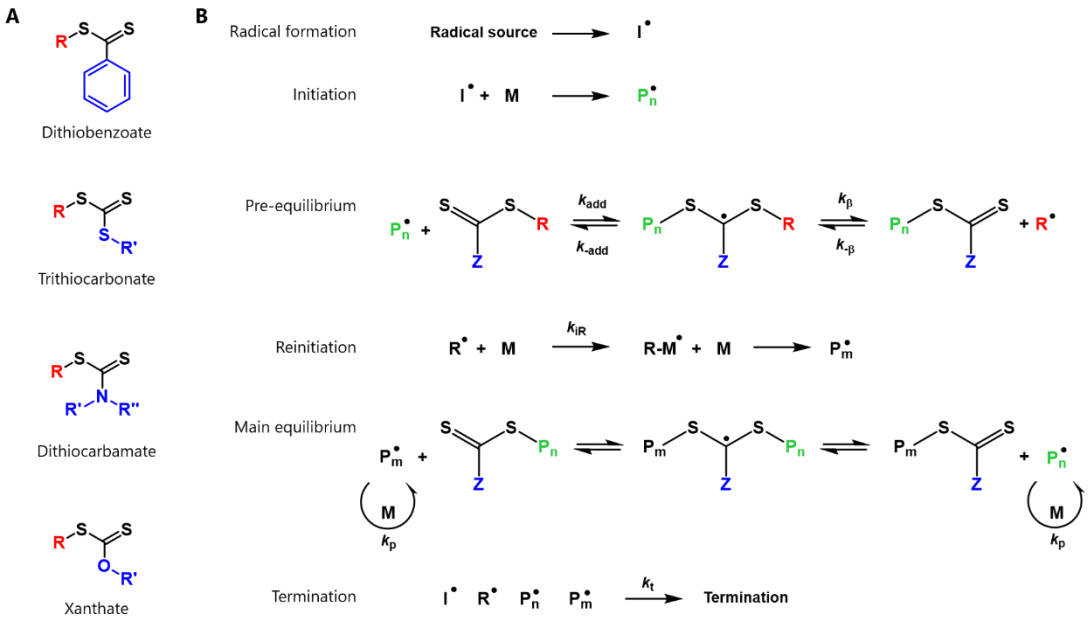

Scheme 2.1 A) General formulas of four RAFT agent classes commonly used for controlling radical polymerisations. **B)** Proposed mechanism of RAFT polymerisation. Adapted from ref. 8.

and "less activated monomers" (LAMs) such as those with a vinyl group next to a heteroatom lone pair (e.g., vinyl acetate[15], *N*-vinylpyrrolidone,[16] and vinyl chloride[17]). The relatively stable radicals of MAMs require a RAFT agent with a high chain transfer constant to provide sufficient stabilisation of the intermediate radical, whereas less stable radicals of LAMs benefit from less stabilising Z groups to aid radical fragmentation.

The mechanism of RAFT polymerisation involves an initiation step similar to conventional radical polymerisation in which an initiator-derived radical ($I^{\bullet}$) reacts with monomer to form a propagating chain radical ($P_n^{\bullet}$) (Scheme 2.1B).[5, 8, 11] In the early stages of the reaction, this radical can take part in a pre-equilibrium step, in which radical addition to the RAFT agent results in the formation of an intermediate radical and fast fragmentation of an R group radical ($R^{\bullet}$). The newly formed radical may reinitiate the polymerisation, thus forming a new chain radical ($P_m^{\bullet}$). Once all R groups have been consumed in the reaction, the system enters the main equilibrium in which a rapid exchange of the thiocarbonylthio groups between propagating radicals allows all chains to grow at equal rates. The prerequisites for a successful RAFT polymerisation are rapid fragmentation of the intermediate radical (high k_{β}), favourable fragmentation of the R group over the polymer chain radical ($k_{\beta} \geq k_{-\mathrm{add}}$), a reactive C=S bond after the displacement of the original R group (high k_{add}), and

efficient reinitiation by the R group radical (high k_{iR}).[11] Bimolecular termination of polymer chains may take place through disproportionation or combination. Since the number of polymer chains generated in a RAFT polymerisation equals the number of all initiating radicals ($R^{\bullet} + I^{\bullet}$) but the number of thiocarbonylthio groups available for chain-end capping is only equal to the number of R group-initiated chains ($R^{\bullet}$), the key to retaining high livingness is to keep the number of initiator-derived radicals small relative to the number of RAFT agents ($I^{\bullet} \ll R^{\bullet}$).

RAFT polymerisation may be used to prepare graft copolymers with any of the three general approaches.[18] Its use to construct the backbone and/or side-chain polymers for *grafting to* offers the general benefits and limitations of RAFT polymerisation.[8] In particular, its good compatibility with various functional groups and the reactivity of the thiocarbonyl end-group[19] may offer useful advantages for selecting coupling chemistries. The main limitation of the approach is steric hindrance near the reactive sites, which sets a practical upper limit on the achievable grafting density. In contrast, *grafting through* RAFT polymerisation may be used to prepare densely grafted polymers. However, such reactions generally suffer from poor control even at moderate backbone lengths due to steric congestion near the propagating and dormant chain-ends.[20]

The *grafting from* approach is very well suited for RAFT polymerisation and is a versatile strategy for constructing highly complex graft copolymer designs.[21] A typical synthesis involves the preparation of a linear polymer, post-modification to introduce RAFT agents along the chain, and subsequent polymerisation to form the grafts. Recent discoveries in the field of RAFT polymerisation have allowed circumvention of the post-modification step by polymerising a chain transfer agent (CTA) -functionalised monomer directly into the backbone.[22, 23] The CTA may be coupled to the backbone via the R group or the Z group, giving rise to two mechanistically distinct approaches (Scheme 2.2).[24] Polymerisation of grafts with the R group approach involves propagating grafts staying attached to the backbone. A successful synthesis requires careful selection of reaction conditions as high radical concentrations may lead to intramolecular and intermolecular coupling.[21, 25, 26] In the Z group approach – more generally referred to as *transfer to* polymerisation – the formation of propagating graft radicals involves their fragmentation off the backbone

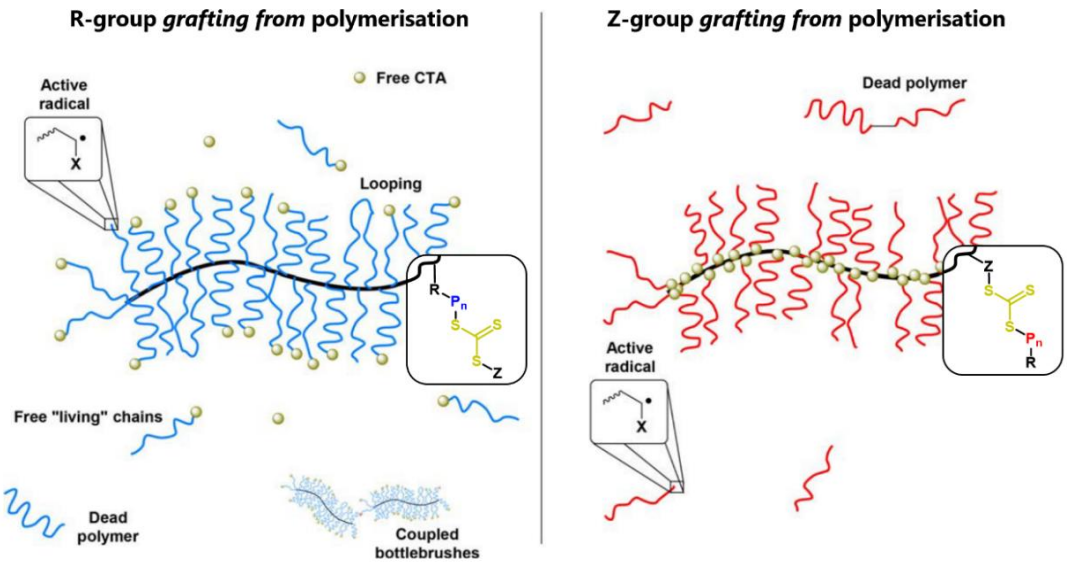

Scheme 2.2 A comparison of R group and Z group approaches. Adapted from ref 27.

and diffusion into the surrounding medium. Similar to *grafting to* reactions, such graft sites may be shielded by neighbouring chains and radical addition to the CTA becomes increasingly demanding with increasing graft lengths. Sterically hindered chain transfer kinetics may lead to poor control over the polymerisation. Freely diffusing chain radicals can undergo termination, thus leading to unattached linear side-products and a reduced grafting density.

2.1.2 New Avenues for Heterograft Copolymer Synthesis

As a result of the detachment of grafts in the *transfer to* polymerisation mechanism, intermolecular graft exchange will occur if the rate of radical diffusion is sufficiently high relative to the rate of chain transfer to the grafting site. We hypothesised this could allow the preparation of heterograft copolymers by mixing distinct graft copolymers prepared via *transfer to* polymerisations and by re-initiating fragmentation of the grafts. This will lead to an exchange of grafts between the backbones, resulting in a heterograft product with a composition dependent on the initial molar ratio of the starting materials. The preparation of a large graft copolymer library would only require two starting materials, and this strategy could therefore find use in systematic studies where a gradual change in a polymer property is of interest. Examples here include heterograft emulsifiers,[28] self-assemblies[29], and antimicrobials.[30] Considering that arguably the most practical ways to prepare heterograft copolymers today are the *grafting to* and *grafting through* approaches, with

the latter suffering from the previously discussed limitations when conducted as a RAFT polymerisation, this new synthetic route may be a highly effective choice for graft copolymer synthesis.

The prerequisite for successful exchange between backbones is the detachment, intermolecular diffusion, and chain transfer of graft radicals from one grafting site to another, despite steric congestion and some probability of termination. Detachment from the original grafting site involves breakage of a C−S bond and chain diffusion into the bulk solvent. This diffusion competes with radical addition back to the original grafting site, with the relative rate constants determining the frequency of successful detachment events. Diffusion sufficiently close to a new grafting site can be hindered by termination and excluded volume interactions of nearby grafts, and the rate of chain transfer may be further limited by the surrounding polymer segments.[31]

A recent literature review by Foster *et al*. discussed various parameters that dictate the reaction kinetics of *transfer to* polymerisations and which may aid or disfavour intermolecular exchange.[27] Detailed studies have investigated the effect of reaction stoichiometry, concentration, CTA selection, temperature, and shielding effects on the quality of the polymerisation product in the preparation of star polymers, graft copolymers, and polymerisations on solid substrates. The appropriate selection of a CTA for the selected monomer(s) is key to ensure the pre-equilibrium step and further radical addition to the substrate is fast enough to control the polymerisation.[32] As in any RAFT polymerisation, each initiating radical leads to a dead chain and the amount of consumed initiator should be kept small relative to the amount of CTA.[33] A relatively low instantaneous radical concentration reduces the probability of termination and may be achieved by slow decomposition of the initiator. While termination can be reduced by selecting appropriate reaction conditions, it cannot be avoided completely, inevitably leading to some reduction in the original grafting density. The relative rate of termination to chain transfer is known to increase with increasing graft length.[34, 35] While this is undesirable, it should alleviate shielding effects and therefore aid intermolecular exchange for the remaining grafts.

Solvent selection and reaction temperature have also been shown to impact the outcome of *transfer to* polymerisations. Monte Carlo simulations of polymerisations for four-arm star polymers have suggested that, while shielding effects near backbone are strongly graft length-dependent under good solvent conditions, they become less

pronounced in a theta solvent.[36] An exponential relationship between the graft length (n) and steric shielding was obtained, expressed as a factor K for which it was found

$$K = An^{-0.45}, \quad (2.1)$$

where A is a scaling constant and K is defined as the ratio of the rate constant of bimolecular polymer-polymer reaction and a similar reaction not located at a polymer chain (k/k_0). The steric shielding factor was shown to decrease rapidly as $n \rightarrow 100$, after which rate of addition to substrate was ten times slower than in the absence of steric interactions. Temperature effects on such polymerisations are complex, influencing rates of propagation and termination, CTA stability, polymer solubility, and solvent viscosity, and need to be evaluated individually for each system.[24]

2.1.3 Complex Architectures Using Photoiniferters

Some of the focal points in the current development of RAFT polymerisation have involved a renaissance of using RAFT agents as the initiator, chain transfer agent, and terminator of a reaction – commonly referred to as an iniferter. Inspired by recent literature in this field, we wanted to harness the photochemical properties of RAFT agents to realise our graft exchange concept. The discovery of photoiniferters was first reported by Otsu long before the invention of RAFT polymerisation, who showed the dissociation of di- and polysulfides into free radicals upon heating or under ultraviolet-visible (UV-Vis) irradiation.[37, 38] This phenomenon may be exploited in RAFT polymerisation to eliminate the need for exogenous initiators, yielding an *α,ω*-bifunctional telechelic polymer with the R and Z groups of the RAFT agent incorporated into the polymer chain-ends.[39] Our current understanding of the iniferter reaction mechanism is similar to that of a conventional RAFT polymerisation,[8] except that the initiation and pre-equilibrium steps are replaced by the photolysis of the C−S bond to form two radicals (Figure 2.1A).[39, 40] Radical formation may lead to subsequent propagation, degenerative chain transfer, termination, or reversible combination of the propagating chain and CTA radicals. While the inherent termination arising from added initiators is absent in iniferter polymerisations, chain termination and decomposition of the *ω*-end-group do occur and lead to dead chains.[41] Recent studies have found ways to suppress these reactions by optimising reaction conditions and introducing additives such as tertiary amines.[42-45]

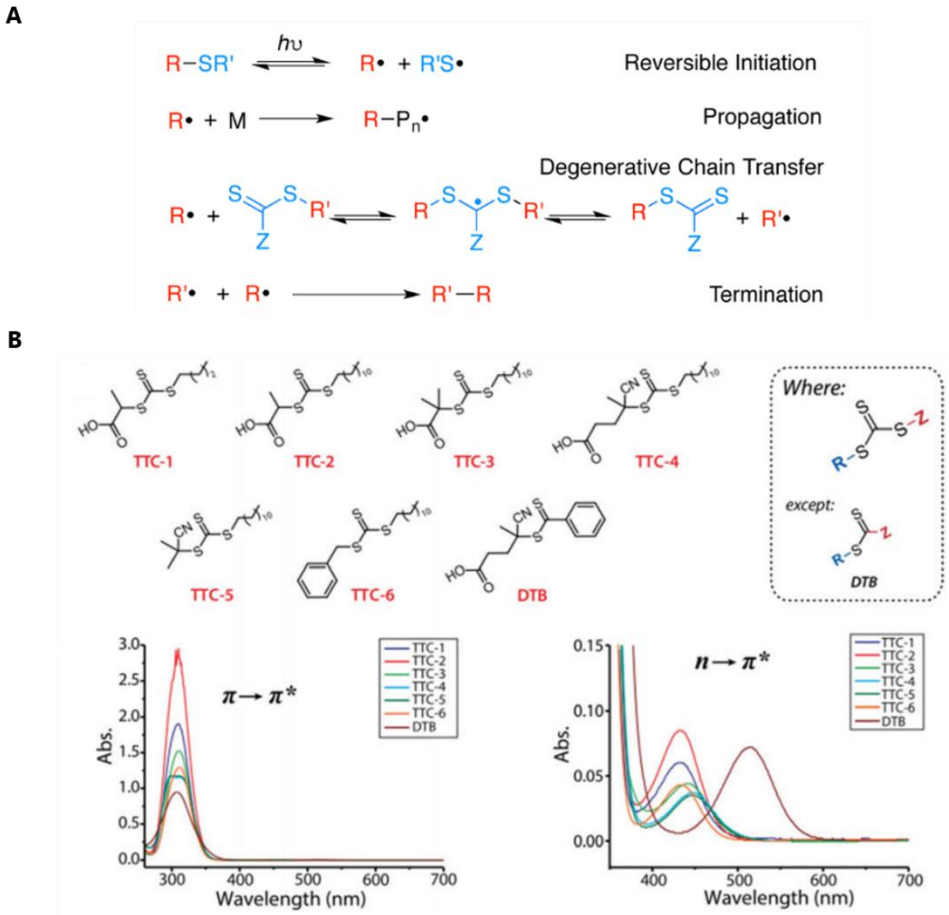

Figure 2.1 A) Proposed reaction mechanism of photoiniferter RAFT polymerisation. Adapted from ref 40. **B)** Various RAFT agents and their UV-Vis absorption spectra in DMSO at 0.1 mM (left) and 1.0 mM (right) concentrations. Adapted from ref 45.

The UV-Vis absorption characteristics of RAFT agents depend mainly on the selected R and Z groups and also on solvent polarity (Figure 2.1B).[45-48] A strong absorption is generally seen around 280-350 nm corresponding to the $\pi \rightarrow \pi^*$ transition, with a roughly constant absorption maximum for all RAFT agents regardless of their structure.[46] A second absorption band is found between 380-550 nm corresponding to the $n \rightarrow \pi^*$ transition, which may shift markedly and typically has a molar absorptivity of 2-3 orders of magnitude smaller than the $\pi \rightarrow \pi^*$ transition.[46] The photolysis of trithiocarbonates and dithiobenzoates was recently studied in detail to show that their lowest singlet and triplet excited-state energies lie near or below their C–S bond dissociation energies.[47] While the quantum yields are low and the excitation of trithiocarbonates to S_1 only leads to a small number of radicals, the corresponding wavelengths of 520 nm (green) and 465 nm (blue) have nonetheless been successfully used for photoiniferter RAFT polymerisations of acrylates and

methacrylates.[22] The addition of photocatalysts have also been used to aid radical generation via electron or energy transfer.[40]

Photoinitiated systems are appealing to polymer chemists due to the convenience of using an external stimulus to regulate the polymerisation, the capability of attaining spatiotemporal control over the reaction, and low operation temperatures. Various studies have already utilised the versatile photochemical properties of RAFT agents to construct complex architectures such as block copolymers and branched polymers,[23, 42, 49, 50] and there is growing interest in externally regulated polymerisations.[9] Notably, the wavelength-dependent electronic transitions and various possibilities for fine-tuning the RAFT agent structure likely holds many opportunities for achieving orthogonal polymerisations via divergent stimuli, and may provide more straightforward synthetic protocols for preparing complex architectures in the future.

2.1.4 Project outline

The Z group approach was envisioned to provide two new synthetic routes for preparing heterograft copolymers. The first route involved a graft exchange reaction between two graft copolymers prepared separately using the Z group approach. A library of graft copolymers with different backbone and graft lengths were prepared to conduct graft exchange reactions initiated either by a thermal initiator or by blue light irradiation. Reactions were monitored with SEC and the products were visualised by AFM to study changes in size due to intermolecular exchange. Alternatively, graft exchange could be conducted between a graft copolymer and a linear polymer capable of forming a radical. The second route involved chain transfer of linear polymers directly to a linear polymer carrying Z group-tethered RAFT agents, thus eliminating the need for graft copolymer starting materials. The fraction of transferred chains was quantified with SEC by monitoring changes in the mass ratios of reactants and the formation of UV-active by-products. The effect of reaction stoichiometry on the degree of linear chain transfer was evaluated to estimate the achievable grafting densities. Finally, the graft length control provided by the approach was compared to that of the Z group polymerisations.

2.2 Results and Discussion

2.2.1 Synthesis and Characterisation of Starting Materials

A library of linear polymers, CTA-functionalised backbones (pCTAs), and graft copolymers were prepared to be used as the starting materials in graft exchange reactions and those involving grafting of pCTAs with linear polymers (*transfer to* reactions) (Scheme 2.3A). The degrees of polymerisation (DPs) of the polymers were selected to suit SEC analysis such that the instrument resolution was sufficient to separate the starting materials in each reaction. Graft copolymer pairs with identical backbones but distinct graft lengths were prepared from short to moderate pCTAs (DP 23 and 133) for the SEC studies, and a longer backbone (DP 300) was used to prepare larger graft copolymers for easier visualisation by AFM. Linear chains (DP 20-44) used in *transfer to* reactions were kept sufficiently long to resolve them from small molecule peaks, but short enough to avoid overlap with the $pCTA_{300}$. Monomers were selected from acrylate and acrylamide families for their fast rates of propagation[8] and applicability to photoiniferter RAFT polymerisations.[42, 44] The reactions were controlled by readily-synthesised trithiocarbonate RAFT agents, which were known to be suitable for the selected monomers.[8]

The precursors of the three pCTAs with DPs of 23, 133, and 300 were prepared via photoiniferter RAFT polymerisation of 2-hydroxyethyl acrylate (HEA) with

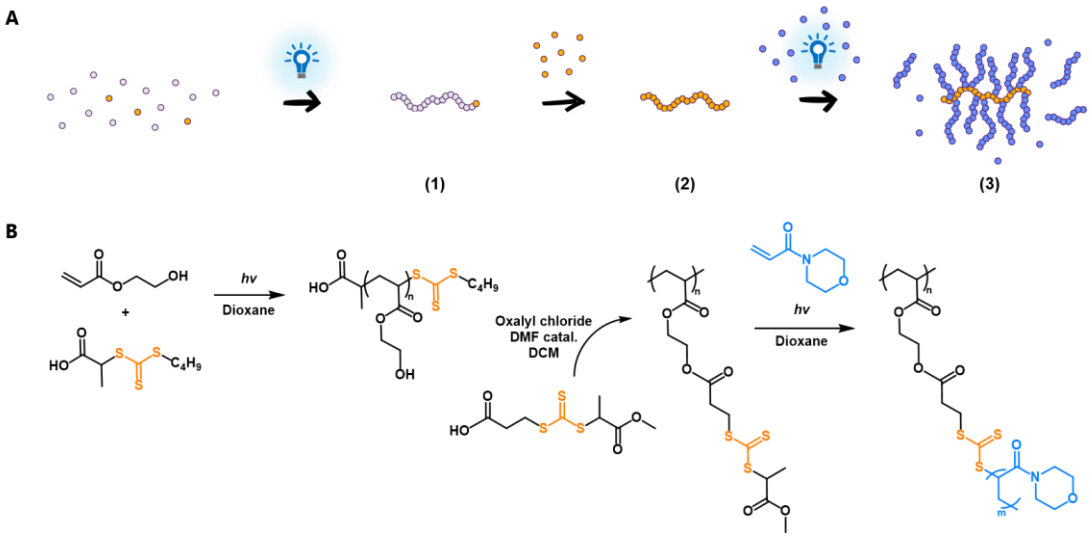

Scheme 2.3 A) An illustration of the synthetic approach used in this work to prepare all starting materials, including linear polymers (1), functionalised backbones (2), and graft copolymers (3). **B)** Reaction scheme for the preparation of graft copolymers. The synthesis involved photoiniferter RAFT polymerisation of 2-hydroxyethyl acrylate, subsequent functionalisation with a RAFT agent, and a polymerisation of grafts via the Z group approach.

2-(((butylthio)carbonothioyl)thio)propanoic acid (PABTC) under blue light irradiation (Scheme 2.3B). Monomer conversion was quantified with ^{1}H NMR spectroscopy (Figure 2.2A) and the products were characterised by SEC in DMF (Figure 2.3A). The reactions proceeded to 80-90% conversion in roughly 15 h, yielding polymers with reasonably narrow dispersities (Table 2.1). The hydroxy groups were subsequently functionalised with 3-((((1-methoxy-1-oxopropan-2-yl)thio)carbonothioyl)thio) propanoic acid (MPPATC) to create initiating sites for graft polymerisation. ^{1}H NMR spectroscopy confirmed successful functionalisation as a downfield shift of poly(2-hydroxyethyl acrylate) (pHEA) side-group protons (−C$\underline{H}_2$-OH, 4.0 ppm) (Figure 2.2B). DMF SEC profiles of the pCTAs showed a high molecular weight shoulder, possibly due to a side-reaction of HEA with oxalyl chloride to form the oxalic acid ester[51] or reaction between pHEA α-end and a hydroxy group which resulted in bimolecular coupling (Figure 2.3).

Using such pCTAs as photoiniferters, a series of graft copolymers was prepared via polymerisation of 4-acryloylmorpholine (NAM) under blue light irradiation. All but one reaction was stopped at 64-85% conversion to avoid monomer-starved conditions in order to minimise termination reactions between graft radicals. DMF SEC analysis showed the presence of terminated grafts in all products (Figure 2.3B), the mass fraction of which was found to be highest for reactions

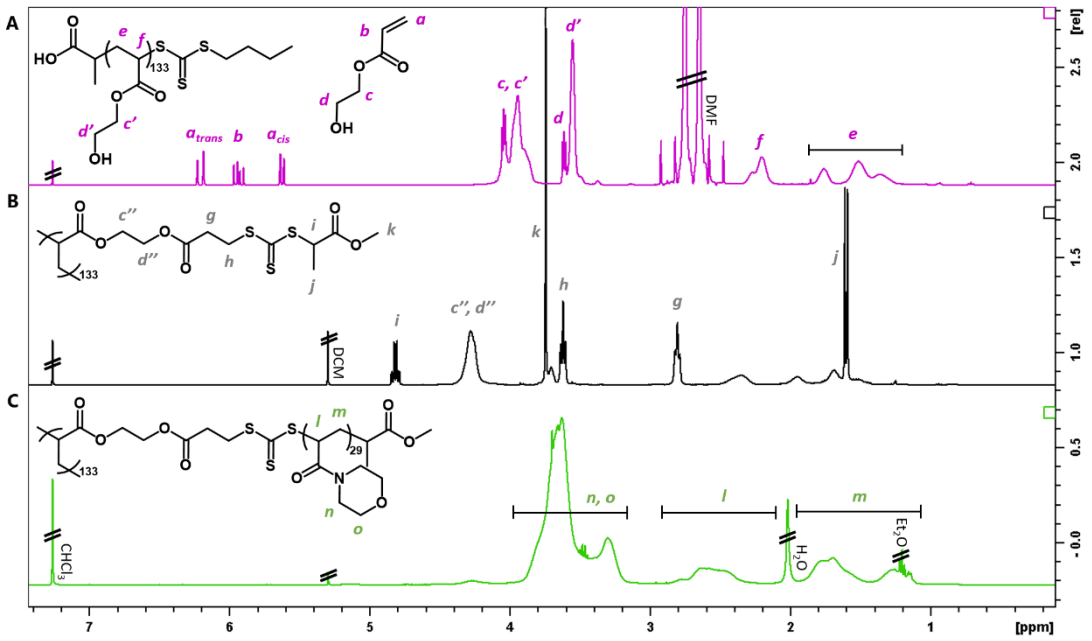

Figure 2.2 ^{1}H NMR spectra of the crude pHEA$_{133}$ backbone (**A**), the backbone after functionalisation (**B**), and pNAM$_{133x29}$ graft copolymer prepared using the functionalised backbone (**C**).

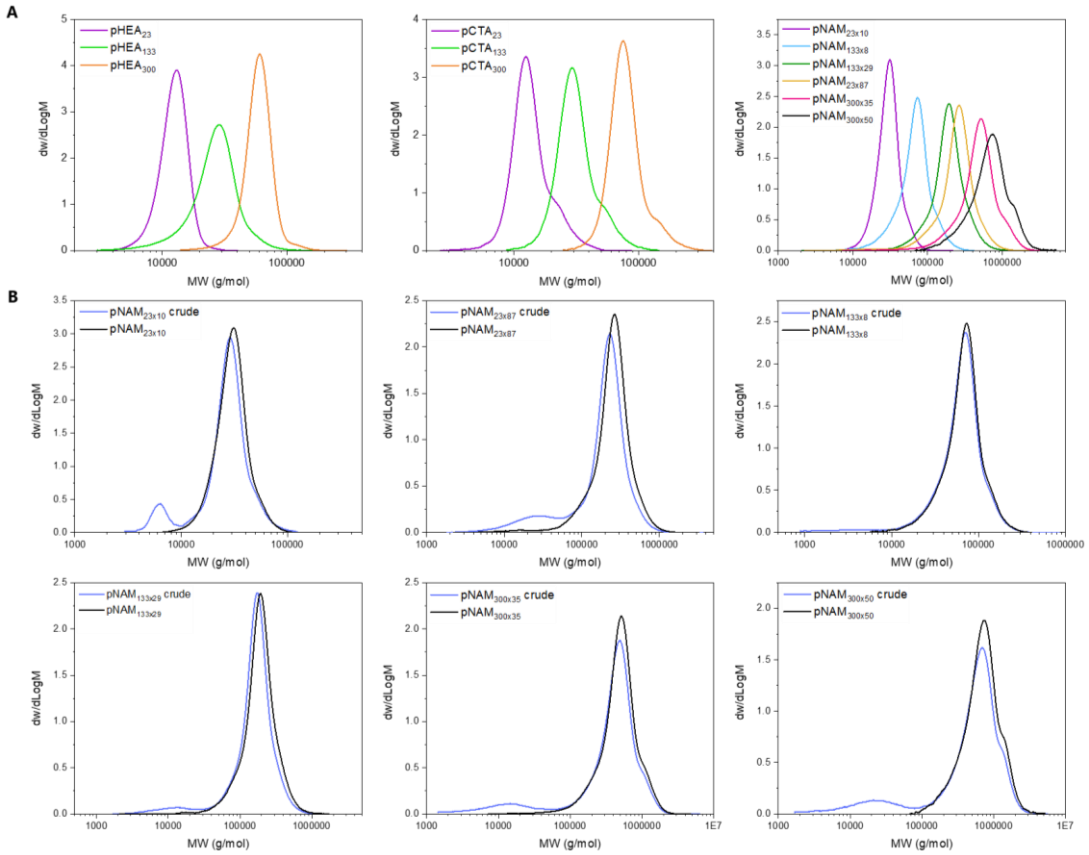

Figure 2.3 A) SEC profiles of all pHEA backbones, functionalised backbones (pCTAs) and graft copolymers employed in this study. pNAM$_{axb}$ denotes the number-average backbone, *a*, and graft lengths, *b*, calculated from conversion. Analysis was carried out in DMF with DRI detection and PMMA calibration. **B)** SEC profiles of each graft copolymer before and after removal of terminated grafts.

targeting long grafts (pNAM$_{23x87}$ and pNAM$_{300x50}$, 30 wt% and 20 wt% respectively) and a reaction continued under monomer-starved conditions (pNAM$_{23x10}$, 8 wt%) (Table 2.1). To compare the number of grafts terminated in each reaction, the relative number of terminated chains (n_{rel}) – descriptive of the loss in grafting density – was calculated from the RI vs. retention time (RT) plots as

$$n_{\mathrm{rel}} = \frac{A_{\mathrm{RI,T}}}{A_{\mathrm{RI,tot}}} \cdot \frac{1}{\mathrm{DP_G}}, \tag{2.2}$$

where $A_{\mathrm{RI,T}}$ is the area of terminated grafts, $A_{\mathrm{RI,tot}}$ is the total area of the sample and $\mathrm{DP_G}$ is the number-average DP of grafts based on conversion. In all reactions stopped at moderate monomer conversions, the number of terminated chains was found to increase with increasing chain length. This was in agreement with the literature, as longer polymer chains have been reported to suffer from shielding effects around the

Table 2.1 Structural information and characterisation details of all polymers synthesised in this work.

	Structure [A]	**Conv.** [B] **(%)**	**DP$_p$** [C]	**m_T** [D] **(%)**	**n_{rel}** [E] **·10^3**	**$M_{n,th}$** [C] **(g/mol)**	**$M_{n,SEC}$** [F] **(g/mol)**	**$Đ$** [F]
.1	$pHEA_{23}$	60	23	-	-	2,900	11,800	1.07
.2	$pHEA_{133}$	85	133	-	-	15,700	23,300	1.23
.3	$pHEA_{300}$	91	300	-	-	35,100	56,400	1.08
1	$pCTA_{23}$	-	23	-	-	8,700	12,800	1.14
2	$pCTA_{133}$	-	133	-	-	48,800	29,500	1.14
3	$pCTA_{300}$	-	300	-	-	110,000	75,600	1.11
1a	$pNAM_{23x10}$	98	10	8	8.1	41,100	28,000	1.14
1b	$pNAM_{23x87}$	85	87	30 [G]	3.5	285,000	178,000	1.56
2a	$pNAM_{133x8}$	64	8	≤2	≤2.5	189,000	56,700	1.32
2b	$pNAM_{133x29}$	82	29	4	1.4	562,000	157,000	1.34
3a	$pNAM_{300x50}$	80	50	20	4.1	2,230,000	548,000	1.43
3b	$pNAM_{300x35}$	85	35	9	2.6	1,590,000	368,000	1.51
4	$pNAM_{20}$	65	20	-	-	3,100	2,900	1.12
5	$pNAM_{30}$	80	30	-	-	4,500	4,500	1.12
6	$pNAM_{44}$	87	44	-	-	6,500	6,100	1.10
7	pyr-$pNAM_{15}$	95	15	-	-	2,600	2,800	1.19

[A] $pNAM_{AxB}$ denotes the DPs of the backbone (A) and grafts (B).

[B] Monomer conversion based on ^{1}H NMR spectroscopy.

[C] Degree of polymerisation calculated from conversion

[D] Mass percent of terminated grafts in the crude product as given by RI vs RT data.

[E] Relative number of terminated chains determined from RI vs RT plots as $n_{rel} = (A_T/A_{tot})/DP$.

[F] Determined by SEC analysis in $CHCl_3$ (7) or DMF (all other polymers) with DRI detection and PMMA calibration. The values reported for graft copolymers were obtained after the removal of terminated grafts.

[G] Estimated by Gaussian distribution fitting of the overlapping distributions.

chain radicals[31] and the graft attachment sites,[34] therefore reducing the number of collisions between the two and increasing the probability of termination. The lower concentration of CTA when targeting longer grafts likely also contributed to termination by increasing the cumulative time each growing chain spent as a propagating radical.[8] Isolation of the products involved repeated precipitation to remove residual monomer and a selective precipitation to remove terminated chains. ^{1}H NMR analysis was used to ensure no monomer remained in the product (Figure 2.2C). DMF SEC analysis confirmed successful removal of terminated chains (Figure 2.3B).

Linear polymers needed for *transfer to* reactions were prepared via photoiniferter RAFT polymerisation of NAM using PABTC (Table 2.1). While the

photoiniferter approach offered practical advantages such as convenient temporal control and a simpler experimental protocol, one notable disadvantage compared to the use of added initiators was our inability to estimate chain livingness. Recent studies have used chain extensions to demonstrate that high living character may be achieved in photoiniferter RAFT polymerisations.[42] However, the rate of termination and end-group decomposition can be highly dependent on the reaction conditions and therefore difficult to predict.[45] In this study, dead chains would not be reactive yet would contribute to the total mass detected with DRI in SEC. This issue could be circumvented by quantifying *transfer to* reactions using the characteristic UV absorption of the trithiocarbonate end-group at 309 nm, which is only present in living chains. Finally, 4-(pyren-1-yl)butyl 2-(((butylthio)carbonothioyl)thio)propanoate was used to conduct the RAFT polymerisation of NAM. The resulting polymer posessed pyrene functionality at the α-end, thus enabling UV detection at 265 nm, where the trithiocarbonate ω-end showed very little absorption (*vide infra*).

2.2.2 Intermolecular Graft Exchange Between Graft Copolymers

Intermolecular graft exchange via the Z group *grafting from* mechanism was studied by employing various backbone and graft lengths and a thermal initiator or photoiniferter chemistry. A successful reaction required the generation of graft radicals, their diffusion away from the original binding site, and sufficiently close to a CTA on another molecule to react with it (Scheme 2.4). The possible outcomes of graft radical formation include:

I. addition to / recombination with the original grafting site,
II. addition to a reactive site of the same molecule,
III. addition to a reactive site of another molecule, or
IV. termination,

with I leading to no exchange, II leading to intramolecular exchange, III leading to intermolecular exchange and therefore being the desired outcome, and IV leading to a reduced grafting density.

Graft radical formation involves breaking of a trithiocarbonate C−S bond photolytically or through an addition-fragmentation event triggered by an initiator-derived radical. The rate of radical formation could be controlled by adjusting the light

intensity (photolysis), reaction temperature (photolysis and thermal initiator), and the CTA or initiator concentration (photolysis and thermal initiator, respectively). Instantaneous radical concentration is known to affect the probability of biradical

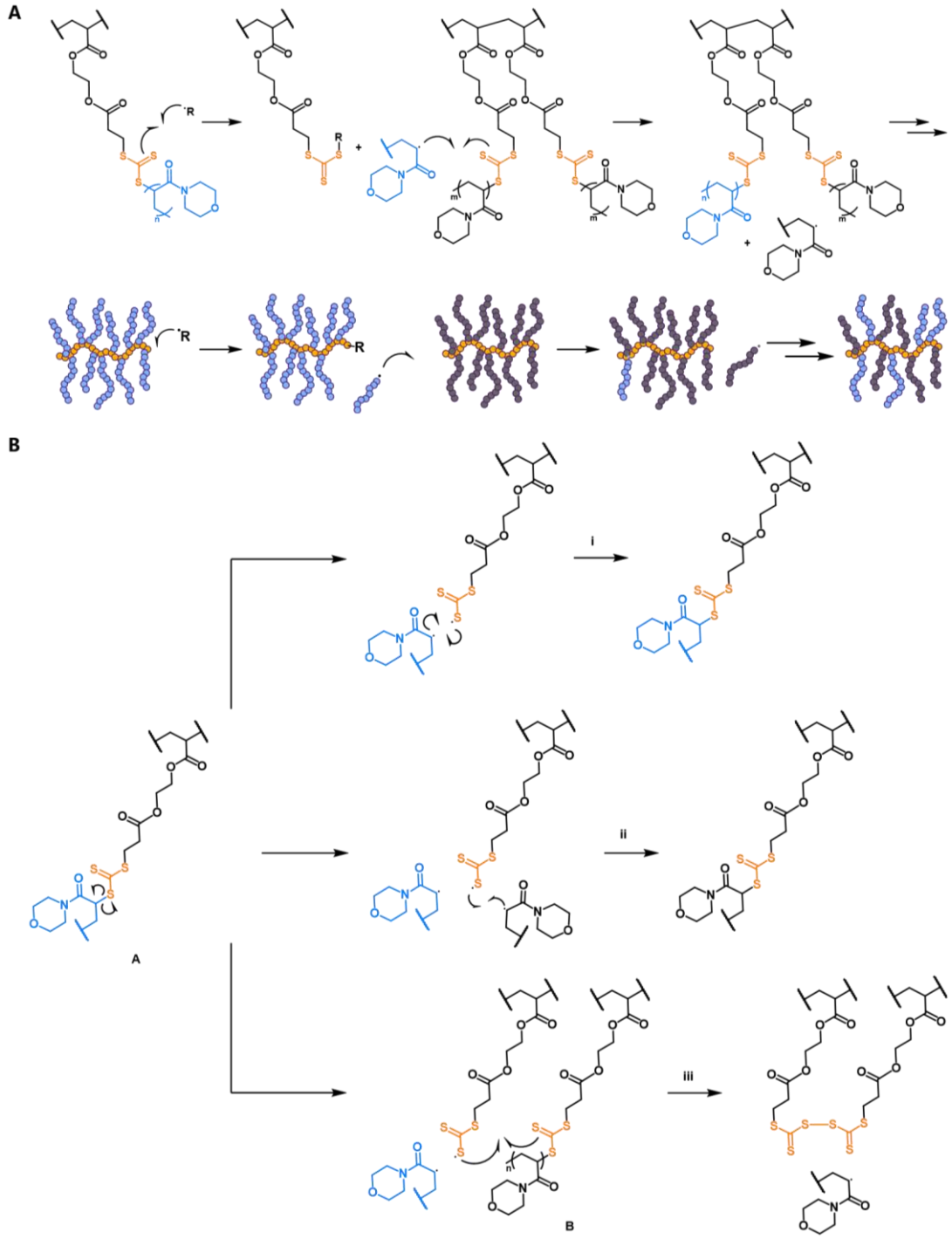

Scheme 2.4 A) Proposed graft exchange mechanism. Radical addition to a grafting site (i) leads to graft fragmentation and intermolecular addition to CTA (ii), consequently fragmenting the original graft. Repeated events give a homogeneous product. **B)** Possible fates of a trithiocarbonate side-chain radical in photoiniferter reactions: recombination with original graft (i), combination with another graft radical (ii), reaction with a trithiocarbonate or a trithiocarbonate radical (iii), and decomposition and other irreversible reactions (not shown). A and B may represent grafts on shared or individual backbones.

termination and should be kept low to moderate.[27] While determining the rate of radical formation was straightforward for a thermal initiator,[52] it could not be estimated quantitatively for the photoiniferter system. It is known, however, that the quantum yield for radical formation through the $n \rightarrow \pi^*$ excitation of trithiocarbonates, corresponding to the blue light regime, is low ($<10^{-4}$).[47] Furthermore, the relative stabilities of the initiator-derived radicals and the graft radicals were known to determine the direction of RAFT equilibrium.[8] Graft radicals should ideally be more stable than initiating radicals to favour graft fragmentation. Initiation with the selected methacrylate-like radicals of V-601 was expected to favour re-fragmentation of the initiating radical over the acrylamide-type graft radicals, leading to a poor fragmentation efficiency.

After radical formation, diffusion was expected to compete with cage reactions[53] (photolysis) or chain transfer back to the original CTA (thermal initiator). The relative rates of reaction and diffusion were anticipated to determine the probability of a successful detachment event. Recombination rate constants are challenging to measure directly. However, the magnitudes of recombination and chain transfer rate constants found in the literature could be used as a qualitative guide. Rate constants of the order of 10^{10} M^{-1} s^{-1} have been reported for methyl radical recombination in liquids,[54] while some rate constants for polymer radical combination in solution have been measured to be in the range of 10^8-10^9 M^{-1} s^{-1}.[31, 55] The values are in stark contrast to the 10^{-6} M^{-1} s^{-1} values reported for monomer addition to dithioesters.[56] Thus the diffusion limit is likely to be much more stringent in photoiniferter reactions. Considering the diffusivities of small molecules in liquids are about 10^{-5} cm^2 sec^{-1} and those of large molecules such as polystyrene about 10^{-7} cm^2 sec^{-1},[55] the rate of diffusion could be expected to vary considerably depending on the mean chain length. Finally, longer chain radicals may be shielded by surrounding polymer segments, leading to a reduced reaction rate.[31]

To test our hypothesis of intermolecular graft exchange taking place in the Z group approach, an exchange reaction was performed between graft copolymers $pNAM_{23x10}$ (**1a**) and $pNAM_{23x87}$ (**1b**) under typical RAFT polymerisation conditions with V-601 ($[CTA]/[I]_0=20$) at 75 °C in dioxane. An equal mass of each polymer was used in the reaction, corresponding to a roughly 7:1 molar ratio of short and long grafts. The polymers comprised identical backbones (DP 23) but different graft lengths (DPs 10 and 87) and were therefore expected to exhibit a unimodal molecular weight

distribution (MWD) upon successful exchange. Samples were withdrawn from the reaction mixture at various time points over 15 h and analysed by DMF SEC to monitor the reaction.

The chromatogram of a sample taken before initiation showed two distinct MWDs, corresponding to $pNAM_{23x10}$ with short grafts at the lower end and $pNAM_{23x87}$ with longer grafts at the higher end of the molecular weight range (Figure 2.4A). A significant change in the MWD was observed after 15 minutes, indicating successful initiation of intermolecular graft exchange. The change became more apparent after 45 min as the smaller and larger species shifted further towards higher and lower molecular weights, respectively. The hydrodynamic volume of the largest polymers seemed most affected, likely due to a significant increase in their backbone flexibility. After 3 h and 50% initiator decomposition the extent of graft exchange was sufficient to result in a nearly uniform MWD with a small peak split still visible in the chromatogram. Terminated grafts were discernible below 5,000 g/mol, and their amount increased up to 4 wt% with further initiator decomposition. Their mass was equal to the expected quantity of termination products calculated from $[CTA]/[I]_0$ and mass fraction of grafts in the reaction (88 wt%), which predicted the termination of 5 mol% of grafts to lead to a 4 wt% mass loss.

The data indicated a successful graft exchange reaction, yielding a product with a slightly reduced grafting density and a dispersity comparable to that of the high-molecular weight starting material (Table 2.2). The main distribution exhibited subtle

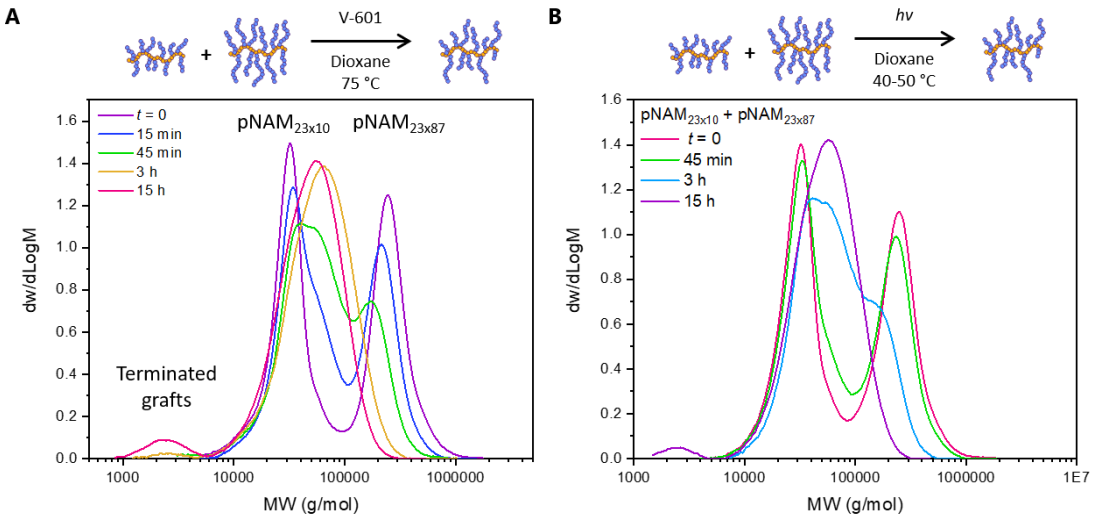

Figure 2.4 SEC data of graft exchange reactions between graft copolymers $pNAM_{23x10}$ and $pNAM_{23x87}$ at an equal mass ratio of the two polymers. Reactions were initiated by thermal initiator (**A**) and under blue light irradiation (**B**). Analysis was performed in DMF with DRI detection and PMMA calibration.

peak asymmetry after the reaction. This is most likely due to the different degrees of termination in the polymerisations of the starting materials, which lead to slightly different grafting densities and therefore distinct chain volumes despite having uniform graft length distributions after the exchange. Considering that the number-average backbone length in this reaction was much shorter than the average graft length, the latter was thought to make a more significant contribution to the overall hydrodynamic volume. Furthermore, since the backbone dispersity ($Đ$=1.14) was lower than the expected overall graft dispersity, the dispersity of the exchange product was thought to primarily depend on the latter. Graft dispersity could be expected to increase in Z group reactions with an increasing graft length (*vide infra*), and therefore the dispersity of the longer grafts would set a rough lower limit for the dispersity of the exchange product.

Table 2.2 SEC analysis results for all graft exchange reactions conducted in this study. Analysis was carried out in $CHCl_3$ (**E4**) or DMF (all other reactions) using DRI detection and PMMA calibration.

				Before exchange		After exchange		
	Initiation	**Starting materials**	**Mixing ratio**	$M_{n,SEC}$ **(g/mol)**	$Đ$	$M_{n,SEC}$ [A] **(g/mol)**	$Đ$ [A]	m_T [B] **(%)**
E1	Δ	$pNAM_{23x10}$ $pNAM_{23x87}$	1:1 mass	28,000 169,000	1.14 1.51	39,600	1.46	4
E2	*hν*	$pNAM_{23x10}$ $pNAM_{23x87}$	1:1 mass	28,000 169,000	1.14 1.51	42,400	1.48	6
E3.1	*hν*	$pNAM_{133x8}$ $pNAM_{133x29}$	1:1 mass	56,700 157,000	1.32 1.34	101,000	1.16	4
E3.2	*hν*	$pNAM_{133x8}$ $pNAM_{133x29}$	1:2 mass	56,700 157,000	1.32 1.34	120,000	1.13	7
E3.3	*hν*	$pNAM_{133x8}$ $pNAM_{133x29}$	2:1 mass	56,700 157,000	1.32 1.34	88,200	1.16	N/A [C]
E4	*hν*	$pNAM_{23x10}$ pyr-$pNAM_{15}$	1:1 mol grafts	37,800 2,800	1.12 1.19	37,800 2,100	1.11 1.23	-
E5	Δ	$pNAM_{23x10}$ $pNAM_{300x51}$	1:1 mol grafts	28,000 480,000	1.14 1.42	N/A[D]	N/A[D]	12

[A] Reported for the main distribution.

[B] Mass percent of terminated grafts.

[C] Below the detection limit.

[D] Not analysed due to significant overlap, see Figure 2.6.

The reaction was repeated in the absence of added initiator under blue light irradiation at 40-50 °C. SEC data showed that a nearly identical transformation of the MWD took place over 15 h; however, the apparent rate of graft exchange was slower than in the initiator-driven reaction (Figure 2.4B). This slower reaction rate implied a reduced frequency of successful detachment events, likely due to a slower rate of radical formation, cage reactions and/or a reduced chain diffusivity due to a reduced temperature and higher solvent viscosity. Repeated attempts at lower temperatures (20-30 °C) resulted in no apparent exchange over 15 h. This observation was ascribed to elevated temperatures aiding bond dissociation. Photoiniferter exchange resulted in roughly 6 wt% terminated chains, which was slightly higher than what was found in the initiator-driven reaction. Given that the MWD of grafts was the same in each reaction, chain length could be excluded as a contributing factor in the probability of termination. Instead, the small difference was attributed to changes inradical concentration, chain diffusivity, and possibly solubility.

The resemblance of the MWD evolution in the two reactions – in particular the comparable amount of termination products – was notable considering their mechanistic differences (*vide supra*). The initiator-driven reaction involved addition-fragmentation events wherein each fragmented graft radical leaves behind a stable side-group which remains dormant until subsequent radical addition. Regardless of the amount of initiator used, an ideal system should retain side-group livingness as initiator-derived radicals may change the original R group but should leave the side-group reactive to further addition-fragmentation. The relative stabilities of the original or initiator-derived R group and graft radicals will, however, dictate the direction of the RAFT equilibrium.[8] While the side-group activity towards incoming radicals may theoretically be preserved even at high initiator concentrations, each initiator-derived radical taking part in the reaction results in a dead graft, therefore reducing the grafting density. These mechanistic considerations are in contrast with the photoiniferter exchange, in which photolytic formation of a graft radical leaves behind a trithiocarbonate side-group radical. Due to their high reactivity the lifetime of both species is expected to be short, raising questions about the fate of the side-group radical when recombination does not occur. The side-group radical may be envisioned to combine with a graft radical fragmented off another side-group thus leading to intra- or intermolecular exchange, to react with another trithiocarbonate or a trithiocarbonate radical to form a disulfide bond, or to undergo decomposition or other irreversible

reactions leading to a dead side-group. While both disulfide formation and decomposition pathways lead to a reduced grafting density, the effect may be reversible in the former case as the bond may be cleaved photolytically or fragmented via radical addition. Given that disulfide formation should result in graft termination, it seemed this reaction did not occur to any large extent. Observations made in some *grafting from* polymerisations of pNAM grafts in which extensive intermolecular coupling took place at high monomer conversions could support the hypothesis of disulfide bond formation taking place under favourable reaction conditions. Due to the backbone CTA still being present, the possibility of backbone-graft coupling could not be excluded, but its probability should be considerably smaller than disulfide bond formation considering steric and statistical factors. Another plausible side-reaction was chain transfer to polymer, which is known to occur with acrylates[57, 58] but may also take place with acrylamides.[59] A low reaction temperature should, however, disfavour such reactions.[8]

One of the advantages of the presented synthetic strategy is that the graft distribution may be conveniently adjusted with reaction stoichiometry. This could be particularly advantageous for carrying out systematic studies across large polymer libraries in which one or multiple properties of the polymer, such as the aspect ratio, rigidity, solubility, charge, or a functionality, are systematically varied. To this end, a series of photoiniferter graft exchange reactions between $pNAM_{133x8}$ (**2a**) and $pNAM_{133x29}$ (**2b**) was carried out using 1:1, 1:2, or 2:1 mass ratios over 15 h. SEC analysis indicated the reaction to yield three products with distinct hydrodynamic volumes (Figure 2.5A). Some termination was observed in all reactions (≤7 wt%), the amount of which increased with increasing average graft length.

Another benefit of this approach is that the reaction mechanism may be used to exchange grafts for any linear polymers capable of forming a chain radical. This was demonstrated by exchanging grafts of $pNAM_{23x10}$ (**1a**) for pyrene-functional linear $pNAM_{15}$ (**7**) under blue light irradiation. Equimolar amounts of linear chains and grafts were used in an attempt to exchange 50% of the original grafts for pyrene-functional grafts. The exchange was monitored with SEC using DRI and multiple-wavelength UV detection. The transfer of pyrene-functional chains to the graft copolymer was monitored at a wavelength of 265 nm at which trithiocarbonate groups absorb only weakly but pyrene has a strong absorption. The data showed a gradual

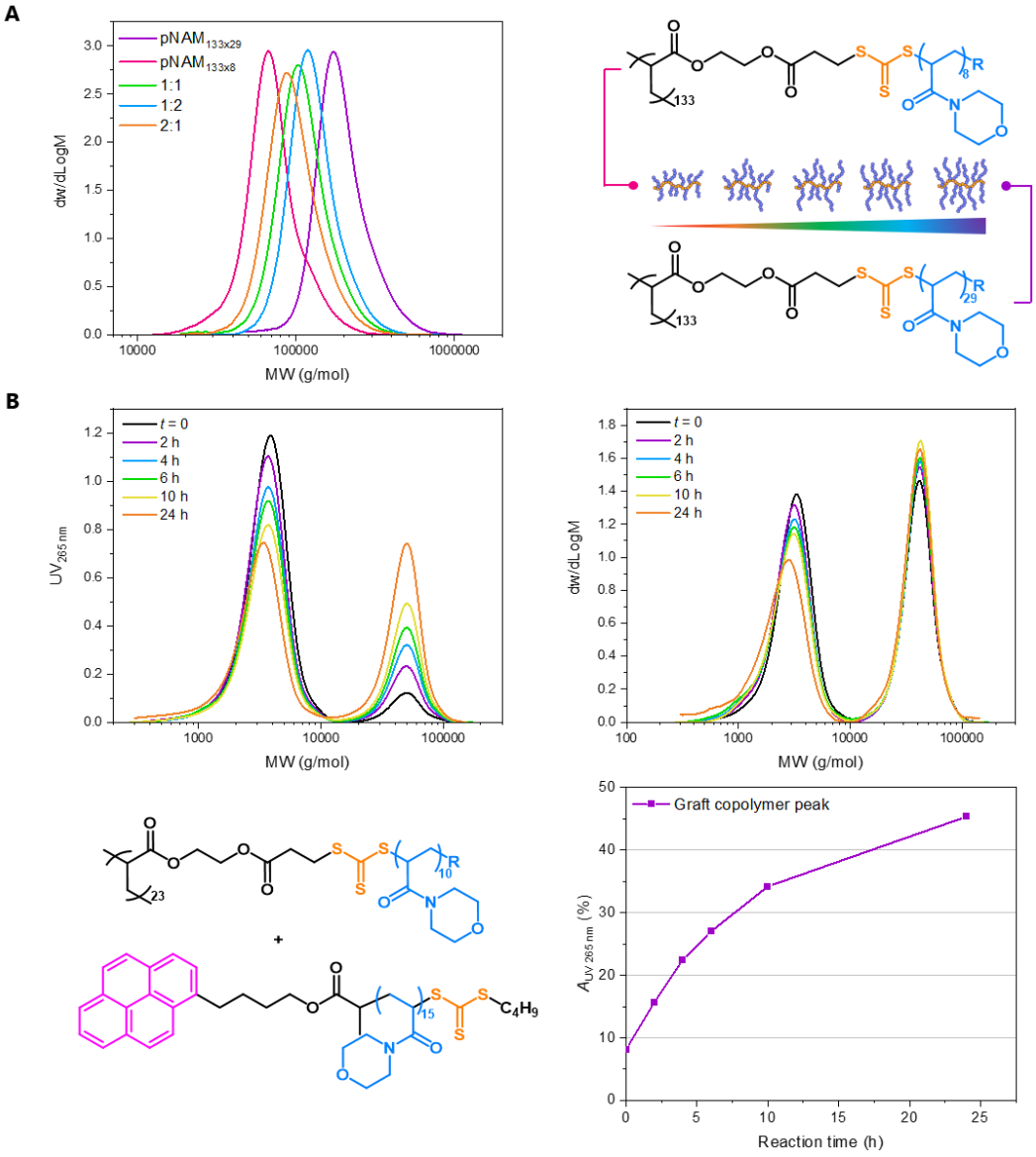

Figure 2.5 A) SEC data of graft exchange reactions between $pNAM_{133x8}$ and $pNAM_{133x29}$ conducted at varying mass ratios of the starting materials. **B)** SEC data showing exchange of $pNAM_{23x10}$ grafts for pyrene-functional linear $pNAM_{10}$ chains. UV detection wavelength (265 nm) was selected to be strongly absorbed by pyrene and only weakly absorbed by the trithiocarbonate groups. Areas under UV vs. MW plots were normalised. Analysis was conducted in $CHCl_3$ with PMMA calibration.

increase in the UV absorption of the graft copolymer relative to the linear polymer over 24 h (Figure 2.5B). DRI detection showed a slight change in the MWDs due to the average DP of the grafts being slightly less than that of the linear chains, resulting in the relative area of the linear chain distribution getting smaller and shifting towards lower molecular weights with increasing reaction time. Formation of low-molecular weight products was not observed at 309 nm, suggesting that the photolytically cleaved trithiocarbonate ω-ends of pyr-$pNAM_{15}$ combined with graft radicals fragmented off the backbone. The data confirmed successful functionalisation of the

original graft copolymer with a fluorescent probe. Using this method, the degree of functionalisation may be conveniently adjusted by varying the reaction stoichiometry.

Graft exchange products were further visualised with AFM on mica to complement SEC analysis. An initiator-driven graft exchange reaction between $pNAM_{133x8}$ (**2a**) and $pNAM_{300x50}$ (**3a**) with dissimilar backbone and graft lengths was monitored using DRI and UV detection at 309 nm to distinguish the UV-active graft copolymers from terminated grafts. UV vs RT plots showed two MWDs after the reaction due to the large difference in the backbone lengths and some 12 wt% terminated grafts (Figure 2.6A). AFM imaging of the diluted reaction mixture before the reaction showed two distinct graft copolymers, differing in length, width, and rigidity (Figure 2.6B). After the reaction, the two could only be distinguished by their backbone lengths, while their graft lengths appeared similar. A considerable number of terminated grafts were also visible on the substrate after the reaction.

The reactions discussed thus far proved the hypothesis of an interchange of Z group tethered grafts leading to uniform products. The reaction mechanism was successfully harnessed to exchange the grafts of distinct starting materials as a proof of concept for heterograft copolymer synthesis. Both external initiators and photoiniferter chemistry were successfully employed as the initiating strategy. This novel, modular approach could find use in systematic studies for which extensive polymer libraries are needed to study gradual changes in polymer structure and properties. In applying the presented approach, particular attention should be paid to the amount of initiator used and its rate of decomposition (or light intensity) to minimise termination reactions, which may be expected to increase with increasing graft length. The dependence of reaction and diffusion rates on the reaction medium and temperature should be considered as parameters that may be used for optimisation. Given that the chain length dependence of shielding effects near the grafting sites has been shown to be less pronounced in a theta solvent than in a good solvent,[36] the effect of solvent quality on the reaction rate and termination remains as a key parameter to explore further. While in this work all exchange reactions were conducted in the absence of monomer, the reactions could alternatively be carried out as a block extension of the original grafts. In reactions employing various monomer families (e.g., methacrylic and acrylic monomers), the relative reactivities of each should be taken into consideration in designing each system.

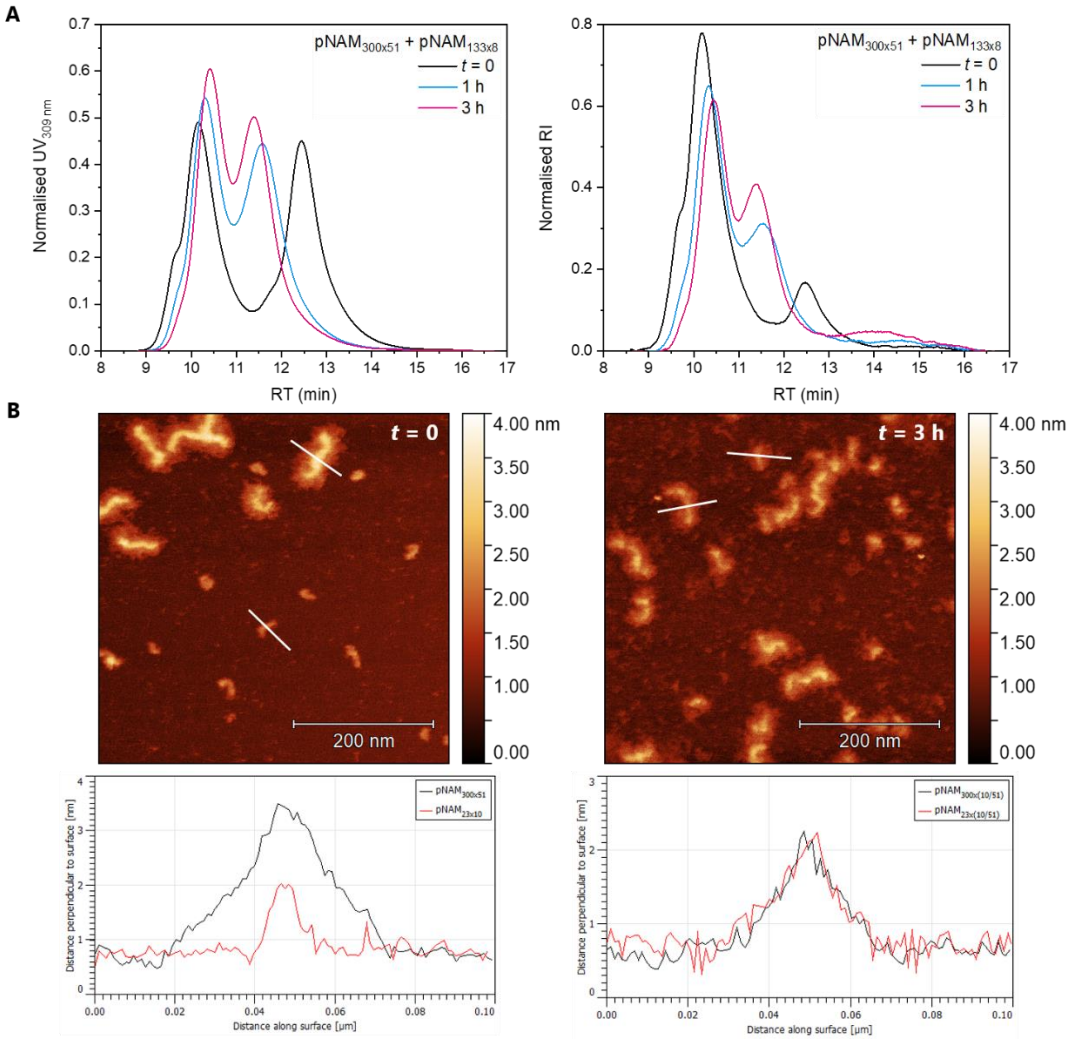

Figure 2.6 A) SEC data of an initiator-driven graft exchange between $pNAM_{133x8}$ and $pNAM_{300x51}$ at an equimolar ratio of grafts. Analysis was conducted in DMF. **B)** AFM images and height profiles show the starting materials to have distinct backbone and graft lengths before the reaction. After 3 h, all polymers appeared to have a similar width, indicating a successful graft exchange.

2.2.3 Transfer of Linear Chains to Functionalised Backbones

The Z group approach mechanism was envisioned to offer an alternative synthetic route for making graft copolymers wherein linear polymer chain radicals are added to a pCTA. Using this approach, the graft copolymer architecture could be accessed directly from a mixture of linear polymers in a similar fashion to the *grafting to* approach. Similar, albeit irreversible grafting strategies with polymeric radicals have been previously studied, for example by grafting TEMPO-functionalised poly(ethylene oxide) to a functionalised pHEA.[60, 61]

Both thermal initiators and iniferters were considered applicable to the reactions. In initiator-driven reactions, grafting involves forming a radical on the linear polymer which may add to a backbone CTA and lead to R group fragmentation

(Scheme 2.5A). The R group radical should be selected to be more stable than the linear polymer chain radical to favour R group fragmentation.[8] The newly added graft may be later fragmented off as a result of radical addition to the same CTA. Each grafted chain was expected to produce a UV-active by-product via combination with an initiator-derived or an R group radical. In photoiniferter reactions, initiating radicals may be formed via photolysis of the linear polymer chain-end and/or the backbone CTAs, depending on the selected wavelength. The grafting step involves an addition-fragmentation event between the linear chain and backbone CTA (Scheme 2.5B) or a radical combination. However, at low radical concentrations the probability of combination is expected to be lower than that of chain transfer. Under a suitable irradiation wavelength, the attached graft may be re-fragmented by photolysis. The expected by-products of graft addition were formed via end-group combination with an R group radical or another end-group to form a disulfide bond. The UV-active by-products provide a convenient way to monitor the reaction with SEC.

Due to the ability of grafts to continuously fragment off the backbone, the reaction was expected to reach an equilibrium wherein the addition and fragmentation of grafts would take place at equal rates. Therefore, the reactions were expected to

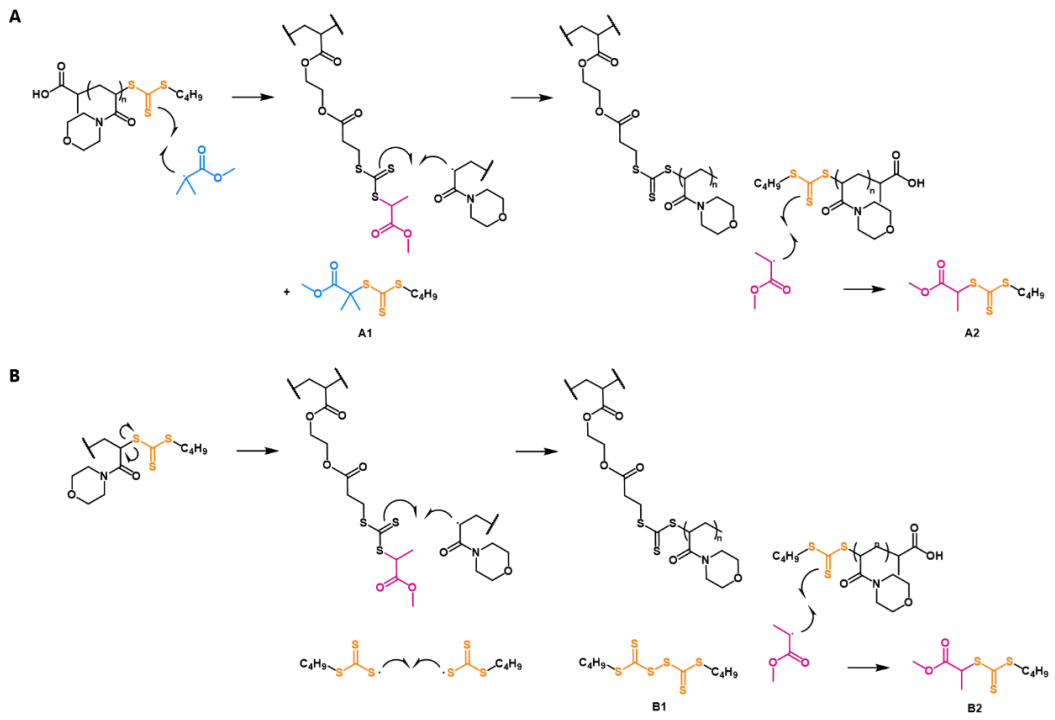

Scheme 2.5 Reaction schemes for transferring linear polymers to a functionalised backbone using a thermal initiator (**A**) and the photoiniferter approach (**B**) and expected by-products (**A1-2**, **B1-2**). Product **B2** may also be formed through combination of methyl propionate and trithiocarbonate radicals.

result in a mixture of graft copolymers and linear chains which would need to be separated to isolate the desired product. The ratio of linear chains to backbone CTAs was expected to determine the number of linear chains attached to the backbone at the end of the reaction. In the absence of an initiator, the theoretical maximum number of grafts per backbone repeating unit was

$$n_{\mathrm{G,max}} = \frac{n_{\mathrm{L}}}{n_{\mathrm{L}} + n_{\mathrm{CTA}}}, \tag{2.3}$$

where n_{L} and n_{CTA} are the number of linear chains and backbone CTAs, respectively.

To this end, linear pNAM$_{44}$ (**6**) was reacted with pCTA$_{300}$ (**3**) in a 1:1 mol ratio of linear chains to backbone CTAs in the presence of V-601 ([CTA]$_0$/[I]$_0$=20,) in dioxane at 75 °C. SEC showed a rapid increase in the hydrodynamic volume of pCTA$_{300}$ within the first 30 min as linear chains were grafted to the polymer (Figure 2.7A). Samples taken at longer reaction times showed very little change in the MWD as the reaction reached an equilibrium.

The fraction of grafted chains was quantified by comparing the areas of the three peaks in UV vs. RT plot, corresponding to pCTA$_{300}$ or the graft copolymer, linear polymer, and the end group-derived by-products. The molar ratio of pNAM$_{44}$ to backbone CTAs ($\mathrm{R_{L/CTA}}$) at $t = 0$ was estimated as $A_{\mathrm{UV,pNAM}_0}/A_{\mathrm{UV,pCTA}_0}$. However, the molar absorptivities of the CTA and pNAM$_{44}$ end-group were not known to be equal and the relative areas were only used here as an approximation.[46] The relative fraction of transferred linear chains (f_{Rel}), which is descriptive of the grafting density, was calculated for each time point as

$$f_{\mathrm{Rel,UV}} = \mathrm{R_{L/CTA}}\, f_{\mathrm{pNAM,UV}} = \frac{A_{\mathrm{UV,pNAM}_0}}{A_{\mathrm{UV,pCTA}_0}} \cdot \frac{A_{\mathrm{UV,CTA}}}{A_{\mathrm{UV,CTA}} + A_{\mathrm{UV,pNAM}}}, \tag{2.4}$$

where $f_{\mathrm{pNAM,UV}}$ is the fraction of consumed pNAM$_{44}$ at time t estimated with UV detection, and $A_{\mathrm{UV,pNAM}}$ and $A_{\mathrm{UV,CTA}}$ are the areas of peaks corresponding to pNAM$_{44}$ and end-group derived by-products, respectively. Equation 2.4 approximates the molar absorptivities of the by-products to be equal to that of pNAM$_{44}$ and therefore $A_{\mathrm{UV,pNAM}_0} = \left(A_{\mathrm{UV,CTA}} + A_{\mathrm{UV,pNAM}}\right)_t$ at any time t. The reaction appeared to plateau after 39% of the original backbone R groups had been exchanged for a pNAM$_{44}$ chain (Figure 2.7B). To complement the quantification based on UV detection, the relative

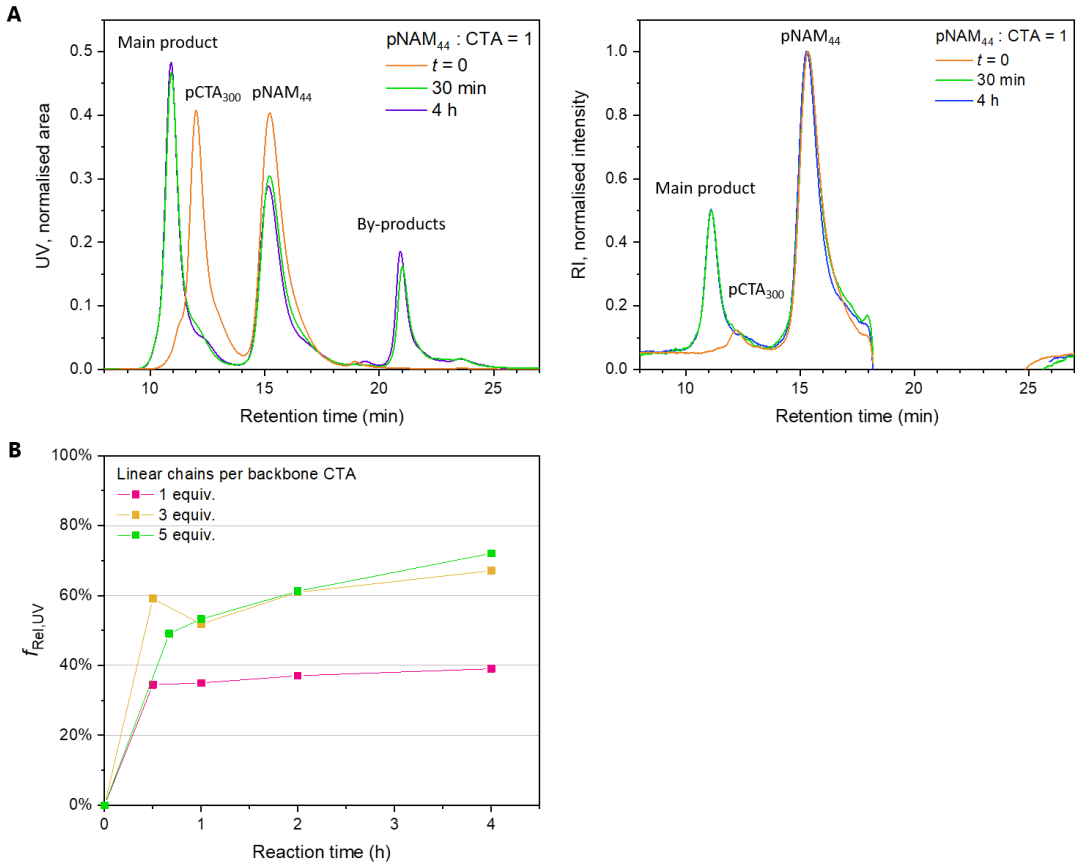

Figure 2.7 A) SEC data for the transfer of $pNAM_{44}$ to $pCTA_{300}$ in the presence of V-601 at 75 °C in dioxane. **B)** Relative fraction of transferred linear chains ($f_{Rel,UV}$), descriptive of the grafting density, plotted against reaction time in reactions with 1:1, 3:1 and 4:1 pNAM to backbone CTA ratios.

fraction of transferred chains was estimated from the RI vs. RT plots by calculating the change in the mass fraction of the linear chains, $\Delta A_{RI,pNAM}/A_{RI,tot}$. The result was in reasonably good agreement with the UV data, suggesting a plateau at 31% (Table 2.3). Due to the weak RI signal intensity, UV detection was considered more reliable despite the approximations of equal absorptivity.

An excess of linear chains was used in subsequent reactions to yield polymers with higher grafting densities. Steric shielding effects near the reactive sites were anticipated to set a practical upper limit for the number of grafts per backbone. Grafting was conducted using 3:1 and 5:1 molar ratios of linear chains to backbone CTAs, reaching 67% and 72% relative transfer efficiencies after 4 h, respectively (Figure 2.7B). The data suggested that, even with a large excess of linear polymer, roughly 30% of backbone repeating units remained without a graft, and that an increase from a 3-fold to a 5-fold excess had little effect on the relative transfer efficiency. The results suggested grafting densities above 70% would be challenging

Table 2.3 Transfer efficiencies observed in reactions between linear pNAMs and $pCTA_{300}$. SEC analysis with DRI and $UV_{309\ nm}$ detection was used to follow reaction kinetics.

					DRI detection		UV detection	
	Initiation	**Linear polymer**	**[pNAM]/[CTA]**	***t*** **(h)**	**% Transferred**	f_{Rel} [A]	**% Transferred**	f_{Rel} [A]
T1.1	Δ	$pNAM_{44}$	1:1	4	24	31	31	39
T1.2	Δ	$pNAM_{44}$	3:1	4	13	35	24	67
T1.3	Δ	$pNAM_{44}$	5:1	4	0	2	15	72
T2.1	*hv*	$pNAM_{44}$	1:1	15	20	23	31	36
T2.2	*hv*	$pNAM_{44}$	3:1	24	7	20	33	103
T2.3	*hv*	$pNAM_{44}$	5:1	15	6	30	17	77
T3.1	*hv*	$pNAM_{20}$	1:1	1.5	28	35	31	40
T3.2	*hv*	$pNAM_{30}$	1:1	1.5	25	31	31	38
T3.3	*hv*	$pNAM_{44}$	1:1	1.5	23	28	27	34

[A] The relative fraction of transferred linear chains was calculated as ([pNAM]/[CTA])·(%Transferred chains).

to reach with this graft length. The data collected with UV and DRI detection were in considerable disagreement due to the poor sensitivity of the DRI detector for the small amount of $pCTA_{300}$ employed in these reactions (Table 2.3). Therefore, quantification with UV was considered more reliable despite the assumption of equal molar absorptivities.

The reactions were repeated under blue light irradiation in the absence of initiator (Figure 2.8). UV detection suggested a reaction with $R_{L/CTA} = 1$ to result in roughly 36% transfer of linear chains, which was very close to the 39% transfer observed in the equivalent initiator-driven reaction. However, the degree of linear transfer calculated from DRI detection was found to be considerably lower (Table 2.3). Most notably, when an excess of linear chains was used, $f_{Rel,UV}$ seemed not to plateau with increasing reaction time, implying that UV-active by-products were generated continuously by photolysis. DRI detection revealed the formation of a third polymeric species at RT=13 min, with $M_{n,SEC} \approx 45{,}000$ g/mol. Considering the higher concentration of linear chains in these reactions, a possible explanation is the combination of two ω-end-groups to form disulfide **B1**, followed by

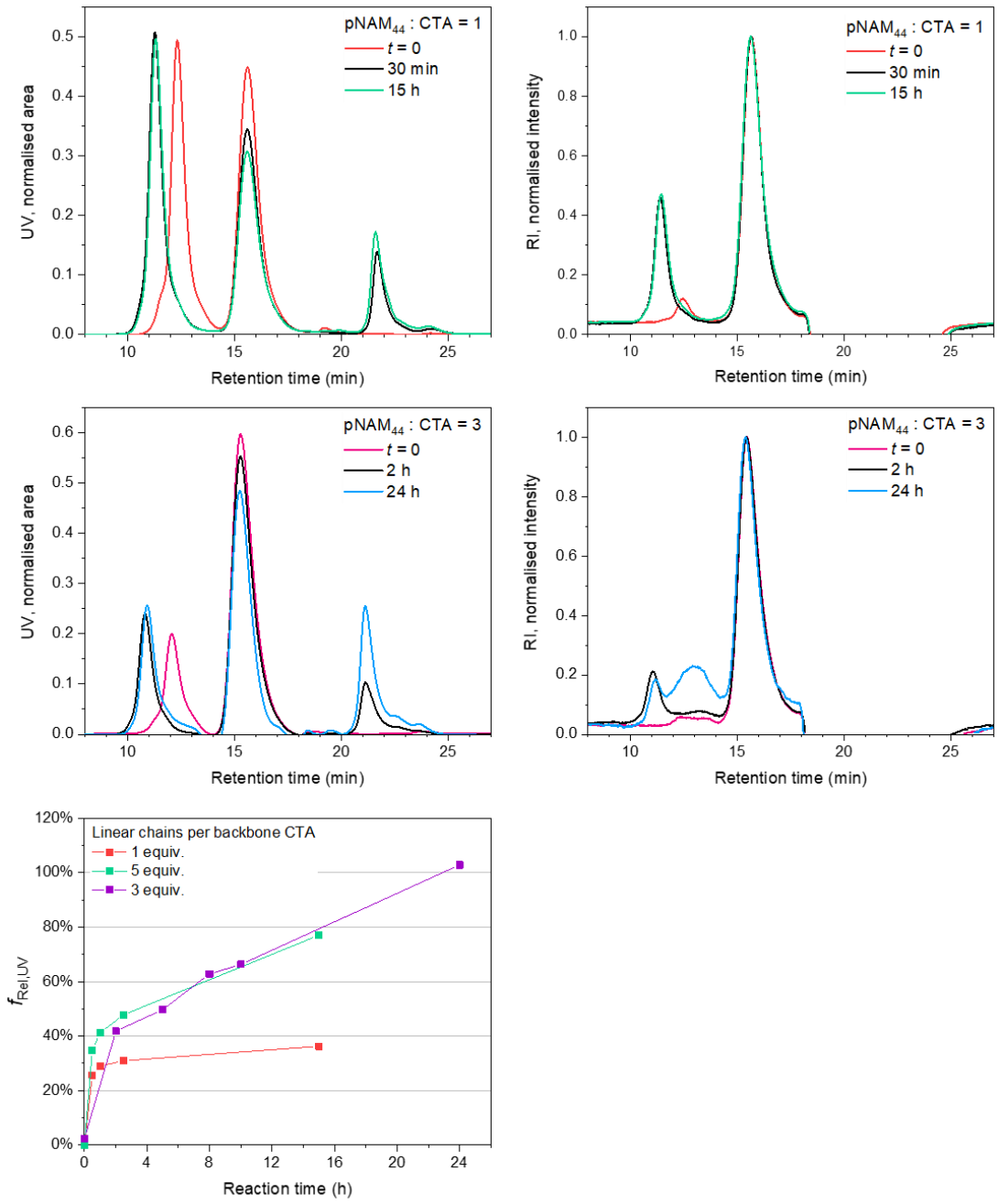

Figure 2.8 SEC data for blue light-induced transfer of $pNAM_{44}$ to $pCTA_{300}$ in dioxane. Analysis was carried out in DMF.

disproportionation of the linear chains and subsequent polymerisation of the newly formed vinyl groups.[62] Due to the overlap in the RI vs RT plots, the relative fraction of transferred chains could not be quantified reliably using these data.

While the presented approach sets a practical upper limit for achievable grafting densities, it was found to give better control over graft dispersity than Z group polymerisation. A comparison was made between graft copolymers synthesised via photoiniferter Z group polymerisations and those prepared by transferring linear

pNAM chains with DPs of 20, 30, and 44 to $pCTA_{300}$. Transfer reactions were conducted photolytically over 1.5 h using an equimolar ratio of linear chains to backbone CTAs, resulting in a 30-35% grafting density (Table 2.3). Both UV and DRI detection suggested the fraction of transferred chains to decrease some 6% across the two-fold increase in chain length due to increased steric shielding. After isolating the graft copolymers from linear chains through repeated precipitations, the grafts were fragmented off the backbone with blue light irradiation in the presence of a hydrogen donor and subsequently analysed by SEC (Figure 2.9). The cleaved grafts prepared through the Z group approach exhibited broad MWDs ($Đ$=1.58-1.98) regardless of the graft or backbone length (Table 2.4), suggesting chain growth was overall poorly controlled in these reactions. Consequently, the experimental number-average molecular weights of the grafts deviated significantly from their theoretical values. As an example, the $M_{n,SEC}$ = 4,500 g/mol of linear $pNAM_{30}$ (**5**) was in good agreement with $M_{n,th}$ = 4,500 g/mol, whereas the experimental molecular weight of $pNAM_{29}$ grafts cleaved off $pNAM_{133x29}$ (**2b**) was much higher, $M_{n,SEC}$ = 6,900 g/mol.

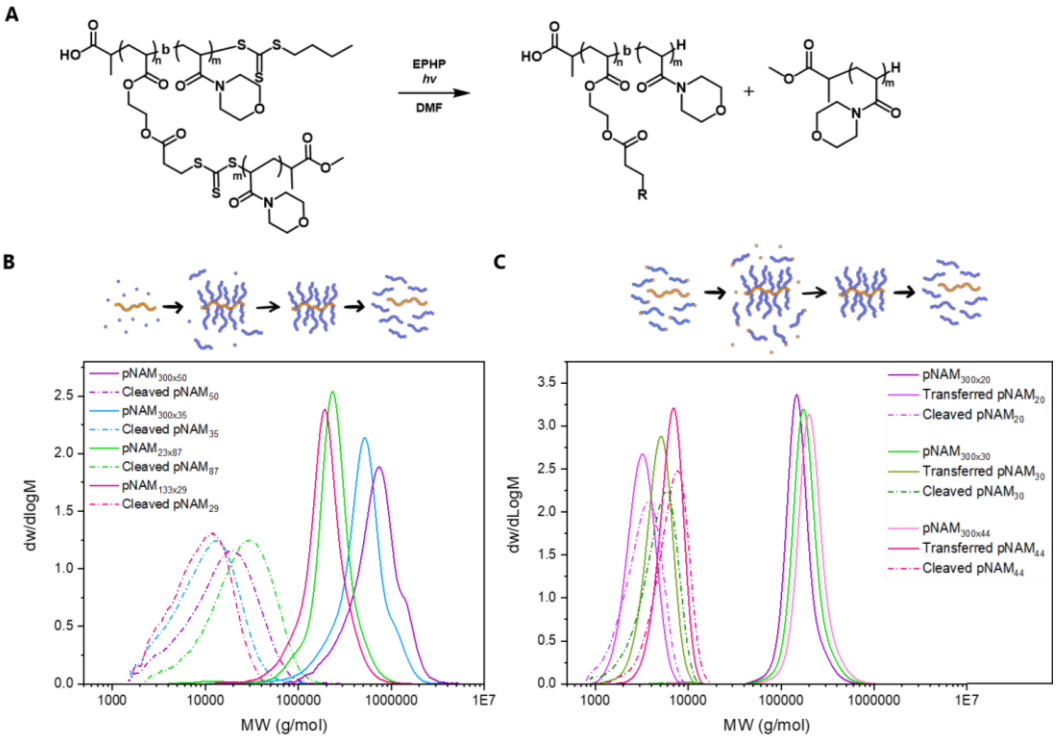

Figure 2.9 A) Reaction scheme for cleaving grafts off the backbone under blue light irradiation using 1-ethylpiperidine hypophosphite as a hydrogen donor. **B)** SEC data for graft copolymers prepared via the Z group approach. **C)** SEC data for graft copolymers prepared by transferring linear pNAM to $pCTA_{300}$. Linear pNAMs used in the reactions are shown as a reference. Data were collected in DMF with DRI detection and analysed with PMMA calibration.

The poor control was to be expected from descriptions of similar systems in the literature,[27] and ascribed to a combination of steric effects near the CTAs and the fast propagation rate of NAM. The transferred linear chains of **T3.1-3.3** were found to retain their size distributions rather well and the hydrodynamic volumes of the graft copolymers obtained from the reactions increased systematically with increasing graft length.

The newly described linear chain transfer strategy was successfully used to prepare graft copolymers with moderate grafting densities (≤70%) using a range of graft lengths. The approach allows for the separate preparation of the grafts prior to attachment, enabling improved control of molecular weight and structure over the Z group approach. Since the linear polymers used for grafting may be prepared or functionalised with any available RAFT agent or other radical-forming group, the method may be used to overcome the limitation of poor availability of Z group functional CTAs needed for the preparation pCTAs.[27] Furthermore, the approach is applicable to any polymer that may be coupled to a radical-forming functionality and can therefore be used when the selected materials cannot be polymerised through the *grafting from* method. The versatile UV absorption characteristics of RAFT agents and radical stabilities may be further explored to develop more sophisticated or even orthogonal grafting strategies.

Table 2.4 Experimental molecular weights ($M_{n,SEC}$) and dispersities ($Đ$) found in the graft cleavage reactions. Analysis was carried out in DMF with DRI detection and PMMA calibration.

		Bottlebrush		**Linear polymer**		**Cleaved grafts**	
		$M_{n,SEC}$ (g/mol)	$Đ$	$M_{n,SEC}$ (g/mol)	$Đ$	$M_{n,SEC}$ (g/mol)	$Đ$
	Linear transfer to pCTA						
C-T3.1	$pCTA_{300}$ $pNAM_{20}$	138,000	1.17	2,900	1.12	2,850	1.22
C-T3.2	$pCTA_{300}$ $pNAM_{30}$	148,000	1.29	4,500	1.12	4,150	1.24
C-T3.3	$pCTA_{300}$ $pNAM_{44}$	182,000	1.22	6,100	1.10	5,930	1.18
	Z group approach						
C-3b	$pNAM_{300x35}$	368,000	1.51	-	-	7,700	1.74
C-3a	$pNAM_{300x50}$	548,000	1.43	-	-	10,400	1.98
C-1b	$pNAM_{23x87}$	178,000	1.56	-	-	17,500	1.79
C-2b	$pNAM_{133x29}$	157,000	1.34	-	-	6,900	1.58

2.3 Conclusions and Outlook

In this work the Z group approach was harnessed to realise two new synthetic routes, akin to *grafting to* reactions with reversible radical addition, for preparing graft copolymers. RAFT polymerisation was used to prepare graft copolymers and linear polymers to explore the new synthetic routes, and to provide a proof-of-concept for heterograft copolymer synthesis. The first approach involved an intermolecular graft exchange reaction between distinct graft copolymers prepared via the Z group approach. The reaction was successfully conducted with a range of backbone and graft lengths by re-fragmenting the existing grafts using a thermal initiator or blue light irradiation. Despite the mechanistic differences between the two initiating methods, changes in the MWDs monitored by SEC over the course of the reactions were found to be nearly identical. Grafts were also successfully exchanged for fluorescent-labelled linear polymers to demonstrate a convenient way to introduce functionality into the graft copolymer structure. The most notable limitation of the new approach was the inevitable termination of some grafts due to steric shielding near the grafting sites, commonly encountered in any Z group polymerisations. The modular approach provides a convenient means to prepare extensive graft copolymer libraries by simply adjusting the stoichiometry in each exchange reaction.

The second approach involved reversible grafting of linear chains to CTA-functionalised backbones. Grafting efficiencies could be estimated with SEC by following the formation of UV-active by-products, which showed that different grafting densities could be obtained by varying the amount of linear polymer added to the reaction. The achievable grafting densities were limited by the graft length using this method. However, depending on the desired properties of the product the limitation may be outweighed by the superior control over graft dispersity compared to conventional Z group polymerisations. The most notable benefit of this strategy is its applicability to any polymer capable of forming a chain radical, such as functionalised commercial polymers or those prepared through other controlled polymerisation techniques. The presented work successfully expanded the toolbox for graft copolymer synthesis by utilising the unique features of RAFT chemistry.

2.4 Experimental

2.4.1 Instrumental Methods

2.4.1.1 Size-Exclusion Chromatography

SEC was carried out using the following two instrument setups and solvent conditions (Table 2.5). All analyte samples were filtered through a syringe filter prior to injection. Experimental molar mass ($M_{n,SEC}$) and dispersity ($Đ$) values were determined by employing conventional calibration with poly(methyl methacrylate) (PMMA) standards (Agilent EasyVials) using Agilent GPC/SEC software.

Table 2.5 Instrument conditions used in SEC analysis.

	DMF	**$CHCl_3$**
Instrument	Agilent Infinity II MDS	Agilent Infinity II MDS
Detectors [A]	DRI, VS, DALS, single-wavelength UV	DRI, VS, DALS, multi-wavelength UV
Guard column	PLgel 5 µm	PLgel 5 µm
Analytical columns	2 x PLgel Mixed D 300 x 7.5 mm, 200-400,000 g/mol linear operating range [B]	2 x PLgel Mixed C 300 x 7.5 mm, 200-2,000,000 g/mol linear operating range [B]
Calibration [C]	PMMA 500-900,000 g/mol	PMMA 600-2,200,000
Eluent	DMF, cont. 5 mmol NH_4BF_4	$CHCl_3$, no additives
Sample filter	Nylon membrane, 0.22 µm pore size	PTFE membrane, 0.22 µm pore size
Flow rate	1 ml/min	1 ml/min
Temperature	50 °C	30 °C

[A] DRI, VS and DALS stand for differential refractive index, viscometry and dual-angle light scattering detectors, respectively. DALS was detected at 15° and 90° angles.

[B] Polystyrene equivalent.

[C] Calibration range is given as a representative example on a given month.

2.4.1.2 Atomic Force Microscopy

Samples were prepared by drop-casting a 0.005 mg/ml polymer solution in chloroform onto freshly cleaved mica and drying under a gentle N_2 flow for 10 s. Images were collected directly after sample preparation using a Bruker Dimension Icon instrument with ScanAsyst in Air and PeakForce tapping and ScanAsyst-Air probes. Images were processed with Gwyddion software.

2.4.1.3 Nuclear Magnetic Resonance Spectroscopy

^{1}H Nuclear Magnetic Resonance (NMR) spectra and ^{1}H-^{13}C Heteronuclear Single Quantum Coherence (HSQC) spectra were recorded in $CDCl_3$ or CD_3OD on Bruker Avance III HD (300 MHz or 400 MHz) spectrometer at 300 K. Chemical shift values (δ) are reported in ppm. Solvent residual signals were used for calibration.

2.4.2 Materials

Acetonitrile (Sigma), 4,4′-azobis(4-cyanovaleric acid) (ACVA, 98%, Alfa Aesar), carbon disulfide (CS_2, ≥99.9%), 1,4-dioxane (≥99%, Sigma-Aldrich), dichloromethane anhydrous (DCM, 99.8%, Sigma-Aldrich), *N*,*N*-Dicyclohexylcarbodiimide (DCC, 99%, Acros Organics), 4-(dimethylamino)pyridine (DMAP, ≥99.0%, Alfa Aesar), diethyl ether (≥99.8%, Sigma-Aldrich), *N*,*N*-dimethylformamide (DMF, HPLC-grade, Merck), 1-ethylpiperidine hypophosphite (EPHP, 95%, Sigma-Aldrich), magnesium sulfate (drying agent, anhydrous, Sigma-Aldrich), methanol (≥99.9%, HPLC grade, Sigma-Aldrich), methyl 2-bromopropionate (99%, Acros Organics), 3-mercaptopropionic acid (99+%, Acros Organics), methanol-d_4 (CD_3OD, 99.8 atom% D, Sigma-Aldrich), chloroform-d ($CDCl_3$, 99.8 atom% D, Sigma-Aldrich), oxalyl chloride solution (2.0 M in methylene chloride, Sigma-Aldrich), 1-pyrenebutanol (99%, Sigma-Aldrich), sodium methoxide solution (25 wt% in methanol, Sigma-Aldrich), were used as received from the supplier.

2-Hydroxyethyl acrylate (HEA, ≥96%, Sigma-Aldrich) and 4-acryloylmorpholine (NAM, 97%, Sigma-Aldrich) were passed through aluminium oxide (activated, basic, Brockman I standard grade) to remove the inhibitor. 2-(((Butylthio)-carbonothioyl)thio)propanoic acid (PABTC) was synthesised according to the literature[63] and recrystallised twice from hexane before use.

Blue LED lights (exact wavelength not known) were purchased from Amazon.com and attached around the inner surface of a metal mesh cylinder (Ø=8 cm) (Figure 2.10). Vials containing the reaction mixtures were placed at the bottom of the holder at roughly 4 cm distance from the light source. The reactor was placed inside a fume hood under 0.5 m/s air flow. The temperature was controlled using a cardboard housing and measured with a thermometer in contact with the bottom of the reactor.

Figure 2.10 LED reactor used for photoiniferter reactions.

2.4.3 Synthetic Protocols and Characterisation

2.4.3.1 Synthesis of 3-((((1-methoxy-1-oxopropan-2-yl)thio)carbonothioyl)thio) propanoic acid (MPPATC)

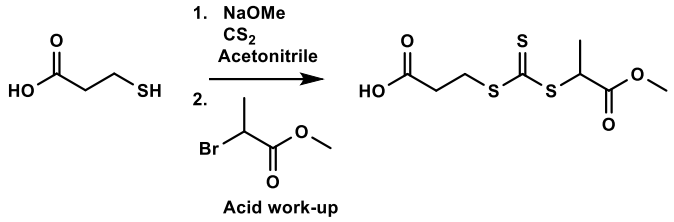

Scheme 2.6 Reaction scheme for the preparation of the Z group functional RAFT agent used in the functionalisation of pHEA.

In a 500 ml round-bottom flask immersed in an ice bath, mercaptopropionic acid (12.3 ml, 0.14 mol, 1.0 eq.) was dissolved in acetonitrile (250 ml) and sodium methoxide solution (25 wt% sol. in methanol) (66 ml, 0.29 mol, 2.1 eq.) was added dropwise. After 5 min, carbon disulfide (9.3 ml, 0.16 mol, 1.1 eq.) was added dropwise to the reaction mixture, the flask was removed from the ice bath and stirring was continued at room temperature for 1 h. Methyl 2-bromopropionate (17.4 ml, 0.16 mol, 1.1 eq.) was added and stirring was continued at room temperature overnight.

The product was isolated by adding concentrated HCl (1.5 eq.) to the stirred reaction mixture, followed by the addition of deionised water until an oil separated. The oil was dried over $MgSO_4$ in DCM and volatiles were removed with rotary evaporation (30 °C) to give the product as an orange oil. The structure was confirmed by ^{1}H NMR spectroscopy in $CDCl_3$ (Figure 2.11). The product was used for functionalisation without further purification.

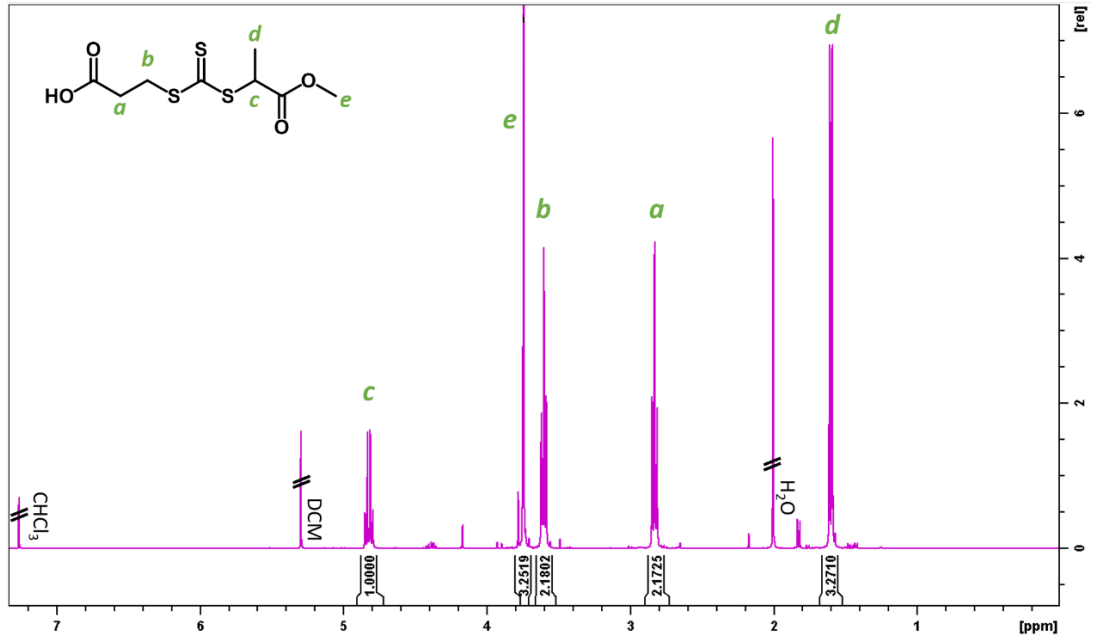

Figure 2.11 ^{1}H NMR spectrum of the synthesised RAFT agent, MPPATC, in $CDCl_3$.

2.4.3.2 Synthesis of 4-(pyren-1-yl)butyl 2-(((butylthio)carbonothioyl)thio) propanoate

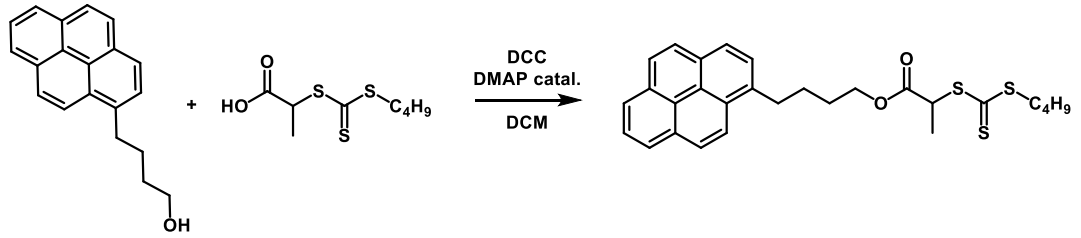

Scheme 2.7 Reaction scheme for the synthesis of pyrene-functional RAFT agent, pyr-PBTC.

1-Pyrenebutanol (250 mg, 0.911 mmol) and PABTC (239 mg, 1.00 mmol) were dissolved in anhydrous DCM (5 ml) under nitrogen and cooled with an ice bath. DMAP (1.11 mg, 0.091 mmol) and then DCC (216 mg, 1.05 mmol) were added to the reaction mixture and the mixture was stirred overnight at room temperature. Solids were filtered off, the solution was passed through a silica plug using a hexane/ethyl acetate (2:1) eluent and volatiles were removed with a rotary evaporator to give a yellow oil (440 mg, 97%). The structure was confirmed with ^{1}H NMR spectroscopy in $CDCl_3$ (Figure 2.12).

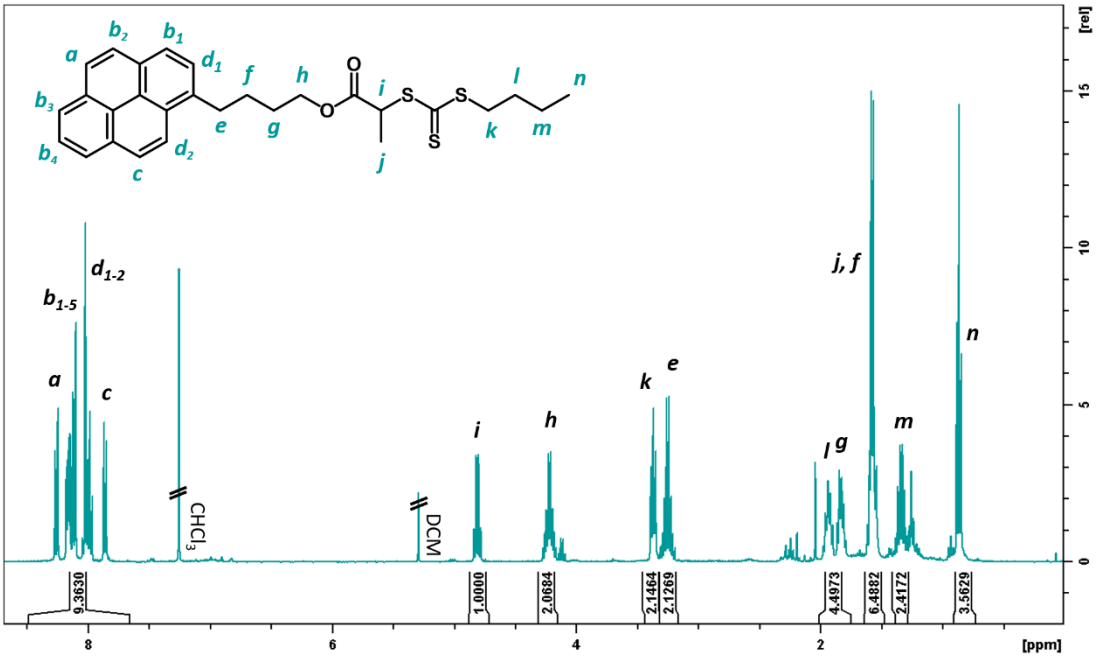

Figure 2.12 ^{1}H NMR analysis of pyrene-functionalised RAFT agent, pyr-PBTC, in $CDCl_3$.

2.4.3.3 Synthesis of MPPATC-functionalised poly(2-hydroxyethyl acrylates) (pCTAs)

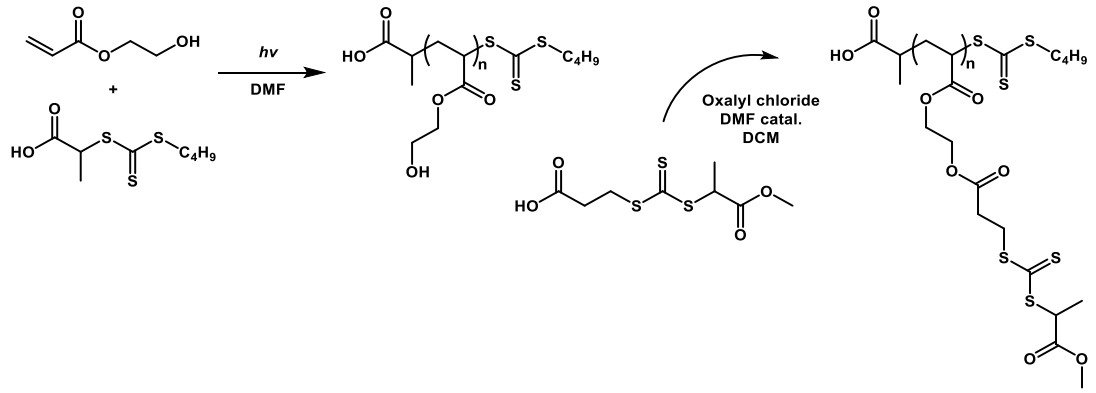

Scheme 2.8 Reaction scheme for the preparation of CTA-functionalised backbone precursors.

The following general protocol was used to prepare all functionalised backbones. To prepare the functionalised $pHEA_{133}$ ($pCTA_{133}$, **2**) PABTC (39.9 mg, 0.167 mmol) and HEA (3.22 g, 27.7 mmol) were weighed into a 25 ml vial and dissolved in DMF (13.1 g, $[M]_0$=2 M). A sample was taken for ^{1}H NMR analysis. The vial was sealed with a rubber septum and the solution was deoxygenated by bubbling N_2 into the solution for 15 min. Polymerisation was carried out over 15 h by subjecting the vial to blue LED irradiation (20-30 °C). Samples were taken after the reaction for SEC analysis in DMF and ^{1}H NMR analysis in CD_3OD.

A fraction of the reaction mixture (7.4 mmol −OH, 1 eq.) was transferred into a dry round-bottom flask and anhydrous DMF was added. In a separate dry round-bottom flask, MPPATC (3.00 g, 11.2 mmol, 1.5 eq.) was dissolved in anhydrous DCM and oxalyl chloride (1.1 ml, 13 mmol, 1.8 eq.) and anhydrous DMF (2 drops) were added. Solution was stirred for 1 h and volatiles were removed under vacuum. The residue was redissolved in anhydrous DMF and added dropwise to the polymer solution. Stirring was continued overnight. The reaction mixture was concentrated, and the polymer was collected through precipitation into methanol followed by centrifugation. The polymer was further redissolved in DCM, reprecipitated twice and dried under vacuum to yield a yellow tacky product. The structure was confirmed with ^{1}H NMR and ^{1}H-^{13}C HSQC in $CDCl_3$ (Figure 2.14).

Conversion of HEA was determined by ^{1}H NMR spectroscopy in CD_3OD using monomer −C$\underline{H_2}$OH signal at 3.76 ppm as a reference and by monitoring the

disappearance of vinyl protons at 5.90 ppm (Figure 2.13). The mean degree of polymerisation was calculated as

$$\mathrm{DP}_p = \frac{[\mathrm{HEA}]_0}{[\mathrm{PABTC}]_0}\, p_{\mathrm{HEA}}\,, \tag{2.5}$$

and the theoretical number-average molar mass as

$$M_{\mathrm{n,th}} = M_{\mathrm{PABTC}} + \mathrm{DP}_p M_{\mathrm{HEA}} + \mathrm{DP}_p M_{\mathrm{MPPATC}}\,, \tag{2.6}$$

where $[\mathrm{HEA}]_0$ and $[\mathrm{CTA}]_0$ are the initial HEA and CTA concentrations, respectively, p is the monomer conversion as determined by ^{1}H NMR spectroscopy, and M_{HEA}, M_{PABTC}, and M_{MPPATC} are the molar masses of HEA, PABTC and MPPATC, respectively.

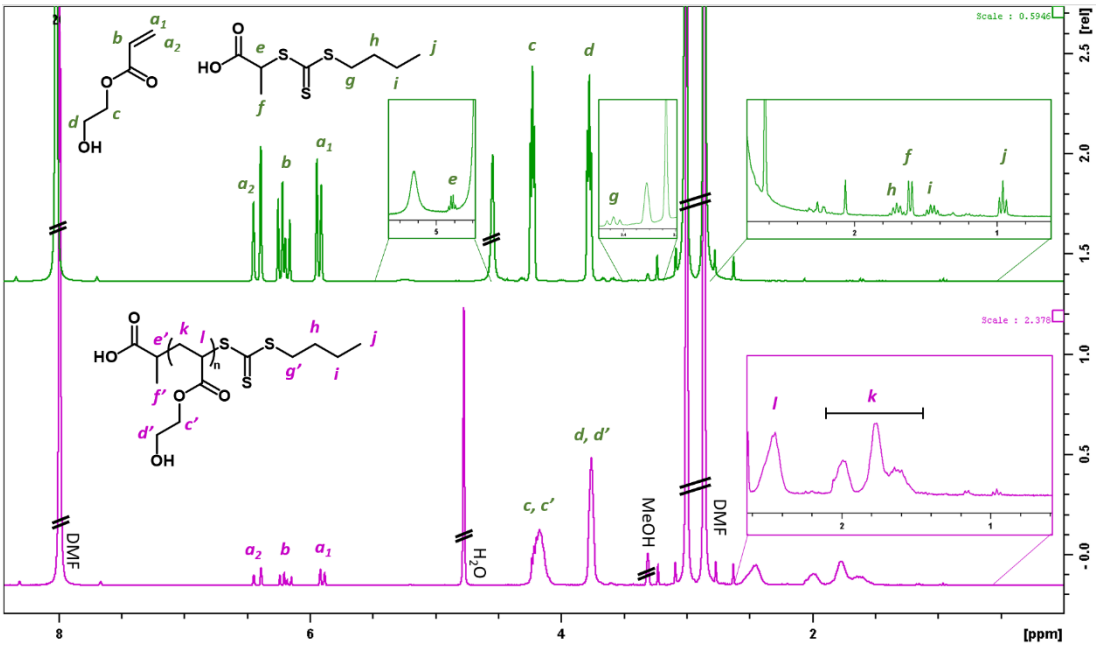

Figure 2.13 ^{1}H NMR analysis of the RAFT polymerisation of 2-hydroxyethyl acrylate at *t*=0 (top) and after the reaction (bottom). Spectra were acquired in CD_3OD.

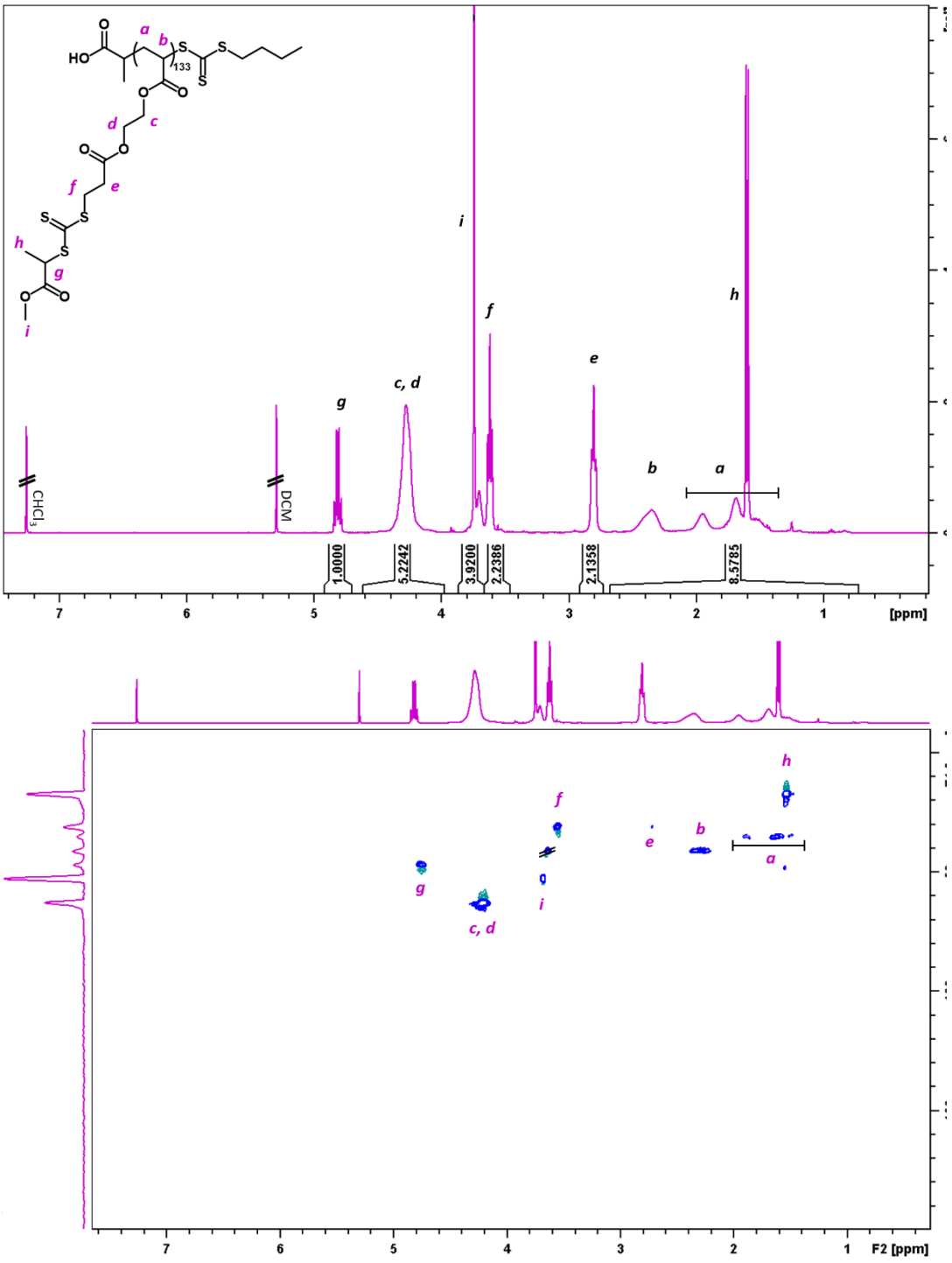

Figure 2.14 ^{1}H NMR (top) and ^{1}H-^{13}C HSQC (bottom) spectra of MPPATC-functionalised pHEA$_{133}$ in $CDCl_3$.

2.4.3.4 Photoiniferter Polymerisation of Graft Copolymers

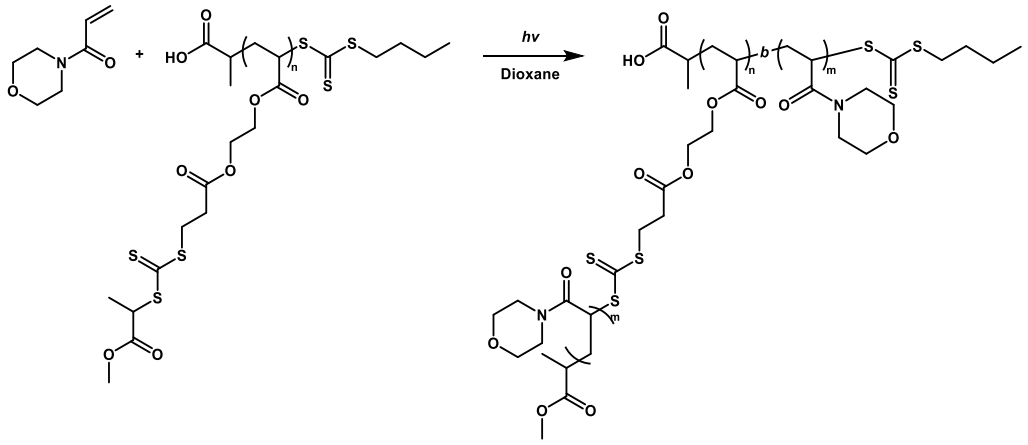

Scheme 2.9 General reaction scheme for the photoiniferter Z group polymerisation used to prepare graft copolymers.

The following general procedure was used for polymerising graft copolymer side-chains. For preparing $pHEA_{133x8}$ (**2a**), $pCTA_{133}$ (**2**) (49.76 mg, 0.136 mmol) and NAM (240.34 mg, 1.70 mmol) were weighed in a 2 ml vial. Dioxane (1.55 ml, $[M]_0$ = 1 M) and DMF (30 µl) were added and sealed vial was left on a stirring plate to solubilise reactants. A sample as taken for ^{1}H NMR analysis, and the vial was sealed with a septum cap and purged with N_2 for 10 min. Polymerisation was carried out by placing the vial under blue LED light for 3 h. Samples were taken after reaction for SEC analysis in DMF and ^{1}H NMR analysis in $CDCl_3$.

The polymer was precipitated in diethyl ether, collected by centrifugation, redissolved in DCM and reprecipitated twice to remove residual monomer. The product was dried in a vacuum oven (38 °C, 30 min) to give a pale yellow powder.

To remove the linear by-product of terminated grafts, 120 mg of polymer was dissolved in DCM (10 mg/ml) in a 15 ml centrifuge tube. While agitating on a vortex mixer, diethyl ether was added dropwise until polymer separated from the solution. After centrifugation the supernatant was discarded, and the pellet was redissolved in DCM to repeat the procedure. The glassy polymer was redissolved in DCM, precipitated into diethyl ether and vacuum dried (38 °C, 30 min) to give a pale yellow powder (90 mg, 75%).

Conversion of NAM was determined by ^{1}H NMR spectroscopy in $CDCl_3$ using DMF as an internal standard and by monitoring the disappearance of vinyl protons at 5.68 ppm. The mean DP of the grafts was calculated as

$$\mathrm{DP}_p = \frac{[\mathrm{NAM}]_0}{[\mathrm{MPPATC}]_0}\, p_{\mathrm{NAM}} \tag{2.7}$$

and the theoretical number-average molar mass of the graft copolymer as

$$M_{\mathrm{n,th}} = M_{\mathrm{pCTA}} + \mathrm{DP}_{\mathrm{pCTA}} \mathrm{DP}_p M_{\mathrm{NAM}} \tag{2.8}$$

where $[\mathrm{NAM}]_0$ and $[\mathrm{MPPATC}]_0$ are the initial NAM and side-chain MPPATC concentrations, respectively, p is the monomer conversion as given by ^{1}H NMR analysis, and M_{pCTA} and M_{NAM} are the molar masses of the pCTA and NAM, respectively. The final structure was confirmed with ^{1}H NMR spectroscopy in $CDCl_3$ (Figure 2.2).

2.4.3.5 Photoiniferter Polymerisation of Linear Polymers

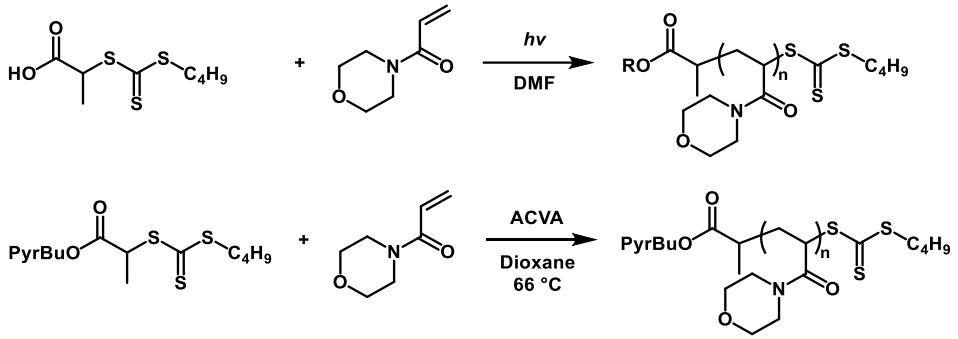

Scheme 2.10 Reaction scheme for the synthesis of linear poly(4-acryloylmorpholines).

The following general protocol was used to prepare linear poly(4-acryloylmorpholines) without a fluorescent tag. To prepare $pNAM_{44}$ (**6**), PABTC (33.74 mg, 0.14 mmol, 1 eq.) and NAM (1.013 g, 7.18 mmol, 51 eq.) were dissolved in 2.65 ml dioxane ($[M]_0$=2 M) in an 8 ml vial. DMF (30 µL) was added as an internal standard and a sample was taken for ^{1}H NMR analysis. The reaction mixture was deoxygenated by bubbling N_2 into the solution for 15 min and the vial was irradiated with blue LED light (20-30 °C) for 3 h. After the reaction was stopped, a sample of the crude product was taken for ^{1}H NMR and SEC analysis. The polymer was isolated by precipitating into diethyl ether three times and drying in a vacuum oven (30 min, 38 °C). The product was characterised by ^{1}H NMR in $CDCl_3$ and by SEC in DMF.

To prepare pyrene-functional $pNAM_{15}$ (pyr-$pNAM_{15}$, **7**), NAM (100 mg, 0.71 mmol), pyr-PBTC (29.2 mg, $5.9 \cdot 10^{-2}$ mmol) and ACVA (0.2 mg, $7.08 \cdot 10^{-4}$ mmol) were dissolved in dioxane (147 µl) in a 1.5 ml screw cap glass vial. The mixture was degassed with nitrogen for 10 min and placed in an oil bath heated to 75 °C for 24 h. Conversion was determined by ^{1}H NMR in $CDCl_3$. The reaction mixture was precipitated twice into ice-cold diethyl ether and dried overnight in a vacuum oven (40 °C).

2.4.3.6 Graft Exchange Using a Thermal Initiator

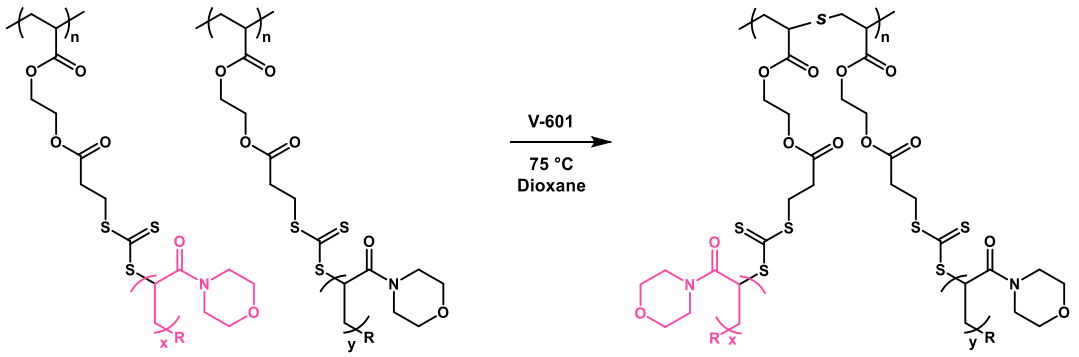

Scheme 2.11 General reaction scheme for graft exchange reactions conducted using a thermal initiator.

The following general protocol was used for all reactions. For exchanging short and long pNAM grafts at an equal mass ratio (**E1**), $pNAM_{23x10}$ (12.61 mg, $3.1 \cdot 10^{-4}$ mmol) and $pNAM_{23x87}$ (12.58 mg, $4.4 \cdot 10^{-5}$ mmol) were weighed into a 2 ml screw-cap septum vial. Dioxane (0.40 ml) and initiator stock solution (0.90 mg/ml in dioxane, $[CTA]/[I]_0 = 20$) were added to dissolve the polymers and the solution was purged with nitrogen for 10 min. The vial was placed in a pre-heated oil bath set at 75 °C. Samples were withdrawn for SEC analysis through the septum with a nitrogen-flushed syringe.

2.4.3.7 Graft Exchange Using the Photoiniferter Approach

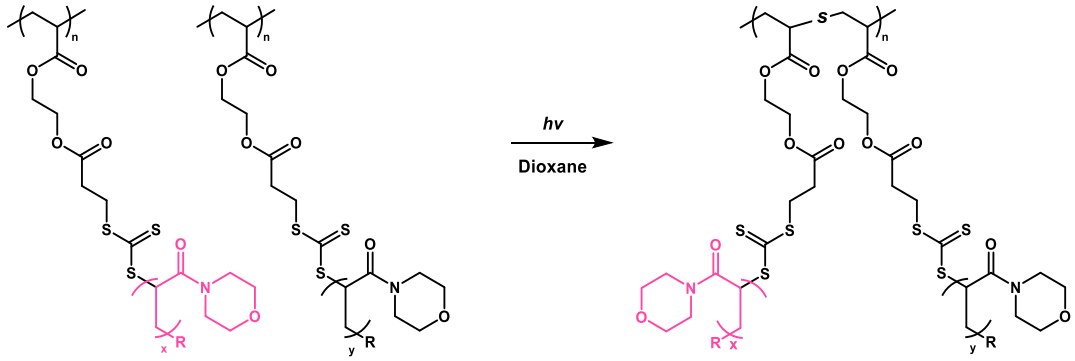

Scheme 2.12 General reaction scheme for graft exchange reactions conducted using the photoiniferter approach.

The following general protocol was used for all reactions. For exchanging short and long pNAM side-chains at an equal mass ratio (**E2**), $pNAM_{23x10}$ (10.02 mg, $2.4 \cdot 10^{-4}$ mmol) and $pNAM_{23x87}$ (10.05 mg, $3.5 \cdot 10^{-4}$ mmol) were weighed into a 2 ml screw-cap septum vial. Dioxane (0.40 ml) was added to dissolve the polymers. The solution was purged with nitrogen for 10 min and the vial was placed in a photoreactor equipped with a blue LED light strip (40-50 °C). Samples were taken for SEC analysis through the septum with a nitrogen-flushed syringe.

2.4.3.8 Transfer of Linear Polymer to pCTAs

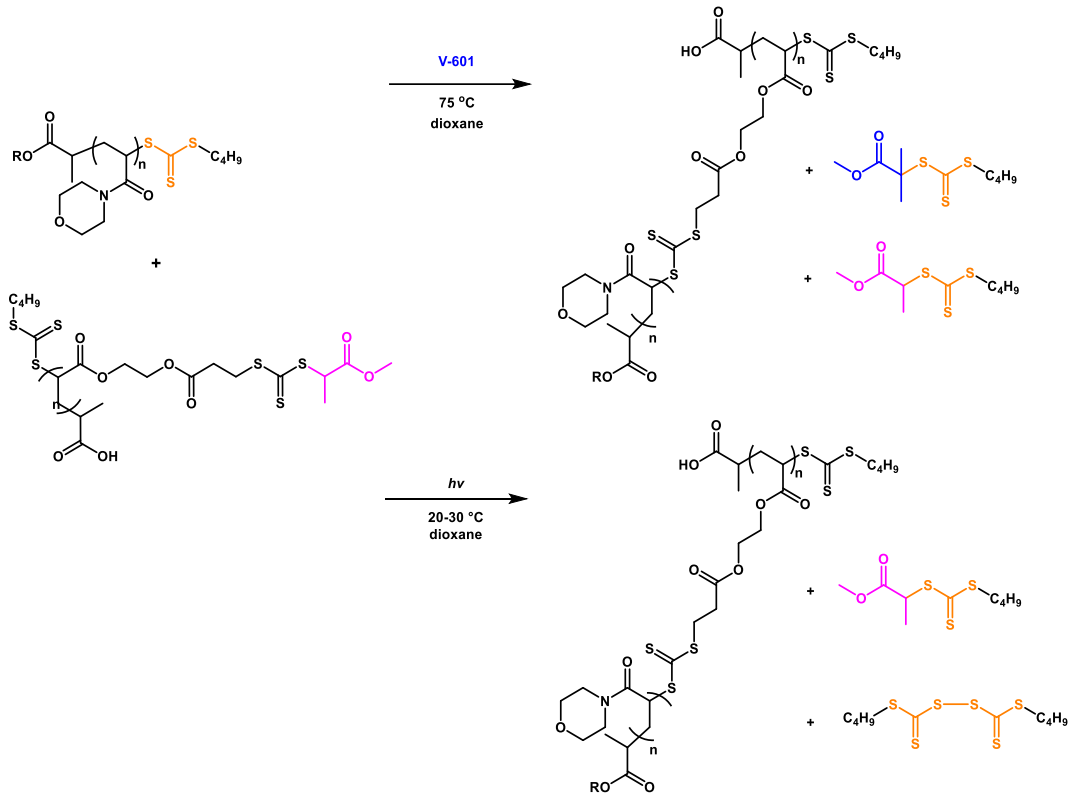

Scheme 2.13 Reaction schemes for the transfer of linear chains to pCTAs using an added initiator (top) or the photoiniferter approach (bottom). Two UV-active by-products were expected in each case.

The following general protocol was used for all reactions. For transferring $pNAM_{44}$ side-chains to $pCTA_{300}$ at an equimolar ratio of linear polymer to $pCTA_{300}$ repeat unit, $pCTA_{300}$ (1.49 mg, $1.4 \cdot 10^{-8}$ mol, 1 eq. with respect to MPPATC units) and $pNAM_{44}$ (25.22 mg, $3.9 \cdot 10^{-6}$ mol, 1 eq.) were weighed into a 2 ml screw-cap septum vial. Dioxane (c_{tot}=50 mg/ml) was added to dissolve the polymers. For the reaction employing a thermal initiator, V-601 ([MPPATC]/$[I]_0$=20) was added. The solution was purged with nitrogen for 10 min and the vial was either immersed in a pre-heated oil bath set at 75 °C for 4 h (with added initiator, **T1.1**) or placed under blue LED light (no added initiator, **T2.1**). Reaction was monitored by sampling through the septum with a nitrogen-purged needle. SEC analysis of the samples was carried out in DMF.

Transfer efficiencies were calculated from the areas under the SEC $UV_{\lambda=309nm}$ detector responses arising from the $pCTA_{300}$ (A_{pCTA}), linear polymer (A_{Lin}), CTA-derived by-product (A_{CTA}), and the graft copolymer (A_{BB}). The linear polymer to backbone CTA ratio was calculated as

$$\mathrm{R} = \frac{A_{\mathrm{Lin}}}{A_{\mathrm{pCTA}}}. \tag{2.9}$$

The fraction of linear chains consumed in the reaction was estimated as

$$f_{\mathrm{Lin,UV}} = \frac{A_{\mathrm{CTA}}}{A_{\mathrm{CTA+Lin}}}. \tag{2.10}$$

The relative transfer efficiency, related to the grafting density, was calculated by taking into account the initial ratio of linear chains to backbone CTA as

$$f_{\mathrm{Rel,UV}} = \mathrm{R}\, f_{\mathrm{Lin,UV}}. \tag{2.11}$$

The transfer efficiencies could also be estimated using the DRI detector response when the signal-to-noise ratio was sufficiently large. When a large excess of linear chains was used, a small deviation in A_{pCTA} could result in a significant error. The mass fraction of linear chains at time *t* was calculated as

$$\%\ \mathrm{Lin}_t = \frac{A_{\mathrm{Lin},t}}{A_{\mathrm{tot},t}}, \tag{2.12}$$

where $A_{\mathrm{tot},t}$ is the sum of all areas at time t. The change in the mass fraction of linear chains by time *t* was then

$$\Delta\ \mathrm{Lin}_t = \frac{A_{\mathrm{Lin},t}}{A_{\mathrm{Lin},0}}, \tag{2.13}$$

where $A_{Lin,0}$ is the mass fraction at $t = 0$. The fraction of linear chains consumed after time t was then calculated as

$$f_{\mathrm{Lin,RI}} = \frac{\Delta\mathrm{Lin}_t}{\%\ \mathrm{Lin}_t} \tag{2.14}$$

and the relative transfer efficiency as

$$f_{\mathrm{Rel,RI}} = \mathrm{R}\, f_{\mathrm{Lin,RI}}. \tag{2.15}$$

2.4.3.9 Graft Cleavage Reactions

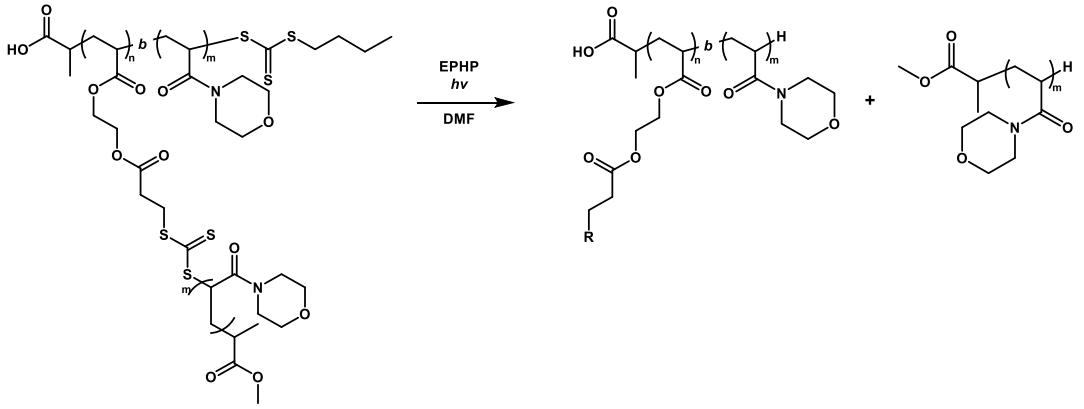

Scheme 2.14 General reaction scheme for cleaving grafts off a backbone to study their dispersity with size-exclusion chromatography.

Grafts were cleaved off the backbones by using blue light-induced fragmentation in the presence of 1-ethylpiperidine hypophosphite with the following general protocol adapted from the literature.[64] To cleave the grafts of $pNAM_{300x35}$, the copolymer (10.32 mg, $1.9 \cdot 10^{-3}$ mmol CTA, 1 eq.) was dissolved with EPHP (5.2 mg, $2.9 \cdot 10^{-2}$ mmol, 15 eq.) in DMF (0.20 ml). The solution was deoxygenated for 10 min and the vial was irradiated under blue LED light (20-30 °C) for 12 h. The product was analysed by DMF SEC without isolation.

2.5 References

1. Seo, S. E.; Hawker, C. J., The Beauty of Branching in Polymer Science. *Macromolecules* **2020,** *53* (9), 3257-3261.
2. Verduzco, R.; Li, X.; Pesek, S. L.; Stein, G. E., Structure, Function, Self-Assembly, and Applications of Bottlebrush Copolymers. *Chemical Society Reviews* **2015,** *44* (8), 2405-2420.
3. Ren, J. M.; McKenzie, T. G.; Fu, Q.; Wong, E. H.; Xu, J.; An, Z.; Shanmugam, S.; Davis, T. P.; Boyer, C.; Qiao, G. G., Star Polymers. *Chemical Reviews* **2016,** *116* (12), 6743-836.
4. Xie, G.; Martinez, M. R.; Olszewski, M.; Sheiko, S. S.; Matyjaszewski, K., Molecular Bottlebrushes as Novel Materials. *Biomacromolecules* **2019,** *20* (1), 27-54.
5. Chiefari, J.; Chong, Y. K.; Ercole, F.; Krstina, J.; Jeffery, J.; Le, T. P. T.; Mayadunne, R. T. A.; Meijs, G. F.; Moad, C. L.; Moad, G.; Rizzardo, E.; Thang, S. H., Living Free-Radical Polymerization by Reversible Addition−Fragmentation Chain Transfer: The RAFT Process. *Macromolecules* **1998,** *31* (16), 5559-5562.
6. Corpart, P.; Charmot, D.; Biadatti, T.; Zard, S. Z.; Michelet, D. Method for Block Copolymer Synthesis by Controlled Radical Polymerization. US 6153705A, 1998.
7. Le, T. P. T.; Moad, G.; Rizzardo, E.; Thang, S. H. Polymerisation with Living Characteristics. WO 1998001478A1, 1998.
8. Perrier, S., 50th Anniversary Perspective: RAFT Polymerization - A User Guide. *Macromolecules* **2017,** *50* (19), 7433-7447.
9. Parkatzidis, K.; Wang, H. S.; Truong, N. P.; Anastasaki, A., Recent Developments and Future Challenges in Controlled Radical Polymerization: A 2020 Update. *Chem* **2020,** *6* (7), 1575-1588.
10. Destarac, M., Industrial Development of Reversible-Deactivation Radical Polymerization: Is the Induction Period Over? *Polymer Chemistry* **2018,** *9* (40), 4947-4967.
11. Moad, G.; Solomon, D. H., *The Chemistry of Radical Polymerization*. 2nd Edition ed.; Elsevier: Amsterdam, 2006.
12. Jitchum, V.; Perrier, S., Living Radical Polymerization of Isoprene via the RAFT Process. *Macromolecules* **2007,** *40* (5), 1408-1412.
13. Tanaka, J.; Gurnani, P.; Cook, A. B.; Häkkinen, S.; Zhang, J.; Yang, J.; Kerr, A.; Haddleton, D. M.; Perrier, S.; Wilson, P., Microscale synthesis of multiblock copolymers using ultrafast RAFT polymerisation. *Polymer Chemistry* **2019,** *10* (10), 1186-1191.
14. Kopeć, M.; Krys, P.; Yuan, R.; Matyjaszewski, K., Aqueous RAFT Polymerization of Acrylonitrile. *Macromolecules* **2016,** *49* (16), 5877-5883.
15. Etchenausia, L.; Rodrigues, A. M.; Harrisson, S.; Deniau Lejeune, E.; Save, M., RAFT Copolymerization of Vinyl Acetate and N-Vinylcaprolactam: Kinetics, Control, Copolymer Composition, and Thermoresponsive Self-Assembly. *Macromolecules* **2016,** *49* (18), 6799-6809.
16. Guinaudeau, A.; Mazières, S.; Wilson, D. J.; Destarac, M., Aqueous RAFT/MADIX Polymerisation of N-Vinyl Pyrrolidone at Ambient Temperature. *Polymer Chemistry* **2012,** *3* (1), 81-84.
17. Abreu, C. M. R.; Mendonça, P. V.; Serra, A. C.; Coelho, J. F. J.; Popov, A. V.; Gryn'ova, G.; Coote, M. L.; Guliashvili, T., Reversible Addition–Fragmentation Chain Transfer Polymerization of Vinyl Chloride. *Macromolecules* **2012,** *45* (5), 2200-2208.

18. Barner, L.; Davis, T. P.; Stenzel, M. H.; Barner-Kowollik, C., Complex Macromolecular Architectures by Reversible Addition Fragmentation Chain Transfer Chemistry: Theory and Practice. *Macromolecular Rapid Communications* **2007,** *28* (5), 539-559.
19. Willcock, H.; O'Reilly, R. K., End Group Removal and Modification of RAFT Polymers. *Polymer Chemistry* **2010,** *1* (2), 149-157.
20. Floyd, T. G.; Häkkinen, S.; Hall, S. C. L.; Dalgliesh, R. M.; Lehnen, A.-C.; Hartlieb, M.; Perrier, S., Cationic Bottlebrush Copolymers from Partially Hydrolyzed Poly(oxazoline)s. *Macromolecules* **2021,** *54* (20), 9461-9473.
21. Kerr, A.; Hartlieb, M.; Sanchis, J.; Smith, T.; Perrier, S., Complex Multiblock Bottle-Brush Architectures by RAFT Polymerization. *Chemical Communications* **2017,** *53* (87), 11901-11904.
22. Shanmugam, S.; Cuthbert, J.; Kowalewski, T.; Boyer, C.; Matyjaszewski, K., Catalyst-Free Selective Photoactivation of RAFT Polymerization: A Facile Route for Preparation of Comblike and Bottlebrush Polymers. *Macromolecules* **2018,** *51* (19), 7776-7784.
23. Tanaka, J.; Häkkinen, S.; Boeck, P. T.; Cong, Y.; Perrier, S.; Sheiko, S. S.; You, W., Orthogonal Cationic and Radical RAFT Polymerizations to Prepare Bottlebrush Polymers. *Angewandte Chemie International Edition* **2020,** *59* (18), 7203-7208.
24. Radzinski, S. C.; Foster, J. C.; Matson, J. B., Synthesis of Bottlebrush Polymers via Transfer-To and Grafting-Through Approaches Using a RAFT Chain Transfer Agent With a ROMP-Active Z-Group. *Polymer Chemistry* **2015,** *6* (31), 5643-5652.
25. Zheng, Z.; Ling, J.; Müller, A. H. E., Revival of the R-Group Approach: A "CTA-shuttled" Grafting from Approach for Well-Defined Cylindrical Polymer Brushes via RAFT Polymerization. *Macromolecular Rapid Communications* **2014,** *35* (2), 234-241.
26. Kerr, A. Complex Bottle-Brush Copolymers by Reversible Addition Fragmentation Chain Transfer Polymerisation: Synthesis and Applications. University of Warwick, Coventry, England, 2019.
27. Foster, J. C.; Radzinski, S. C.; Matson, J. B., Graft Polymer Synthesis by RAFT Transfer-To. *Journal of Polymer Science Part A: Polymer Chemistry* **2017,** *55* (18), 2865-2876.
28. Hsieh, T.-L.; Martinez, M. R.; Garoff, S.; Matyjaszewski, K.; Tilton, R. D., Interfacial Dilatational Rheology as a Bridge to Connect Amphiphilic Heterografted Bottlebrush Copolymer Architecture to Emulsifying Efficiency. *Journal of Colloid and Interface Science* **2021,** *581*, 135-147.
29. Yildirim, I.; Bus, T.; Sahn, M.; Yildirim, T.; Kalden, D.; Hoeppener, S.; Traeger, A.; Westerhausen, M.; Weber, C.; Schubert, U. S., Fluorescent Amphiphilic Heterografted Comb Polymers Comprising Biocompatible PLA and PEtOx Side Chains. *Polymer Chemistry* **2016,** *7* (39), 6064-6074.
30. Laroque, S.; Reifarth, M.; Sperling, M.; Kersting, S.; Klöpzig, S.; Budach, P.; Storsberg, J.; Hartlieb, M., Impact of Multivalence and Self-Assembly in the Design of Polymeric Antimicrobial Peptide Mimics. *ACS Applied Materials & Interfaces* **2020,** *12* (27), 30052-30065.
31. Buback, M.; Hesse, P.; Junkers, T.; Theis, T.; Vana, P., Chain-Length-Dependent Termination in Acrylate Radical Polymerization Studied via Pulsed-Laser-Initiated RAFT Polymerization. *Australian Journal of Chemistry* **2007,** *60* (10), 779-787.

32. Boschmann, D.; Mänz, M.; Pöppler, A. C.; Sörensen, N.; Vana, P., Tracing arm-growth initiation in Z-RAFT star polymerization by NMR: The impact of the leaving R-group on star topology. *Journal of Polymer Science Part A: Polymer Chemistry* **2008,** *46* (21), 7280-7286.
33. Gody, G.; Maschmeyer, T.; Zetterlund, P. B.; Perrier, S., Rapid and Quantitative One-Pot Synthesis of Sequence-Controlled Polymers by Radical Polymerization. *Nature Communications* **2013,** *4*, 2505-2514.
34. Fröhlich, M. G.; Vana, P.; Zifferer, G., Shielding Effects in Polymer-Polymer Reactions, 1: Z-RAFT Star Polymerization of Four-Arm Stars. *Macromolecular Theory and Simulations* **2007,** *16* (6), 610-618.
35. Radzinski, S. C.; Foster, J. C.; Lewis, S. E.; French, E. V.; Matson, J. B., Factors Affecting Bottlebrush Polymer Synthesis by the Transfer-To Method Using Reversible Addition–Fragmentation Chain Transfer (RAFT) Polymerization. *Polymer Chemistry* **2017,** *8* (10), 1636-1643.
36. Fröhlich, M. G.; Nardai, M. M.; Förster, N.; Vana, P.; Zifferer, G., Shielding Effects in Polymer–Polymer Reactions, 3. Z-RAFT Star Polymerization Under Various Solvent Conditions. *Polymer* **2010,** *51* (22), 5122-5134.
37. Otsu, T., Organic Polysulfides as Polymerization Initiators. *Journal of Polymer Science* **1956,** *21* (99), 559-561.
38. Otsu, T.; Nayatani, K., Vinyl Polymerization XXVIII. The Polymerization of Styrene Initiated by Tetralkyl Thiuram Disulfides. *Die Makromolekulare Chemie* **1958,** *27* (1), 149-156.
39. Otsu, T.; Yoshida, M., Role of Initiator-Transfer Agent-Terminator (Iniferter) in Radical Polymerizations: Polymer Design by Organic Disulfides as Iniferters. *Die Makromolekulare Chemie, Rapid Communications* **1982,** *3* (2), 127-132.
40. Chen, M.; Zhong, M.; Johnson, J. A., Light-Controlled Radical Polymerization: Mechanisms, Methods, and Applications. *Chemical Reviews* **2016,** *116* (17), 10167-10211.
41. Wang, H.; Li, Q.; Dai, J.; Du, F.; Zheng, H.; Bai, R., Real-Time and in Situ Investigation of "Living"/Controlled Photopolymerization in the Presence of a Trithiocarbonate. *Macromolecules* **2013,** *46* (7), 2576-2582.
42. Carmean, R. N.; Sims, M. B.; Figg, C. A.; Hurst, P. J.; Patterson, J. P.; Sumerlin, B. S., Ultrahigh Molecular Weight Hydrophobic Acrylic and Styrenic Polymers through Organic-Phase Photoiniferter-Mediated Polymerization. *ACS Macro Letters* **2020,** *9* (4), 613-618.
43. Fu, Q.; McKenzie, T. G.; Tan, S.; Nam, E.; Qiao, G. G., Tertiary Amine Catalyzed Photo-Induced Controlled Radical Polymerization of Methacrylates. *Polymer Chemistry* **2015,** *6* (30), 5362-5368.
44. Carmean, R. N.; Becker, T. E.; Sims, M. B.; Sumerlin, B. S., Ultra-High Molecular Weights via Aqueous Reversible-Deactivation Radical Polymerization. *Chem* **2017,** *2* (1), 93-101.
45. McKenzie, T. G.; Costa, L. P. d. M.; Fu, Q.; Dunstan, D. E.; Qiao, G. G., Investigation into the Photolytic Stability of RAFT Agents and the Implications for Photopolymerization Reactions. *Polymer Chemistry* **2016,** *7* (25), 4246-4253.
46. Skrabania, K.; Miasnikova, A.; Bivigou-Koumba, A. M.; Zehm, D.; Laschewsky, A., Examining the UV-Vis Absorption of RAFT Chain Transfer Agents and Their Use for Polymer Analysis. *Polymer Chemistry* **2011,** *2* (9), 2074-2083.
47. Thum, M. D.; Wolf, S.; Falvey, D. E., State-Dependent Photochemical and Photophysical Behavior of Dithiolate Ester and Trithiocarbonate Reversible Addition–

Fragmentation Chain Transfer Polymerization Agents. *The Journal of Physical Chemistry A* **2020,** *124* (21), 4211-4222.
48. Allegrezza, M. L.; De Alwis Watuthanthrige, N.; Wang, Y.; Garcia, G. A.; Ren, H.; Konkolewicz, D., Substituent Effects in Iniferter Photopolymerization: Can Bond Homolysis Be Enhanced by Electronics? *Polymer Chemistry* **2020,** *11* (38), 6129-6133.
49. Corrigan, N.; Trujillo, F. J.; Xu, J.; Moad, G.; Hawker, C. J.; Boyer, C., Divergent Synthesis of Graft and Branched Copolymers through Spatially Controlled Photopolymerization in Flow Reactors. *Macromolecules* **2021,** *54* (7), 3430-3446.
50. Maksym, P.; Tarnacka, M.; Bernat, R.; Bielas, R.; Mielańczyk, A.; Hachuła, B.; Kaminski, K.; Paluch, M., Pressure-Assisted Strategy for the Synthesis of Vinyl Pyrrolidone-Based Macro-Star Photoiniferters. A Route to Star Block Copolymers. *Journal of Polymer Science* **2020,** *58* (10), 1393-1399.
51. Adams, R.; Weeks, L. F., Action of Oxalyl Chloride on Primary, Secondary and Tertiary Alcohols. *Journal of the American Chemical Society* **1916,** *38* (11), 2514-2519.
52. Gody, G.; Barbey, R.; Danial, M.; Perrier, S., Ultrafast RAFT Polymerization: Multiblock Copolymers Within Minutes. *Polymer Chemistry* **2015,** *6* (9), 1502-1511.
53. Barry, J. T.; Berg, D. J.; Tyler, D. R., Radical Cage Effects: The Prediction of Radical Cage Pair Recombination Efficiencies Using Microviscosity Across a Range of Solvent Types. *Journal of the American Chemical Society* **2017,** *139* (41), 14399-14405.
54. Chapter 2 Diffusion-Controlled Reactions in Solution. In *Comprehensive Chemical Kinetics*, Bamford, C. H.; Tipper, C. F. H.; Compton, R. G., Eds. Elsevier: 1985; Vol. 25, pp 3-46.
55. Allen, P. E. M.; Patrick, C. R., Diffusion-Controlled Reactions in Free Radical Polymerisation. *Die Makromolekulare Chemie* **1961,** *47* (1), 154-167.
56. Moad, G.; Rizzardo, E.; Thang, S. H., Radical Addition–Fragmentation Chemistry in Polymer Synthesis. *Polymer* **2008,** *49* (5), 1079-1131.
57. Heatley, F.; Lovell, P. A.; Yamashita, T., Chain Transfer to Polymer in Free-Radical Solution Polymerization of 2-Ethylhexyl Acrylate Studied by NMR Spectroscopy. *Macromolecules* **2001,** *34* (22), 7636-7641.
58. Ahmad, N. M.; Charleux, B.; Farcet, C.; Ferguson, C. J.; Gaynor, S. G.; Hawkett, B. S.; Heatley, F.; Klumperman, B.; Konkolewicz, D.; Lovell, P. A.; Matyjaszewski, K.; Venkatesh, R., Chain Transfer to Polymer and Branching in Controlled Radical Polymerizations of n-Butyl Acrylate. *Macromolecular Rapid Communications* **2009,** *30* (23), 2002-2021.
59. Boschmann, D.; Vana, P., Z-RAFT Star Polymerizations of Acrylates: Star Coupling via Intermolecular Chain Transfer to Polymer. *Macromolecules* **2007,** *40* (8), 2683-2693.
60. Sun, F.; Lu, G.; Feng, C.; Li, Y.; Huang, X., A PHEA-g-PEO Well-Defined Graft Copolymer Exhibiting the Synchronous Encapsulation of Both Hydrophobic Pyrene and Hydrophilic Rhodamine 6G. *Polymer Chemistry* **2017,** *8* (2), 431-440.
61. Wang, G.; Huang, J., Versatility of Radical Coupling in Construction of Topological Polymers. *Polymer Chemistry* **2014,** *5* (2), 277-308.
62. Giz, A.; Çatalgil-Giz, H.; Alb, A.; Brousseau, J.-L.; Reed, W. F., Kinetics and Mechanisms of Acrylamide Polymerization from Absolute, Online Monitoring of Polymerization Reaction. *Macromolecules* **2001,** *34* (5), 1180-1191.

63. Larnaudie, S. C.; Brendel, J. C.; Jolliffe, K. A.; Perrier, S., Cyclic Peptide–Polymer Conjugates: Grafting-To vs Grafting-From. *Journal of Polymer Science Part A: Polymer Chemistry* **2016,** *54* (7), 1003-1011.
64. Carmean, R. N.; Figg, C. A.; Scheutz, G. M.; Kubo, T.; Sumerlin, B. S., Catalyst-Free Photoinduced End-Group Removal of Thiocarbonylthio Functionality. *ACS Macro Letters* **2017,** *6* (2), 185-189.

Chapter 3

Polymerisation-Induced Self-Assembly of Graft Copolymers

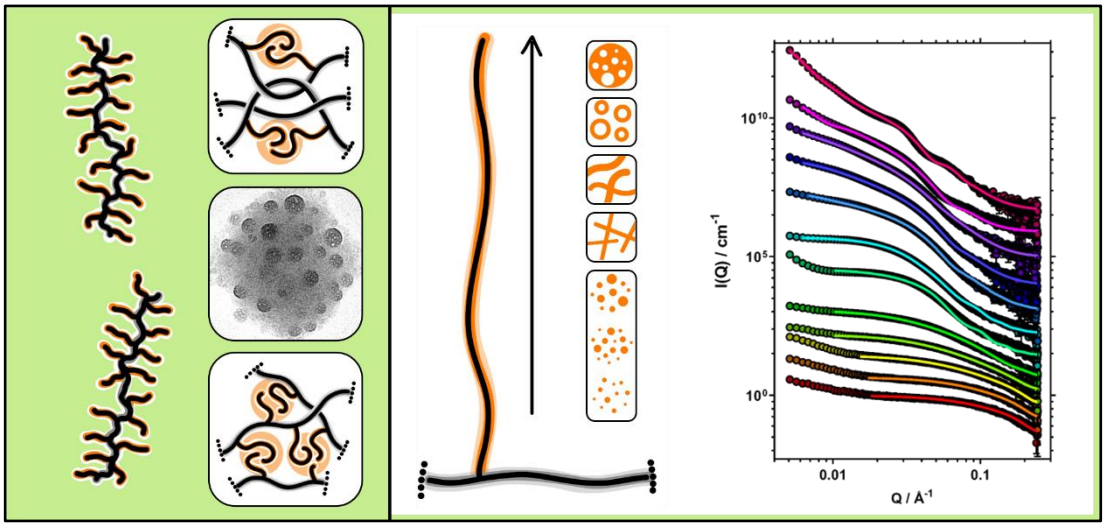

The field of polymer self-assembly has allowed the realisation of various functional polymer materials that find use in everyday life. Amongst the explored avenues of solution self-assembly, the role of polymer architecture has been studied as a parameter that may be used to direct the evolution of aggregate morphologies. In this study, the polymerisation-induced self-assembly of sparsely grafted copolymers was explored to understand how their self-assembly behaviour differs from those of linear diblock copolymers. Electron microscopy revealed the aggregation pathways to be strongly influenced by chain entanglements, immobilised by the phase separation of solvophobic grafts. Small-angle X-ray scattering suggested the graft copolymer architecture promoted formation of multicore aggregates, the core morphology of which evolved with increasing volume fraction of the solvophobe. The key characteristics of the reported system may be expected to apply to similar systems regardless of their chemistry and provides direction for further work.

3.1 Introduction

Polymer self-assembly has been extensively studied both in bulk and solution and has been an active area of polymer research for decades.[1, 2] A significant amount of work in this field has been driven by the search for three-dimensional, spatially periodic composition patterns in the 1-1,000 nm size range to be used in various applications in nanotechnology.[3, 4] Microphase separation of polymers in selective solvents yields materials that have been envisioned for use in energy storage,[5] drug delivery,[6] thin films,[7] and lubrication,[8] amongst other applications. Wide-ranging work in this area has laid a good foundation for the exploration of new opportunities.

3.1.1 Self-Assembly of Block Copolymers

The self-assembly of amphiphilic molecules has intrigued scientists for over a century, with the first publications relating to the micellisation of surfactants dating back to the early 1900s.[9] Attention later shifted towards macromolecular amphiphiles such as block copolymers. In a similar fashion to small molecule surfactants in solution, macromolecules in selective solvents or in the bulk are thermodynamically driven to self-assemble to minimise unfavourable polymer-solvent interactions.

The microphase separation of diblock copolymers in the bulk depends on the volume fractions of the two blocks, the total degree of polymerisation (DP), and the Flory-Huggins interaction parameter, which describes the free-energy cost per monomer of contacts between A and B (i.e., the enthalpic incompatibility between the building blocks):

$$\chi_{\mathrm{AB}} = \left(\frac{Z}{k_B T}\right)\left[\varepsilon_{\mathrm{AB}} - \frac{1}{2}(\varepsilon_{\mathrm{AA}} + \varepsilon_{\mathrm{BB}})\right], \tag{3.1}$$

where Z is the number of nearest neighbours per repeat unit in the polymer, $k_B T$ is the thermal energy, and $\varepsilon_{\mathrm{AB}}$, $\varepsilon_{\mathrm{AA}}$, and $\varepsilon_{\mathrm{BB}}$ are the interaction energies per monomer between A−B, A−A, and B−B, respectively, with negative values indicating a free-energy drive towards mixing.[1] In contrast to small molecules, the entropic gain from mixing distinct polymer chains is relatively small and therefore even minor incompatibilities between their constituting blocks are sufficient to produce excess free energy contributions that disfavour mixing. Self-assembly in solution involves additional χ-parameters to account for segment-solvent interactions between each type of monomer repeat unit and solvent involved. The free energy of aggregation involves

the competing factors of unfavourable loss in entropy owing to core chain stretching, interfacial energy at the separation boundary, and interchain interactions in the corona.[10]

The solution self-assembly of block copolymers may be used to access a range of morphologies. In aggregates of linear AB diblocks, the morphology evolves with a change in the volume fractions of the two blocks and may generally be predicted by the packing parameter p, which relates the volume and length of the solvophobic segment and the contact area of the solvophile (Figure 3.1A).[2, 5] The starting morphology encountered at a high fraction of the soluble block is typically a spherical micelle, which consists of a soluble corona surrounding a solvophobic core with a maximum radius of that of a fully stretched solvophobic block (Figure 3.1B). At smaller volume fractions of the soluble block the polymer may form rod or worm-like micelles, bicontinuous rods, bilayers including lamellae and vesicles, or phase-

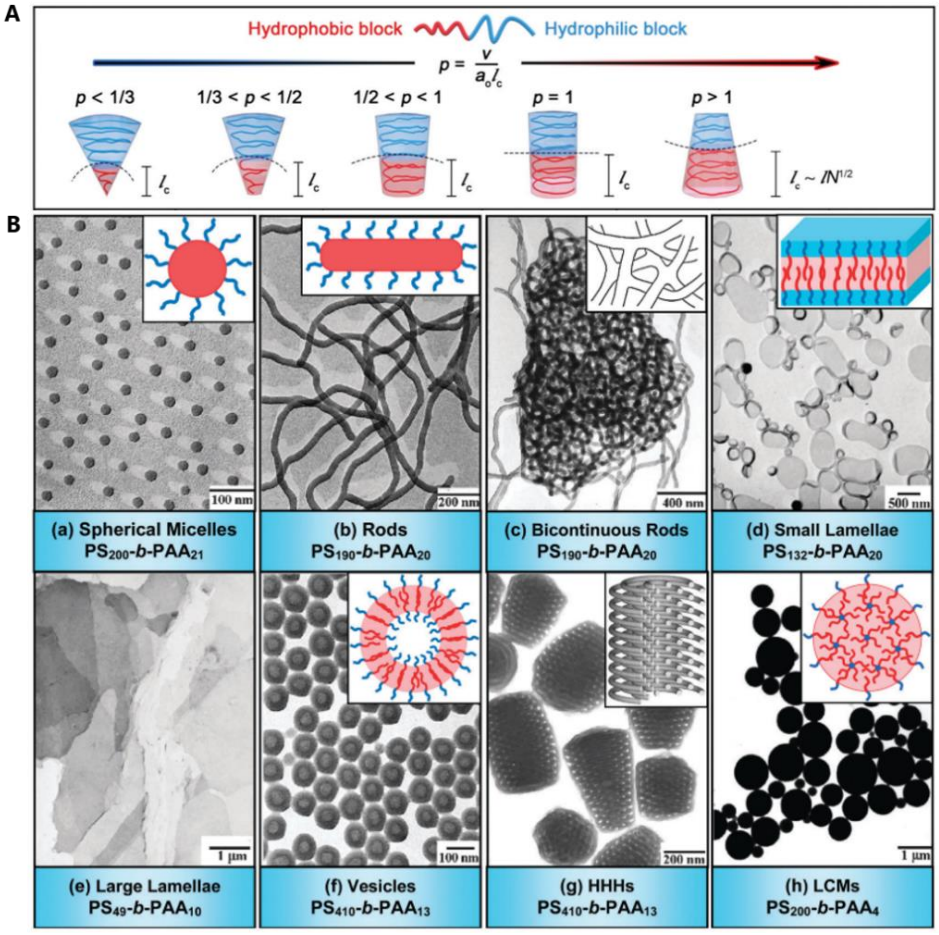

Figure 3.1 A) Dependence of packing parameter, p, on the relative block lengths and the resulting interfacial curvature. Parameters v, a_0, and l_c represent the volume and length of the hydrophobic segment and contact area of the hydrophilic block, respectively. **B)** Evolution of aggregate morphologies with changing volume fractions of the two blocks. Adapted from refs 2, 5.

inverted morphologies such as hexagonally packed hollow hoops and large compound micelles. The resulting morphology may be controlled by adjusting the three previously mentioned parameters contributing to the free energy of the system, for example by changing the solvent, polymer concentration, or through the use of additives such as salts.

Advances in polymer synthesis have allowed the exploration of block copolymer aggregates by employing various polymer architectures with practically unlimited possibilities. The simplest and most studied block copolymer structure is the linear AB diblock, the self-assembly of which is well understood. The introduction of a second solvophobic block allows the preparation of more complex morphologies such as multicompartment micelles with separated core domains.[4] Subtle changes in the polymer structure such as changing the block order from ABC to BAC may lead to different morphologies,[4] and even more minor structural variations such as those arising from molecular weight and composition dispersity – inherent to all polymerisation techniques – have been shown to influence the outcome.[11-13] The self-assembly of branched architectures such as graft copolymers has also been widely studied and shown to provide access to striking morphologies which would be difficult if not impossible to access with linear copolymers.[14-17] The increasing level of complexity in such systems imposes considerable challenges for achieving a comprehensive understanding, but offers many opportunities for new discoveries.

3.1.2 Preparation of Block Copolymer Aggregates

Block copolymer aggregates may be prepared through various methods.[2] Perhaps the most widely used conventional approach is the co-solvent method (also known as a solvent switch), in which a selective solvent is slowly added to a dilute copolymer solution prepared in a good solvent for each block. After sufficient solvent addition, the copolymer solution is typically dialysed to remove the good solvent. An alternative "solvent-free" approach involves the rehydration of a block copolymer film directly into a selective solvent.[18] Other strategies such as microfluidic techniques[19] have also been developed. The main drawback of these methods is the low concentration of the self-assembled structures in resulting solutions, limiting the prospective applications of the resulting materials.

Research involving controlled radical polymerisation techniques gave rise to an alternative self-assembly approach to conventional strategies whereby aggregation

takes place during polymerisation in a selective solvent. This polymerisation-induced self-assembly (PISA) strategy exploits the increasing solvophobicity of a propagating polymer chain to induce its self-assembly *in situ*, giving access to nanoparticles of various morphologies and chemistries in a wide range of reaction media at high concentrations without the need for post-polymerisation protocols.[20, 21] A typical reaction involves the chain extension of a soluble polymer – commonly prepared via solution polymerisation or modification of a commercial polymer – with a second monomer in a dispersion or an emulsion polymerisation. The convenience of the method has been manifested in the substantial popularity of its exploration and the fast-growing number of publications that followed its discovery, as well as the versatile uses proposed for the materials.[8, 22-24] Some recent points of interests and advances made in the field include the development of high-throughput processes,[25, 26] the employment of new initiation mechanisms,[27, 28] and the preparation of organic/inorganic hybrid materials.[29, 30]

3.1.3 Polymerisation-Induced Self-Assembly of Complex Polymer Architectures

In recent years, the use of complex polymer architectures for PISA has sparked some interest and pioneering studies have revealed new possibilities using triblock[31-35] and star-like architectures.[36-39] To highlight some of the discoveries, Armes and co-workers found AB diblock copolymer vesicles formed framboidal vesicles upon chain extension to produce a double solvophobic ABC triblock terpolymer.[34] The surface roughness of the vesicles could be controlled by varying the mean DP of the C block. On the other hand, the employment of double solvophobic BAB-type triblock structures have been reported to yield clustered particles, arising from the phase separation of B blocks into separate core domains and therefore A block bridges connecting adjacent particles.[33, 35, 40] These examples amongst suggest that exploration of PISA systems beyond the classical AB diblock copolymer systems may broaden the scope of the obtainable materials.

While the PISA of graft copolymers has not yet been the focal point of published studies, some research has been done at the boundary of linear and grafted polymers by using oligomeric ethylene glycol[41] or polydimethylsiloxane[42] macromonomers, or monomers with large alkyl side-groups such as lauryl[43] or stearyl[44] methacrylates. Furthermore, Torres-Rocha *et al.* used a polynorbornene-*graft*-poly(ethylene glycol) block to stabilise poly(cyclooctadiene) in water, thus

resulting in brush-coil type copolymers.[45] During the course of our study, the first PISA of graft copolymers was reported for poly(vinyl alcohol)-*graft*-poly(2-hydroxypropyl methacrylate) and poly(vinyl alcohol)-*graft*-poly(diacetone acrylamide) copolymers.[46] The study did not reveal aggregation characteristics specific to the graft copolymer architecture, possibly due to inefficient functionalisation with initiating sites and therefore a low grafting density and an overall poorly controlled architecture. We hypothesised that a systematic study of the PISA of graft copolymers should reveal clear differences to their linear diblock analogues due to the influence of branching on core chain packing or other factors.

3.1.4 Project Outline

We set out to study the PISA synthesis of graft copolymers to learn how their self-assembly differs from that of linear diblock copolymers. To this end, RAFT dispersion polymerisation of sparsely grafted poly(lauryl methacrylate)-*graft*-poly(benzyl methacrylate) (pLMA-*g*-pBzMA) copolymers was conducted in *n*-dodecane using the *grafting from* approach. The linear diblock copolymer analogue, poly(lauryl methacrylate)-*block*-poly(benzyl methacrylate), has been studied in detail in non-polar solvents by Armes and co-workers, and shown to yield spherical micelles, worm-like micelles, and vesicles across a range of block ratios.[43, 47, 48] The influence of structural parameters and concentration on the outcome of these reactions was examined by systematically varying the backbone length, graft length, grafting density, and copolymer concentration. The overall structures of the obtained dispersions and gel-like materials were screened using electron microscopy techniques, and the pBzMA core morphologies were studied in detail using small-angle X-ray scattering (SAXS). A time-resolved SAXS experiment was used to observe morphological transitions *in situ* throughout a polymerisation to better understand the evolution of phase-inverted morphologies.

3.2 Results and Discussion

To study the PISA behaviour of graft copolymers, a previously reported diblock copolymer/solvent system of solvophobic pBzMA and solvophilic pLMA in *n*-dodecane was adapted.[43] In this work, pLMA constituted the graft copolymer backbone, thus making it the solvophile, whereas pBzMA grafts became gradually solvophobic with increasing DP. A backbone with pendent thiocarbonylthio grafting sites was constructed first using a two-step synthetic protocol, followed by the dispersion polymerisation of BzMA grafts to induce the self-assembly of the copolymer (Scheme 3.1). The effects of structural parameters on the self-assembly process were studied by systematically varying the backbone length, graft length, and grafting density.

3.2.1 Preparation of Backbone Copolymers

RAFT copolymerisation of LMA and HEMA was used to prepare linear poly[(lauryl methacrylate)-*stat*-(hydroxyethyl methacrylate)] (p(LMA-*s*-HEMA)) copolymers with controlled molecular weights to construct five backbone precursors (Table 3.1). HEMA was incorporated into the structure to introduce hydroxy groups,

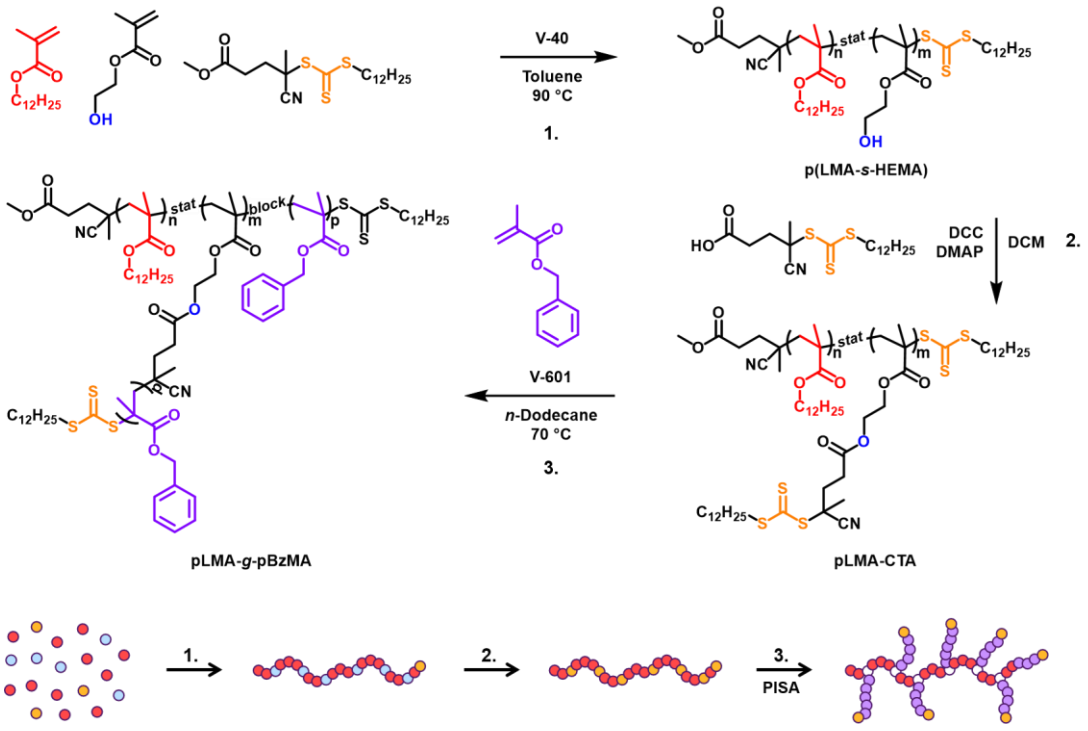

Scheme 3.1 Synthetic route used in this study: statistical RAFT copolymerisation of LMA and HEMA, functionalisation with a RAFT agent, and dispersion polymerisation of BzMA to conduct PISA.

later used for functionalisation with 4-cyano-4-(((dodecylthio)carbonothioyl)thio) pentanoic acid (CPADTC) and graft polymerisation of BzMA. The theoretical maximum number of branching points (n_{CTA}) in each graft copolymer could therefore be adjusted in this step with comonomer stoichiometry. Three copolymers with dissimilar DPs of 206, 474, and 915 but similar comonomer contents (11-12 mol% HEMA) were designed for studying the effects of backbone length on the self-assembly. Conversely, three copolymers with dissimilar comonomer ratios of 2.7, 5.9, and 12 mol% HEMA but similar lengths (DP=896-939) were designed to study the effects of grafting density. Monomer conversions were determined by ^{1}H NMR in $CDCl_3$ (Figure 3.2) and **1a** was further isolated through repeated precipitations to collect a representative ^{1}H-^{13}C HSQC spectrum for resolving overlapping signals (Figure 3.3). SEC analysis of the copolymers **1a-5a** showed unimodal molecular weight distributions and reasonable dispersities for all polymers (Figure 3.4A). Polymers **1a-3a** exhibited a generous shift in the hydrodynamic volume across the series, indicating the three backbones were very different in length. A good overlap was observed for **1a**, **4a**, and **5a**, confirming these polymers were similar in size.

Table 3.1 Structural and characterisation details of backbone copolymers before and after functionalisation.

	Statistical copolymers							
	Structure [A]	**Conversion (%)**		**DP$_{tot}$**	**n_{HEMA}** [A]	**$M_{n,th}$**	**$M_{n,SEC}$** [B]	**$Đ$** [B]
		LMA	HEMA		**(mol%)**	**(g/mol)**	**(g/mol)**	
1a	p(LMA$_{816}$-*s*-HEMA$_{99}$)	88	96	915	11	221,000	152,000	1.38
2a	p(LMA$_{424}$-*s*-HEMA$_{50}$)	90	97	474	11	115,000	80,400	1.24
3a	p(LMA$_{182}$-*s*-HEMA$_{24}$)	76	94	206	12	49,800	40,700	1.16
4a	p(LMA$_{844}$-*s*-HEMA$_{52}$)	84	99	896	6	222,000	140,000	1.32
5a	p(LMA$_{914}$-*s*-HEMA$_{25}$)	88	98	939	3	236,000	143,000	1.37
	Functionalised copolymers							
	Structure	**n_{CTA}/n_{LMA}** [C]		**n_{CTA}** [D]		**$M_{n,th}$**	**$M_{n,SEC}$** [B]	**$Đ$** [B]
		(%)				**(g/mol)**	**(g/mol)**	
1b	pLMA$_{915}$-CTA$_{10\%}$	10		82		254,000	207,000	1.48
2b	pLMA$_{474}$-CTA$_{10\%}$	10		46		133,000	114,000	1.28
3b	pLMA$_{206}$-CTA$_{10\%}$	10		19		57,200	55,900	1.16
4b	pLMA$_{896}$-CTA$_{5\%}$	5		36		236,000	175,000	1.41
5b	pLMA$_{939}$-CTA$_{2\%}$	2		17		243,000	162,000	1.36

[A] Calculated from conversion.

[B] SEC analysis in $CHCl_3$ with DRI detection and PMMA calibration.

[C] Theoretical maximum grafting density, quantified from the ^{1}H NMR spectrum of the isolated product.

[D] Number of CTA functionalities (i.e., grafting sites) per molecule, calculated from n_{HEMA} and n_{CTA}/n_{LMA}.

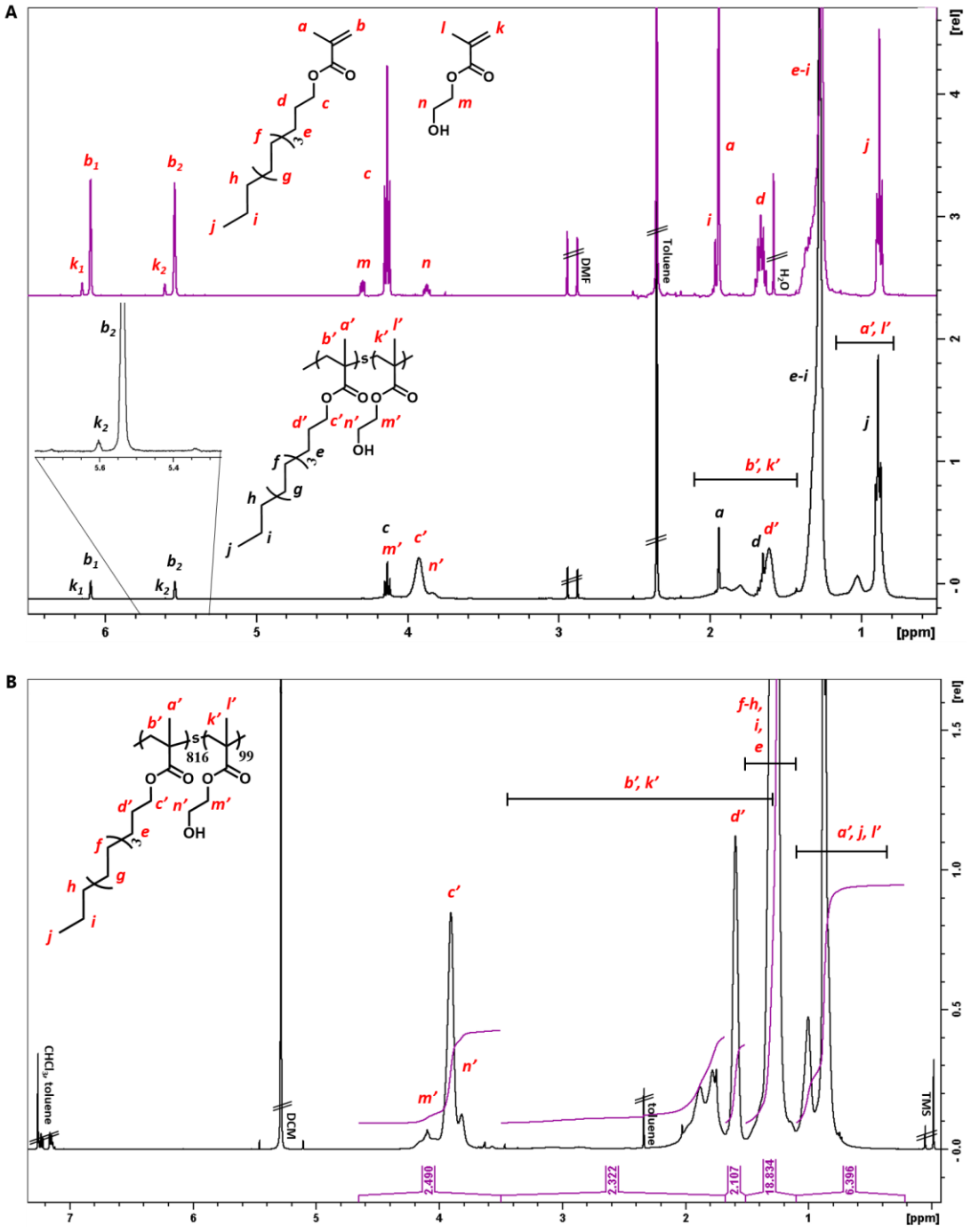

Figure 3.2 Representative ^{1}H NMR spectra of statistical copolymer precursors acquired in $CDCl_3$. **A)** Reaction mixture before and after the reaction. **B)** Isolated p(LMA_{816}-*s*-$HEMA_{99}$) (**1a**).

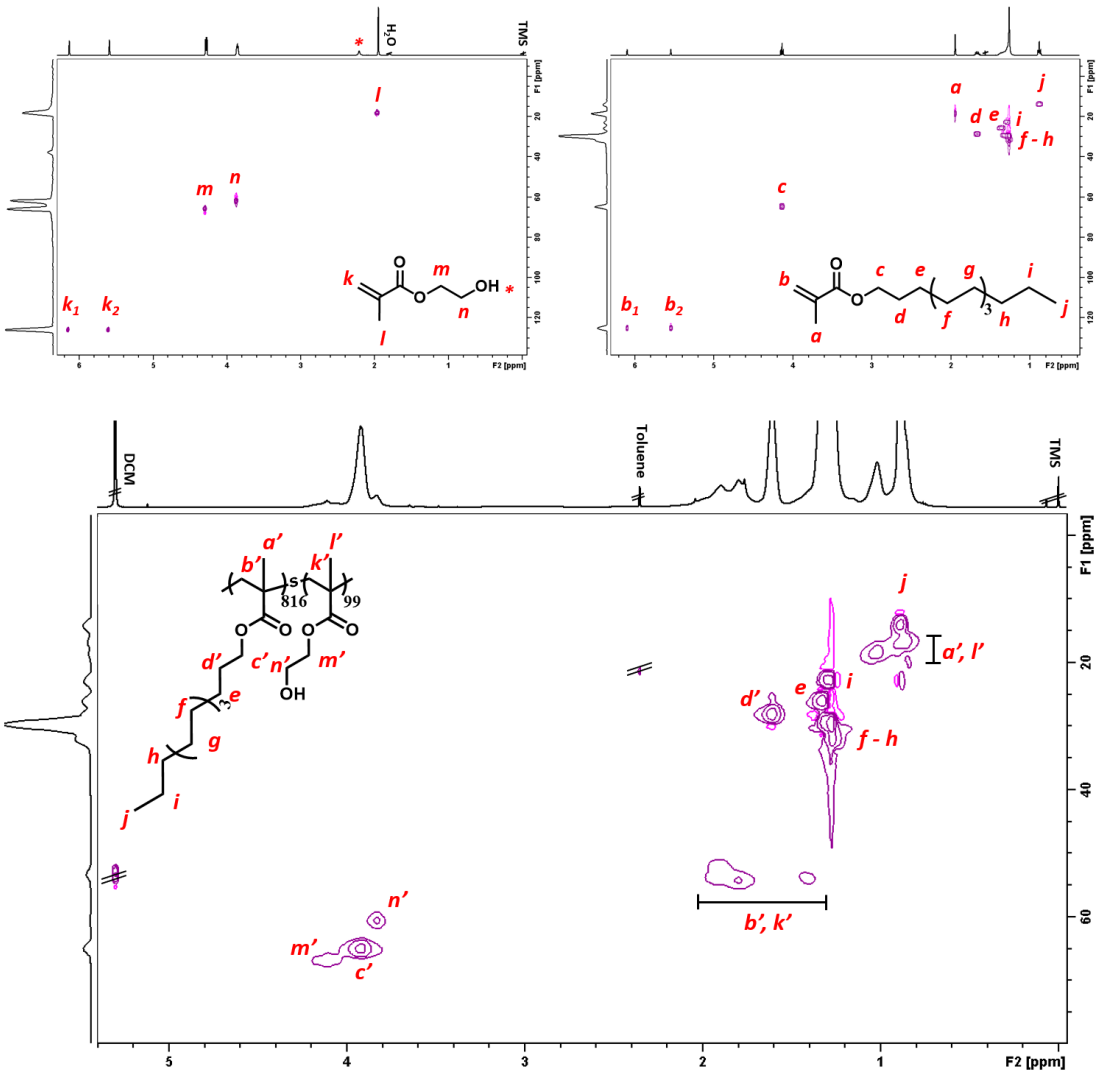

Figure 3.3 ^{1}H-^{13}C HSQC spectrum of p(LMA$_{816}$-*s*-HEMA$_{99}$) (**1a**) (400 MHz, 100 mg/ml in $CDCl_3$). Spectra of LMA and HEMA monomers are shown as a reference.

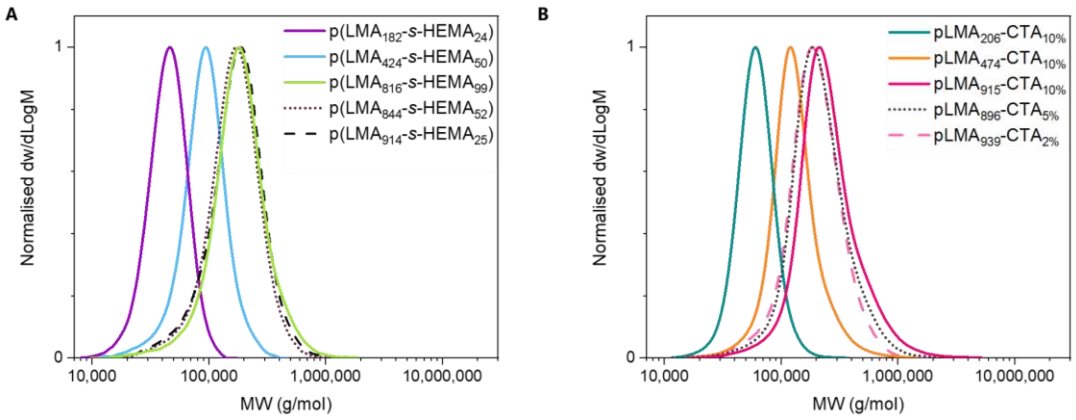

Figure 3.4 SEC profiles of statistical p(LMA-*s*-HEMA) copolymers before (**A**) and after (**B**) functionalisation. Analysis was conducted in $CHCl_3$ with DRI detection and PMMA calibration.

A kinetic study of the statistical copolymerisation of **1a** showed pseudo first-order kinetics during the initial 6 h reaction time and a slightly higher rate of polymerisation for HEMA, suggesting some drift in the monomer distribution and therefore grafts along each chain (Figure 3.5A). SEC analysis showed an increasing M_n and a decreasing dispersity with increasing reaction time, which is indicative of a controlled polymerisation (Figure 3.5B).[49]

To create the loci for the graft polymerisation of BzMA, CPADTC was coupled onto the hydroxy groups of the copolymer using the Steglich esterification method with 4-dimethylaminopyridine and dicyclohexylcarbodiimide,[50] yielding CTA-functionalised backbones (pLMA-CTA) **1b-5b**. After removing excess CTA through repeated precipitation, ^{1}H NMR spectra were recorded to quantify the CTA to LMA ratio (n_{CTA}/n_{LMA}) (Figure 3.6). This ratio corresponded well to the HEMA/LMA molar ratio in the copolymer, suggesting near-quantitative functionalisation of the hydroxy groups. These data were supported by the absence of the $-C\underline{H_2}OH$ signal assigned to HEMA repeat units in the ^{1}H-^{13}C HSQC spectra. SEC profiles of the functionalised copolymers showed a slight increase in M_n due to changes in molecular weight, solubility, and/or bulkiness of the side-groups but otherwise similar molecular weight distributions to that of their precursors (Figure 3.4B).

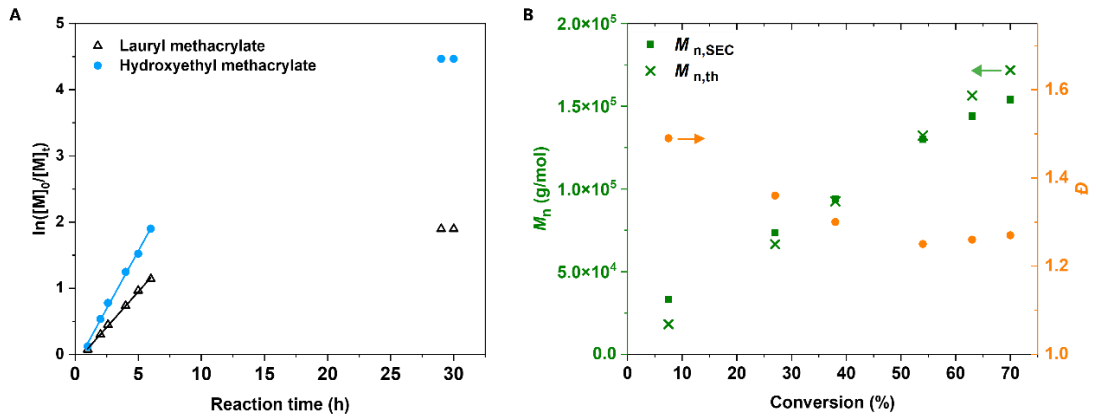

Figure 3.5 A) Pseudo first-order kinetic plot for the statistical copolymerisation of lauryl methacrylate and 2-hydroxyethyl methacrylate (9:1) with $[M]_0$ = 2 M, $[CTA]_0/[I]_0$ = 5, and V-40 at 90 °C in toluene. Linear fits ($r^2 > 0.99$) are indicated by solid lines. **B)** Corresponding SEC data shows the evolution of experimental molecular weight ($M_{n,SEC}$) and dispersity ($Đ$) as given by SEC in $CHCl_3$ using DRI detection and PMMA calibration.

3.2.2 Polymerisation-Induced Self-Assembly of pLMA-g-pBzMA

RAFT dispersion polymerisation of BzMA was conducted at 70 °C in *n*-dodecane using the functionalised copolymers and dimethyl 2,2'-azobis(2-methylpropionate) (V-601) as a thermal initiator. The conversion of BzMA was followed by ^{1}H NMR (Figure **3.7**). Total solids content ($m_{\text{pLMA-CTA}} + m_{\text{BzMA}}$) of 20 wt% was used in all reactions unless otherwise specified.

Owing to the design of the functionalised backbones, the polymerisation of

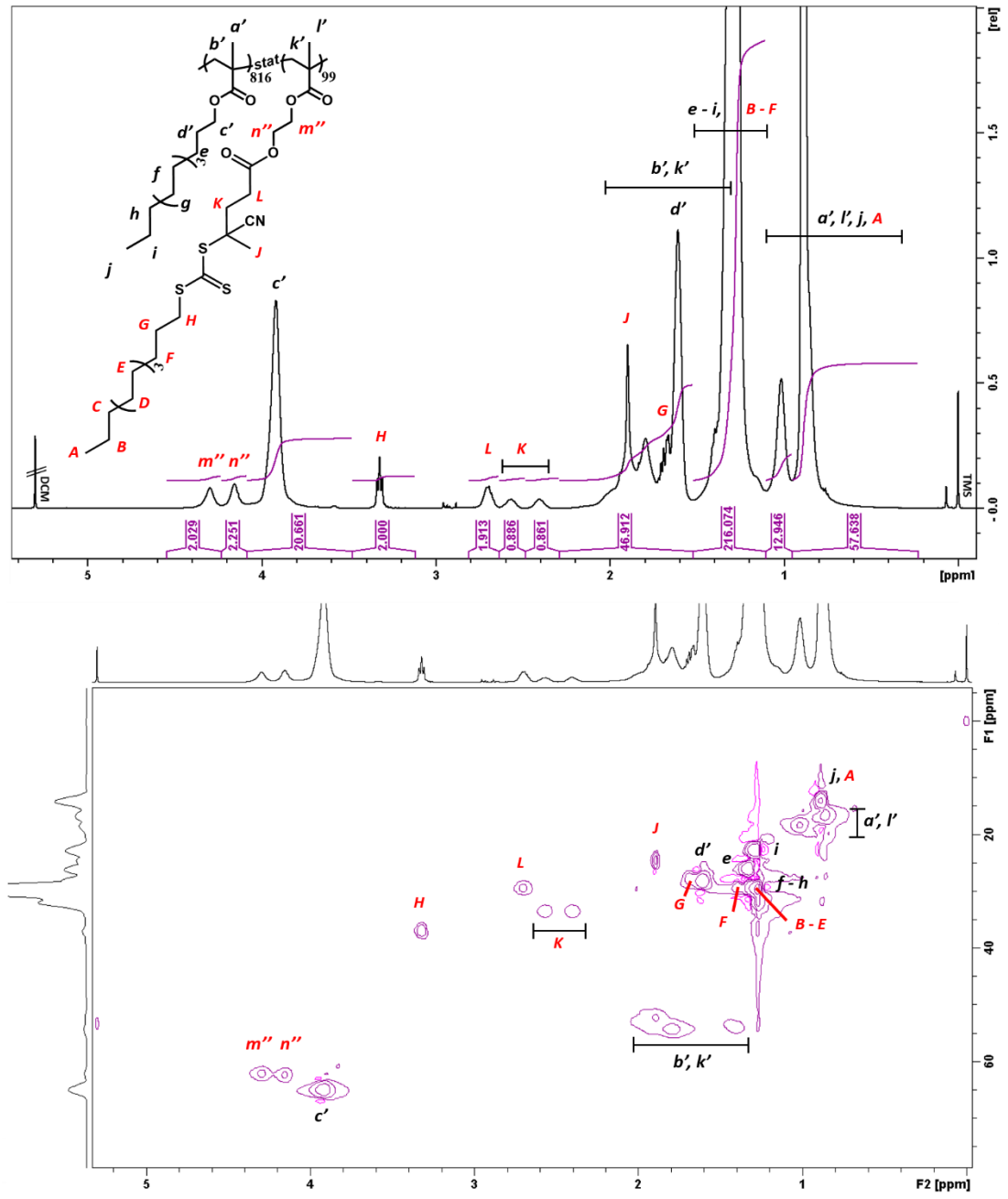

Figure 3.6 ^{1}H NMR and ^{1}H-^{13}C HSQC spectra of pLMA$_{915}$-CTA$_{10\%}$ (**5b**) (400 MHz, 100 mg/ml in $CDCl_3$).

pBzMA grafts took place via the R group approach in which propagating grafts remained covalently bound to the backbone.[51] This grafting strategy is prone to intermolecular graft-graft coupling due to termination via combination especially at high radical concentrations and under monomer-starved conditions.[52, 53] SEC analysis of graft copolymers prepared using backbones **1b**-**3b** showed a unimodal distribution for polymers prepared using the shortest backbone regardless of the graft length (Figure 3.8). Prominent high molecular weight shoulders were observed for polymers with a long backbone. The data suggested that graft coupling could be suppressed in some reactions using moderate initiator concentrations and a slow radical flux, or by targeting very long graft lengths. However, at a constant backbone mass concentration, coupling events were very pronounced in the SEC profiles of longer backbones due to a higher probability of coupling events per molecule, and therefore affecting a larger fraction of the sample as a whole. Aggregation of the propagating grafts may have further increased the probability of coupling by bringing them into closer proximity.

The statistical variation of graft lengths resulted in a considerable fraction of uninitiated CPADTC side-groups remaining after the reactions, particularly in the polymerisation of short grafts. To our surprise, ^{1}H NMR analysis showed the presence

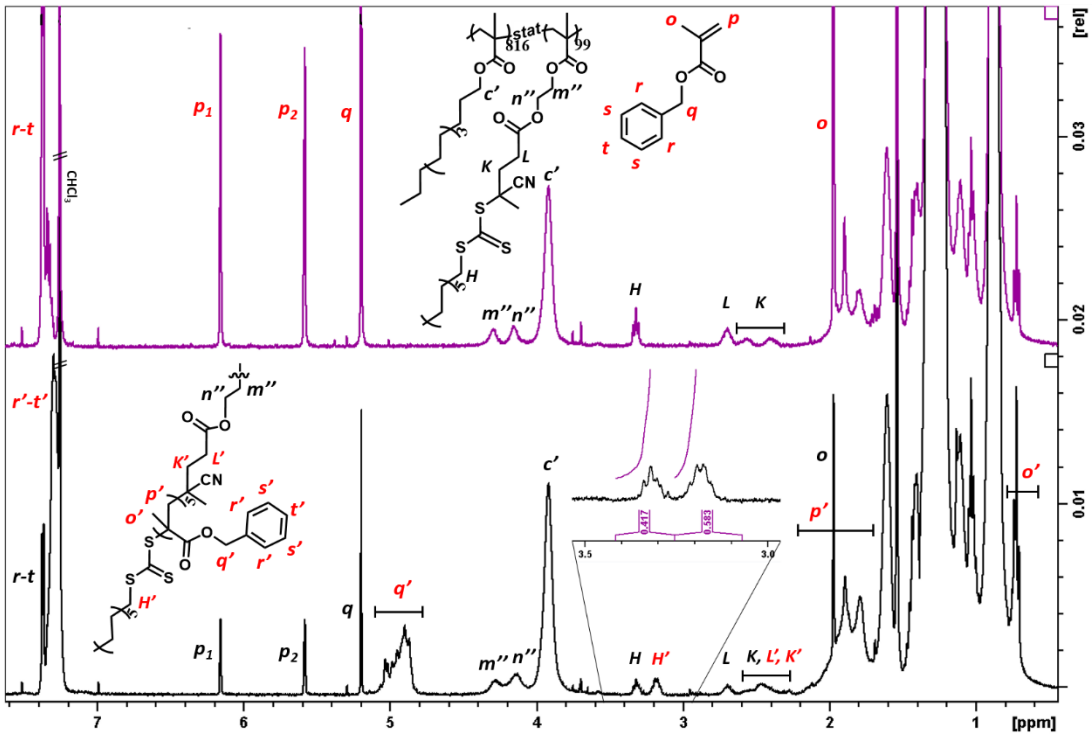

Figure 3.7 Representative ^{1}H NMR spectra of a RAFT dispersion polymerisation of BzMA before and after reaction using pLMA$_{915}$-CTA$_{10\%}$ (**1b**) and targeting graft length of 5 repeating units (400 MHz, $CDCl_3$)**.** Spectrum after reaction shows 42% unreacted pendent CTA (δ=3.32 ppm).

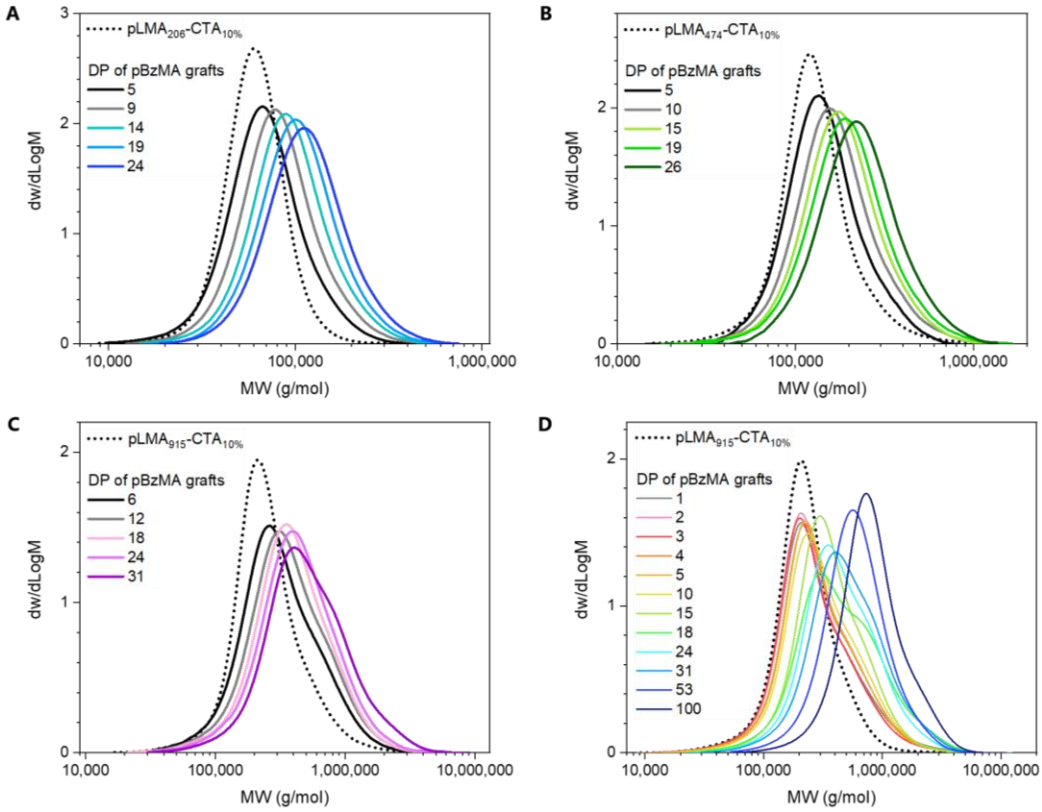

Figure 3.8 SEC profiles of pLMA-*g*-pBzMA copolymers analysed in $CHCl_3$ with DRI detection and PMMA calibration**. A-C)** A comparison between different backbone lengths but similar grafting densities. **D)** A series of reactions targeting a wider range of graft lengths.

of ~15% uninitiated CPADTC even at the highest attempted graft lengths, with reinitiation efficiency quickly plateauing at DP 15-25 and ranging from 30-85% for targeted DPs 1-46 (Figure 3.9). This trend was apparent in all PISA reactions regardless of backbone length, graft length or concentration and resulted in deviation from the targeted grafting densities. A series of solution polymerisation control experiments was carried out in toluene (a non-selective solvent) with $pLMA_{915}$-$CTA_{10\%}$ (**1b**) to rule out effects of self-assembly. A lognormal cumulative distribution function was fitted to data gathered across 44 PISA reactions and used to calculate apparent graft lengths and apparent grafting densities resulting from incomplete reinitiation.

3.2.2.1 Effect of Polymer Architecture on Macroscopic Transitions

The self-assembly behaviour of pLMA-*g*-pBzMA graft copolymers was first assessed by conducting a series of reactions targeting a range of graft lengths

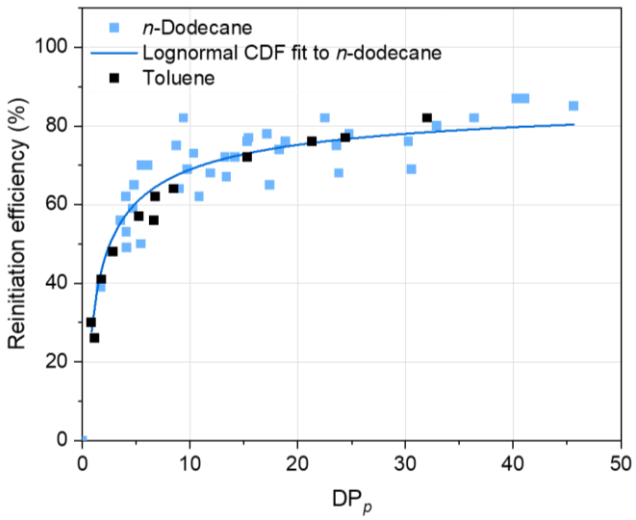

Figure 3.9 Reinitiation efficiency of side-chain CTA, CPADTC, as a function of graft DP$_p$ calculated from conversion. Data were gathered from 44 PISA reactions conducted in this work in *n*-dodecane. Lognormal cumulative distribution fit was made to the data with Origin software (r^2=0.771). A series of reactions was carried out in toluene as a control experiment.

(DP 1-100) at 20 wt% with pLMA$_{915}$-CTA$_{10\%}$ (**1b**) (Table 3.2). The solvophobe to solvophile ratio required for the self-assembly to take place was found to be very low (n_{BzMA}/n_{LMA}<0.1). The appearance of the reaction mixtures changed from dispersions with an increasing viscosity (DP≤5) into a gel-like consistency (DP 10), and further into a low-viscosity milky dispersion (DP 100) (Figure 3.10A). Within the gel-like regime, an increase in turbidity (DP 15) was followed by a partial expulsion of solvent from the polymer phase at longer graft lengths (DP 50). No changes in the consistency of these materials were observed over the course of several months.

TEM, SEM and cryo-SEM imaging of the reaction mixtures revealed the presence of discrete spherical particles at the shortest and longest targeted graft lengths of DP 1 and 100, respectively, and a clustered/fused regime at moderate graft lengths (DP 10) (Figure 3.10C-E). The spherical particles formed at DP 1 were found to have an intricate internal structure and a rough surface with spherical protuberances. Detailed elucidation of the internal morphology of the spheres was unsuccessful due to the destructive effect of the electron beam. Cryo-SEM was used to image the gel-like phase at DP 10, indicating polydisperse spheres and clusters thereof. Despite appearing gel-like at short time scales, such dispersions exhibited flow at long time scales (Figure 3.10B).

Further reactions were carried out using functionalised backbones **2b**-**5b** (see Experimental section 3.4.3.4 for details). TEM studies of the reaction mixture obtained

Table 3.2 Structural and characterisation details of $pLMA_{915}$-*g*-$pBzMA_x$ graft copolymers prepared with $pLMA_{915}$-$CTA_{10\%}$ for studying the effect of graft length on PISA transitions.

	Conversion (%)	**DP_p** [A]	**I_{eff}** [B] **(%)**	**DP_{app}** [B]	**$n_{g,\%}$** [B]	**n_{BzMA}/n_{LMA}** [C]	**$M_{n,th}$ (g/mol)**	**$M_{n,SEC}$** [D] **(g/mol)**	**$Đ$** [D]
6.1	76	1	30	3	3	0.086	266,000	206,000	1.82
6.2	79	2	45	4	4	0.17	279,000	203,000	1.71
6.3	82	3	53	5	5	0.28	293,000	199,000	1.76
6.4	84	4	57	6	5	0.36	305,000	218,000	1.76
6.5	84	5	60	8	5	0.47	321,000	221,000	1.73
6.6	91	10	69	14	6	1.0	394,000	236,000	1.72
6.7	96	15	73	21	7	1.6	477,000	288,000	1.56
6.8	99	18	74	24	7	1.8	518,000	315,000	1.95
6.9	97	24	77	31	7	2.4	598,000	341,000	1.68
6.10	99	31	78	40	7	3.1	696,000	383,000	1.72
6.11	98	53	N/A	-	-	5.3	1,018,000	481,000	1.50
6.12	99	105	N/A	-	-	11	1,773,000	661,000	1.48

[A] Calculated from conversion.

[B] Reinitiation efficiency of side-chain CTAs (I_{eff}), apparent degrees of polymerisation (DP_{app}), and apparent grafting densities ($n_{g,\%}$) calculated from lognormal CDF fit (see Figure 3.9).

[C] BzMA/LMA molar ratio in the graft copolymer.

[D] SEC analysis in $CHCl_3$ with DRI detection and PMMA calibration.

at DP 10 with $pLMA_{474}$-$CTA_{10\%}$ (**2b**) revealed the presence of clustered spherical particles with a complex core morphology (Figure 3.10F), shining light on the origin of the observed high viscosities. The image was obtained after attempted dilution and vigorous vortexing of the reaction mixture with macroscopic agglomerates remaining afterwards, suggesting that the interactions holding individual particles together are relatively strong. Clustered spherical particles have been previously reported by other groups to result from the phase separation of B blocks in double solvophobic BAB triblock copolymers into separate core domains, thus forming solvophilic bridges between individual particles.[33, 40] Similar phenomena were hypothesised to be at play in our system and the observed clusters were ascribed to physical crosslinks arising from backbone bridges and entanglements (Figure 3.10G).

The initial observations made herein suggested that the graft copolymer architecture promoted different PISA transitions compared to the linear diblock equivalent, which has been reported to form spherical micelles, worm-like micelles and vesicles.[43] These differences presumably arise from backbone entanglements and

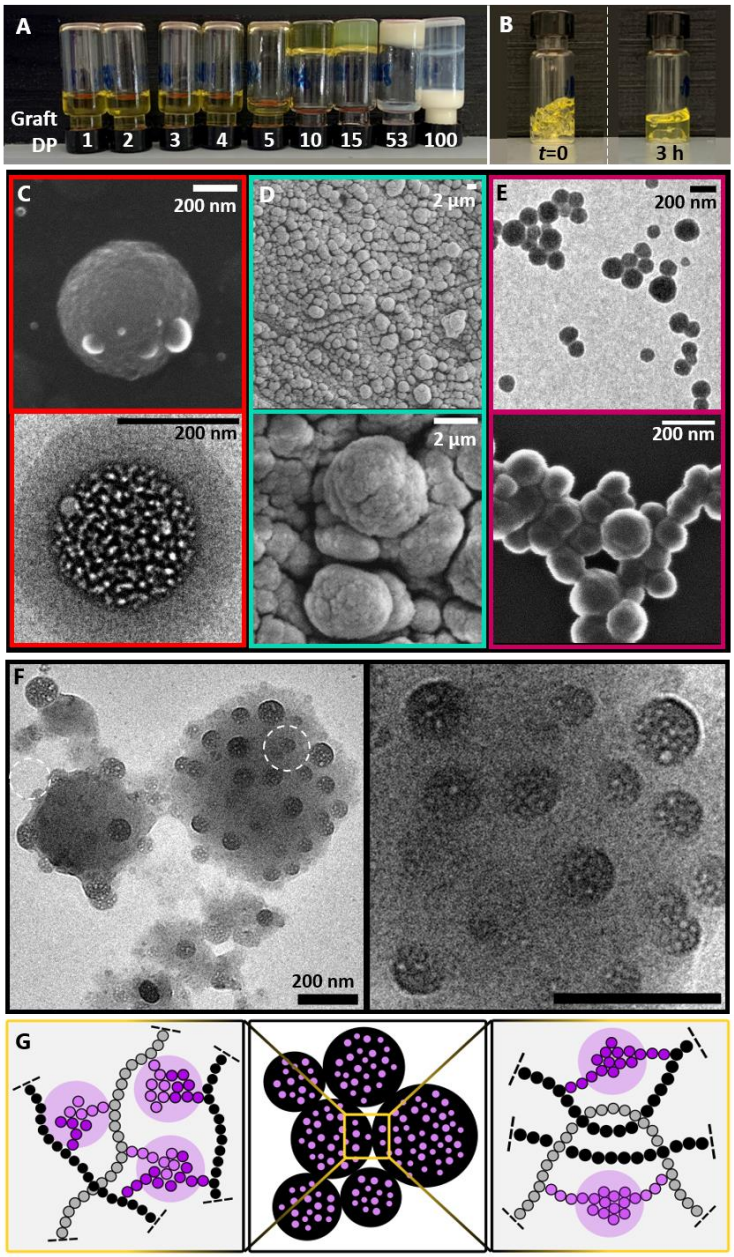

Figure 3.10 A) Appearances of reaction mixtures after PISA targeting various graft lengths with $pLMA_{915}$-$CTA_{10\%}$. **B)** Flow of gel-like material (DP 10) after agitation. **C)** SEM (top) and TEM (bottom) images of reaction mixture targeting graft DP 1. **D)** Cryo-SEM images of reaction targeting DP 10. **E)** TEM (top) and SEM (bottom) images of reaction targeting DP 100. **F)** Particle clusters obtained with $pLMA_{474}$-$CTA_{10\%}$ targeting DP 10. **G)** Illustration of clustered spheres held together by physical crosslinks arising from backbone bridging (left) and entanglements (right).

the incorporation of insoluble grafts of one molecule into multiple core domains, resulting in physical crosslinks and directing the self-assembly process. At a constant mass concentration of the final product, the backbone concentration and therefore entanglements were greatly reduced in reactions targeting longer graft lengths and macroscopic gelation did not occur. At extremely short target graft lengths, the grafted chains may have retained sufficient mobility such that any clusters that may have been

formed in the reactions could break apart under shear during sample preparation, resulting in discrete spherical particles on substrates.

Similar transitions from a dispersion to a gel-like consistency and TEM findings were observed with all five backbones, regardless of their length or grafting density. The physical appearance of the reaction mixtures suggested delayed gelation for shorter backbones; however, this could also result from subtle differences in graft length and graft-graft coupling. Partial expulsion of solvent from the polymer phase took place at shorter graft lengths with shorter backbones. For backbones of similar length but different grafting density, the gel-like consistency was reached at similar graft lengths (DP≈10) as opposed to similar n_{BzMA}/n_{LMA} ratios, suggesting that the solubility and thus mobility of pBzMA grafts was a predominant factor in this transition. The formation of precipitates at a reduced concentration (10 wt%) suggested intermolecular and/or interparticle interactions played a key role in the stabilisation of the dispersions. Attempts to employ a higher grafting density backbone $pLMA_{194}$-$CTA_{29\%}$ resulted in unstable aggregates even at short graft lengths (DP 5-20), indicating a practical lower limit for the number of pLMA units per graft.

3.2.2.2 Evaluation of Core Morphologies with SAXS

Small-Angle X-ray Scattering (SAXS) was used as a complementary, non-destructive technique to gain insight into the internal structure of the dispersions and gel-like materials obtained with $pLMA_{915}$-$CTA_{9\%}$ (**1b**) within the achievable *Q* range (0.005-0.24 $Å^{-1}$), thus including the size, composition, and morphology of small features but not the larger structures observed with electron microscopy (Figure 3.11). Due to the similarity in the chemical composition and thus the SLD of *n*-dodecane and the pLMA backbone, solvated pLMA could not be differentiated from the solvent. Therefore, rather than probing the overall particle structure, these data described the structures formed by the phase-separated pBzMA grafts. To avoid compromising sample integrity, data were collected directly from the reaction mixtures without dilution.

For the shortest graft lengths (DP 1-5), the data indicated the formation of small pBzMA spheres with substantially smaller radii (16-18 nm) than the overall particle radii observed by electron microscopy (Table 3.3). Some general trends could be identified in the fitted parameters. The radii of the spheres increased with increasing

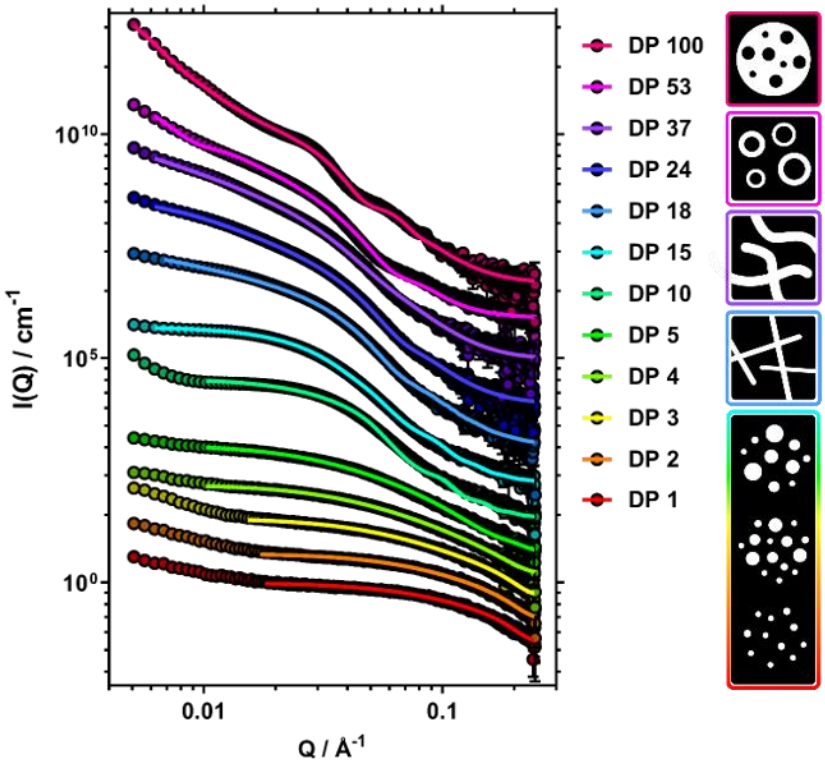

Figure 3.11 SAXS data (points) and associated structural fits (lines) for the $pLMA_{915}$-*g*-$(pBzMA_n)_m$ graft copolymers. Graft DP was varied from 1-100 (bottom to top data, vertically offset for clarity). Scheme illustrates the suggested multicore micelle, rigid cylinder, flexible cylinder, vesicle, and inverse multicore micelle morphologies of the pBzMA cores (in white) against pLMA and *n*-dodecane (in black) (not to scale).

graft length, with an associated increase in the radial polydispersity. For the shortest graft lengths, an increasing inter-sphere interaction was also observed, as indicated by the lower "stickiness" parameter of the sticky hard sphere structure factor. This interaction between the pBzMA cores could also be seen in the scattering patterns as a low-*Q* increase in the scattering intensity, possibly arising from the formation of new cores with the increasing number and solvophobicity of grafts. Combining the information obtained by electron microscopy and SAXS, the observed spherical particles were hypothesised to have a multicore micellar structure in which grafts of multiple main chains phase-separated into small spherical globules, stabilised by a large pLMA continuum. Undoubtedly, backbone entanglements and bridging effects played a key role in the formation of these structures. A decrease in inter-core interactions was observed at longer graft lengths (DP 10-15), as suggested by both a larger "stickiness" fitting parameter and a smaller increase in scattering intensity at low-*Q*. This observation could possibly be explained by the cores becoming

Table 3.3 Parameters obtained through fitting SAXS data for $pLMA_{915}$-*g*-$(pBzMA_x)_y$ samples of increasing graft length to models consisting of a spherical form factor and a sticky hard sphere structure factor (DP 1-15), cylinder (DP 18) or flexible cylinder (DP 24, 37) form factors, vesicle form factor (DP 53) and raspberry form factor (DP 100). Radii (*r*), radial polydispersities (PDI), volume fractions (χ), Kuhn lengths (*b*), and diameters (*d*) extracted from the fits. More detailed descriptions can be found in the experimental section 3.4.1.4.

Sticky hard sphere				
DP	***r* (Å)**	**PDI$_r$**	**$\underline{\chi_V}$**	**Stickiness**
1	16.0 ± 0.08	0.16 ± 0.004	0.09 ± 0.0005	0.22 ± 0.0014
2	15.8 ± 0.07	0.21 ± 0.003	0.12 ± 0.0006	0.21 ± 0.0008
3	16.4 ± 0.06	0.21 ± 0.003	0.13 ± 0.0006	0.16 ± 0.0003
4	16.8 ± 0.09	0.26 ± 0.002	0.11 ± 0.0005	0.13 ± 0.0021
5	17.9 ± 0.19	0.35 ± 0.003	0.12 ± 0.0003	0.12 ± 0.0004
10	64.0 ± 0.05	0.45 ± 0.002	0.26 ± 0.0005	0.44 ± 0.0004
15	67.2 ± 0.12	0.40 ± 0.001	0.19 ± 0.0004	0.59 ± 0.0063
Cylinder				
DP	***r* (Å)**	**PDI$_r$**	**$\underline{\chi_V}$**	***b* (Å)**
18	48.0 ± 0.03	0.32 ± 0.001	0.25 ± 0.0001	-
24	54.6 ± 0.02	0.25 ± 0.001	0.14 ± 0.0001	107.1 ± 0.2
37	59.4 ± 0.12	0.35 ± 0.001	0.12 ± 0.0004	125.3 ± 1.3
Vesicle					
DP	**r_{core} (Å)**	**PDI$_r$**	**$d_{bilayer}$ (Å)**	**PDI$_d$**	**$\underline{\chi}$**
53	174 ± 0.04	0.60 ± 0.001	92.3 ± 0.04	0.26 ± 0.001	0.16 ± 0.00003
Multicore inverse micelle						
DP	**r_{large} (Å)**	**r_{small} (Å)**	**PDI$_r$**	**$\chi_{V,large}$**	**$\chi_{V,small}$**	**$\chi_{surface}$**
100	569.5 ± 0.23	100.0 ± 0.06	0.25 ± 0.0002	0.25 ± 0.0003	0.21 ± 0.0003	0.25 ± 0.0018

increasingly solvophobic, resulting in their further collapse, stretching of the main chain bridges, and thus a larger inter-domain distance.

A further increase in graft length (DP 18) led to a substantial observable difference in the scattering pattern, especially at low values of *Q* where the scattered intensity scaled as Q^{-1}, indicating the formation of elongated cylindrical structures. The total length of these rigid cylinders was not determinable within the achievable *Q* range and was therefore fixed throughout the analysis. The findings suggested a sphere-to-cylinder transition occurs through fusion of individual solvophobic cores, driven by a change in the packing parameter for each graft-backbone segment. Similar to the multicore micelles, these cylindrical pBzMA domains were hypothesised to exist within a larger pLMA continuum. As the graft length increased further (DP 24-37), a flexible cylinder form factor was required to obtain adequate fits to these data, suggesting that continued growth of the grafts led to the formation of worm-like

structures, the radii and Kuhn lengths of which were found to increase with increasing graft length.

Another large change in the scattering pattern was observed at DP 53 for which the best fit was obtained using a polydisperse vesicular form factor. These fits suggested a worm-to-vesicle transition for the pBzMA cores, whereby the length of the solvophobic component became too long to be stabilised in a micellar structure. The vesicle wall thickness was found to be smaller than the diameter of the cylindrical micelles, suggesting interdigitation of the pBzMA chains within the vesicle wall.[54, 55] The observed morphological transitions were hypothesised to take place within a physically crosslinked pLMA/solvent matrix. The partial expulsion of solvent that was observed for this reaction could be explained by vesicles growing inwards[55] after the worm-to-vesicle transition had taken place.

Finally, at DP 100 a further change in the observed scattering pattern was found. The best fits to these data were obtained with a model describing a large spherical particle consisting of a pBzMA continuum with smaller spherical pockets of pLMA situated within the particle, implying a transition to an inverted multicore micellar structure. With pBzMA now forming the continuous phase within the particle and providing a good contrast against the solvent, the overall particle size and shape could be observed in addition to the small spherical pLMA domains. While the total particle radius was found to be close to that observed by TEM (57 nm and 62 nm, respectively, see Experimental section 3.4.3.4 for details), due to the restricted *Q* range resulting in the lack of an observable Guinier region, the accuracy with which the total radius could be determined by SAXS was limited. Given the colloidal stability of these particles in solution, a substantial fraction of pLMA must be located at the surface. This was supported by the SAXS fitting parameters that suggested 25% of the particle surface comprised of pLMA.

3.2.2.3 Time-Resolved SAXS Study of the Formation of Inverted Multicore Micelles

In order to learn about the transitions leading up to the previously described inverse multicore micelles, the polymerisation targeting a DP 100 graft length was repeated to perform an *in situ* SAXS study of the reaction. A deoxygenated reaction mixture was introduced into a capillary to collect SAXS data continuously over 320 min at 70 °C. The data binned to a 5-minute time resolution showed a clear

increase in scattering intensity throughout the reaction, indicating successful PISA (Figure 3.12A).

The scattering patterns collected over the first 50 min showed no self-assembly and suggested that individual molecules remained as Gaussian chains. The increasing radius of gyration (R_g) of the chains and an increase in zero-angle intensity (I_0) were consistent with the growth of the grafts (Figure 3.12B). After 50 min, a change in the

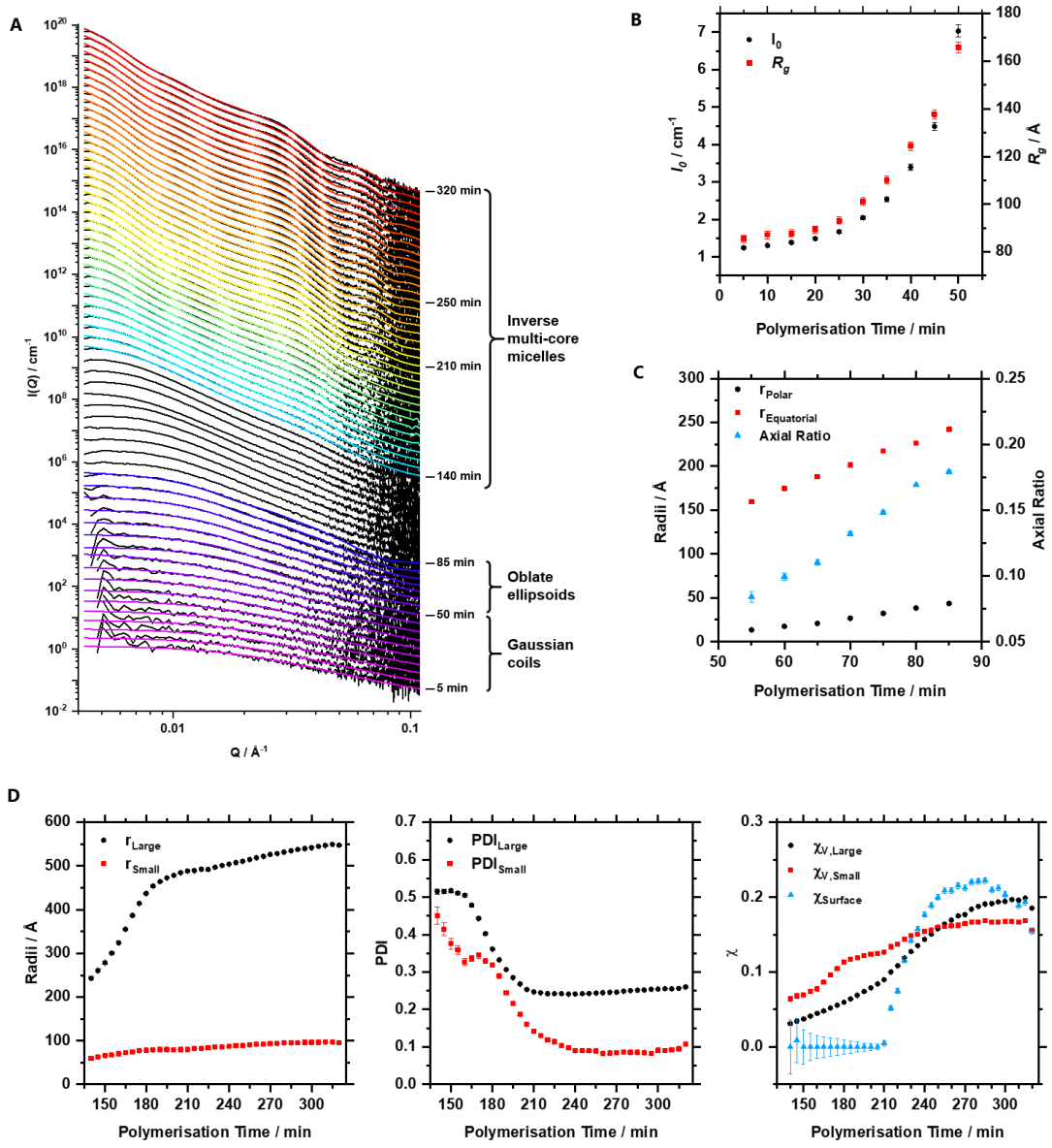

Figure 3.12 A) Time-resolved SAXS data (black traces) collected *in situ* during PISA of pLMA-*g*-pBzMA. Fits to the data are shown as coloured lines. Error bars have been omitted for clarity and datasets have been vertically offset. **B)** I_0 and R_g values obtained through fitting time-resolved SAXS data to Gaussian coil models. **C)** Parameters obtained through fitting time-resolved SAXS data to an ellipsoidal model. **D)** Parameters obtained through fitting time-resolved SAXS data to a raspberry model describing inverse multicore micelles.

gradient of the scattering patterns could be identified at $Q = 0.02$ Å^{-1}, indicating the onset of a coil-to-globule transition for pBzMA. Best fits to these data were obtained using a model describing oblate ellipsoids. A longer reaction time led to gradual growth of these ellipsoids with the equatorial radius increasing faster than the axial radius, indicating swelling towards a less oblate morphology (Figure 3.12C). This ellipsoidal phase was relatively short-lived, suggesting a narrow region within the phase diagram where these structures can be formed. Notably, the ellipsoidal morphology was not observed in our earlier SAXS measurements at full monomer conversion, and here the core volumes were substantially larger (1,400-13,000 nm^3) than the spherical cores of the multicore micelles found previously (17-1,300 nm^3). The differences in the observed morphologies were hypothesised to arise from differences in backbone concentrations and thus entanglements, the presence of BzMA in the solvent phase that may have influenced the solubility of grafts at low conversions in the *in situ* experiment, and possibly the measurement temperature.

Between 90 and 135 min, the data lacked distinct features in the scattering patterns, suggesting a high polydispersity for the particles or the presence of multiple interacting form factors. Similar observations have been previously made for PISA reactions in the literature.[55, 56] After 140 min, two minima were identified at $Q = 0.02$ and 0.05 Å^{-1} that were consistent with the previously encountered inverse multicore micelle morphology. Fitting these data indicated the radii of the large pBzMA continuum and the small pLMA pockets grow in size over time, with an increase in volume fraction and reduction in radial polydispersity for both components (Figure 3.12D). While the increase in radius and volume fraction of the pBzMA phase could be explained by an increase in DP, the reason for the increase in volume fraction of the pLMA phase was less evident. A possible explanation for this could be a change in solvation of the solvophilic pLMA domains, now embedded within the particle interior, resulting in their swelling or fusion. The data suggested the surface fraction of pLMA remained close to zero throughout this first phase. This observation could provide an explanation for why the previously discussed DP 50 reaction had an unusual ‘dry’ consistency, indicative of solvent encapsulation within the particles. While the transition from ellipsoids to the inverted structure remained somewhat unclear based on this experiment alone, previous works sharing some similarities could suggest the final morphology evolved through an ellipsoid fusion-type pathway.[57]

3.3 Conclusions and Outlook

The PISA of graft copolymers was carried out to study their self-assembly behaviour and to reveal possible differences between their linear diblock copolymer counterparts reported in the literature. The system selected for this work comprised a stabilising pLMA backbone, core-forming pBzMA grafts and *n*-dodecane solvent. PISA was conducted by carrying out an R group *grafting from* dispersion polymerisation of BzMA using CTA-decorated pLMA backbones in *n*-dodecane. Regardless of the targeted graft length, the copolymers were found to form only spherical particles or spherical clusters, as opposed to the spherical and worm-like particles obtained with their linear diblock equivalent and many other comonomer-solvent systems. The particle clusters were thought to arise from physical crosslinks due to the backbones entangling and forming bridges across several core domains. These physical crosslinks were identified as the key difference between the grafted and linear diblock architectures and had a considerable influence on the self-assembly pathway.

SAXS studies of the pBzMA cores suggested morphological transitions took place within a pLMA backbone matrix. The physical constraints imposed by the backbone directed the overall particle/gel morphology to transition from a multicore spherical micelle to a multicore worm-like structure and further to vesicles and inverted multicore micelles. Similar multicore structures are not commonly encountered in PISA studies and the employment of the graft copolymer architecture could potentially provide a convenient way to access such morphologies in the future.

Two critical structural parameters could be identified in this study: the backbone concentration influenced the degree of entanglements and thus macroscopic gelation, while the targeted graft length determined the core morphology. An inherent limitation of such copolymer syntheses was our inability to target much higher grafting densities, as each addition of a branching point to the structure effectively removed a stabilising LMA unit, making densely grafted polymers unstable. Alternative designs such as double-grafted structures could be used to study the self-assembly of rigid, bottlebrush-like polymers which may be anticipated to exhibit very different self-assembly behaviour due to lack of backbone entanglements and limited conformational freedom.

3.4 Experimental

3.4.1 Instrumental Methods

3.4.1.1 Nuclear Magnetic Resonance Spectroscopy

^{1}H Nuclear Magnetic Resonance (NMR) spectra and ^{1}H-^{13}C Heteronuclear Single Quantum Coherence (HSQC) spectra were recorded in deuterated chloroform ($CDCl_3$) on Bruker Avance III HD (300 MHz or 400 MHz) spectrometer at 300 K. Chemical shift values (δ) are reported in ppm. Tetramethylsilane (TMS) was used as the internal standard.

3.4.1.2 Scanning Electron Microscopy

Scanning electron microscopy (SEM) was carried out using a Zeiss SUPRA 55-VP instrument operating at 2-12 kV accelerating voltage. Polymer samples were spin-coated or merely deposited onto silicon wafers directly from reaction mixtures and placed under vacuum overnight. Samples were coated with carbon using an Emitech K950X turbo-pumped evaporator prior to imaging.

Cryo-SEM images were taken on a Zeiss Supra 55VP fitted with a Gatan Alto 2500 cryo transfer system.

3.4.1.3 Size Exclusion Chromatography

Size Exclusion Chromatography (SEC) was carried out using an Agilent Infinity II MDS instrument equipped with differential refractive index (DRI), viscometry (VS), dual angle light scattering (DALS) and multiple wavelength UV detectors. The system was equipped with 2×PLgel Mixed C columns (300×7.5 mm, 200 to 200,000 g/mol operating range for polystyrene equivalent) and a PLgel 5 μm guard column. Analyte samples were prepared in $CHCl_3$ and filtered through a Fisherbrand PTFE syringe filter with 0.2 μm pore size before injection. Samples were run in $CHCl_3$ at 1 ml/min at 30 °C. Experimental number-average molar mass ($M_{n,SEC}$) and dispersity ($Đ$) values were determined with Agilent GPC/SEC software by using Agilent EasyVial PMMA calibration.

3.4.1.4 Small-Angle X-Ray Scattering

Small-Angle X-ray Scattering (SAXS) measurements were performed using a Xenocs Xeuss 2.0 equipped with a micro-focus Cu K_α source collimated with scatterless slits providing a 0.8 mm diameter beam. SAXS patterns were recorded

using a Pilatus 300K detector with a pixel size of 0.172 mm×0.172 mm. The sample to detector distance was calibrated using silver behenate ($AgC_{22}H_{43}O_2$) providing a value of 2.481(5) m, which gave an effective scattering vector Q range of 0.005-0.24 Å^{-1}, where Q is defined as

$$Q = \frac{4\pi \sin\theta}{\lambda}\ , \tag{3.2}$$

where 2θ is the scattering angle and λ is the X-ray wavelength. Reaction mixtures were mounted at 20 wt% without dilution in 1 mm (Ø) borosilicate glass capillaries or a Perspex holder with Kapton tape if too viscous for the capillaries. Data were collected for 20 min at 25 °C unless otherwise stated. A radial integration of the 2D scattering profile was performed using FOXTROT software and the resulting data corrected for the absorption, sample thickness and background.[58] Finally, the scattering intensity was then rescaled to absolute intensity using glassy carbon as a standard.[59]

SAXS data were analysed using model-dependent analysis implemented in SasView software.[60] The scattering length density (SLD) is the "scattering power" of a material: it is defined as the sum of X-ray scattering lengths, b_i, of N atoms within a given molecular or particle volume, V_m, as given by

$$\text{SLD} = \frac{\sum_{i=1}^{N} b_i}{V_m}\ . \tag{3.3}$$

The SLD of a material can also be calculated using the bulk density ρ, atomic molar mass M_i and Avogadro's constant N_A,[61] where

$$\text{SLD} = \frac{\rho N_A \sum_{i=1}^{N} b_i}{\sum_{i=1}^{N} M_i}. \tag{3.4}$$

In this study, the SLD of *n*-dodecane, LMA and BzMA were calculated to be 7.41×10^{-6} Å^{-2}, 8.22×10^{-6} Å^{-2}, and 9.52×10^{-6} Å^{-2}, respectively, and fixed for the fitting procedure.

Graft length series: Graft DP 1 to 15 were analysed using a spherical form factor with a Gaussian radial polydispersity applied and a sticky hard sphere structure factor (Table 3.4).[62, 63] Graft DP 18 was analysed using a cylindrical form factor with a Gaussian radial polydispersity applied.[64] Graft DPs 24 and 37 were analysed using a flexible cylinder form factor, describing a cylinder with a total persistence length which can be split into shorter rigid segments, as described by the Kuhn length (Table 3.5).[65, 66] Similar to the cylindrical form factor described above, a Gaussian radial

polydispersity was also applied to the flexible cylinder model. Graft DP 53 was analysed using a vesicular form factor with parameters describing the wall thickness and vesicle radius (Table 3.6).[63] A Gaussian polydispersity was applied to the wall thickness and vesicle radius. Finally, graft DP 100 was analysed using a "raspberry" form factor,[67] describing small spheres within a larger spherical structure (Table 3.7). In this case, the SLD of the small spheres was fixed to that of LMA, and the SLD of the larger spheres fixed to that of BzMA. The fractional penetration depth of small spheres within the larger spheres was set to 1, representing small spheres distributed throughout the larger sphere. Similar to models above, a Gaussian radial polydispersity was also applied.

Table 3.4 Parameters obtained through fitting SAXS data for samples of increasing graft length to a model consisting of a spherical form factor and a sticky hard sphere structure factor. Values marked with * were held constant throughout the fitting procedure.

	DP 1	**DP 2**	**DP 3**	**DP 4**	**DP 5**	**DP 10**	**DP 15**
Solvent SLD ($\times10^{-6}$ Å^{-2})	7.41*	7.41*	7.41*	7.41*	7.41*	7.41*	7.41*
Sphere SLD ($\times10^{-6}$ Å^{-2})	9.52*	9.52*	9.52*	9.52*	9.52*	9.52*	9.52*
Volume fraction	0.09 ± 0.0005	0.12 ± 0.0006	0.13 ± 0.0006	0.11 ± 0.0005	0.12 ± 0.0003	0.26 ± 0.0005	0.19 ± 0.0004
Sphere radius (Å)	16.0 ± 0.08	15.8 ± 0.07	16.4 ± 0.06	16.8 ± 0.09	17.9 ± 0.19	64.0 ± 0.05	67.2 ± 0.12
Radial polydispersity	0.16 ± 0.004	0.21 ± 0.003	0.21 ± 0.003	0.26 ± 0.002	0.35 ± 0.003	0.45 ± 0.002	0.40 ± 0.001
Perturbation	0.05*	0.05*	0.05*	0.05*	0.05*	0.05*	0.05*
Stickiness	0.22 ± 0.0014	0.21 ± 0.0008	0.16 ± 0.0003	0.13 ± 0.0021	0.12 ± 0.0004	0.44 ± 0.0004	0.59 ± 0.0063

Table 3.5 Parameters obtained through fitting SAXS data for increasing graft length from DP 18 to 37 to models consisting of a cylinder (DP 18) or flexible cylinder (DP 24 and 37) form factor. Values marked with * were held constant throughout the fitting procedure.

	DP 18	**DP 24**	**DP 37**
Solvent SLD ($\times10^{-6}$ Å^{-2})	7.41*	7.41*	7.41*
Shell SLD ($\times10^{-6}$ Å^{-2})	9.52*	9.52*	9.52*
Volume fraction	0.25 ± 0.0001	0.14 ± 0.0001	0.12 ± 0.0004
Cylinder length (Å)	2000*	2000*	5000*
Kuhn length (Å)	-	107.1 ± 0.2	125.3 ± 1.3
Cylinder radius (Å)	48.0 ± 0.03	54.6 ± 0.02	59.4 ± 0.12
Radial polydispersity	0.32 ± 0.001	0.25 ± 0.001	0.35 ± 0.001

Table 3.6 Parameters obtained through fitting SAXS data for graft length DP 53 to a model consisting of a vesicle form factor. Values marked with * were held constant throughout the fitting procedure.

	DP 53
Solvent SLD ($\times 10^{-6}$ Å^{-2})	7.41*
Shell SLD ($\times 10^{-6}$ Å^{-2})	9.52*
Volume fraction	0.16 ± 0.00003
Core radius (Å)	173.9 ± 0.04
Wall thickness (Å)	92.3 ± 0.04
Wall thickness polydispersity	0.26 ± 0.001
Radial polydispersity	0.60 ± 0.001

Table 3.7 Parameters obtained through fitting SAXS data for graft length DP 100 to a raspberry form factor describing small pLMA spheres within a larger pBzMA particle. Values marked with * were held constant throughout the fitting procedure.

	DP 100
Solvent SLD ($\times 10^{-6}$ Å^{-2})	7.41*
Large particle SLD ($\times 10^{-6}$ Å^{-2})	9.52*
Small particle SLD ($\times 10^{-6}$ Å^{-2})	8.22*
Volume fraction, large	0.25 ± 0.0003
Volume fraction, small	0.21 ± 0.0003
Surface fraction	0.25 ± 0.0018
Radius, large (Å)	569.5 ± 0.23
Radius, small (Å)	100.0 ± 0.06
Fractional penetration	1*
Radial polydispersity	0.25 ± 0.0002

Time-resolved SAXS experiment: The reaction mixture was prepared in a septum-capped vial, deoxygenated with argon, and transferred into a 1 mm (Ø) borosilicate glass capillary. The capillary was kept at room temperature, in the dark and under an argon atmosphere until mounting (< 2 h). The capillary was mounted at room temperature, aligned, and then heated up to 70 °C at the rate of 5 °C/min to start the reaction using a Linkam HFSX 350 temperature stage. Data were collected at 70 °C continuously over 320 min and binned to a 5 min time resolution.

Data collected from 5 to 50 min were fitted using a Gaussian coil form factor describing individual polymer chains in terms of the zero-angle intensity, I_0, proportional to the volume fraction of polymer chains in solution, the volume of an individual chain and the SLD contrast between polymer and solvent, and the radius of gyration, R_g.[68] Data from 55 to 85 min were fitted using an ellipsoidal form factor with

parameters describing the radii along the polar and equatorial axes.[69] Data collected from 140 to 320 min were fitted using the raspberry form factor as described above.

3.4.1.5 Transmission Electron Microscopy

Transmission electron microscopy (TEM) was conducted using a JEOL 2100Plus instrument operating at 80-200 kV and equipped with a Gatan Orius 11-megapixel digital camera. Samples were deposited directly from reaction mixtures unless otherwise stated onto 300 mesh carbon-coated copper grids. Excess sample was blotted off using filter paper.

3.4.2 Materials

Chloroform-*d* ($CDCl_3$, 99.8 atom % D) and dichloromethane anhydrous (DCM, ≥99.8%) were purchased from Sigma-Aldrich. 1,1'-Azobis(cyclohexane-carbonitrile) (V-40, 98%), carbon disulfide (CS_2, ≥99.9%), and 1-dodecanethiol (≥98%) were purchased from Aldrich. *N*,*N*-Dicyclohexylcarbodiimide (DCC, 99%) and iodine were purchased from Acros Organics. 4,4′-Azobis(4-cyanovaleric acid) (ACVA, 98%), 4-(dimethylamino)pyridine (DMAP, ≥99.0%), and *n*-dodecane (99+%) were purchased from Alfa Aesar. Diethyl ether, ethyl acetate, and toluene were purchased from Merck. Sodium hydroxide was purchased from Fisher Scientific. Dimethyl 2,2'-azobis(2-methylpropionate) (V-601) was purchased from Wako Chemicals.

Benzyl methacrylate (BzMA, 96%), 2-hydroxyethyl methacrylate (HEMA, >99%), and lauryl methacrylate (LMA, 96%) were purchased from Sigma-Aldrich and passed through neutral aluminium oxide to remove inhibitors prior to use.

Methyl 4-cyano-4-(((dodecylthio)carbonothioyl)thio)pentanoate (MCPDTC) had been previously synthesised in the group using the reported protocol and was verified spectroscopically prior to use.[70] ^{1}H NMR (400 MHz, $CDCl_3$, δ): 0.88 (t, 3H, -C$\underline{H}_3$), 1.19-1.35 (br s + m, 16H, -CH_2-(C$\underline{H}_2$)$_8$-CH_3), 1.40 (m, 2H, -S-CH_2-CH_2-C$\underline{H}_2$-), 1.70 (m, 2H, -S-CH_2-C$\underline{H}_2$-), 1.89 (s, 3H, -S(CN)C$\underline{H}_3$-), 2.32-2.62 (m, 2H, -OOC-C$\underline{H}_2$-CH_2-), 2.63 (t, 2H, -OOC-CH_2-C$\underline{H}_2$-), 3.33 (t, 2H, -S-C$\underline{H}_2$-), 3.71 (s, 3H, $\underline{H}_3$C-COO-).

3.4.3 Synthetic Protocols and Characterisation

3.4.3.1 Synthesis of 4-Cyano-4-(((dodecylthio)carbonothioyl)thio)pentanoic Acid

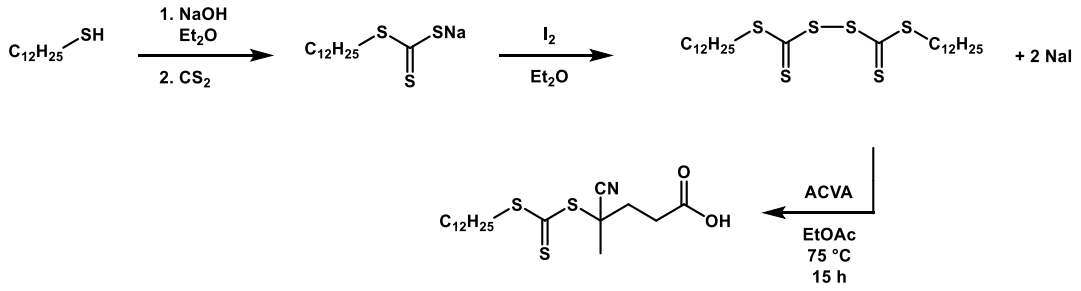

Scheme 3.2 Synthetic scheme for the preparation of CPADTC.

4-Cyano-4-(((dodecylthio)carbonothioyl)thio)pentanoic acid (CPADTC) was prepared by adapting a previously reported protocol.[71] Ground NaOH (6.23 g, 0.16 mol) was suspended in 500 ml diethyl ether using an overhead stirrer. 1-Dodecanethiol (30.0 g, 0.15 mol) was added dropwise and stirred for 10 min. Carbon disulfide (11.9 g, 0.16 mol) was added in one shot and stirring was continued for 1 h. The mixture was cooled down in the freezer and solids were collected, washed with cold diethyl ether and dried, giving sodium dodecyl carbonotrithioate as a yellow solid (25.2 g, 57%). The product was used in the next step without purification.

Sodium dodecyl carbonotrithioate (12.5 g, 42 mmol) was suspended in 250 ml diethyl ether using an overhead stirrer. Solid iodine (5.38 g, 21 mmol) was added portionwise and stirring was continued for 1 h. Salts were removed, and the filtrate was washed with aqueous sodium thiosulfate (0.4 M, 3x), deionised water (1x) and brine (1x). The organic layer was dried over $MgSO_4$ and solvent was removed to give bis-(dodecylsulfanylthiocarbonyl) disulfide an orange solid (9.20 g, 17 mmol, 80%).

Bis-(dodecylsulfanylthiocarbonyl) disulfide (9.20 g, 17 mmol) was dissolved in 250 ml ethyl acetate and 4,4′-azobis(4-cyanopentanoic acid) (6.97 g, 25 mmol) was added. The mixture was refluxed at 75 ^{o}C for 15 h. Solids and volatiles were removed, and 200 ml dichloromethane was added. The solution was washed with deionised water (5x) and brine (1x) and dried over $MgSO_4$. Volatiles were removed and the product was recrystallised from hexane and dried under vacuum yielding CPADTC as a pale yellow solid (6.30 g, 16 mmol, 47%). ^{1}H NMR (400 MHz, $CDCl_3$, δ): 0.88 (t, 3H, -C$\underline{H}_3$), 1.19-1.35 (br s + m, 16H, -CH$_2$-(C$\underline{H}_2$)$_8$-CH$_3$), 1.40 (m, 2H, -S-CH$_2$-CH$_2$-C$\underline{H}_2$-), 1.70 (m, 2H, -S-CH$_2$-C$\underline{H}_2$-), 1.89 (s, 3H, -S(CN)C$\underline{H}_3$-), 2.32-2.62 (m, 2H, HOOC-C$\underline{H}_2$-), 2.69 (t, 2H, HOOC-CH$_2$-C$\underline{H}_2$-), 3.33 (t, 2H, -S-C$\underline{H}_2$-).

3.4.3.2 Polymerisation of Backbone Copolymers

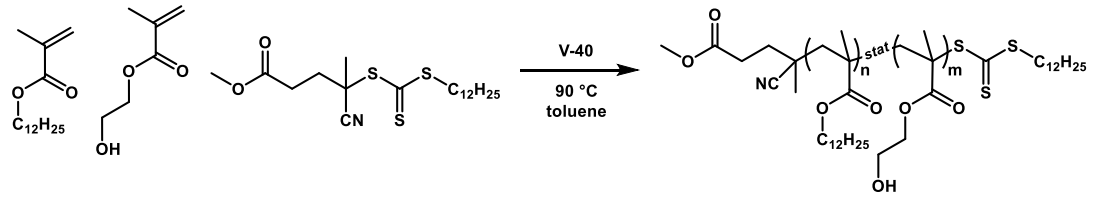

Scheme 3.3 RAFT solution polymerisation of LMA and HEMA used in this work to construct graft copolymer backbones.

A series of poly[(lauryl methacrylate)-*stat*-(2-hydroxyethyl methacrylate)] (p(LMA-*s*-HEMA)) copolymers (**1-5**) were prepared by RAFT polymerisation using the following general procedure. For preparing p(LMA_{816}-*s*-$HEMA_{99}$), MCPDTC (11.90 mg, 0.289 mmol), HEMA (394 mg, 3.03 mmol), LMA (7.00 g, 27.5 mmol) and toluene (6.18 ml, $[M]_0$=2 M) were added to a 25 ml glass vial. V-40 initiator was added as a stock solution (70 µl, 20 mg/ml in toluene, $[CTA]_0/[I]_0$ = 5). The vial was sealed with a rubber septum and N_2 gas was bubbled into solution for 20 min. Polymerisation was initiated by immersing the vial in a pre-heated oil bath set to 90 °C. Polymerisation was stopped at 70-98% conversion after ≥ 14 h by cooling to room temperature. A portion of polymer was precipitated in methanol three times to obtain a ^{1}H NMR spectrum of an isolated product (Figure 3.3). The crude product was used directly for the functionalisation step.

Monomer conversion was determined using ^{1}H NMR spectroscopy in $CDCl_3$ by setting the area δ = 3.5-4.5 ppm as a constant and quantifying the disappearance of the vinyl signals, δ_{LMA} = 5.5 ppm and δ_{HEMA} = 5.6 ppm (Figure 3.2). SEC samples were sampled directly from reaction mixtures (Figure 3.4) and analysed in $CHCl_3$.

Theoretical number-average molar masses ($M_{n,th}$) were calculated as

$$M_{\mathrm{n,th}} = M_{\mathrm{CTA}} + \frac{[\mathrm{LMA}]_0}{[\mathrm{CTA}]_0}\, p_{\mathrm{LMA}} M_{\mathrm{LMA}} + \frac{[\mathrm{HEMA}]_0}{[\mathrm{CTA}]_0}\, p_{\mathrm{HEMA}} M_{\mathrm{HEMA}}\,, \qquad (3.5)$$

where $[LMA]_0$, $[HEMA]_0$, and $[CTA]_0$, are the initial LMA, HEMA, and CTA concentrations, respectively, p is the monomer conversion as determined by ^{1}H NMR spectroscopy and M_{LMA}, M_{HEMA}, and M_{CTA} are the molar masses of LMA, HEMA, and the CTA, respectively.

3.4.3.3 Functionalisation of Backbone Copolymers

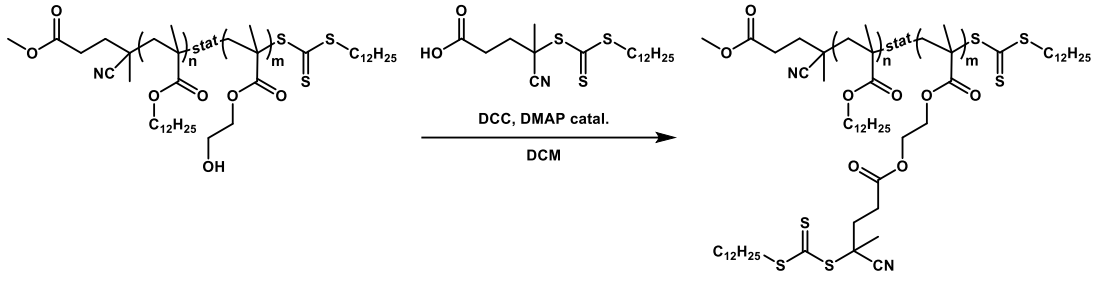

Scheme 3.4 Synthetic route used in this work for backbone functionalisation.

The Steglich esterification was used with the following general procedure to couple CPADTC onto p(LMA-*s*-HEMA) copolymers to yield functionalised backbones. An aliquot of the polymer solution from the copolymerisation step (4.00 g p(LMA_{424}-*s*-$HEMA_{50}$), 2.1 mmol HEMA) was added to a dry 250 ml round-bottom flask and toluene was removed by rotary evaporation at room temperature. CPADTC (1.26 g, 3.1 mmol) and a stir bar were added, and the flask was sealed with a septum. Anhydrous DCM (125 ml) was transferred via cannula into the flask and the mixture was stirred at room temperature until the polymer and CPADTC had fully dissolved. DMAP (25 mg, 0.2 mmol) was added as a solid and the flask was immersed in an ice bath. Solid DCC (0.612 g, 3.0 mmol) was quickly added and the flask was re-sealed. Stirring was continued for 15 minutes, during which time dicyclohexylurea started to precipitate out of solution. The flask was removed from the ice bath and stirring was continued overnight.

The reaction mixture was filtered twice through cotton wool and concentrated using a rotary evaporator at room temperature. The product was precipitated into methanol, centrifuged, isolated, and redissolved in DCM. Precipitations ($n \geq 3$) were carried out until no free CTA remained in the product, as indicated by UV detection at a 309 nm wavelength using SEC. The polymers were characterised with ^{1}H NMR spectroscopy in $CDCl_3$ (Figure 3.6) and SEC in $CHCl_3$ (Figure 3.4).

The extent of functionalisation, or the theoretical maximum number of grafting points per backbone (n_{CTA}), was calculated from the ^{1}H NMR spectra of the isolated polymers as

$$n_{\mathrm{CTA}} = \frac{n_{\mathrm{CPADTC,NMR}}}{n_{\mathrm{CPADTC,ideal}}}\, n_{\mathrm{HEMA}} = \frac{\frac{\int \mathrm{H}_H}{\int \mathrm{H}_{c'+n''+m''}}}{\frac{2n_{\mathrm{HEMA}}}{4n_{\mathrm{HEMA}} + 2n_{\mathrm{LMA}}}}\, n_{\mathrm{HEMA}}, \qquad (3.6)$$

where n_{HEMA} and n_{LMA} are the number of HEMA and LMA units, respectively, as given by conversion. The degree of functionalisation ($n_{CTA\%}$) of the backbone was defined as

$$n_{\mathrm{CTA\%}} = \frac{n_{\mathrm{CTA}}}{\mathrm{DP_{tot}}} \cdot 100 = \frac{n_{\mathrm{CTA}}}{\mathrm{DP_{LMA+HEMA}}} \cdot 100. \quad (3.7)$$

Theoretical number-average molar masses ($M_{n,th}$) of the functionalised backbones, $pLMA_{DP,tot}$-CTA$n_{CTA\%}$, were calculated as

$$M_{\mathrm{n,th}} = M_{\mathrm{pre,th}} + n_{\mathrm{CTA}} M_{\mathrm{CPADTC}} \quad (3.8)$$

where $M_{pre,th}$ is the theoretical molar mass of the precursor copolymer, p(LMA-*s*-HEMA), and M_{CPADTC} is the molar mass of CPADTC.

3.4.3.4 "Grafting from" Dispersion Polymerisation of Benzyl Methacrylate

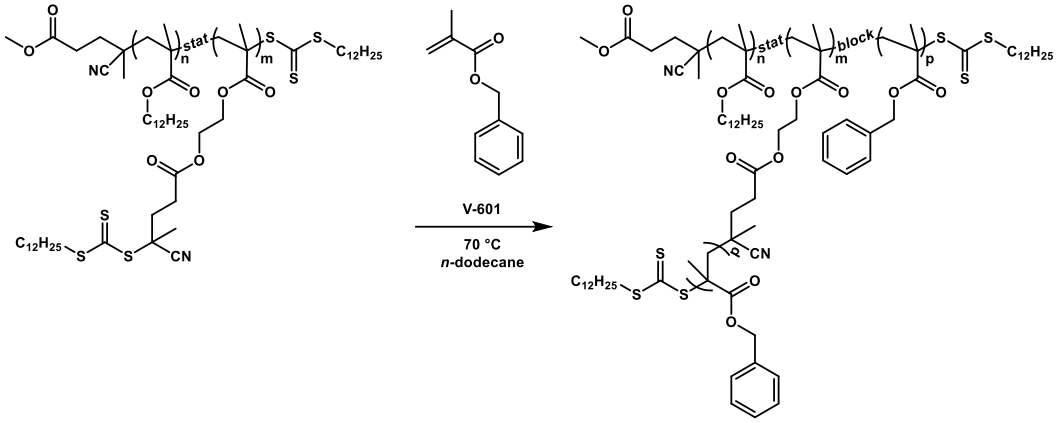

Scheme 3.5 Dispersion polymerisation conditions used in this work for studying PISA of graft copolymers.

All RAFT dispersion polymerisations of BzMA were carried out at either 10 wt% or 20 wt% (w/w) concentration. The following general procedure and $[CTA]_0/[I]_0 = 40$ was used for all reactions. To target a graft length of 5 repeating units at 20 wt% using $pLMA_{915}$-$CTA_{10\%}$, a stock solution of $pLMA_{915}$-$CTA_{10\%}$ (211 mg, 32.2 wt% in *n*-dodecane, 23.0 μmol CPADTC units) was weighed into a 2 ml septum screw-cap vial. BzMA (23.50 mg, 128 μmol), *n*-dodecane (145 μl), and V-601 stock solution (1.0 mg/ml in *n*-dodecane) were added, the mixture was homogenised thoroughly using a roller mixer, and purged with nitrogen through the septum for 10 min. The vial was immersed in a pre-heated oil bath set at 70 °C. Reactions were carried out overnight (≤ 12 h) without stirring and stopped by letting the solutions cool to room temperature. The resulting dispersions were stored at room temperature (20-30 °C). The graft copolymers were characterised using ^{1}H NMR spectroscopy in $CDCl_3$ (Figure **3.7**) and SEC in $CHCl_3$ (Figure 3.8 and Figure 3.14) by sampling directly from the reaction mixture.

Conversion (p) was calculated from the ^{1}H NMR spectrum as

$$p = \frac{\int \mathrm{H}_{q'}}{\int \mathrm{H}_{q} + \int \mathrm{H}_{q'}} = \frac{\int \mathrm{H}_{4.60-5.16\ \mathrm{ppm}}}{\int \mathrm{H}_{4.60-5.30\ \mathrm{ppm}}}. \quad (3.9)$$

Theoretical number-average molar masses ($M_{\mathrm{n,th}}$) of the graft copolymers, pLMA-*g*-pBzMA, were calculated as

$$M_{\mathrm{n,th}} = M_{\mathrm{mc,th}} + n_{\mathrm{CTA}} \mathrm{DP}_p M_{\mathrm{BzMA}} \quad (3.10)$$

where $M_{mc,th}$ is the theoretical molar mass of the functionalised backbone, pLMA$_{DP,tot}$-CTA$n_{CTA\%}$, and M_{BzMA} is the molar mass of BzMA. Reinitiation efficiency of the CPADTC units (I_{eff}) was calculated as

$$I_{eff} = \frac{\int H_{H'}}{\int H_H + \int H_{H'}} = \frac{\int H_{3.07-3.25\ ppm}}{\int H_{3.07-3.42\ ppm}}. \quad (3.11)$$

The apparent number of grafts (n_g) was calculated by accounting for the maximum number of grafting points and the reinitiation efficiency of CPADTC as given by ^{1}H NMR. The apparent number of grafts was calculated as

$$n_g = n_{CTA} \cdot I_{eff}. \quad (3.12)$$

The apparent grafting density was defined as

$$n_{g,\%} = \frac{n_g}{DP_{tot}}, \quad (3.13)$$

where DP_{tot} is the length of the backbone. The resulting apparent DP (DP_{app}) of the pBzMA grafts was calculated by correcting for the apparent number of grafts as

$$DP_{app} = \frac{n_{CTA}\, DP_p}{I_{eff}}, \quad (3.14)$$

where DP_p is the graft length given by conversion assuming 100% reinitiation efficiency, that is

$$DP_p = \frac{[BzMA]_0}{n_{CTA}}\, p_{BzMA}. \quad (3.15)$$

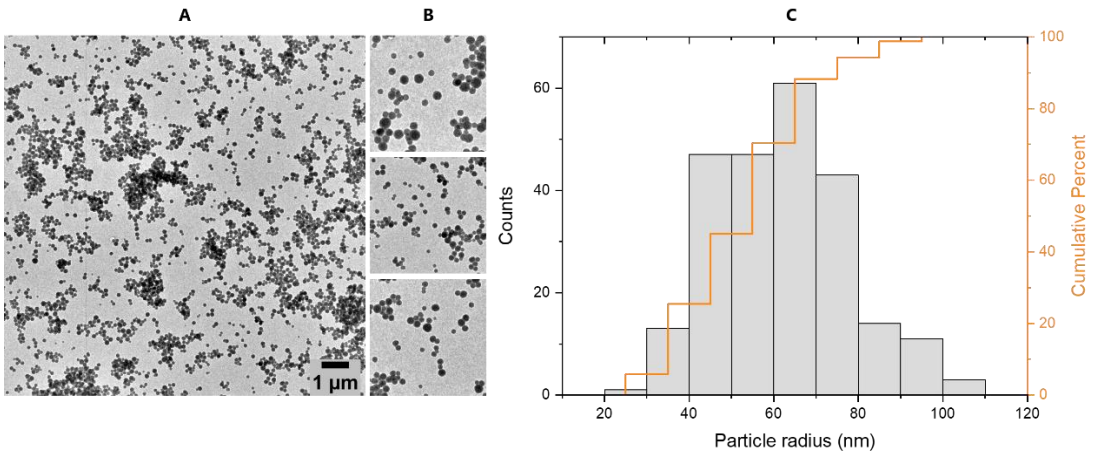

Figure 3.13 Particle size analysis of pLMA$_{915}$-*g*-pBzMA$_{105}$. **A)** Original TEM image. **B)** Three areas selected for analysis. **C)** Particle size distribution as given by 240 manual measurements. Arithmetic mean was 62 nm (SD 15).

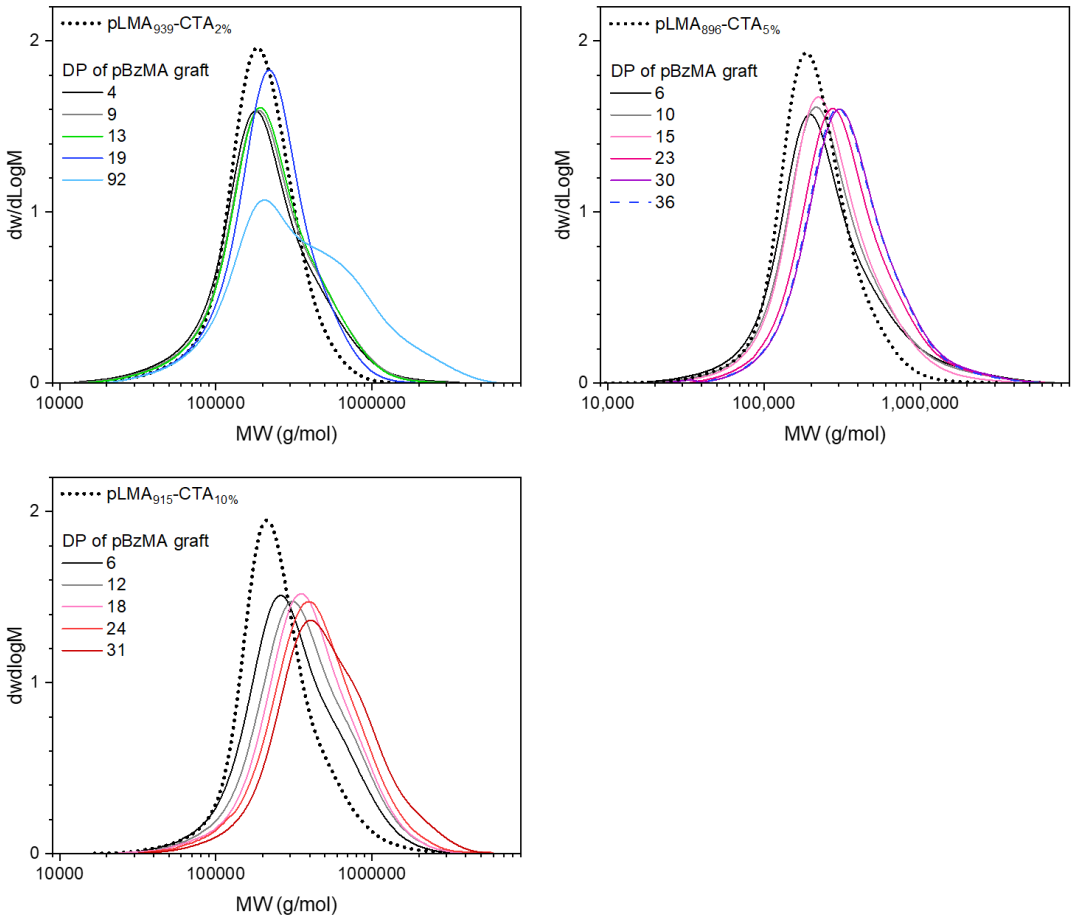

Figure 3.14 SEC profiles of pLMA-*g*-pBzMA graft copolymers prepared targeting various graft lengths and grafting densities**.** Analysis was conducted in $CHCl_3$ with DRI detection and PMMA calibration.

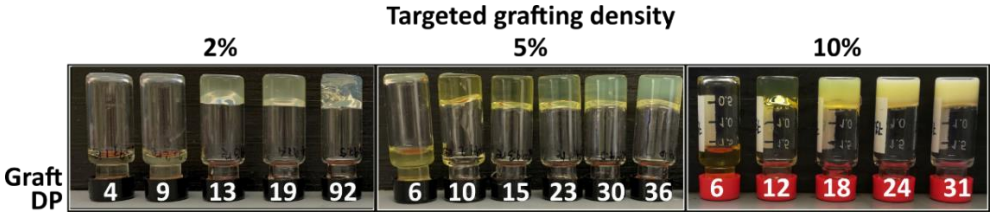

Figure 3.15 Appearances of the reaction mixtures obtained in the grafting density study using functionalised backbones **1b**, **4b**, and **5b**

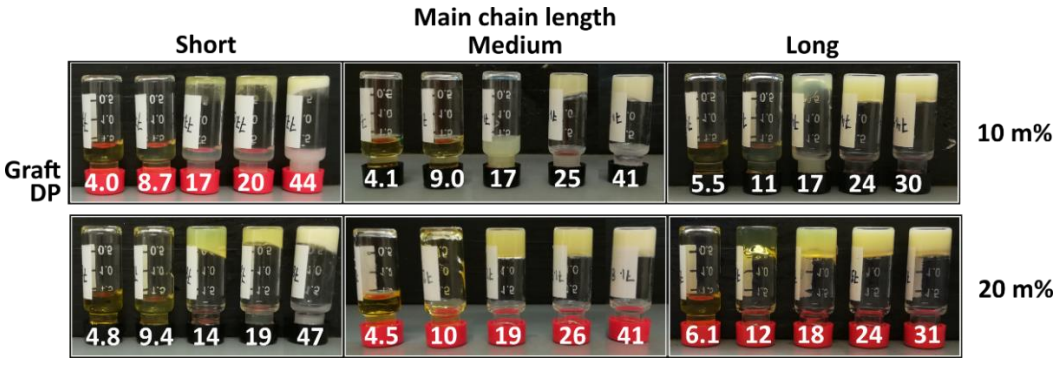

Figure 3.16 Appearance of the reaction mixtures obtained in the concentration study using functionalised backbones **1-3b**.

Table 3.8 Structural and characterisation details of graft copolymers prepared to study the influence of grafting density on their PISA.

Main chain	Entry	Conversion (%)	DP_p [A]	n_{BzMA}/n_{LMA} [B]	$M_{n,th}$ [A] (g/mol)	$M_{n,SEC}$ [C] (g/mol)	$Đ$ [C]
$pLMA_{915}$-$CTA_{10\%}$	**(6.13)**	97	6	0.61	342,000	242,000	1.63
	(6.14)	97	12	1.2	426,000	282,000	1.66
	(6.8)	99	18	1.8	518,000	301,000	1.61
	(6.9)	97	24	2.4	598,000	333,000	1.63
	(6.10)	99	31	3.1	696,000	383,000	1.72
$pLMA_{896}$-$CTA_{5\%}$	**(7.1)**	86	6	0.23	271,000	156,000	1.57
	(7.2)	89	10	0.44	301,000	159,000	1.55
	(7.3)	89	15	0.65	332,000	166,000	1.50
	(7.4)	98	23	0.95	378,000	182,000	1.53
	(7.5)	98	30	1.3	427,000	197,000	1.66
	(7.6)	99	36	1.5	465,000	210,000	1.55
$pLMA_{939}$-$CTA_{2\%}$	**(8.1)**	83	4	0.076	255,000	155,000	1.74
	(8.2)	89	9	0.16	269,000	164,000	1.69
	(8.3)	92	13	0.25	283,000	169,000	1.64
	(8.4)	96	19	0.34	297,000	182,000	1.45
	(8.5)	97	92	1.71	519,000	N/A [D]	N/A [D]

[A] Calculated from conversion.

[B] Molar ratio of BzMA and LMA in the graft copolymer.

[C] SEC analysis in $CHCl_3$ with DRI detection and PMMA calibration.

[D] Could not be analysed due to crosslinking.

3.5 References

1. Bates, F. S.; Fredrickson, G. H., Block Copolymers - Designer Soft Materials. *Physics Today* **1999,** *52* (2), 32-38.
2. Mai, Y.; Eisenberg, A., Self-Assembly of Block Copolymers. *Chemical Society Reviews* **2012,** *41* (18), 5969-5985.
3. Ober, C. K.; Cheng, S. Z. D.; Hammond, P. T.; Muthukumar, M.; Reichmanis, E.; Wooley, K. L.; Lodge, T. P., Research in Macromolecular Science: Challenges and Opportunities for the Next Decade. *Macromolecules* **2009,** *42* (2), 465-471.
4. Moughton, A. O.; Hillmyer, M. A.; Lodge, T. P., Multicompartment Block Polymer Micelles. *Macromolecules* **2011,** *45* (1), 2-19.
5. Li, C.; Li, Q.; Kaneti, Y. V.; Hou, D.; Yamauchi, Y.; Mai, Y., Self-Assembly of Block Copolymers Towards Mesoporous Materials for Energy Storage and Conversion Systems. *Chemical Society Reviews* **2020,** *49* (14), 4681-4736.
6. Stevens, C. A.; Kaur, K.; Klok, H. A., Self-Assembly of Protein-Polymer Conjugates for Drug Delivery. *Advanced Drug Delivery Reviews* **2021,** *174*, 447-460.
7. Xiao, M.; Li, Y.; Allen, M. C.; Deheyn, D. D.; Yue, X.; Zhao, J.; Gianneschi, N. C.; Shawkey, M. D.; Dhinojwala, A., Bio-Inspired Structural Colors Produced via Self-Assembly of Synthetic Melanin Nanoparticles. *ACS Nano* **2015,** *9* (5), 5454-5460.
8. Derry, M. J.; Smith, T.; O'Hora, P. S.; Armes, S. P., Block Copolymer Nanoparticles Prepared via Polymerization-Induced Self-Assembly Provide Excellent Boundary Lubrication Performance for Next-Generation Ultralow-Viscosity Automotive Engine Oils. *ACS Applied Materials & Interfaces* **2019,** *11* (36), 33364-33369.
9. Nagarajan, R., *One Hundred Years of Micelles: Evolution of the Theory of Micellization*. CRC Press: USA, 2014.
10. Cameron, N. S.; Corbierre, M. K.; Eisenberg, A., 1998 E.W.R. Steacie Award Lecture Asymmetric amphiphilic block copolymers in solution: a morphological wonderland. *Canadian Journal of Chemistry* **1999,** *77* (8), 1311-1326.
11. Lynd, N. A.; Hillmyer, M. A., Influence of Polydispersity on the Self-Assembly of Diblock Copolymers. *Macromolecules* **2005,** *38* (21), 8803-8810.
12. Widin, J. M.; Schmitt, A. K.; Schmitt, A. L.; Im, K.; Mahanthappa, M. K., Unexpected Consequences of Block Polydispersity on the Self-Assembly of ABA Triblock Copolymers. *Journal of the American Chemical Society* **2012,** *134* (8), 3834-44.
13. Zhang, C.; Bates, M. W.; Geng, Z.; Levi, A. E.; Vigil, D.; Barbon, S. M.; Loman, T.; Delaney, K. T.; Fredrickson, G. H.; Bates, C. M.; Whittaker, A. K.; Hawker, C. J., Rapid Generation of Block Copolymer Libraries Using Automated Chromatographic Separation. *Journal of the American Chemical Society* **2020,** *142* (21), 9843-9849.
14. Ma, H.; Kim, K. T., Self-Assembly of Bottlebrush Block Copolymers into Triply Periodic Nanostructures in a Dilute Solution. *Macromolecules* **2020,** *53* (2), 711-718.
15. Shi, Y.; Zhu, W.; Yao, D.; Long, M.; Peng, B.; Zhang, K.; Chen, Y., Disk-Like Micelles with a Highly Ordered Pattern from Molecular Bottlebrushes. *ACS Macro Letters* **2014,** *3* (1), 70-73.

16. Yang, C.; Gao, L.; Lin, J.; Wang, L.; Cai, C.; Wei, Y.; Li, Z., Toroid Formation through a Supramolecular "Cyclization Reaction" of Rodlike Micelles. *Angewandte Chemie International Edition* **2017,** *56* (20), 5546-5550.
17. Le Fer, G.; Le Cœur, C.; Guigner, J.-M.; Amiel, C.; Volet, G., Biocompatible Soft Nanoparticles with Multiple Morphologies Obtained from Nanoprecipitation of Amphiphilic Graft Copolymers in a Backbone-Selective Solvent. *Langmuir* **2017,** *33* (11), 2849-2860.
18. Rideau, E.; Wurm, F. R.; Landfester, K., Giant Polymersomes from Non-Assisted Film Hydration of Phosphate-Based Block Copolymers. *Polymer Chemistry* **2018,** *9* (44), 5385-5394.
19. Wang, L.; Sanchez, S., Self-assembly via Microfluidics. *Lab on a Chip* **2015,** *15* (23), 4383-4386.
20. Canning, S. L.; Smith, G. N.; Armes, S. P., A Critical Appraisal of RAFT-Mediated Polymerization-Induced Self-Assembly. *Macromolecules* **2016,** *49* (6), 1985-2001.
21. Penfold, N. J. W.; Yeow, J.; Boyer, C.; Armes, S. P., Emerging Trends in Polymerization-Induced Self-Assembly. *ACS Macro Letters* **2019,** *8* (8), 1029-1054.
22. Blanazs, A.; Verber, R.; Mykhaylyk, O. O.; Ryan, A. J.; Heath, J. Z.; Douglas, C. W.; Armes, S. P., Sterilizable Gels from Thermoresponsive Block Copolymer Worms. *Journal of the Amerocan Chemical Society* **2012,** *134* (23), 9741-9748.
23. Chan, D. H. H.; Kynaston, E. L.; Lindsay, C.; Taylor, P.; Armes, S. P., Block Copolymer Nanoparticles are Effective Dispersants for Micrometer-Sized Organic Crystalline Particles. *ACS Applied Materials & Interfaces* **2021,** *13* (25), 30235-30243.
24. Binch, A. L. A.; Ratcliffe, L. P. D.; Milani, A. H.; Saunders, B. R.; Armes, S. P.; Hoyland, J. A., Site-Directed Differentiation of Human Adipose-Derived Mesenchymal Stem Cells to Nucleus Pulposus Cells Using an Injectable Hydroxyl-Functional Diblock Copolymer Worm Gel. *Biomacromolecules* **2021,** *22* (2), 837-845.
25. Zaquen, N.; Yeow, J.; Junkers, T.; Boyer, C.; Zetterlund, P. B., Visible Light-Mediated Polymerization-Induced Self-Assembly Using Continuous Flow Reactors. *Macromolecules* **2018,** *51* (14), 5165-5172.
26. Cockram, A. A.; Bradley, R. D.; Lynch, S. A.; Fleming, P. C. D.; Williams, N. S. J.; Murray, M. W.; Emmett, S. N.; Armes, S. P., Optimization of the High-Throughput Synthesis of Multiblock Copolymer Nanoparticles in Aqueous Media via Polymerization-Induced Self-Assembly. *Reaction Chemistry & Engineering* **2018,** *3* (5), 645-657.
27. Piogé, S.; Tran, T. N.; McKenzie, T. G.; Pascual, S.; Ashokkumar, M.; Fontaine, L.; Qiao, G., Sono-RAFT Polymerization-Induced Self-Assembly in Aqueous Dispersion: Synthesis of LCST-type Thermosensitive Nanogels. *Macromolecules* **2018,** *51* (21), 8862-8869.
28. Zhang, B.; Wang, X.; Zhu, A.; Ma, K.; Lv, Y.; Wang, X.; An, Z., Enzyme-Initiated Reversible Addition-Fragmentation Chain Transfer Polymerization. *Macromolecules* **2015,** *48* (21), 7792-7802.
29. Qiao, X. G.; Lambert, O.; Taveau, J. C.; Dugas, P. Y.; Charleux, B.; Lansalot, M.; Bourgeat-Lami, E., Nitroxide-Mediated Polymerization-Induced Self-Assembly of Block Copolymers at the Surface of Silica Particles: Toward New Hybrid Morphologies. *Macromolecules* **2017,** *50* (10), 3796-3806.

30. Tan, J.; Sun, H.; Yu, M.; Sumerlin, B. S.; Zhang, L., Photo-PISA: Shedding Light on Polymerization-Induced Self-Assembly. *ACS Macro Letters* **2015,** *4* (11), 1249-1253.
31. Wang, X.; Xu, J.; Zhang, Y.; Zhang, W., Polymerization of Styrene in Alcohol/Water Mediated by a Macro-RAFT Agent of Poly(N-Isopropylacrylamide) Trithiocarbonate: From Homogeneous to Heterogeneous RAFT Polymerization. *Journal of Polymer Science Part A: Polymer Chemistry* **2012,** *50* (12), 2452-2462.
32. Chambon, P.; Blanazs, A.; Battaglia, G.; Armes, S. P., Facile Synthesis of Methacrylic ABC Triblock Copolymer Vesicles by RAFT Aqueous Dispersion Polymerization. *Macromolecules* **2012,** *45* (12), 5081-5090.
33. Gao, C.; Li, S.; Li, Q.; Shi, P.; Shah, S. A.; Zhang, W., Dispersion RAFT Polymerization: Comparison Between the Monofunctional and Bifunctional Macromolecular RAFT Agents. *Polymer Chemistry* **2014,** *5* (24), 6957-6966.
34. Mable, C. J.; Warren, N. J.; Thompson, K. L.; Mykhaylyk, O. O.; Armes, S. P., Framboidal ABC Triblock Copolymer Vesicles: a New Class of Efficient Pickering Emulsifier. *Chemical Science* **2015,** *6* (11), 6179-6188.
35. Biais, P.; Beaunier, P.; Stoffelbach, F.; Rieger, J., Loop-Stabilized BAB Triblock Copolymer Morphologies by PISA in Water. *Polymer Chemistry* **2018,** *9* (35), 4483-4491.
36. Wang, X.; Figg, C. A.; Lv, X.; Yang, Y.; Sumerlin, B. S.; An, Z., Star Architecture Promoting Morphological Transitions during Polymerization-Induced Self-Assembly. *ACS Macro Letters* **2017,** *6* (4), 337-342.
37. Mellot, G.; Beaunier, P.; Guigner, J. M.; Bouteiller, L.; Rieger, J.; Stoffelbach, F., Beyond Simple AB Diblock Copolymers: Application of Bifunctional and Trifunctional RAFT Agents to PISA in Water. *Macromolecular Rapid Communications* **2019,** *40* (2), 1800315-1800322.
38. Zeng, R.; Chen, Y.; Zhang, L.; Tan, J., R-RAFT or Z-RAFT? Well-Defined Star Block Copolymer Nano-Objects Prepared by RAFT-Mediated Polymerization-Induced Self-Assembly. *Macromolecules* **2020,** *53* (5), 1557-1566.
39. Zhang, Y.; Cao, M.; Han, G.; Guo, T.; Ying, T.; Zhang, W., Topology Affecting Block Copolymer Nanoassemblies: Linear Block Copolymers versus Star Block Copolymers under PISA Conditions. *Macromolecules* **2018,** *51* (14), 5440-5449.
40. Biais, P.; Colombani, O.; Bouteiller, L.; Stoffelbach, F.; Rieger, J., Unravelling the Formation of BAB Block Copolymer Assemblies During PISA in Water. *Polymer Chemistry* **2020,** *11* (28), 4568-4578.
41. Zhao, W.; Gody, G.; Dong, S.; Zetterlund, P. B.; Perrier, S., Optimization of the RAFT Polymerization Conditions for the In Situ Formation of Nano-Objects via Dispersion Polymerization in Alcoholic Medium. *Polymer Chemistry* **2014,** *5* (24), 6990-7003.
42. Richez, A. P.; Farrand, L.; Goulding, M.; Wilson, J. H.; Lawson, S.; Biggs, S.; Cayre, O. J., Poly(dimethylsiloxane)-Stabilized Polymer Particles from Radical Dispersion Polymerization in Nonpolar Solvent: Influence of Stabilizer Properties and Monomer Type. *Langmuir* **2014,** *30* (5), 1220-1228.
43. Fielding, L. A.; Lane, J. A.; Derry, M. J.; Mykhaylyk, O. O.; Armes, S. P., Thermo-Responsive Diblock Copolymer Worm Gels in Non-Polar Solvents. *Journal of the American Chemical Society* **2014,** *136* (15), 5790-5798.
44. Docherty, P. J.; Derry, M. J.; Armes, S. P., RAFT Dispersion Polymerization of Glycidyl Methacrylate for the Synthesis of Epoxy-Functional Block Copolymer Nanoparticles in Mineral Oil. *Polymer Chemistry* **2019,** *10* (5), 603-611.

45. Torres-Rocha, O. L.; Wu, X.; Zhu, C.; Crudden, C. M.; Cunningham, M. F., Polymerization-Induced Self-Assembly (PISA) of 1,5-Cyclooctadiene Using Ring Opening Metathesis Polymerization. *Macromolecular Rapid Communications* **2018,** *39* (2), 1800326-1800333.
46. Georgiou, P. G.; Kontopoulou, I.; Congdon, T. R.; Gibson, M. I., Ice Recrystallisation Inhibiting Polymer Nano-Objects via Saline-Tolerant Polymerisation-Induced Self-Assembly. *Materials Horizons* **2020,** *7* (7), 1883-1887.
47. Fielding, L. A.; Derry, M. J.; Ladmiral, V.; Rosselgong, J.; Rodrigues, A. M.; Ratcliffe, L. P. D.; Sugihara, S.; Armes, S. P., RAFT Dispersion Polymerization in Non-Polar Solvents: Facile Production of Block Copolymer Spheres, Worms and Vesicles in n-Alkanes. *Chemical Science* **2013,** *4* (5), 2081-2087.
48. Derry, M. J.; Fielding, L. A.; Armes, S. P., Industrially-Relevant Polymerization-Induced Self-Assembly Formulations in Non-Polar Solvents: RAFT Dispersion Polymerization of Benzyl Methacrylate. *Polymer Chemistry* **2015,** *6* (16), 3054-3062.
49. Stenzel, M. H.; Barner-Kowollik, C., The Living Dead - Common Misconceptions About Reversible Deactivation Radical Polymerization. *Materials Horizons* **2016,** *3* (6), 471-477.
50. Neises, B.; Steglich, W., Simple Method for the Esterification of Carboxylic Acids. *Angewandte Chemie International Edition* **1978,** *17* (7), 522-524.
51. Barner, L.; Davis, T. P.; Stenzel, M. H.; Barner-Kowollik, C., Complex Macromolecular Architectures by Reversible Addition Fragmentation Chain Transfer Chemistry: Theory and Practice. *Macromolecular Rapid Communications* **2007,** *28* (5), 539-559.
52. Zheng, Z.; Ling, J.; Müller, A. H. E., Revival of the R-Group Approach: A "CTA-shuttled" Grafting from Approach for Well-Defined Cylindrical Polymer Brushes via RAFT Polymerization. *Macromolecular Rapid Communications* **2014,** *35* (2), 234-241.
53. Kerr, A.; Hartlieb, M.; Sanchis, J.; Smith, T.; Perrier, S., Complex Multiblock Bottle-Brush Architectures by RAFT Polymerization. *Chemical Communications* **2017,** *53* (87), 11901-11904.
54. Battaglia, G.; Ryan, A. J., Bilayers and Interdigitation in Block Copolymer Vesicles. *Journal of the American Chemical Society* **2005,** *127* (24), 8757-8764.
55. Czajka, A.; Armes, S. P., In Situ SAXS Studies of a Prototypical RAFT Aqueous Dispersion Polymerization Formulation: Monitoring the Evolution in Copolymer Morphology During Polymerization-Induced Self-Assembly. *Chemical Science* **2020,** *11* (42), 11443-11454.
56. Derry, M. J.; Fielding, L. A.; Warren, N. J.; Mable, C. J.; Smith, A. J.; Mykhaylyk, O. O.; Armes, S. P., In Situ Small-Angle X-ray Scattering Studies of Sterically-Stabilized Diblock Copolymer Nanoparticles Formed During Polymerization-Induced Self-Assembly in Non-Polar Media. *Chemical Science* **2016,** *7* (8), 5078-5090.
57. Wang, L.; Jiang, T.; Lin, J., Self-Assembly of Graft Copolymers in Backbone-Selective Solvents: a Route Toward Stable Hierarchical Vesicles. *RSC Advances* **2013,** *3* (42), 19481-19491.
58. David, G.; Pérez, J., Combined Sampler Robot and High-Performance Liquid Chromatography: A Fully Automated System for Biological Small-Angle X-Ray Scattering Experiments at the Synchrotron SOLEIL SWING Beamline. *Journal of Applied Crystallography* **2009,** *42* (5), 892-900.

59. Zhang, F.; Ilavsky, J.; Long, G. G.; Quintana, J. P. G.; Allen, A. J.; Jemian, P. R., Glassy Carbon as an Absolute Intensity Calibration Standard for Small-Angle Scattering. *Metallurgical and Materials Transactions A* **2010,** *41* (5), 1151-1158.
60. SasView. https://www.sasview.org/ (accessed 16.12.2021).
61. Clifton, L. A.; Hall, S. C. L.; Mahmoudi, N.; Knowles, T. J.; Heinrich, F.; Lakey, J. H., *Structural Investigations of Protein–Lipid Complexes Using Neutron Scattering*. Springer: New York, 2019.
62. Menon, S. V. G.; Manohar, C.; Rao, K. S., A New Interpretation of the Sticky Hard Sphere Model. *The Journal of Chemical Physics* **1991,** *95* (12), 9186-9190.
63. Guinier, A.; Fournet, G., *Small-Angle Scattering of X-Rays*. Wiley: USA, 1955.
64. Pedersen, J. S., Analysis of Small-Angle Scattering Data from Colloids and Polymer Solutions: Modeling and Least-Squares Fitting. *Advances in Colloid and Interface Science* **1997,** *70*, 171-210.
65. Pedersen, J. S.; Schurtenberger, P., Scattering Functions of Semiflexible Polymers with and without Excluded Volume Effects. *Macromolecules* **1996,** *29* (23), 7602-7612.
66. Chen, W.-R.; Butler, P. D.; Magid, L. J., Incorporating Intermicellar Interactions in the Fitting of SANS Data from Cationic Wormlike Micelles. *Langmuir* **2006,** *22* (15), 6539-6548.
67. Larson-Smith, K.; Jackson, A.; Pozzo, D. C., Small Angle Scattering Model for Pickering Emulsions and Raspberry Particles. *Journal of Colloid and Interface Science* **2010,** *343* (1), 36-41.
68. Debye, P., Molecular-Weight Determination by Light Scattering. *The Journal of Physical and Colloid Chemistry* **1947,** *51* (1), 18-32.
69. Feigin, L. A.; Svergun, D. I., *Structure Analysis by Small-Angle X-Ray and Neutron Scattering*. Springer: USA, 1987.
70. Zhang, Q.; Hong, J.-D.; Hoogenboom, R., A Triple Thermoresponsive Schizophrenic Diblock Copolymer. *Polymer Chemistry* **2013,** *4* (16), 4322-4325.
71. Moad, G.; Chong, Y. K.; Postma, A.; Rizzardo, E.; Thang, S. H., Advances in RAFT Polymerization: the Synthesis of Polymers with Defined End-Groups. *Polymer* **2005,** *46* (19), 8458-8468.

Chapter 4

Graft Copolymers as Friction Modifier Additives in Non-Polar Media

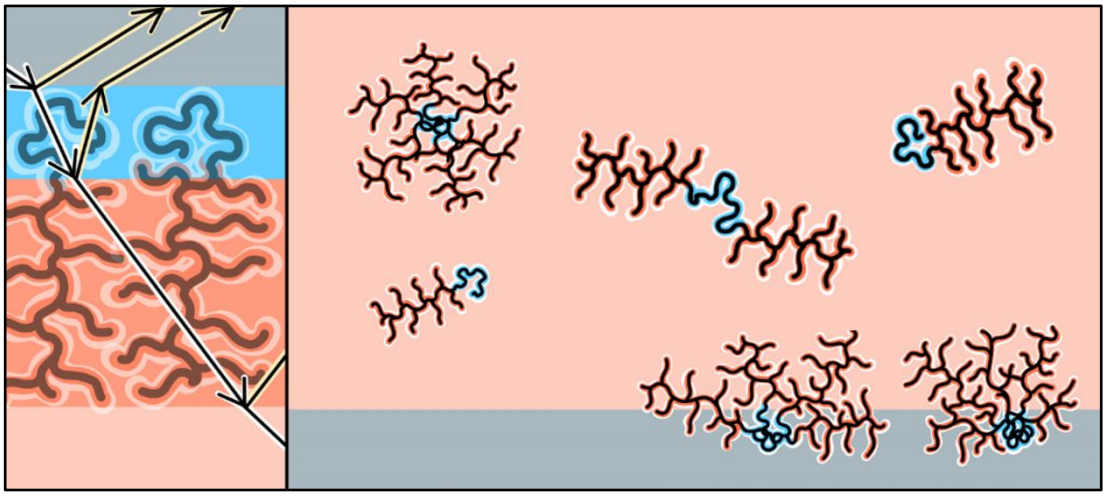

Industry seeks to develop next-generation friction modifier additives to increase fuel efficiency. Surface-tethered polymers have been shown to be an efficient lubrication strategy for boundary and mixed lubrication regimes by providing a viscoelastic fluid layer between interacting surfaces. The use of bottlebrush-like graft copolymers has recently sparked interest in this field due to their exceptional lubricant properties arising from their dense and extended structure. Graft copolymers capable of binding to surfaces via non-covalent interactions could find use in commercial oil-based lubrication as dynamic friction modifiers that may be easily replenished after degradation. Previous research in our group has assessed the performance of a range of surface-active densely-grafted copolymers as friction modifier additives and showed them to hold promise for this application. In this work, a library of sparsely grafted copolymers with analogous architectures was prepared to gain a better understanding of their structure-property relationships in lubrication applications. Detailed surface adsorption experiments showed the studied polymers to have distinct surface interaction and boundary film formation properties arising from their different architectures. Despite these significant differences, macrotribological tests showed only subtle dissimilarities between the new polymers and those studied previously.

4.1 Introduction

Amongst various applications that have been envisioned and realised for graft copolymers is their use as lubricants. Surface-tethered bottlebrush-like polymers have shown remarkable lubrication properties by forming dense, solvated films with suppressed chain interpenetration, which are capable of retaining a solvent layer in a contact. Inspiration has been taken from nature's own bottlebrush polymer lubricants, such as those protecting joints,[1] to create synthetic analogues with equal performance.[2-5] Thus far, such research has focused on aqueous systems but the field shows interest towards oil-soluble graft copolymer lubricants for industry and technology in which moving parts and machinery are lubricated with non-polar fluids.

Some general guidelines have been established to direct the design of efficient polymer lubricants.[1, 6, 7] Studies have demonstrated the impact of polymer architecture on lubricant performance by employing surface-active blocks, grafted segments, and various copolymer compositions – sometimes conjoined in a single design.[3, 4, 8, 9] Advances made in polymer synthesis over the past 20 years have made the exploration of complex architecture materials increasingly attractive due to the industrial applicability of controlled polymerisation techniques.[10] Various polymers with complex architectures have already made their way into commercial products,[11] and more will be undoubtedly seen in the future.

4.1.1 Friction and the Field of Tribology

Friction is a phenomenon that occurs between two surfaces sliding against each other and can be described using

$$F = \mu N, \tag{4.1}$$

where F is the frictional force, μ is the coefficient of friction, and N is the normal force. The friction force resists the relative motion of the two surfaces and arises from molecular adhesion, surface roughness and surface deformation. Mechanical kinetic energy of the interacting surfaces may be transferred to their surroundings through various processes. At an atomic scale, the processes that mediate the dissipation of frictional energy include molecular vibrations of the surface atoms, electronic excitations and chemical reactions, manifested at the macroscopic scale as heat and sometimes wear.[12]

It has been estimated that one fifth of all the energy produced worldwide is used annually to overcome friction.[13] Consequently, the study of friction plays an important part in pursuing reduced energy costs and emissions. In particular, the development and implementation of new friction-reducing technologies in road transport has been proposed to hold great promise for the reduction of energy consumption worldwide.[14, 15] Generally, friction between solid surfaces is reduced by introducing a layer of viscous liquid into the contact, but solid and gaseous lubrication are also known.[16] When liquid lubricants are used, friction is primarily controlled by modifying the rheological properties of the fluid but can be further reduced by employing small amounts of friction modifier additives.[6] Rheological modifications typically involve reducing fluid viscosity to minimise friction arising from hydrodynamic shear, and generally result in a reduced film thickness in the contact. Such modifications come with a trade-off as thinner oils may be more easily displaced from the contact, therefore providing no lubrication or wear protection. Friction modifier additives are molecules that directly bind to the surface to form a nanoscale film and hence reduce the friction without affecting the bulk rheological properties of the lubricant. They are most beneficial when the distance between the surfaces is small and they complement the use of low-viscosity fluids well. The four general classes of friction modifier additives used today are surfactant-like organic friction modifiers such as glyceryl monooleate, organo-molybdenum compounds, functionalised polymers, and dispersed nanoparticles.[6] Chemical compounds used as friction modifiers for oils generally carry a polar functionality for surface adsorption and a long hydrocarbon chain, and exhibit good chemical stability and compatibility with the base oil formulation.[15]

Interactions between surfaces in relative motion, and related phenomena such as friction, adhesion, and wear, make up the field of tribology and may be studied across a range of scales with various instruments. Macrotribological studies involve forces in the range of newtons and are generally carried out using tribometers with pin-on-disk or ball-on-disk contact geometries. The former consists of a stationary pin and a rotating disk that holds the sample, and a fixed load that can be applied on the pin-sample contact. Modern instruments include mini traction machines for which various rolling and sliding conditions may be selected, thus simulating more complex applications such as rolling bearings and gears. Macroscopic measurements are prone to wear, which may result in the formation of debris and a subsequent increase in

measured friction.[13] Until the 1980s, most of the research on friction modifier additives only involved friction measurements under various operating conditions. Some of the key problems standing in the way of fully understanding lubricant performance were – and to an extent still are – their thin film nature and weakly bound character, which made their direct observation challenging. The emergence of new experimental techniques eventually allowed thin films to be studied directly on surfaces and in contacts.[6] New techniques such as atomic force microscopy and the surface force apparatus allowed nanotribological studies to be performed at the millinewton or nanonewton range with single asperity contact areas, thus excluding roughness effects.[13] While the use of complementary tribological techniques may be generally considered advantageous, it has been reported that different types of friction measurements may involve different energy dissipation pathways, making results difficult to interpret.[13] Other techniques such as the quartz crystal microbalance and neutron reflectometry have provided detailed information about the surface adsorption behaviour and molecular orientation of lubricants, as well as the nanoscopic structure of the resulting film. Techniques such as neutron and X-ray reflectometry have been combined with rheometers and tribometers to study lubricant performance and film formation *in situ*: this constitutes a powerful approach to solve problems associated with the correlation of data gathered across separate experiments with different techniques.[17-19]

4.1.2 Lubricating Polymer Layers

The lubricating effects of polymers in oil were noted long before they were used as friction modifiers. Linear polymers used as viscosity modifiers were known to have a friction-reducing effect in environments with considerable asperity contacts between interacting surfaces. However, due to the lack of appropriate techniques this observation could not be studied in depth until the 1990s.[20, 21] It is now known that lubrication is provided by a polymer film adsorbed onto the surface which under good solvent conditions can retain a fluid interface in contacts from which solvent alone would be otherwise squeezed out.[8] This lubricating effect has been ascribed to an increased viscosity in the contact resulting in hydrodynamic lift but a viscoelastic contribution has also been hypothesised.[6] Systematic studies have aimed to understand the effects of polymer molecular weight, functionality, and the distribution thereof on lubricating properties.[8, 22]

In addition to the use of free polymer additives in the bulk phase, lubrication with surface-tethered linear polymers has been studied extensively.[13] The earliest examples involved polystyrene tethered to mica via zwitterionic chain-ends.[23] Surface modification may also be achieved covalently by using controlled radical polymerisation techniques to grow chains from initiating sites on the surface or by attaching polymer chains onto a functionalised surface using robust coupling chemistry. The non-covalent attachment and coupling strategies may be hindered by steric congestion near the surface, which limits the achievable grafting density. Sparse grafting may enable chain interpenetration and entanglement, leading to frictional dissipation.[13] The *grafting from* approach allows for dense grafting at the surface, which drives the extension of the chains to form a film with an extremely high viscosity localised to the surface and a high load-bearing capacity. Glass transition and melting temperatures of the polymer have been suggested to influence film hardness and thus viscoelastic energy dissipation pathways.[7] While covalent surface modification has been established as an effective way to reduce friction, this approach is not feasible for all applications. Dynamic alternatives are needed whereby the lubricating film is generated *in situ* so that it may be replenished after polymer degradation to maintain good performance over long time periods.

Bottlebrush-like, densely-grafted copolymers with surface-active segments have been recently explored as efficient non-covalently tethered boundary lubricants.[2, 3] Inspiration has been drawn from nature to design synthetic analogues of biomacromolecules such as lubricin and aggrecan – large bottlebrush-like glycoproteins that provide the lubrication of articular cartilages.[1, 4, 24] The densely grafted, rigid structure of bottlebrush polymers provides a thick, viscoelastic, and highly solvated boundary layer with limited chain interpenetration, resulting in extremely low coefficients of friction. Efforts have been made to understand the performance of such lubricants in aqueous environments,[2, 3, 24, 25] but bottlebrush polymer lubrication in non-polar solvents remains unexplored in the literature. Despite some of the focal points of aqueous lubrication such as charge and salt effects[5, 26, 27] not being applicable to non-polar formulations, parameters such as molecular orientation, graft length, grafting density, anchoring, and solvation[2, 5, 28, 29] are universal, so what is known about aqueous lubrication can be used to direct the design of oil-soluble lubricants. The attention in this area of research may be soon expected to turn towards oil additives given the strong incentives for better fuel economy.

4.1.3 Project Outline

Previous research conducted in our group showed bottlebrush-like graft copolymers to hold promise as next-generation friction modifier oil additives.[30] Macrotribological experiments involving 1 wt.% of the poly(lauryl acrylate)-based polymers in oil showed lower friction coefficients than plain base oil or commercial additives in boundary and mixed lubrication regimes. The addition of a polar poly(4-acryloylmorpholine) linear segment into the graft copolymer structure was found to increase surface adsorption onto metal surfaces and hence promoted better lubrication. In this work we set out to assess the effect of grafting density (n_g) on lubricant performance by testing a library of sparsely-grafted copolymers with analogous architectures to the fully-grafted polymers (n_g = 100%) reported previously, but a reduced number of grafts ($n_g \approx 35\%$). The interplay between architectural details, lubricant performance, and surface adsorption properties of the polymers was investigated via macrotribological testing, quartz crystal microbalance experiments, atomic force microscopy, and neutron reflectometry.

4.2 Results and Discussion

4.2.1 Graft Copolymer Synthesis and Characterisation

Four sparsely grafted ($n_g \approx 35\%$) comb-like copolymers were prepared using RAFT polymerisation and the R group *grafting from* approach (Scheme 4.1). The four polymer architectures consisting of grafted, non-polar segments of poly(lauryl acrylate) (pLA) grafts separated by *n*-butyl acrylate units and linear, polar poly(4-acryloylmorpholine) (pNAM) anchor segments were selected to complement previously studied polymers.[30] The targeted degrees of polymerisation (DPs) of the grafted segments, linear pNAM segments, and pLA grafts were selected to match those reported previously, whilst targeting a reduced grafting density of 33%.

The backbone precursors for the grafted segments were constructed by statistical RAFT copolymerisation of *n*-butyl acrylate (BuA) and *N*-hydroxyethyl acrylamide (HEAm) and subsequent esterification to functionalise the hydroxy groups of HEAm with 2-(((dodecylthio)carbonothioyl)thio)-2-methylpropanoic acid (MPADTC) (Scheme 4.2A). The BuA/HEAm molar ratio was adjusted to target a grafting density of 33% such that each functionalised HEAm repeat unit in the chain would serve as an initiating site for graft polymerisation. Kinetic data collected throughout statistical copolymerisation of these two monomers showed a small difference in their polymerisation rates (Figure 4.1). HEAm exhibited a slightly higher rate of propagation despite being the less activated monomer of the two. This resulted in a small drift in the comonomer distribution across the polymer, with HEAm being more abundant at the α-end. The polymerisations were stopped before all HEAm was consumed at roughly 80-90% conversion to ensure the incorporation of initiating sites across the whole chain length (Table 4.1).

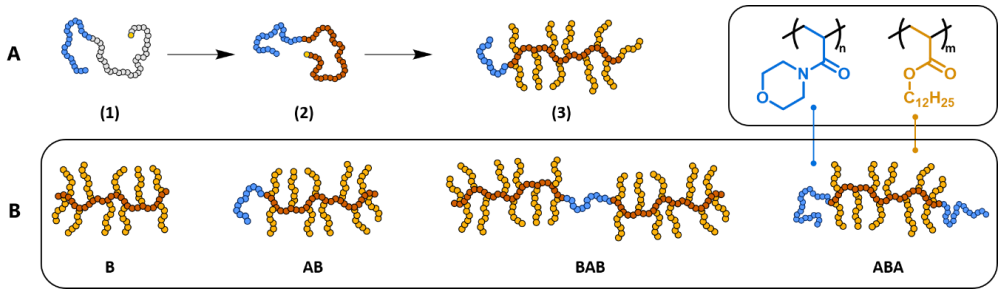

Scheme 4.1 A) The synthetic approach used in this study involved the preparation of a (block) copolymer backbone precursor (**1**), functionalisation with a RAFT agent to incorporate initiating sites along the chain (**2**), and finally graft polymerisation to yield a graft copolymer. **B)** The four polymer architectures explored in this study included the simple graft copolymer B and the three AB, BAB and ABA block copolymers with polar linear segments to promote adsorption to polar surfaces.

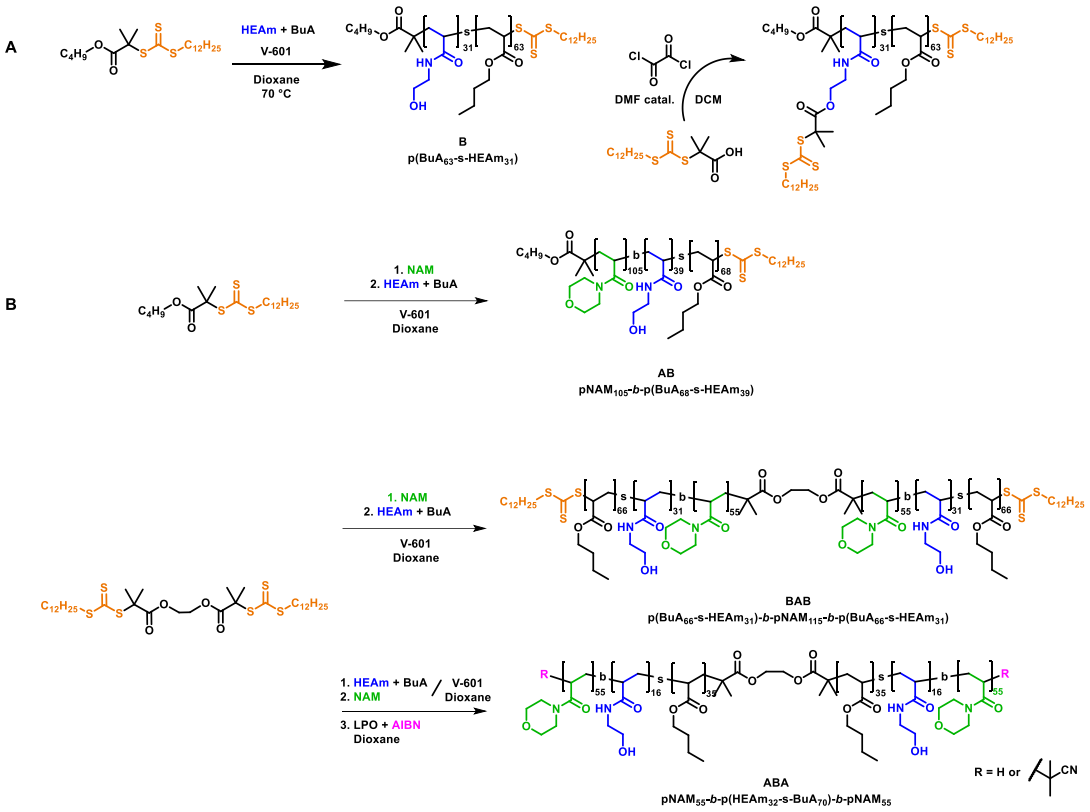

Scheme 4.2 A) RAFT copolymerisation of *n*-butyl acrylate and *N*-hydroxyethyl acrylamide, and subsequent functionalisation used to construct the backbones of grafted segments for all graft copolymers. **B)** Synthetic approach used for the preparation of diblock and triblock backbone copolymers. Each polymer was subsequently functionalised similarly to copolymer B.

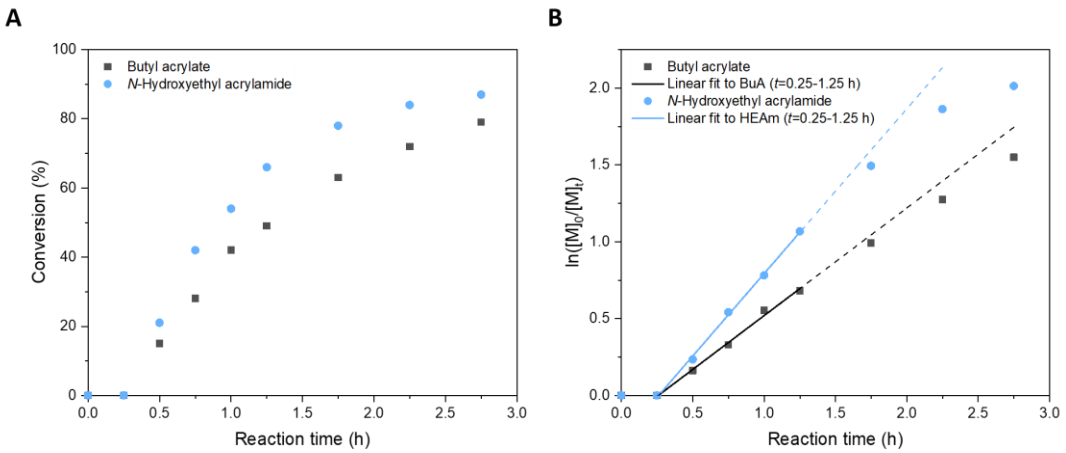

Figure 4.1 Kinetic data for the RAFT statistical copolymerisation of *n*-butyl acrylate and *N*-hydroxyethyl acrylamide. Conversion data (**A**) were converted into a pseudo first-order linear plot (**B**). Linear fits (t = 0.25-1.25 h, $r^2 \geq 0.995$) and their extrapolations are indicated by solid and dashed lines, respectively.

Table 4.1 Conversion and SEC analysis details for the preparation of graft copolymer library. Graft copolymer structure notation $p(LA_n)_{x,y}$ indicates the graft length (n), backbone length of the grafted segment (x) and the grafting density, i.e. the number of grafts per backbone repeating unit (y).

Corresponding polymers studied in previous work[30]							
B	$(pLA_{46})_{100,100\%}$						
AB	$pNAM_{100}$-*b*-$(pLA_{53})_{100,100\%}$						
BAB	$(pLA_{46})_{100,100\%}$-*b*-$pNAM_{100}$-*b*-$(pLA_{46})_{100,100\%}$						
ABA	$pNAM_{50}$-*b*-$(pLA_{48})_{100,100\%}$-*b*-$pNAM_{50}$						
Polymers prepared in this work							
	Conversion (%)		**Structure**	**HEAm** [A] **(%)**	$M_{n,th}$ [A] **(g/mol)**	$M_{n,SEC}$ [B] **(g/mol)**	$Đ$ [B]
B	BuA 62 HEAm 76		$p(BuA_{63}$-*s*-$HEAm_{31})$	33	12,100	9,800	1.14
	$p(BuA_{63}$-*s*-$CTA_{31})$				22,800	16,600 [C]	1.14 [C]
	LA	76	$p(LA_{42})_{94,33\%}$		336,000	346,000 [D]	1.21 [D]
AB	NAM	79	$pNAM_{104}$	36	15,100	8,000	1.22
	BuA 65 HEAm 91		$pNAM_{104}$-*b*-$p(BuA_{68}$-*s*-$HEAm_{38})$		28,200	21,100	1.37
	$pNAM_{104}$-*b*-$p(BuA_{68}$-*s*-$CTA_{38})$				42,000	36,900 [C]	1.37 [C]
	LA	72	$pNAM_{104}$-*b*-$p(LA_{40})_{105,36\%}$		407,100	429,000 [D]	1.15 [D]
BAB	NAM	89	$pNAM_{115}$	33	17,000	14,900	1.07
	BuA 62 HEAm 77		$p(BuA_{62}$-*s*-$HEAm_{31})$-*b*-$pNAM_{110}$-*b*-$p(BuA_{62}HEAm_{31})$		39,000	39,600	1.15
	$p(BuA_{62}$-*s*-$CTA_{31})$-*b*-$pNAM_{110}$-*b*-$p(BuA_{62}CTA_{31})$				61,600	47,400 [C]	1.37 [C]
	LA	75	$p(LA_{41})_{93,33\%}$-*b*-$pNAM_{110}$-*b*-$p(LA_{41})_{93,33\%}$		673,000	1,050,000 [D]	1.42 [D]
ABA	BuA 70 HEAm 82		$p(BuA_{70}$-*s*-$HEAm_{32})$	31	13,400	15,200	1.08
	NAM	88	$pNAM_{56}$-*b*-$p(BuA_{70}$-*s*-$HEAm_{32})$-*b*-$pNAM_{56}$		29,200	26,700	1.11
	After end-group removal				28,400	24,400	1.45
	$pNAM_{56}$-*b*-$p(BuA_{70}$-*s*-$CTA_{32})$-*b*-$pNAM_{56}$				40,000	29,600 [C]	1.22 [C]
	LA	79	$pNAM_{56}$-*b*-$p(LA_{39})_{102,31\%}$-*b*-$pNAM_{56}$		340,000	573,000 [D]	1.29 [D]

[A] Calculated based on conversion as given by ^1H NMR analysis.
[B] Determined by SEC with DRI in DMF using PMMA calibration.
[C] Determined by SEC with DRI in $CHCl_3$ using PMMA calibration.
[D] Determined by SEC with triple detection in THF.

For the preparation of architectures with linear pNAM segments, a two-step polymerisation protocol was required to construct the copolymer backbone prior to functionalisation (Scheme 4.2B). The AB diblock structure was prepared by chain-extending $pNAM_{105}$ with a mixture of BuA and HEAm. A difunctional RAFT agent, ethane-1,2-diyl bis(2-(((dodecylthio)carbonothioyl)thio)-2-methylpropanoate) (bis-MPDTC), was used to synthesise the triblock backbone precursors for BAB and ABA in a two-step fashion either by chain-extending $pNAM_{110}$ from both chain-ends with a mixture of BuA and HEAm (BAB), or by chain-extending $p(BuA\text{-}s\text{-}HEAm)_{100}$ with NAM (ABA). The amount of initiator consumed in the polymerisation of each first block was kept low relative to the amount of added CTA to retain a high theoretical livingness (> 99%) of the chains.[31] The theoretical livingness (L) of each polymer was estimated as

$$L = \frac{[\mathrm{CTA}]_0}{[\mathrm{CTA}]_0 + 2f[\mathrm{I}]_0(1 - e^{-k_d t})\left(1 - \frac{f_c}{2}\right)}, \quad (4.2)$$

where $[\mathrm{CTA}]_0$ and $[\mathrm{I}]_0$ are the initial CTA and initiator concentrations, respectively, f is the initiator efficiency,[32] k_d is the decomposition rate coefficient of the initiator, t is the reaction time, and f_c is the coupling factor for radical-radical termination events with $f_c = 1$ corresponding to 100% bimolecular termination by combination.[33] Retention of the RAFT end-group was confirmed by SEC: chain extension was observed for each product as an increase in the experimental number-average molecular weight ($M_{n,SEC}$) and absence of the starting material (Figure 4.2A).

The ABA end-groups of were removed with a previously reported method to prevent chain extension of the $pNAM_{55}$ segments during the graft polymerisation of LA.[30, 34] Reaction with lauroyl peroxide and azobisisobutyronitrile successfully fragmented and terminated the chain-ends, as indicated by the disappearance of the characteristic $UV_{309\,nm}$ absorption of the trithiocarbonate end-group in the SEC trace (Figure 4.2B) and the yellow colour of the polymer. Some chain termination via combination was apparent in the data, as indicated by a high-molecular weight shoulder.

NMR spectroscopy was used to assess the degree of functionalisation of the polymers (Figure 4.3). Relative areas of monomer signals at 4.03 ppm and 4.16 ppm in the ^{1}H NMR spectra corresponding to side-group protons $-COOC\underline{H}_2-$ and $-CONHCH_2C\underline{H}_2-$ of BuA and HEAm, respectively, and the absence of $-C\underline{H}_2$-OH

signal at 3.7 ppm; 61 ppm in the ^{1}H-^{13}C HSQC spectra indicated successful functionalisation of the polymers. The data were corroborated by a significant increase in the characteristic UV absorption of the trithiocarbonate moiety at 309 nm in the SEC curves.

The functionalised backbones were used to graft polymerise LA (Scheme 4.3). Due to the attachment of the CTA functionalities via the R group, the reactions involved the R group *grafting from* mechanism. A well-known drawback of the

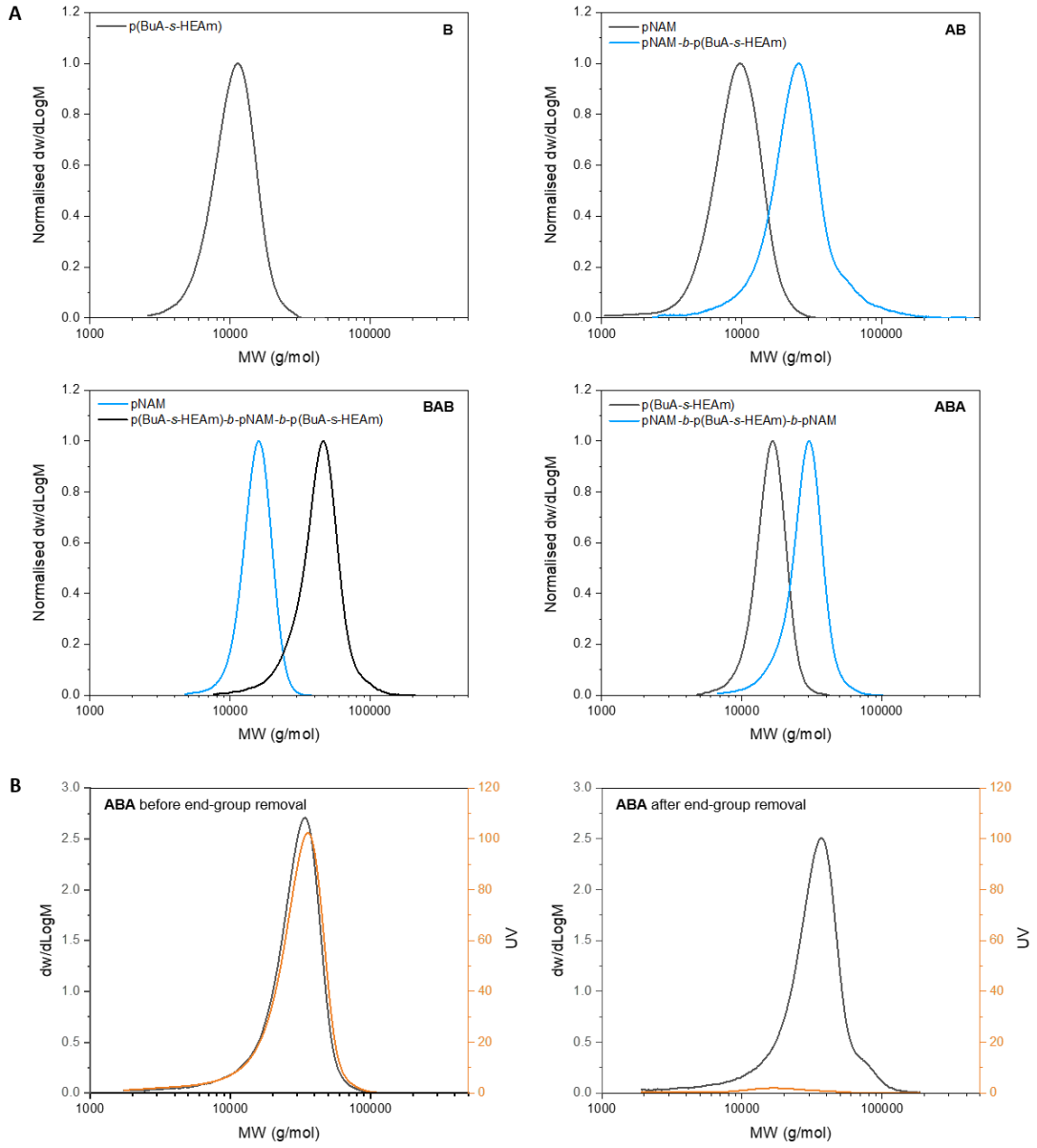

Figure 4.2 SEC data for all backbone copolymers (**A**) and the ABA backbone before and after end-group removal (**B**). Analysis was carried out in DMF with DRI and $UV_{309\ nm}$ detection and PMMA calibration.

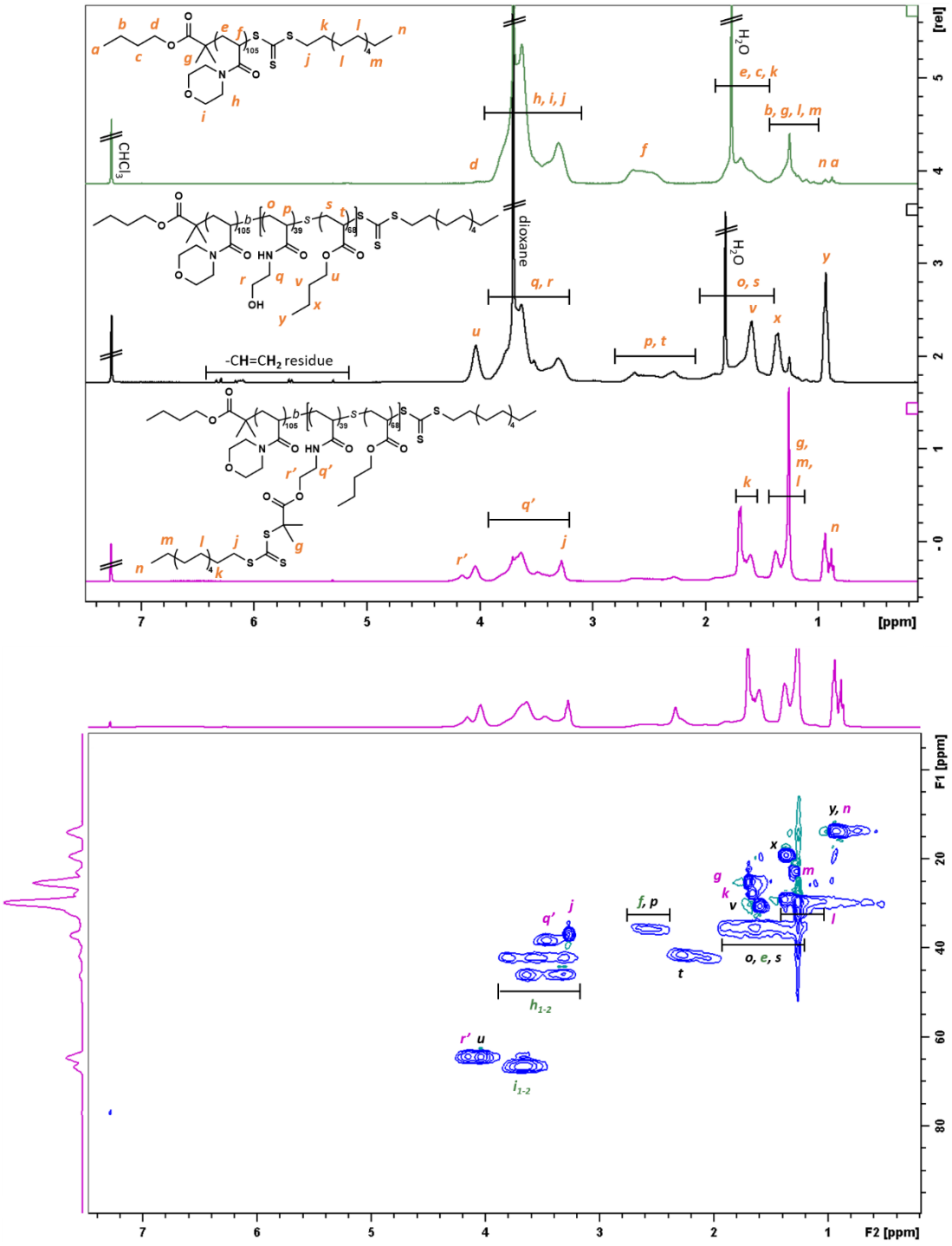

Figure 4.3 Representative ^{1}H NMR and ^{1}H-^{13}C HSQC spectra of the CTA-functionalised backbones at each intermediate stage, acquired in $CDCl_3$ at 20 mg/ml and 100 mg/ml concentrations, respectively. Spectra for the AB diblock copolymer are shown.

approach is the possibility of side-chain radicals terminating through combination, some of which may cause intermolecular coupling and loss of the bottlebrush-like topology.[35] The selection of appropriate reaction conditions is the key to a successful

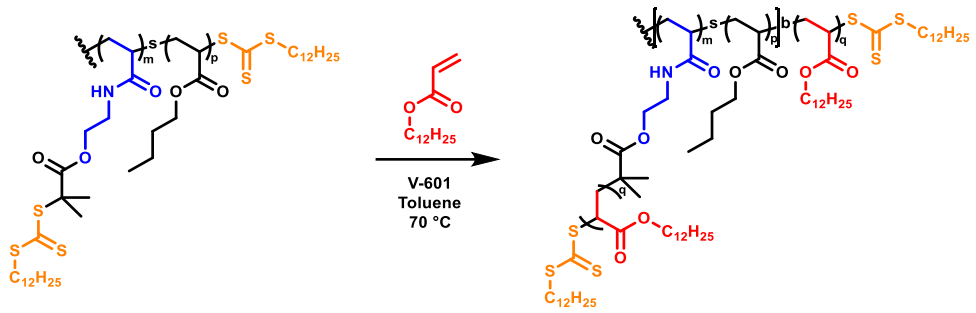

Scheme 4.3 Polymerisation of pLA grafts was conducted using the R group *grafting from* approach with functionalised p(BuA-*s*-HEAm) backbones.

polymerisation in which such reactions are minimised. Intermolecular coupling may be prevented by selecting monomers for which disproportionation is preferred over combination, or by employing a low radical concentration (i.e., a high $[CTA]_0/[I]_0$ and a slow rate of initiator decomposition), by keeping the concentration of initiating sites low to moderate (i.e. a low backbone concentration), and by stopping the polymerisation before the full consumption of monomer to maintain a slow rate of termination relative to the rate of propagation.[36] In reactions where intermolecular coupling cannot be avoided by other means, a small amount of free CTA may be added to the reaction to mediate the transfer of chain radicals from one bottlebrush polymer to another, thus reducing the probability of graft-graft coupling.[35]

The graft polymerisation of LA was conducted in the absence of a shuttle-CTA at 1 M monomer concentration with $[CTA]_0/[I]_0$ = 20-40, using V-601 initiator at 70 °C to maintain a moderate radical concentration. Reactions were stopped below 80% conversion to avoid monomer-starved conditions. SEC analysis showed reasonably well-controlled products for all reactions. The formation of a linear pLA by-product with a strong UV absorption at 309 nm suggested the presence of residual free CTA from the functionalisation step which effectively acted as a shuttle-CTA (Figure 4.4).[35] Products B and AB showed a small high MW shoulder, which could be ascribed to intermolecular coupling but might also arise to some extent from the inherent branching of the acrylate-containing backbone becoming more pronounced in the chromatogram after grafting the side-chains. The latter hypothesis was supported by the high MW shoulder in the AB diblock before functionalisation of the backbone. ABA and BAB triblock copolymers showed pronounced high MW shoulders likely due to graft-graft coupling, and for the former partly as a result of

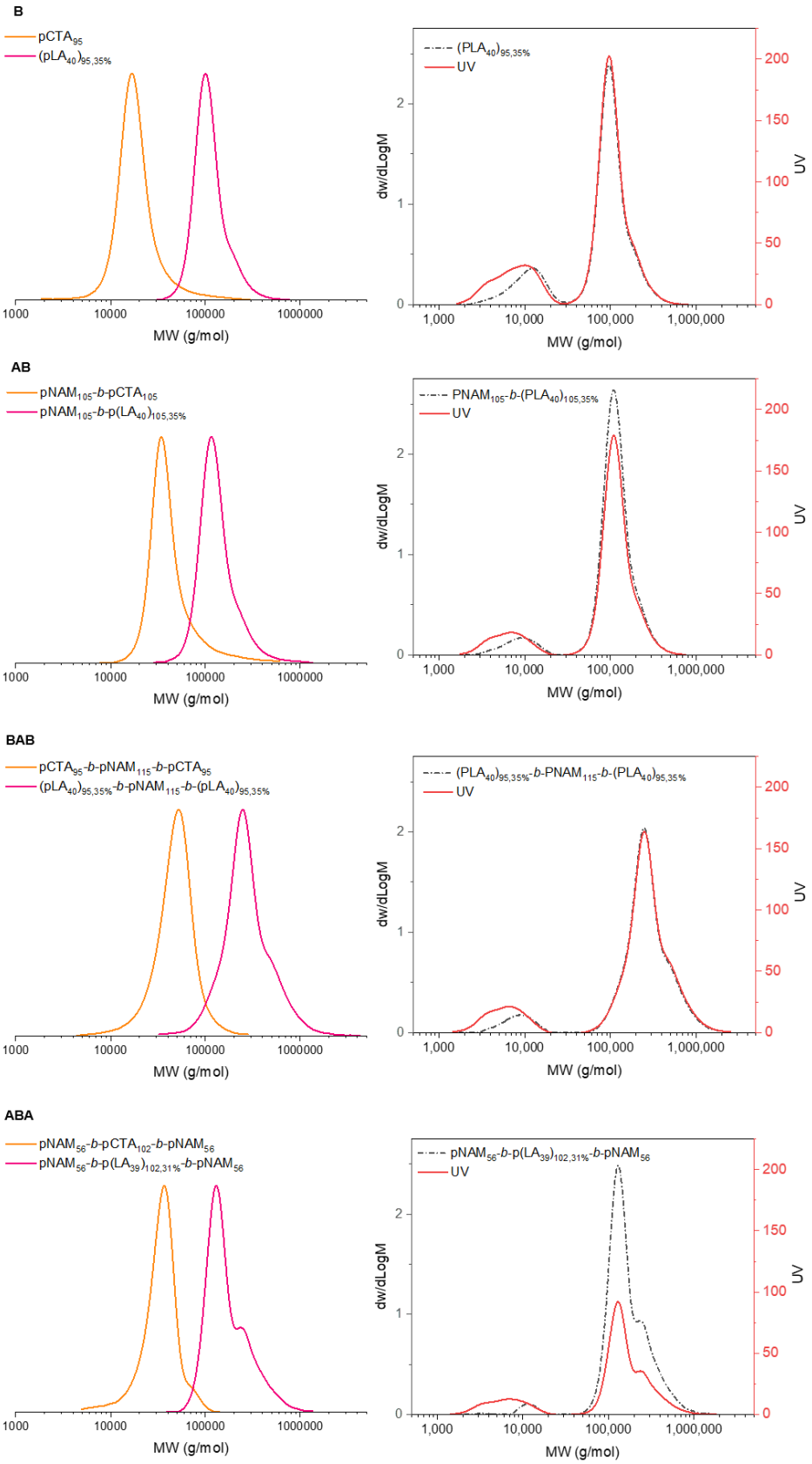

Figure 4.4 SEC data for graft copolymers and their precursors plotted as normalised differential log molecular weight distribution (dw/dLogM vs. MW). Functionalised backbones and graft copolymers were analysed in $CHCl_3$ and THF, respectively, with DRI and UV (309 nm) detection and PMMA calibration.

intermolecular coupling in the end-group removal step. The analysis of all intermediate and final products was limited by their solubility after each step. Thus, three different instrument setups were used to analyse the polymers in either DMF, $CHCl_3$, or THF. Comparison of the data was therefore made while bearing in mind the distinct polymer solubilities, solvent conditions, and separation ranges of each instrument.

The ABA triblock was found to be insoluble in oil and was omitted from further experiments. The insolubility was attributed to the polar pNAM segments collapsing into physical crosslinks under poor solvent conditions. The network formation resulted in a spongy, opaque appearance of the polymer in its dry state, while the other three products had a viscous and transparent consistency. Similar bulk characteristics have been reported for ABA-type bottlebrush polymers which were employed as plastic elastomers for their tissue-like mechanical properties.[37]

AFM was used to visualise the graft copolymers in the dry state by drop-casting them from chloroform, a non-selective solvent, onto highly oriented pyrolytic graphite. The images showed somewhat different appearances for each polymer, with B appearing less cylindrical than AB. This suggests that the latter had a slightly longer backbone and/or shorter grafts while BAB appeared less rigid than the other two due to the flexible central linear block (Figure 4.5). Height profiles showed all polymers to have a roughly 20 nm end-to-end distance for the grafted chains, which was in good agreement with the predicted 22 nm end-to-end distance for extended pLA_{40} grafts attached to the backbone. Manual image analysis was used to measure the rigid backbones of B and AB to estimate an average contour length of 18 nm and 23 nm, respectively, which seemed reasonable for a backbone with a DP of 100 and some flexibility due to the reduced grafting density.

4.2.2 Lubricant Performance Tests

Lubricant performance of these graft copolymers was assessed using a mini traction machine (MTM). The instrument consisted of a 19 mm steel ball loaded against a 46 mm (Ø) steel disc with each having independent movement controls, and a force transducer to measure the frictional force between the surfaces (Figure 4.6A). The frictional force was described by Stribeck curves in which friction coefficient is plotted against the so-called Hersey number (x), which is given by

$$x = \frac{\eta v}{N}, \tag{4.3}$$

where η is the viscosity, v is the entrainment speed and N is the normal load. Under a constant load and viscosity, the friction coefficient may be plotted as a function of the entrainment speed. A small Hersey number typically indicates a thin lubricant layer

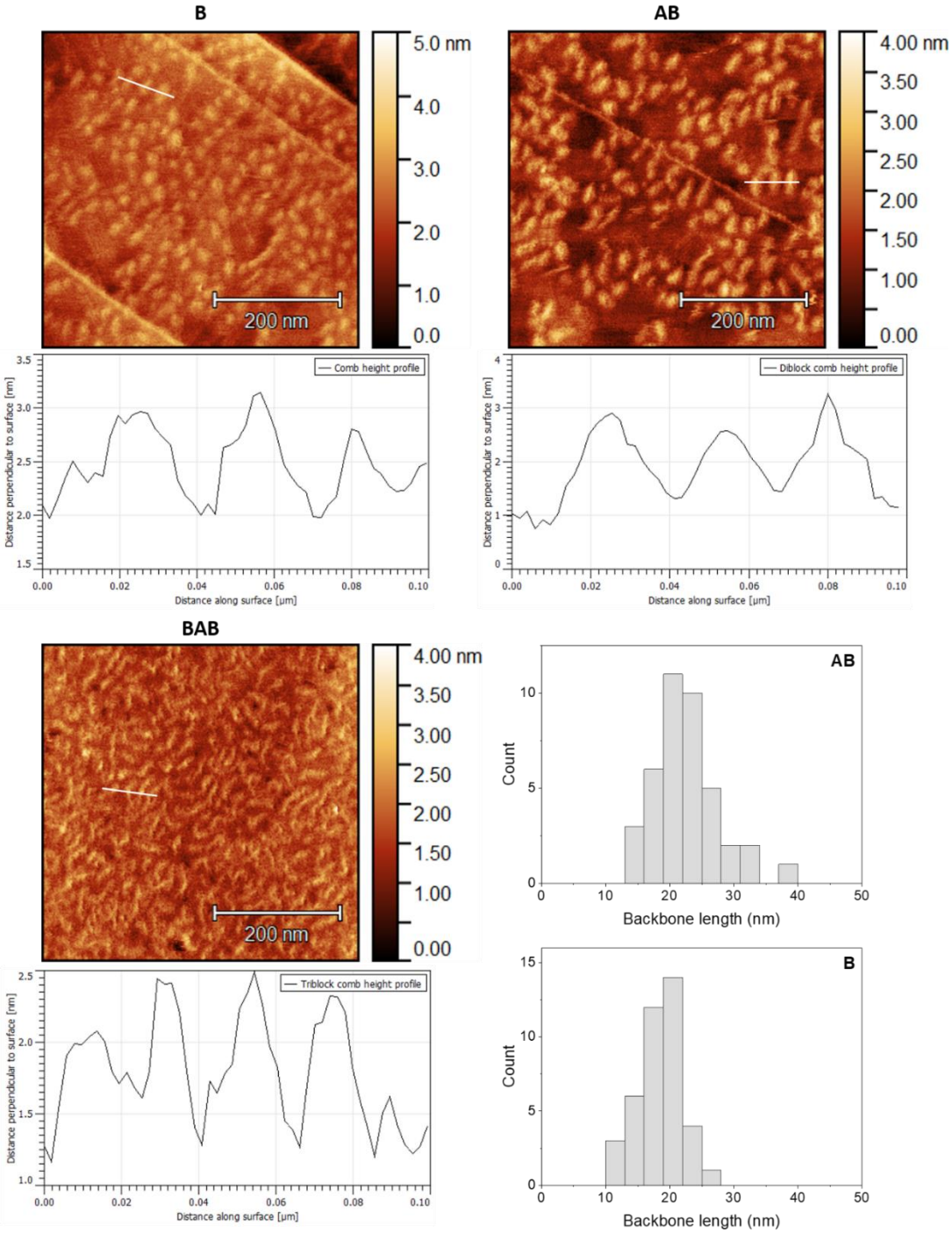

Figure 4.5 AFM images and height profiles of graft copolymers drop-casted from chloroform onto highly oriented pyrolytic graphite. Histograms show backbone lengths as given by 40 individual manual measurements per sample.

where the load rests primarily on asperity contacts leading to high friction, commonly referred to as the boundary lubrication regime (Figure 4.6B). Increasing the Hersey number leads to a mixed regime in which the distance between surfaces increases, the load becomes increasingly supported by the fluid, and the friction is reduced. The distance may increase further until eventually the load is fully supported by the fluid. The point of minimum friction is observed where fluid thickness exceeds the surface roughness, marking the beginning of the hydrodynamic lubrication regime. Past this point, a gradual increase in friction arises from shearing of the fluid.

Performance tests were conducted with 1 wt.% additive in Yubase 4 mineral oil. Each sample was tested across 10-3,000 mm/s rolling speeds and a temperature range of 40-140 °C at 50% slide-to-roll ratio under a 37 N load. The Stribeck curves showed all treated oils to provide enhanced lubrication across the boundary and mixed lubrication regimes (Figure 4.7). The superior performance was particularly notable in the boundary lubrication regime in which asperity contacts were abundant and the role of friction modifiers generally becomes more pronounced.[6] All treated oils provided a 20-30% reduction in the friction coefficient in the boundary regime at 40 °C and a larger reduction of 30-50% at 140 °C when compared to base oil. The results were similar to previously reported tests carried out with densely grafted copolymers of corresponding architectures, for which the highest reduction of 50% was recorded at 120 °C for the densely grafted analogue of BAB, p(LA_{46})$_{100}$-*b*-pNAM_{100}-*b*-p(LA_{46})$_{100}$.[30] The greater improvement seen at elevated temperatures and

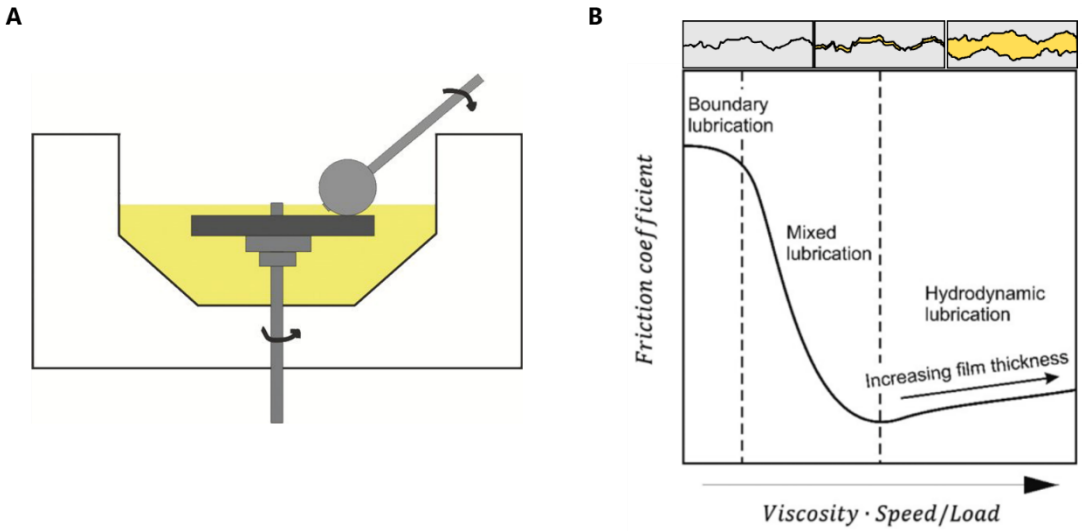

Figure 4.6 A) Cross-sectional illustration of an MTM instrument. **B)** A Stribeck curve with fluid film lubrication and boundary film lubrication regimes. Adapted from refs. 13 and 38.

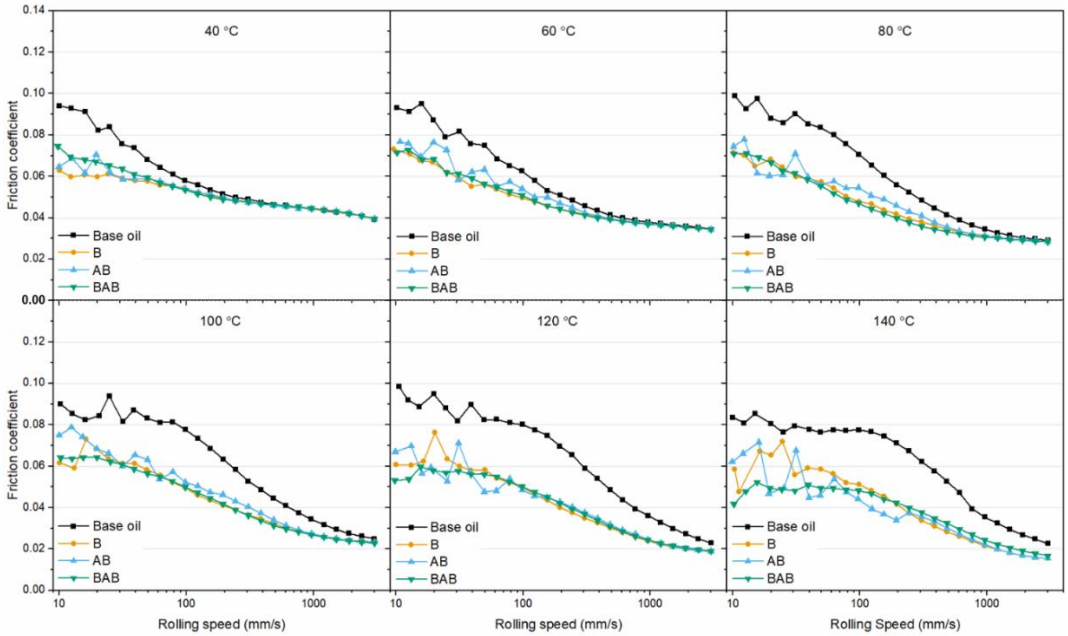

Figure 4.7 MTM data collected for pure base oil and 1 wt.% polymer blends across 10-3,000 mm/s rolling speeds at 50% slide-to-roll ratio and 37 N load.

the extension of the boundary regime to higher rolling speeds was due to the reduced viscosity of the oil leading to a thinner layer in the contact. The treated oils seemed to transition from the mixed lubrication regime to boundary lubrication at lower rolling speeds, indicating the ability of the polymers to prevent the solvent from being squeezed out of the contact. The friction coefficients recorded for B and AB at low rolling speeds were found to be unstable and resulted in poor control of the slide-to-roll ratio. While a stable reading was recorded for BAB across all measurements, at 120-140 °C control over the slide-to-roll ratio was lost at low speeds due to slippage.

Contrary to our hypothesis, the incorporation of surface-active pNAM segments into the polymer structure was not found to have a significant effect on the performance, which was overall comparable for all polymers. This was in stark contrast to the previous study in which densely grafted copolymers with pNAM segments were found to outperform those without one. The incorporation of polar segments into oil-soluble linear polymers has been reported to promote enhanced lubrication as a result of adsorption of onto metal surfaces, driving the formation of a solvated layer that is harder to displace than freely diffusing polymers.[8] Furthermore, the effect has been found to be greater when polar units are introduced into the structure as a block rather than statistically distributed across the main chain. This was

explained in terms of the probability of desorption of the polar segment being much smaller for a block than for individual units. While polymer B carried no polar segment, the RAFT end-groups of the pLA grafts or the amide/ester groups of the backbone monomers may have conferred some surface activity to the polymer, with a mechanism of adsorption something akin to multivalent binding.

Overall, the performance tests showed all three polymers to be promising candidates for next-generation lubricants. Given the complexity of the synthetic approach used in this study, polymer B seemed the most attractive option from a practical point of view based on these tests alone. Considering the data collected in the previous study, in which the incorporation of a pNAM segment was found to significantly improve the performance, further exploration of all three polymers seemed fitting. The MTM tests were generally found to suffer from poor repeatability which made direct comparison of data collected across the whole study unreliable. The synthetic approach set a limitation for sample quantity, due to which re-assessment of the most promising candidates was not possible. These limitations should inform future work, in which scaling up the synthetic protocols could allow more elaborate testing.

4.2.3 Film Formation and Solution Behaviour

Further experiments were carried out to gain a better understanding of the surface adsorption and solution properties of the three polymers. The aim was to reveal characteristics and phenomena that could aid the design and selection of polymers for future work, particularly for scaling up and further friction testing. Previous studies of graft copolymers in aqueous environments suggest that, to perform well as a lubricant, the polymer should be densely-grafted to avoid chain interpenetration between opposing surfaces, well-solvated to provide a fluid interface, and firmly anchored to increase load bearing capacity and to counteract energy dissipation arising from shear-induced sliding.[1-3] A selection of techniques was used in this work to assess these properties in more detail. A quartz crystal microbalance with dissipation (QCM-D) was first used to quantify polymer adsorption onto steel from bulk solvent to gain information on surface interactions, timescales of film formation, and the rigidity of the resulting film. Polarised neutron reflectometry (PNR) was then used to complement this data at the nanometre length scale to collect detailed information about film structure and surface coverage. AFM imaging was used to visualise

polymers adsorbed onto steel from solution in their dry state to reveal differences in their solution and adsorption behaviour.

4.2.3.1 QCM-D Experiments

The lubricant performance of these polymers was initially hypothesised to primarily depend on their surface adsorption characteristics, which in turn was anticipated to be dependent on the position of the polar pNAM segment. A linear segment attached to the end of a grafted segment was expected to be more exposed to the environment than one positioned between two grafted segments. In a non-polar environment, the insoluble pNAM block was envisioned to undergo intermolecular aggregation unless prevented by the steric bulk of the grafted segments.[39] Micellisation and screening of the polar segments by steric bulk were considered as factors that could reduce the probability of adsorption.

To assess the role of incorporation and placement of the polar segment, surface adsorption of the polymers and the rigidity of the resulting films were studied with a QCM-D. The technique allows for highly sensitive, *in situ* monitoring of mass deposition onto a surface by employing a piezoelectric quartz crystal, the resonance frequency of which is dependent on the thickness, density, temperature and shear modulus of the crystal and the density or viscosity of the surrounding fluid.[40] In the experiment, an alternating voltage is applied across the crystal, thus causing it to oscillate. By matching the frequency of the voltage to the resonance frequency of the crystal, a standing wave is formed which causes the electrodes to move in opposite directions relative to each other. Mass deposition onto the crystal changes its resonance frequency (f) and can be quantified for rigid masses using the Sauerbrey model for which it holds

$$\Delta f = -\frac{2f_0^2 n}{A\sqrt{\rho_q \mu_q}} \Delta m \,, \tag{4.4}$$

where f_0 is the fundamental resonance frequency, n is the overtone, and A is the crystal area, p_q is the crystal density, μ_q is the shear modulus of the crystal, and Δm is the change in mass. The instrument may also be used to monitor the dissipation (D) of a freely oscillating crystal. By recording the oscillatory decay after switching off the voltage, information about the energy losses at the surface may be obtained. Energy losses per oscillation are different for soft and rigid films and are defined as

$$D = \frac{1}{Q} = \frac{E_d}{2\pi E_s}, \tag{4.5}$$

where Q is the quality factor of the oscillator, E_d is the dissipated energy, and E_s is the stored energy. Hence, dissipation measurements may be used to describe the softness/rigidity of the material and to evaluate the validity of the Sauerbrey relation as an acceptable approximation. For soft films, the Sauerbrey model is not applicable, but mass deposition may be quantified using the Kelvin-Voigt model.[41]

To conduct the QCM-D experiments, 0.01 wt.% polymer solution prepared in *n*-dodecane was passed over a stainless steel-coated chip at 50 µl/min flow rate at 40 °C. The data show a sharp decrease in the resonance frequency for each polymer after injection, arising from mass deposition onto the steel surface (Figure 4.8). After reaching a plateau, pure *n*-dodecane was passed over the chip to remove any loosely adsorbed polymer and that remaining in the bulk phase. The rinse was found to have very little effect on the resonance frequency, suggesting that all adsorbed polymer was tethered to the surface tightly enough to not desorb at the selected flow rate. Each polymer showed distinct adsorption behaviour in both the magnitude of frequency change and its dependence on the overtone frequency. Polymer B was found to adsorb

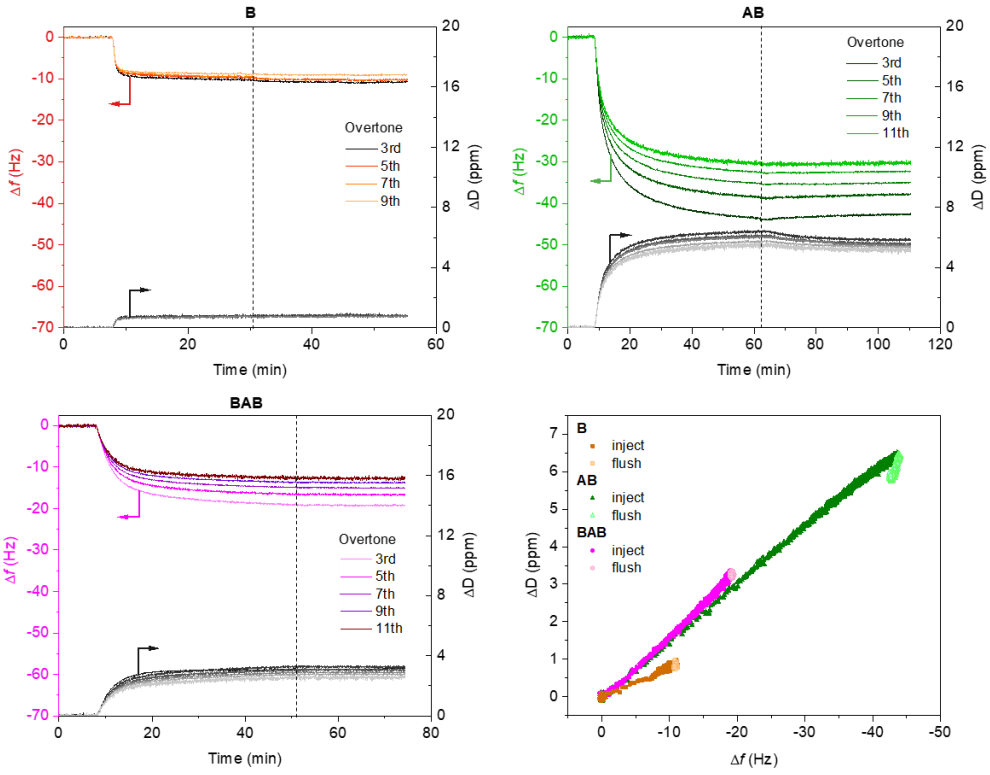

Figure 4.8 QCM-D data collected for the adsorption of comb polymers from *n*-dodecane onto steel. Starting point of rinse with pure solvent is indicated by a dashed line.

least out of the three polymers, as indicated by the smallest frequency change. The incorporation of a polar segment resulted in a substantial increase in adsorption as seen in the data collected for AB and BAB, the former of which was found to deposit on the surface most readily. Furthermore, the data for these two polymers showed considerable overtone splitting, suggesting the formation of a viscoelastic film. By plotting ΔD against Δf a comparison of the viscoelasticities could be made whilst accounting for the overall mass deposition. The data showed AB and BAB formed films with comparable softness. Evidently, the incorporation and placement of a polar segment plays an important role in film formation.

Mass deposition onto steel was quantified for each polymer by using the Sauerbrey or the Kelvin-Voigt model (Figure 4.9). Data collected for B was averaged across the overtones and fitted to the Sauerbrey model to find a total mass deposition of 350 ng/cm^2. Data for AB and BAB were fitted to the Kelvin-Voigt model, giving total deposition of 1,200 ng/cm^2 and 600 ng/cm^2, respectively. The models are often used to calculate layer thicknesses if the density of the layer is known. However, this is only valid for homogeneous layers which cover the whole surface area and

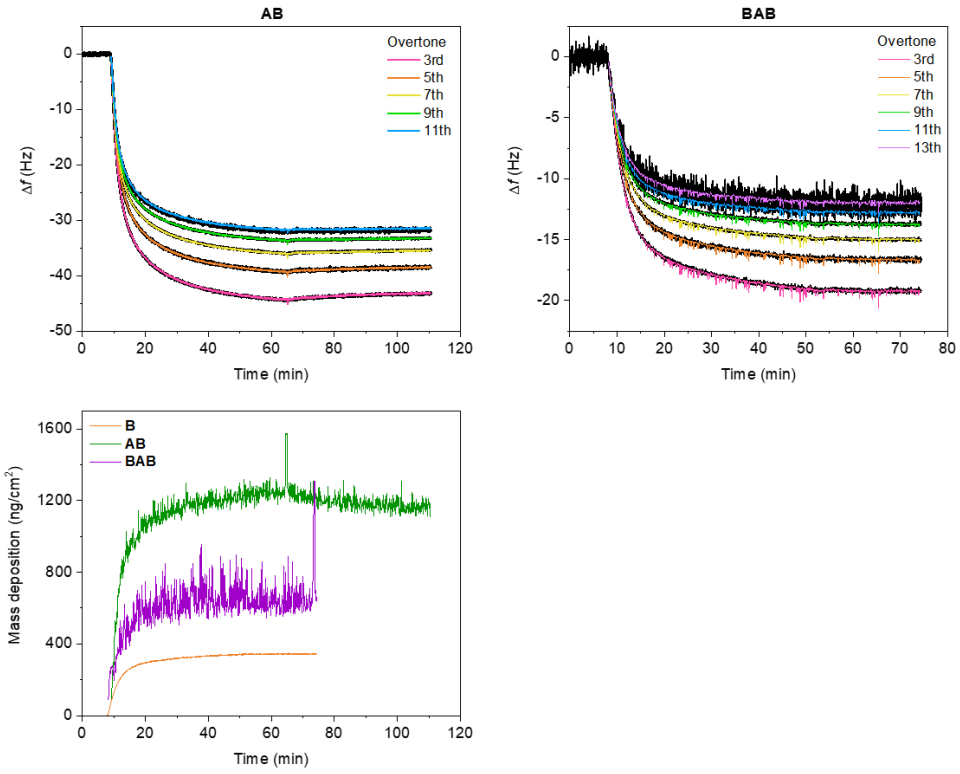

Figure 4.9 QCM-D data analysis was used to quantify mass of polymers adsorbed onto steel surface. Data for polymer B was fitted using the Sauerbrey model describing a rigid film, for which $\Delta f \sim \Delta m$. Data for AB and BAB were fitted using the Kelvin-Voigt model describing a viscoelastic film. Raw data is presented in black with fitted data plotted on top.

have a uniform thickness.[42] While the density of the studied films could have been roughly estimated as the density of pLA, information regarding surface coverage was lacking and therefore film thickness could not be quantified with this technique.

The data showed notable differences in the timescales of adsorption for the three samples, which had important implications for their application. While the sample concentration in the QCM-D experiments was two orders of magnitude smaller than that used in friction tests, the effective concentration may be considered as larger or equal to the MTM concentration due to the continuous injection until no further adsorption took place. This corresponded to roughly 8-20 mg total mass of injected polymer in each measurement. The total injection time varied between 23-53 min and equilibration was particularly slow for the AB sample. The data suggest that the pNAM segment was less exposed to the environment in the AB architecture than it was in BAB, leading to a longer equilibration time. This was contrary to the hypothesis, and could be explained by micellisation which should be more favourable for AB due to the sterically demanding topology of BAB. In addition to the polymer architecture, the adsorption rates may have been affected by differences in molar concentration.

The adsorption study revealed distinct differences in surface activity for the three architectures, but these were not manifested in the MTM tests to any great extent. Considering the differences in the experimental conditions of the two techniques, including instrument sensitivity, surface roughness, and shear rate, direct correlation between the two datasets could be misleading. The higher shear rate of the MTM tests alone could potentially cause desorption and degradation of the polymer and affect its solution properties, thus influencing polymer-surface interactions. It may be concluded, however, that polymer B provides lubrication comparable to AB and BAB despite mainly existing in the bulk solvent. This implies that the improved lubrication achieved with all samples may have been only partially (or not at all) a result of boundary film formation. Overall, correlating lubricant performance with surface adsorption characteristics seems complicated unless the two can be observed simultaneously. The use of instruments combining the two could offer a significant advantage in future work. Advances have been made in this regard by using neutron and X-ray reflectometry in conjunction with rheometers, tribometers and other types of specialised instruments,[17-19, 43] paving the way for a deeper understanding of boundary lubrication.

4.2.3.2 Polarised Neutron Reflectometry

QCM-D studies showed that the AB and BAB polymers readily adsorb onto steel forming a viscoelastic film. However, the surface coverage, film thickness and polymer orientation on the surface remained unknown and have been identified as key parameters for high performance in some boundary lubricants. Both polymers could be envisioned to adopt flat, perpendicular, or tilted orientations on the surface, all of which would result in different layer thicknesses. The layer structure could be further complicated by micelle formation in the bulk phase. While the characterisation of solid-liquid interfaces is not a trivial task, techniques such as liquid-state AFM,[44] neutron reflectometry,[45] and specialised tribometers[46] may be used to collect structural information at a nanometre length scale. For this study, PNR was selected to elucidate the structural ambiguities of the AB layer. The nondamaging nature and high penetration of neutrons makes it a powerful technique for studying buried interfaces and complex sample environments.[43]

Neutron reflectometry experiments involve illuminating the sample of interest with a collimated neutron beam at grazing incidence and measuring the reflected intensity as a function of momentum transfer. The sample consists of one or multiple interfaces of solids, liquids or gases, which cause the neutron beam to reflect and refract at ratios characteristic to the layers meeting at the interface. The reflected intensity is dependent on the structure and SLD (ρ) of the material, which is related to the refractive index and may be defined for polymers as

$$\rho = \frac{\rho_m N_A \sum_{i=1}^{n} b_c}{\sum_{i=1}^{n} M}, \tag{4.6}$$

where ρ_m is the mass density, N_A is Avogadro's constant, n is the number of nuclei within a molecule, b_c is the atomic scattering length, and M is the number-average molar mass.[45] The measured reflectivity profile describes the reflected intensity as a function of momentum transfer perpendicular to the surface normal (Q_z), for which it holds

$$Q_z = \frac{4\pi}{\lambda} \sin\theta\,, \tag{4.7}$$

where λ is the neutron wavelength, and θ is the incidence angle of the beam relative to the sample surface.[45] Neutron reflection from the top and bottom interfaces of a layer may result in constructive and destructive interference which appear in the

reflectivity profile as peaks and troughs, respectively, and are generally known as Kiessig fringes. The distance between the fringes contains information about the thickness (d) of the layer, which may be calculated as

$$d = \frac{2\pi}{Q_{z,2} - Q_{z,1}}, \tag{4.8}$$

where $Q_{z,2} - Q_{z,1}$ is generally the trough-to-trough distance.

In this study, the sample of interest comprised a solvated layer of polymer AB adsorbed onto a solid substrate immersed in *n*-dodecane. The solid substrate was a silicon block polished to < 5 Å roughness and sputter-coated first with permalloy (4:1 Ni:Fe) and then grade 316 stainless steel. The magnetic layers of the substrate provided an additional spin contrast to complement the isotopic solvent contrast when measured with spin-polarised neutrons. The instrument setup consisted of a polarised neutron beam directed at the sample within a laminar flow cell maintained at a 45 °C temperature, to which pure solvent or polymer solution could be injected using a syringe pump connected to a channel switch. Measurements were carried out at 0.5°, 1.5°, and 2.5° incident angles to cover an effective Q_z range of 0.01-0.03 $Å^{-1}$ using spin up (↑) and spin down (↓) polarised neutrons and two isotopic solvent contrasts, hydrogenated and deuterated *n*-dodecane.

The clean substrate was first measured to give four reflectivity profiles describing the solid-solid interfaces within the substrate and the solid-liquid interface of the substrate and the solvent (Figure 4.10). Four layers were required to fit these data, corresponding to SiO_2, permalloy, steel, and a thin oxide layer (Table 4.2), the parameters of which were then fixed for the analysis of the polymer layer. The fits were in good agreement with the expected 150 Å and 250 Å thicknesses of permalloy and steel, respectively. Only a single homogeneous layer corresponding to steel was required to obtain satisfactory fits to the data measured using hydrogenated *n*-dodecane. The SLD of this layer did not split with respect to the neutron spin state and appeared smaller than that expected for pure iron, suggesting the presence of notable quantities of elements with lower neutron scattering lengths. This was in accordance with the steel grade, which includes elements such as chromium, molybdenum, and manganese. An additional thin surface layer was required to obtain satisfactory fits to the data measured with the deuterated solvent, suggesting the formation of

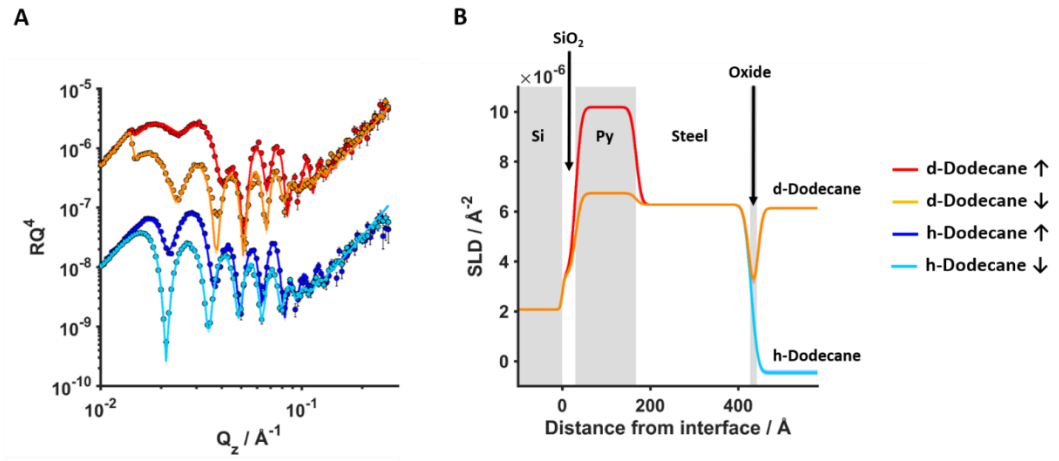

Figure 4.10 A) PNR data (points) and fits (lines) of clean silicon-permalloy-steel (Si-Py-Steel) substrates characterised in hydrogenated and deuterated *n*-dodecane with spin up (↑) and spin down (↓) magnetic contrasts. Data and fits of the deuterated contrast were vertically offset for clarity. **B)** SLD profiles corresponding to the fits. Shaded regions indicate discrete layers included in the model. Shaded line indicates the 95% confidence interval associated with the fit as given by Markov chain Monte Carlo analysis.

a thin oxide layer from exposure to oxygen under either atmospheric or sputtering conditions. Due to the poor contrast of this layer against the hydrogenated solvent, a high level of uncertainty remained in its fitted parameters, most notably with the SLD and solvation which are intrinsically correlated.

Table 4.2 Structural information obtained from PNR measurements for a silicon-permalloy-steel substrate before and after incubation with $pNAM_{104}$-*b*-$p(LA_{40})_{105,36\%}$. The substrate was first characterised with both solvent contrasts using spin up (↑) and spin down (↓) neutrons, and the fitted parameters were fixed for analysis after incubation. Error values were calculated from the 95% confidence intervals estimated from Markov chain Monte Carlo analysis.

Layer	$\rho \cdot 10^{-6}$ ($Å^{-2}$)	*d* (Å)	Solvation (%)	Roughness (Å)
Si	2.07*	-	0*	4^{+2}_{-1}
SiO2	3.47*	30^{+2}_{-2}	0*	11^{+1}_{-1}
Permalloy ↑	$10.19^{+0.03}_{-0.03}$	137^{+1}_{-1}	0*	10^{+1}_{-1}
Permalloy ↓	$6.73^{+0.03}_{-0.03}$			
Steel	$6.27^{+0.03}_{-0.02}$	260^{+1}_{-2}	0*	11^{+1}_{-1}
Oxide	$0.36^{+0.65}_{-0.35}$	15^{+2}_{-2}	7.0^{+9}_{-7}	9^{+1}_{-1}
pNAM	1.26*	47^{+7}_{-7}	67^{+4}_{-4}	19^{+1}_{-2}
pLA	0.14*	156^{+21}_{-22}	95^{+1}_{-1}	16^{+4}_{-10}
n-Dodecane	$-0.53^{+0.07}_{-0.03}$	-	-	-
n-Dodecane-d_{26}	$5.94^{+0.01}_{-0.01}$			

* Parameter was held constant throughout the fitting procedure.

To measure the layer formed by AB, 0.1 % w/v polymer solution prepared in hydrogenated *n*-dodecane was injected into the flow cell at a 0.5 ml/min flow rate and incubated for 2 h, after which pure *n*-dodecane was passed through to remove any weakly bound polymer and that remaining in the bulk phase. Data was collected with each spin contrast, after which deuterated *n*-dodecane was injected into the cell to repeat the measurements. For these data, an additional two layers were required to fit the data, corresponding to the linear pNAM and grafted pLA segments, respectively (Figure 4.11). The fits were in good agreement with the experimental data, showing a total film thickness of roughly 20 nm consisting of a 5 nm pNAM layer and a 16 nm pLA layer. The thickness and roughness of the former were much higher than would be expected of a linear polymer lying flat on a surface, suggesting the pNAM block adopts a different orientation. Considering the insolubility of pNAM in *n*-dodecane, it seems likely that the layer consists of aggregated pNAM chains, covering roughly 30% of the surface as suggested by the degree of solvation. The surface coverage may be limited by steric constraints of the grafted pLA segment. The thickness of the pLA layer corresponds to roughly 60% of the length of a fully extended backbone, which seemed fitting for the sparsely-grafted chain. The 10% roughness of this layer suggest different chain orientations for the grafted segment. No off-specular intensity was observed in the data, indicating that if aggregation took place, it had no long-range order.

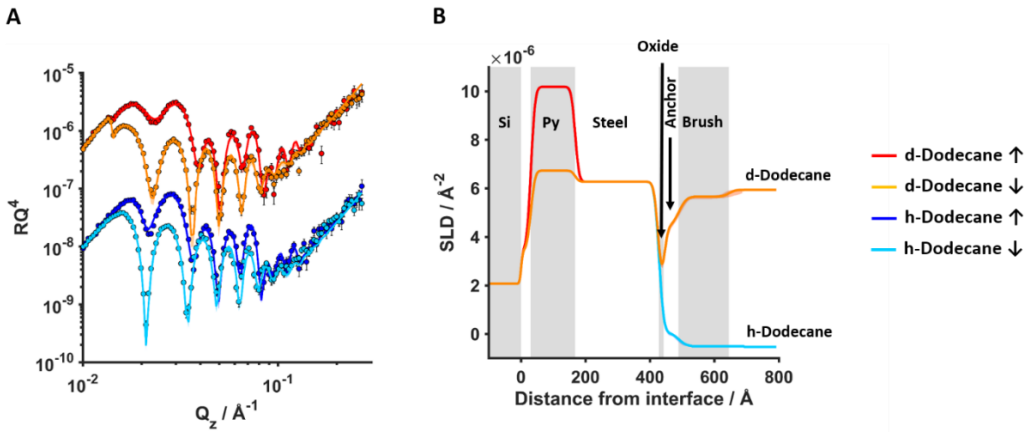

Figure 4.11 A) PNR data (points) and fits (lines) of $pNAM_{104}$-*b*-$p(LA_{40})_{105,36\%}$ film on a silicon-permalloy-steel (Si-Py-steel) substrate characterised in hydrogenated and deuterated *n*-dodecane with spin up (↑) and spin down (↓) magnetic contrasts. Data and fits of the deuterated contrast were vertically offset for clarity. **B)** SLD profiles corresponding to the fits. Shaded regions indicate discrete layers included in the model. Shaded line indicates the 95r% confidence interval associated with the fit as given by Markov chain Monte Carlo analysis.

After conducting the neutron reflectivity measurements, graft copolymers B, AB, and BAB were imaged with AFM in dry state after adsorption from *n*-dodecane onto the steel substrates to mimic the experimental conditions of PNR. Clean substrates were incubated in 0.1 w/v% polymer solution prepared in *n*-dodecane for 1 h. The polymer solution was displaced with pure *n*-dodecane to remove loose polymer, and with *n*-hexane to remove *n*-dodecane for easier drying. The images revealed significant differences across the three architectures (Figure 4.12). Polymers AB and BAB were found to readily adsorb on the surface; however, no polymer was found on the substrate for B. This was in excellent agreement with QCM-D data in which very little mass deposition was measured for B, while AB and BAB adsorbed in larger quantities. Images of AB revealed the presence of star-like micelles with a dense pNAM core surrounded by grafted pLA segments extending radially outwards, corroborating the neutron reflectometry results. The pNAM segments of BAB also seemed to form intermolecular aggregates, however the average aggregation number of 3-4 was much lower than for AB, likely due to the steric bulk flanking both ends of the linear segment. Another stark contrast was the patchy deposition of AB micelles covering only a small part of the substrate, while BAB was found to cover nearly the whole surface in the imaged areas. It seemed the adsorption of AB was hindered

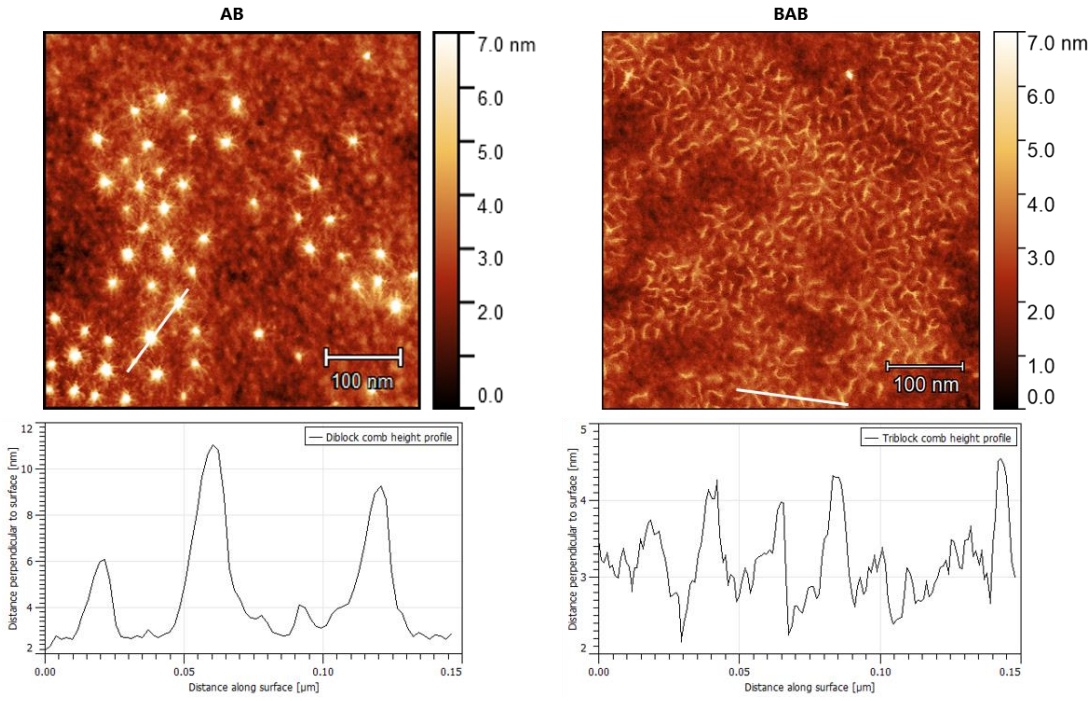

Figure 4.12 AFM images collected for PNR substrates after incubation in polymer solution prepared in *n*-dodecane. The samples were rinsed with pure solvent to remove loose polymer and subsequently with *n*-hexane to remove *n*-dodecane to obtain a dry sample.

by the steric bulk around the polar core, whereas for BAB the main limitation was the steric bulk of neighbouring molecules on the surface. Overall, BAB seemed superior in forming uniform films, showed most consistent data in friction tests, and could be considered the most promising candidate for further testing.

4.3 Conclusions and Outlook

This study involved the preparation and characterisation of graft copolymers and their assessment as boundary film-forming lubricants in oil to guide the design of next-generation friction modifier additives. RAFT polymerisation was combined with a post-modification strategy to prepare three oil-soluble, pLA-based graft copolymers with distinct architectures, two of which carried a linear, polar pNAM block to promote interactions with metal surfaces. Lubricant performance tests conducted with a MTM showed the treatment of base oil with 1 wt.% of polymer to provide a significant reduction of the measured friction coefficients in the boundary and mixed lubrication regimes. While the polymer architecture and the incorporation of a polar block did not result in significant differences in the friction tests, QCM-D experiments showed that both parameters affected the magnitude of surface adsorption and the softness of the polymer layer under low shear conditions. The incorporation of a polar block was found to significantly increase mass deposition onto steel. However, it also resulted in intermolecular aggregation, thus hindering surface interactions and slowing down film formation. PNR and AFM studies suggested that the polymers adsorbed onto the surface mainly as star-like micelles rather than individual molecules.

The work presented herein completes a larger body of research carried out in the group in which the preparation and performance of oil-soluble graft copolymers were studied in detail. We found these polymers to be promising candidates for friction modification and highlighted possible directions for further work. Our research has revealed important structure-property relationships specific to non-polar systems which had not been previously reported and may be used to design polymers with improved performance. Perhaps the most significant limitation of our studies to consider in future work was limited sample quantity, which prevented more elaborate tribological studies to be carried out. The development of scalable synthesis protocols to yield larger sample quantities would allow for the assessment of repeatability, polymer degradation and testing under a range of conditions. Finally, the correlation of additive performance to film structure could be made more reliable by employing instruments that may be used to monitor film formation *in situ* under shear.

4.4 Experimental

4.4.1 Instrumental methods

4.4.1.1 Atomic Force Microscopy

For imaging on highly oriented pyrolytic graphite, samples were prepared by drop-casting a 0.05 mg/ml polymer solution in chloroform onto freshly-cleaved substrate and dried under a gentle N_2 flow for 10 s. For imaging on steel, the substrates were cleaned prior to use in the same manner as described for the neutron reflectometry. Samples were prepared by submerging the steel substrate in a polymer solution prepared in *n*-dodecane (0.1 wt%) for 30 min. The polymer solution was displaced with pure *n*-dodecane to remove excess sample while keeping the substrate submerged. The substrate was then placed in a beaker of pure *n*-hexane (x2) and left to dry for ≥ 10 min before analysis.

Images were collected directly after sample preparation using a Bruker Dimension Icon instrument with ScanAsyst in Air and PeakForce tapping. Images were processed with Gwyddion software.

4.4.1.2 Mass Spectrometry

Mass spectra were acquired on an Agilent 6130B single quadrupole LC/MS system with electrospray ionisation and 50-3,000 m/z range.

4.4.1.3 Mini Traction Machine Experiments

MTM testing was carried out at Lubrizol using a PCS Instruments MTM. Each sample (1 wt% in Yubase 4 mineral oil) was measured using Stribeck step type between 40-140 °C in 20 °C increments at 1.0 GPa Hertz pressure.

4.4.1.4 Nuclear Magnetic Resonance Spectroscopy

^{1}H NMR spectra and ^{1}H-^{13}C HSQC spectra were recorded in deuterated chloroform ($CDCl_3$) on Bruker Avance III HD (300 MHz or 400 MHz) spectrometer at 300 K. Chemical shift values (δ) are reported in ppm. Tetramethylsilane (TMS) was used as the internal standard (δ = 0.08 ppm).

4.4.1.5 Polarised Neutron Reflectometry

Silicon-permalloy-steel substrates were cleaned by UV-ozone irradiation for 20 min and extensively washed with ultrapure water. Substrates were then subjected

to successive sonication in aqueous 2% w/v sodium dodecyl sulfate, ethanol and toluene. After thoroughly drying under N_2 flow, substrates were ozone-cleaned, rinsed with ethanol and mounted into PEEK laminar flow cells submerged in ethanol to avoid the introduction of air bubbles into the cells during assembly.

PNR was performed on the POLREF reflectometer at the ISIS pulsed neutron and muon source, UK, operating in polarised mode using fast flipping such that the neutron spin state is reversed with every neutron pulse, giving ≥ 98% polarisation. A schematic representation of the measurement setup is presented in Scheme 4.4. Flow cells were mounted in horizontal geometry, connected to a glass syringe containing either hydrogenated or deuterated *n*-dodecane via PTFE tubing mounted in a syringe pump, calibrated, and set to a flow rate of 0.5 ml/min. Aluminium top plates of the flow cells were connected to a water bath and the temperature maintained at 45 °C. Iron yokes were placed over the flow cells to ensure a constant magnetic field experienced throughout the sample. Reflected radiation was measured at 0.5°, 1.5°, and 2.5° incident angles using an incident wavelength range of 2-15 Å covering an effective Q_z range of 0.01-0.3 Å^{-1}, where $\delta Q/Q$ = 3%. Inefficiencies in neutron polarisation were corrected for as described by Wildes *et al*.[47] The resultant reflectivity patterns were normalised to the incident flux measured in transmission through each substrate.

The substrate was initially characterised by PNR in two isotopic contrasts, hydrogenated and deuterated *n*-dodecane, with spin up (↑) and spin down (↓) polarised neutrons, yielding four reflectivity curves describing the same interfacial structure. Sample solution (0.1 % w/v in *n*-dodecane) was then injected into the flow cell *via* the syringe pump and incubated for 2 h. The cell was then flushed with hydrogenated *n*-dodecane to remove polymer remaining in the bulk phase and data was collected with both magnetic contrasts, after which deuterated *n*-dodecane was injected into the cell to repeat the measurements.

Data were analysed using RasCAL.[48] This software calculates a reflectivity pattern resulting from a theoretical SLD profile consisting of two bulk phases with a series of interfacial layers each treated as homogeneous ‘slabs’. Each layer within this model is defined by four parameters: thickness, SLD, roughness, and solvation. The four datasets corresponding to the bare substrate were fitted to include four layers, corresponding to SiO_2, permalloy, steel and a thin oxide layer on the surface. These data were co-refined using *a priori* information, such as the SLD of silicon and SiO_2,

to obtain a structural model corresponding to the substrate. The parameters associated with this model were then fixed in the analysis of the polymer layer. To fit the data acquired with the adsorbed polymer layer, two additional layers were required, corresponding to the linear pNAM and the grafted pLA segments, respectively.

The error associated with the parameters in the model were estimated by Markov chain Monte Carlo analysis, enabling covariance between parameters to be accounted for. Here, a Gaussian prior distribution was assumed for all parameters. The posterior distribution was determined by performing 5,000 burn-in iterations for location of the global minima prior to a further 50,000 iterations used to define the posterior distribution. Three independent repeats of this analysis were used to calculate the asymmetric 95% confidence intervals associated with the fits and model parameters.

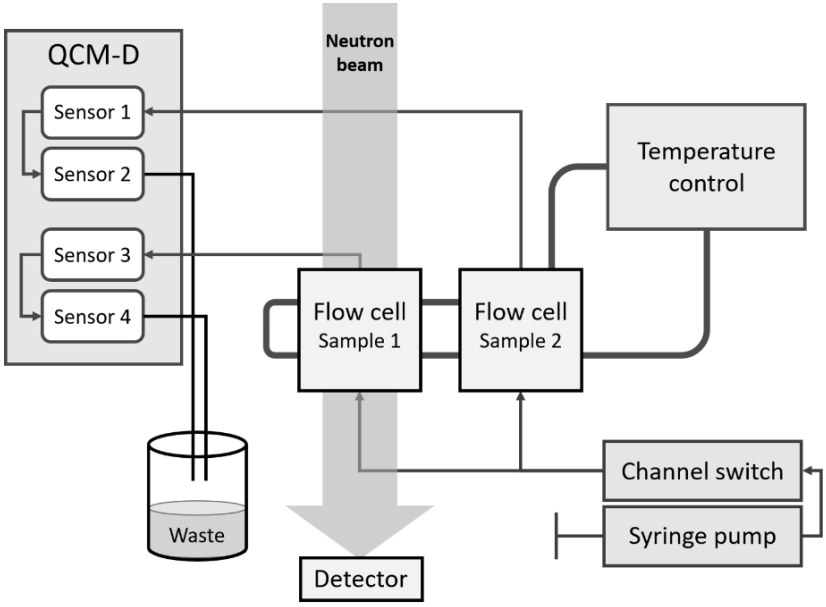

Scheme 4.4 Experimental setup used in PNR measurements.

4.4.1.6 Size-Exclusion Chromatography

SEC was carried out using the following three instrument setups and solvent conditions (Table 4.3). All analyte samples were filtered through a syringe filter prior to injection. Experimental molar mass ($M_{n,SEC}$) and dispersity ($Đ$) values were determined by employing conventional calibration with poly(methyl methacrylate) (PMMA) standards (Agilent EasyVials) or triple detection using Agilent GPC/SEC software.

Table 4.3 Instrument conditions used in SEC analysis.

	DMF	**$CHCl_3$**	**THF**
Instrument	Agilent Infinity II MDS	Agilent Infinity II MDS	Agilent Infinity II MDS
Detectors [A]	DRI, VS, DALS, single-wavelength UV	DRI, VS, DALS, multi-wavelength UV	DRI, VS, DALS, multi-wavelength UV
Guard column	PLgel 5 µm	PLgel 5 µm	
Analytical columns	2 x PLgel Mixed D 300 x 7.5 mm, 200-400,000 g/mol linear operating range [B]	2 x PLgel Mixed C 300 x 7.5 mm, 200-2,000,000 g/mol linear operating range [B]	2 x PLgel Mixed C 300 x 7.5 mm, 200-2,000,000 g/mol linear operating range [B]
Calibration [C]	PMMA 500-900,000 g/mol	PMMA 600-1,600,000	PMMA 1,000-1,500,000 g/mol
Eluent	DMF, cont. 5 mmol NH_4BF_4	$CHCl_3$, no additives	THF, cont. 0.01% butylated hydroxytoluene
Sample filter	Nylon membrane, 0.22 µm pore size	PTFE membrane, 0.22 µm pore size	PTFE membrane, 0.22 µm pore size
Flow rate	1 ml/min	1 ml/min	1 ml/min
Temperature	50 °C	30 °C	30 °C

[A] DRI, VS and DALS stand for differential refractive index, viscometry and dual-angle light scattering detectors, respectively. DALS was detected at 15° and 90° angles.

[B] Polystyrene equivalent.

[C] Calibration range is given as a representative example on a given month.

4.4.1.7 Quartz Crystal Microbalance with Dissipation

QCM-D experiments were carried out at Lubrizol using a QSense E4 system equipped with a peristaltic pump (IPC-C, Ismatec), solvent resistant tubing, and flow cells with solvent resistant gaskets and O-rings. QSense stainless steel-coated (grade SS2343) QCM chips were used for the analysis. Solvent and solutions were filtered using Acrodisc Supor PES syringe syringe filters with 0.2 µm pore size and 32 mm diameter. Prior to the experiment, the chip was cleaned by sonicating in toluene for 10 min, drying under N_2, soaked in Hellmanex solution (1 wt% in deionised water) for 30 min, rinsing with deionised water, dried under N_2, sonicating in ethanol for 10 min and drying under N_2. Finally, the chips were placed in an ozone cleaner for 10 min. The chips were loaded into cells set to 40 °C and pure *n*-dodecane was passed

through the sample cell at a flow rate of 50 µl/min until a stable frequency reading was observed. The sample (0.01 wt% in *n*-dodecane) was then passed over the chip using the same flow rate until the frequency reading reached a plateau. Pure *n*-dodecane was then injected to rinse the system. Frequency and dissipation changes were monitored for all tuned overtones with data collection controlled by QSoft software. Data analysis was performed with QTools software.

4.4.2 Materials

4-Acryloyl morpholine (NAM, 97%, Sigma-Aldrich), azobisisobutyronitrile (AIBN, 98%, Sigma-Aldrich), *n*-butyl acrylate (BuA, ≥ 99%, Sigma-Aldrich), butyl 2-(((dodecylthio)carbonothioyl)thio)-2-methylpropanoate (CTA-1, 70%, Lubrizol), deuterated chloroform ($CDCl_3$, 99.8% D, Aldrich), anhydrous dichloromethane (DCM, 99.8%, Sigma-Aldrich), diethyl ether (≥ 99.8%, Sigma-Aldrich), 1,4-dioxane (≥ 99%, Sigma-Aldrich), *N*,*N*-dimethylformamide (DMF, HPLC-grade, Merck), *n*-dodecane (99+%, Alfa Aesar), dodecane-d_{26} (98% D, Cambridge Isotope Laboratories UK), 2-(((dodecylthio)carbonothioyl)thio)-2-methylpropanoic acid (MPADTC / CTA acid, provided by Lubrizol), ethyl acetate (laboratory reagent grade, Fisher Chemical), ethylene glycol (anhydrous, 99.8%, Sigma-Aldrich), *n*-hexane (laboratory reagent grade, Fisher Chemical), *N*-hydroxyethyl acrylamide (HEAm, ≥ 97%, Sigma-Aldrich), lauroyl peroxide (LPO, 97%, Aldrich), lauryl acrylate (LA, 90%), oxalyl chloride (2.0 M in methylene chloride, Sigma-Aldrich), magnesium sulfate ($MgSO_4$, laboratory reagent grade, Fisher Chemical), methanol (≥ 99.8%, Merck), sodium bicarbonate ($NaHCO_3$, laboratory reagent grade, Fisher Chemical), toluene (laboratory reagent grade, Fisher Chemical), and dimethyl 2,2'-azobis(2-methylpropionate) (V-601, Wako) were used as received unless otherwise stated below.

BuA, LA and NAM were passed through an aluminium oxide column to remove inhibitors prior to polymerisations. MPADTC was recrystallised from *n*-hexane prior to use.

Single crystal silicon substrates used in PNR experiments were purchased from Crystran Ltd (UK). The substrates were 80×50×15 mm in size with a single 80×50 Si(111) face polished to < 5 Å root-mean-square roughness. The surface was sputter-coated with permalloy (4:1 Ni:Fe) and 316-type steel films of 150 and 250 Å

thickness, respectively, by the NanoFab group at the Center for Nanoscale Science and Technology, NIST (USA).

4.4.3 Synthetic Protocols and Characterisation

4.4.3.1 Synthesis of Di-CTA

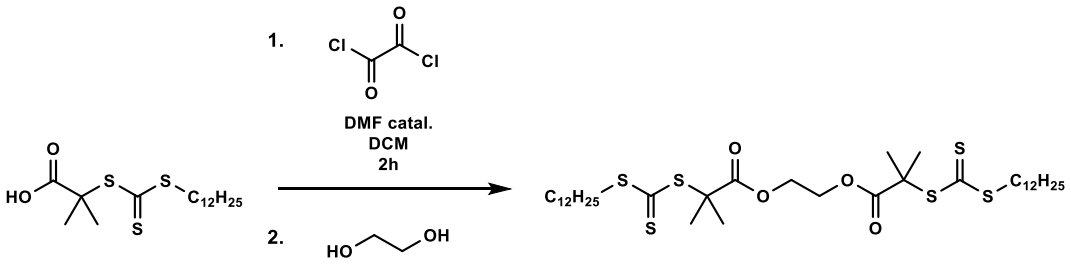

Scheme 4.5 Reaction scheme for the preparation of difunctional RAFT agent, di-CTA.

Dry glassware and anhydrous solvents were used for the reaction. CTA acid (1.5 g, 4.1 mmol, 1.5 eq.) was dissolved in DCM in a round-bottom flask. Under N_2 flow, oxalyl chloride solution (2 M in DCM, 4.1 ml, 8.2 mmol, 3 eq.) and a drop of anhydrous DMF catalyst were added under vigorous stirring and N_2 flow. Stirring was continued for 2 h after which volatiles were removed under vacuum. The remaining oil was re-dissolved in anhydrous DCM and added dropwise to a stirred solution of ethylene glycol in DCM (85 mg, 1.4 mmol, 1 eq. with respect to −OH) immersed in an ice bath under gentle N_2 flow. The flask was removed from the ice bath and N_2 flow was removed after the reaction mixture had reached room temperature. Stirring was continued for 12 h.

The solution was diluted to 50 ml and washed with $NaHCO_3$ (1 M, 3×50 ml) and brine (2×50 ml). The organic phase was dried over $MgSO_4$ overnight, filtered, and volatiles were removed under vacuum. A flash column was used to isolate the pure product by running an elution gradient of *n*-hexane to 5% ethyl acetate. Volatiles were removed and the product was dried in a vacuum oven at 40 °C overnight, giving a yellow crystalline product upon cooling. The product was characterised using ^{1}H and ^{13}C NMR spectroscopy (Figure 4.13) and mass spectrometry (Figure 4.14).

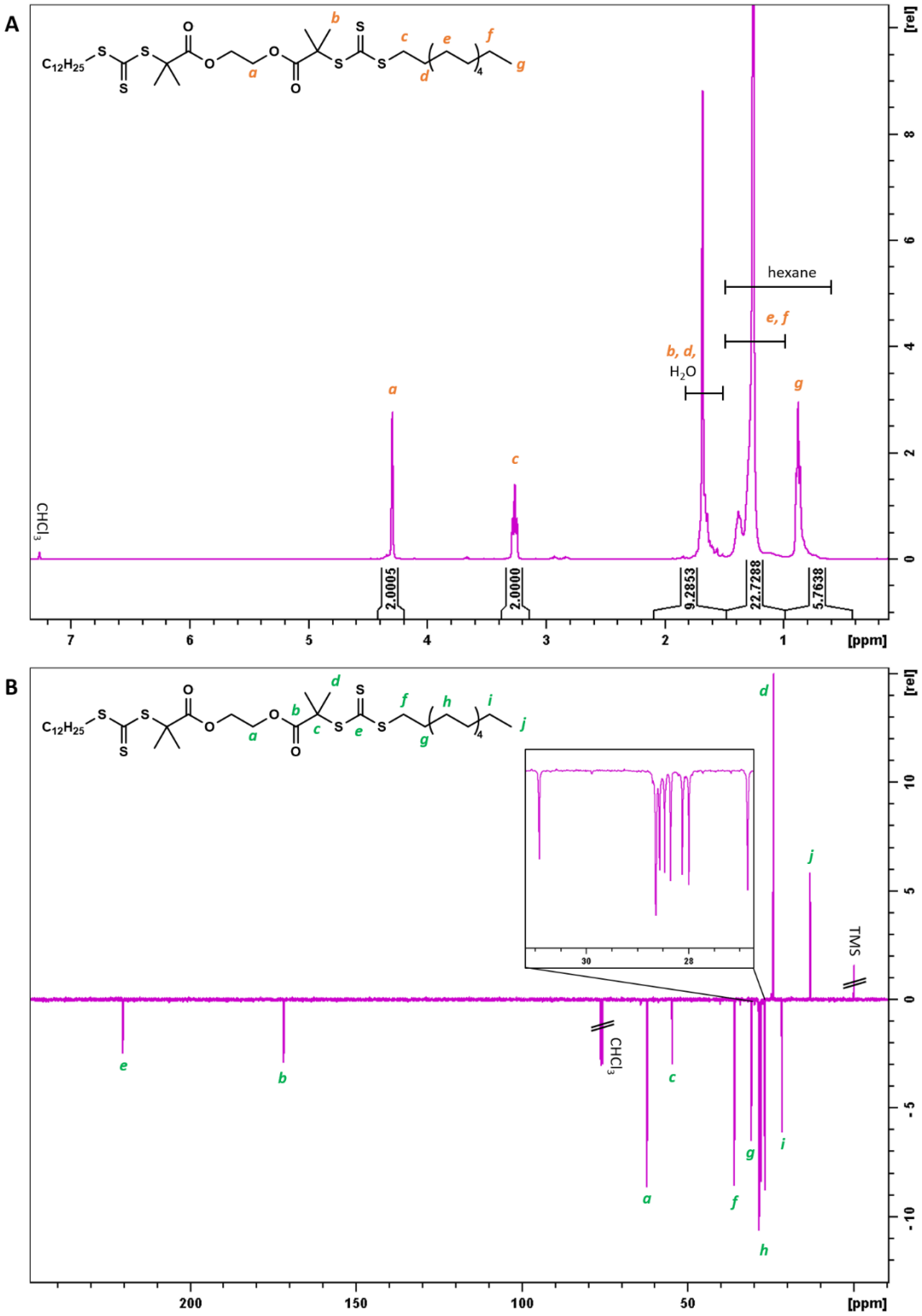

Figure 4.13 ^{1}H NMR (**A**) and ^{13}C NMR (**B**) spectra of the RAFT di-CTA, acquired in $CDCl_3$.

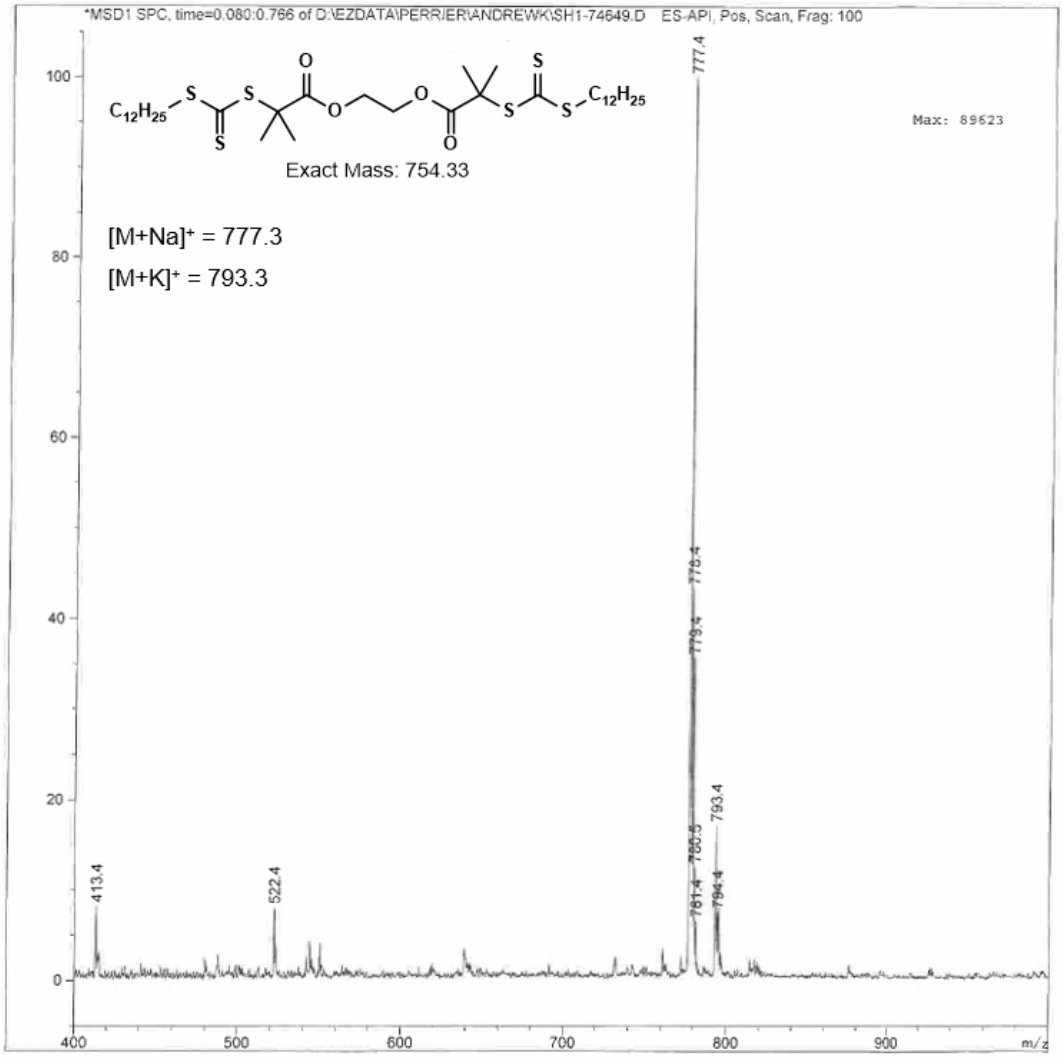

Figure 4.14 Mass spectrum of the RAFT di-CTA. Sample was prepared in acetonitrile/methanol mixture (1:1 vol).

4.4.3.2 RAFT Polymerisation of Backbone Copolymers

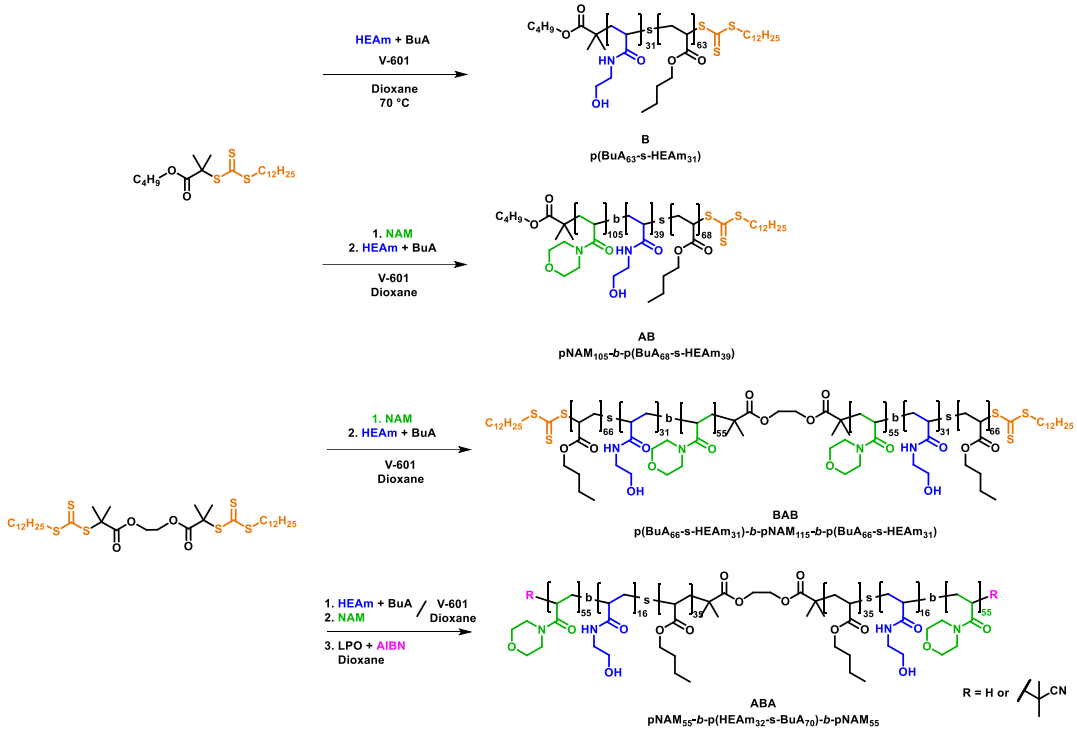

Scheme 4.6 Reaction schemes for the RAFT polymerisation to synthesise backbone precursors.

To prepare the statistical p(HEAm$_{31}$-*s*-BuA$_{63}$) copolymer (B), BuA (1.00 g, 7.80 mmol), HEAm (0.360 g, 3.13 mmol), CTA-1 (32.7 mg, $7.77 \cdot 10^{-2}$ mmol) and V-601 (1.30 mg, $5.65 \cdot 10^{-3}$ mmol) were dissolved in dioxane (3.3 ml) in a 7 ml vial fitted with a stirrer bar and rubber septum. The reaction mixture was degassed with N_2 for 15 min and placed in an oil bath heated to 70 °C. Samples were taken to monitor the consumption of monomers by ^{1}H NMR and the reaction was stopped after 1.5 h at 62% and 76% conversion of BuA and HEAm, respectively. The reaction mixture was diluted, and the polymer was precipitated three times into a methanol/water mixture (4:1) and dried in vacuum oven at 40 °C.

To prepare the diblock copolymer pNAM$_{105}$-*b*-p(HEAm$_{39}$-*s*-BuA$_{68}$) (AB), NAM (1.00 g, 7.08 mmol), BIBDTC (23.0 mg, $5.47 \cdot 10^{-2}$ mmol), V-601 (0.63 mg, $2.73 \cdot 10^{-3}$ mmol) were first dissolved in dioxane (1.5 ml) and polymerised using the protocol described above. Reaction was stopped after 30 min at 77% conversion and the polymer was precipitated three times into diethyl ether and dried yielding a pale yellow powder. The polymer (0.530 g, $3.51 \cdot 10^{-2}$ mmol) was then dissolved in dioxane (1.8 ml) along with BuA (467 mg, 3.64 mmol), HEAm (171 mg, 1.49 mmol) and V-601 (0.57 mg, $2.48 \cdot 10^{-3}$ mmol). Polymerisation was carried out at 70 °C for 1.5 h

and the reaction was stopped at 65% and 91% conversion of BuA and HEAm, respectively. The polymer was purified through repeated precipitations into cold diethyl ether and dried under vacuum.

Synthesis of p(BuA_{66}-*s*-$HEAm_{31}$)-*b*-pNAM_{115}-*b*-p(BuA_{66}-*s*-$HEAm_{32}$) (BAB) was carried out by using the reaction conditions and protocols described above but using the difunctional CTA, di-BIBDTC. In the first step $[M]_0$=3 M, $[NAM]_0/[CTA]_0$=130, and $[CTA]_0/[I]_0$=20. In the second step $[M]_0$=2 M, $[BuA]_0/[HEAm]_0/[mCTA]_0$=200/80/1, and $[CTA]_0/[I]_0$=14.

Finally, pNAM_{55}-*b*-p(BuA_{70}-s-$HEAm_{32}$)-*b*-pNAM_{55} (ABA) was prepared with the described protocols using di-BIBDTC. In the first step $[M]_0$=3 M, $[BuA]_0/[HEAm]_0/[CTA]_0$=100/40/1, and $[CTA]_0/[I]_0$=14. In the second step $[M]_0$=2 M, $[NAM]_0/[mCTA]_0$=130, and $[CTA]_0/[I]_0$=20. The end-groups were removed by using the protocol described by Chen *et al*.[34] Briefly, the copolymer was weighed into a vial and dissolved in dioxane. LPO and AIBN stock solutions were added (CTA:LPO:AIBN=1:3:30) and the mixture was deoxygenated by bubbling N_2 into the solution. Reaction was started by immersing the vial into an 80 °C oil bath. After 4 h, the reaction was stopped by letting the vial cool down to room temperature. The product was purified by precipitating twice into cold diethyl ether and dried. Products were characterised with ^{1}H NMR spectroscopy in $CDCl_3$ (Figure 4.3) and SEC in DMF (Figure 4.2).

4.4.3.3 Functionalisation of Backbone Copolymers

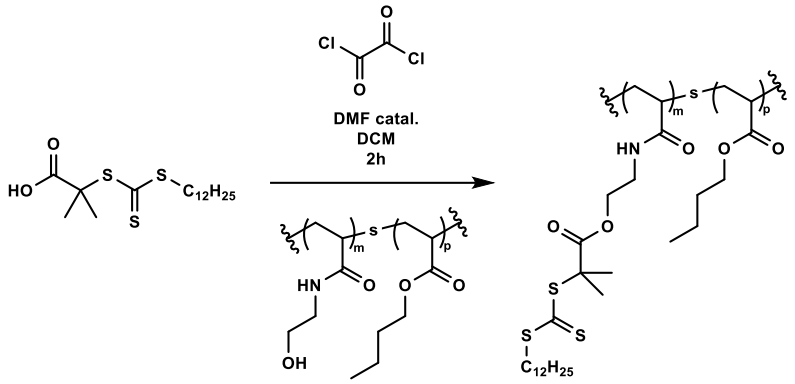

Scheme 4.7 General reaction scheme for the functionalisation of backbone copolymers.

The following general protocol was used to functionalise all copolymer backbones. In a dry round-bottom flask equipped with a stir bar, p(BuA-*s*-HEAm) was dissolved in anhydrous DCM. In a separate flask, MPADTC (2 eq. with respect to HEAm units) was dissolved in anhydrous DCM and oxalyl chloride solution (4 eq.) was added to the solution under N_2 flow and vigorous stirring. A catalytic amount of anhydrous DMF was added to start the reaction (CO↑, CO_2↑) and stirring was continued for 2 h, after which DCM and excess oxalyl chloride were removed using a Schlenk line. The red oil was redissolved in DCM and added dropwise to the polymer solution set in an ice bath. After 2 h, the ice bath was removed and stirring was continued overnight. The reaction mixture was concentrated by rotary evaporation and precipitated into methanol three times or until no free CTA remained in the product. Solvent residue was removed by rotary evaporation and the product was dried in a vacuum oven at 40 °C. Products were characterised with ^{1}H NMR and ^{1}H-^{13}C HSQC in $CDCl_3$ (Figure 4.3), and SEC in $CHCl_3$ (Figure 4.4).

4.4.3.4 RAFT Polymerisation of Grafts

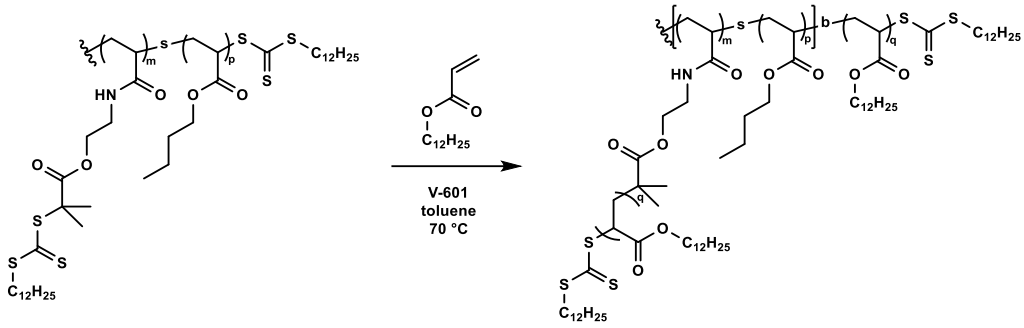

Scheme 4.8 General reaction scheme for the graft polymerisation of lauryl acrylate.

The following general protocol was used for all polymerisations. For all reactions, $[M]_0$ = 1 M, $[M]_0/[CTA]_0$ = 55, and $[CTA]_0/[I]_0$ = 20-40. Lauryl acrylate, CTA-functionalised backbone, and solvent) were added to a round bottom flask and stirred until fully homogenised. V-601 was added and the reaction mixture was deoxygenated with N_2 and placed in an oil bath set to 70 °C for 5 h, or until the desired monomer conversion was reached. The flask was cooled to room temperature and the polymer was precipitated three times into cold methanol and dried under vacuum. Products were characterised with ^{1}H NMR spectroscopy in $CDCl_3$ (Figure 4.3), SEC in THF (Figure 4.4), and with AFM on highly oriented pyrolytic graphite (Figure 4.5).

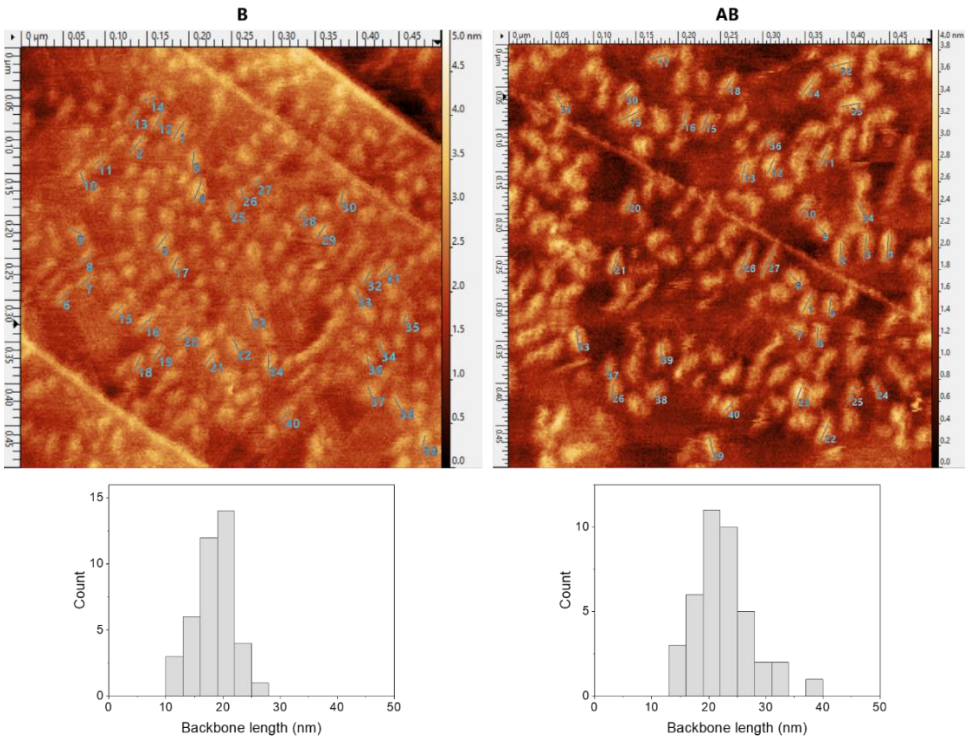

Figure 4.15 Manual image analysis of AFM images collected for graft copolymers B and AB. Backbones of 40 polymers were measured in each image and plotted as histograms. The average backbone lengths, calculated as arithmetic means, were 18 nm and 23 nm for B and AB, respectively.

4.5 References

1. Dėdinaitė, A., Biomimetic Lubrication. *Soft Matter* **2012,** *8* (2), 273-284.
2. Faivre, J.; Shrestha, B. R.; Xie, G.; Delair, T.; David, L.; Matyjaszewski, K.; Banquy, X., Unraveling the Correlations between Conformation, Lubrication, and Chemical Stability of Bottlebrush Polymers at Interfaces. *Biomacromolecules* **2017,** *18* (12), 4002-4010.
3. Faivre, J.; Shrestha, B. R.; Xie, G.; Olszewski, M.; Adibnia, V.; Moldovan, F.; Montembault, A.; Sudre, G.; Delair, T.; David, L.; Matyjaszewski, K.; Banquy, X., Intermolecular Interactions between Bottlebrush Polymers Boost the Protection of Surfaces against Frictional Wear. *Chemistry of Materials* **2018,** *30* (12), 4140-4149.
4. Banquy, X.; Burdyńska, J.; Lee, D. W.; Matyjaszewski, K.; Israelachvili, J., Bioinspired Bottle-Brush Polymer Exhibits Low Friction and Amontons-like Behavior. *Journal of the American Chemical Society* **2014,** *136* (17), 6199-6202.
5. Pettersson, T.; Naderi, A.; Makuška, R.; Claesson, P. M., Lubrication Properties of Bottle-Brush Polyelectrolytes: An AFM Study on the Effect of Side Chain and Charge Density. *Langmuir* **2008,** *24* (7), 3336-3347.
6. Spikes, H., Friction Modifier Additives. *Tribology Letters* **2015,** *60* (1).
7. Bielecki, R. M.; Benetti, E. M.; Kumar, D.; Spencer, N. D., Lubrication with Oil-Compatible Polymer Brushes. *Tribology Letters* **2012,** *45* (3), 477-487.
8. Müller, M.; Topolovec-Miklozic, K.; Dardin, A.; Spikes, H. A., The Design of Boundary Film-Forming PMA Viscosity Modifiers. *Tribology Transactions* **2006,** *49* (2), 225-232.
9. Yin, F.; Bedrov, D.; Smith, G. D.; Kilbey, S. M., A Langevin Dynamics Simulation Study of the Tribology of Polymer Loop Brushes. *The Journal of Chemical Physics* **2007,** *127* (8), 084910.
10. Corrigan, N.; Jung, K.; Moad, G.; Hawker, C. J.; Matyjaszewski, K.; Boyer, C., Reversible-Deactivation Radical Polymerization (Controlled/Living Radical Polymerization): From Discovery to Materials Design and Applications. *Progress in Polymer Science* **2020,** *111*.
11. Destarac, M., Industrial Development of Reversible-Deactivation Radical Polymerization: Is the Induction Period Over? *Polymer Chemistry* **2018,** *9* (40), 4947-4967.
12. Park, J. Y.; Salmeron, M., Fundamental Aspects of Energy Dissipation in Friction. *Chemical Reviews* **2014,** *114* (1), 677-711.
13. Mocny, P.; Klok, H.-A., Tribology of Surface-Grafted Polymer Brushes. *Molecular Systems Design & Engineering* **2016,** *1* (2), 141-154.
14. Holmberg, K.; Andersson, P.; Erdemir, A., Global Energy Consumption Due to Friction in Passenger Cars. *Tribology International* **2012,** *47*, 221-234.
15. Herdan, J. M., Friction Modifiers in Engine and Gear Oils. *Lubrication Science* **2000,** *12* (3), 265-276.
16. Václav Štěpina; Veselý, V., Chapter 3 - Types of Lubricants and their Compositions. In *Tribology Series*, Elsevier: The Netherlands, 1992; Vol. 23, pp 125-254.
17. Yu, C.; Evmenenko, G.; Kmetko, J.; Dutta, P., Effects of Shear Flow on Interfacial Ordering in Liquids: X-ray Scattering Studies. *Langmuir* **2003,** *19* (23), 9558-9561.
18. Corvis, Y.; Barré, L.; Jestin, J.; Gummel, J.; Cousin, F., Asphaltene Adsorption Mechanism Under Shear Flow Probed by In Situ Neutron Reflectivity

Measurements. *The European Physical Journal Special Topics* **2012,** *213* (1), 295-302.
19. Wolff, M.; Kuhns, P.; Liesche, G.; Ankner, J. F.; Browning, J. F.; Gutfreund, P., Combined Neutron Reflectometry and Rheology. *Journal of Applied Crystallography* **2013,** *46* (6), 1729-1733.
20. Cann, P. M.; Spikes, H. A., The Behavior of Polymer Solutions in Concentrated Contacts: Immobile Surface Layer Formation. *Tribology Transactions* **1994,** *37* (3), 580-586.
21. Georges, J. M.; Millot, S.; Loubet, J. L.; Tonck, A., Drainage of Thin Liquid Films Between Relatively Smooth Surfaces. *The Journal of Chemical Physics* **1993,** *98* (9), 7345-7360.
22. Fan, J.; Müller, M.; Stöhr, T.; Spikes, H. A., Reduction of Friction by Functionalised Viscosity Index Improvers. *Tribology Letters* **2007,** *28* (3), 287-298.
23. Klein, J.; Kamiyama, Y.; Yoshizawa, H.; Israelachvili, J. N.; Fredrickson, G. H.; Pincus, P.; Fetters, L. J., Lubrication Forces Between Surfaces Bearing Polymer Brushes. *Macromolecules* **1993,** *26* (21), 5552-5560.
24. Banquy, X.; Faivre, J.; Shrestha, B. R.; Matyjaszewski, K.; Burdynska, J.; Moldovan, F. Bottlebrush Polymer Compositions, Lubricating Fluid, Porous Materials Comprising Said Compositions, and Surface Bearing Said Compositions. WO 2017181274A1, 2021.
25. Faivre, J.; Shrestha, B. R.; Burdyńska, J.; Xie, G.; Moldovan, F.; Delair, T.; Benayoun, S.; David, L.; Matyjaszewski, K.; Banquy, X., Wear Protection Without Surface Modification Using a Synergistic Mixture of Molecular Brushes and Linear Polymers. *ACS Nano* **2017,** *11* (2), 1762–1769.
26. Carrillo, J.-M. Y.; Brown, W. M.; Dobrynin, A. V., Explicit Solvent Simulations of Friction between Brush Layers of Charged and Neutral Bottle-Brush Macromolecules. *Macromolecules* **2012,** *45* (21), 8880-8891.
27. Liu, X.; Thormann, E.; Dedinaite, A.; Rutland, M.; Visnevskij, C.; Makuska, R.; Claesson, P. M., Low Friction and High Load Bearing Capacity Layers Formed by Cationic-Block-Non-Ionic Bottle-Brush Copolymers in Aqueous Media. *Soft Matter* **2013,** *9* (22), 5361-5371.
28. Müller, M.; Lee, S.; Spikes, H. A.; Spencer, N. D., The Influence of Molecular Architecture on the Macroscopic Lubrication Properties of the Brush-Like Co-polyelectrolyte Poly(L-lysine)-g-poly(ethylene glycol) (PLL-g-PEG) Adsorbed on Oxide Surfaces. *Tribology Letters* **2003,** *15* (4), 395-405.
29. Hartung, W.; Drobek, T.; Lee, S.; Zürcher, S.; Spencer, N. D., The Influence of Anchoring-Group Structure on the Lubricating Properties of Brush-Forming Graft Copolymers in an Aqueous Medium. *Tribology Letters* **2008,** *31* (2), 119-128.
30. Kerr, A. Complex Bottle-Brush Copolymers by Reversible Addition Fragmentation Chain Transfer Polymerisation: Synthesis and Applications. University of Warwick, Coventry, England, 2019.
31. Gody, G.; Maschmeyer, T.; Zetterlund, P. B.; Perrier, S., Rapid and Quantitative One-Pot Synthesis of Sequence-Controlled Polymers by Radical Polymerization. *Nature Communications* **2013,** *4*, 2505-2514.
32. Moad, G., A Critical Assessment of the Kinetics and Mechanism of Initiation of Radical Polymerization with Commercially Available Dialkyldiazene Initiators. *Progress in Polymer Science* **2019,** *88*, 130-188.
33. Mandal, B. M., *Fundamentals of Polymerization*. World Scientific: Singapore, 2013.

34. Chen, M.; Moad, G.; Rizzardo, E., Thiocarbonylthio End Group Removal from RAFT-Synthesized Polymers by a Radical-Induced Process. *Journal of Polymer Science Part A: Polymer Chemistry* **2009,** *47* (23), 6704-6714.
35. Zheng, Z.; Ling, J.; Müller, A. H. E., Revival of the R-Group Approach: A "CTA-shuttled" Grafting from Approach for Well-Defined Cylindrical Polymer Brushes via RAFT Polymerization. *Macromolecular Rapid Communications* **2014,** *35* (2), 234-241.
36. Kerr, A.; Hartlieb, M.; Sanchis, J.; Smith, T.; Perrier, S., Complex Multiblock Bottle-Brush Architectures by RAFT Polymerization. *Chemical Communications* **2017,** *53* (87), 11901-11904.
37. Vatankhah-Varnosfaderani, M.; Keith, A. N.; Cong, Y.; Liang, H.; Rosenthal, M.; Sztucki, M.; Clair, C.; Magonov, S.; Ivanov, D. A.; Dobrynin, A. V.; Sheiko, S. S., Chameleon-Like Elastomers with Molecularly Encoded Strain-Adaptive Stiffening and Coloration. *Science* **2018,** *359* (6383), 1509-1513.
38. Zheng, R.; Liu, G.; Devlin, M.; Hux, K.; Jao, T.-C., Friction Reduction of Lubricant Base Oil by Micelles and Crosslinked Micelles of Block Copolymers. *Tribology Transactions* **2009,** *53* (1), 97-107.
39. Khelfallah, N.; Gunari, N.; Fischer, K.; Gkogkas, G.; Hadjichristidis, N.; Schmidt, M., Micelles Formed by Cylindrical Brush-Coil Block Copolymers. *Macromolecular Rapid Communications* **2005,** *26* (21), 1693-1697.
40. Johannsmann, D., *The Quartz Crystal Microbalance in Soft Matter Research*. Springer: Switzerland, 2015.
41. Voinova, M. V.; Rodahl, M.; Jonson, M.; Kasemo, B., Viscoelastic Acoustic Response of Layered Polymer Films at Fluid-Solid Interfaces: Continuum Mechanics Approach. *Physica Scripta* **1999,** *59* (5), 391-396.
42. Reviakine, I.; Johannsmann, D.; Richter, R. P., Hearing What You Cannot See and Visualizing What You Hear: Interpreting Quartz Crystal Microbalance Data from Solvated Interfaces. *Analytical Chemistry* **2011,** *83* (23), 8838-8848.
43. Armstrong, A. J.; McCoy, T. M.; Welbourn, R. J. L.; Barker, R.; Rawle, J. L.; Cattoz, B.; Dowding, P. J.; Routh, A. F., Towards a Neutron and X-Ray Reflectometry Environment for the Study of Solid-Liquid Interfaces Under Shear. *Scientific Reports* **2021,** *11* (1), 9713-9724.
44. *Atomic Force Microscopy in Liquid: Biological Applications*. 2nd ed.; Wiley-VCH: Weinheim, Germany, 2012.
45. Clifton, L. A.; Hall, S. C. L.; Mahmoudi, N.; Knowles, T. J.; Heinrich, F.; Lakey, J. H., *Structural Investigations of Protein–Lipid Complexes Using Neutron Scattering*. Springer: New York, 2019.
46. Glovnea, R. P.; Forrest, A. K.; Olver, A. V.; Spikes, H. A., Measurement of Sub-Nanometer Lubricant Films Using Ultra-Thin Film Interferometry. *Tribology Letters* **2003,** *15* (3), 217-230.
47. Wildes, A. R., Scientific Reviews: Neutron Polarization Analysis Corrections Made Easy. *Neutron News* **2007,** *17* (2), 17-25.
48. SourceForge: RasCAL. https://sourceforge.net/projects/rscl/ (accessed 20.08.2021).

Chapter 5

Conclusions and Outlook

This thesis explored new synthetic strategies, the solution self-assembly behaviour, and lubricating properties of graft copolymers prepared using RAFT polymerisation. While the early motivation for this work was an industrial incentive to use RAFT polymerisation to produce state-of-the-art functional polymers for commercial use, it also led to fundamental research on RAFT polymerisation strategies for graft copolymer synthesis. A critical assessment of the benefits and challenges of this technique was provided throughout these studies. The versatility of the RAFT process is illustrated in the diversity of the chemistries and architectural details of the polymers prepared throughout the experimental work, which included sparsely grafted, densely grafted, brush-coil, and mixed graft architectures. Moreover, two new synthetic strategies were discovered by harnessing the unique RAFT mechanism for graft exchange reactions, providing a convenient route to heterograft structures. This approach may also be envisioned to find use in the preparation of bottlebrush polymer networks, which are easily accessible by conducting graft exchange reactions in the presence of a difunctional linear crosslinker chain. These reactions could potentially provide a unique level of dynamic control over the graft distribution, crosslinking density, and the general parameters of graft copolymers. Given that ROMP and ATRP of macromonomers currently appear to be the most commonly selected synthetic routes for producing bottlebrush polymer networks, the newly developed method is a valuable addition to the current-day synthetic toolbox.

The adaptability of RAFT chemistry to different monomer-solvent systems allowed the self-assembly characteristics of graft copolymers to be studied during *grafting from* polymerisations to provide first examples of their PISA behaviour. Entangled sparsely grafted polymers were found to form clustered spherical particles and therefore steered the reaction towards a different outcome than that reported for the linear diblock equivalent. Furthermore, the physical constraints of the branched architecture promoted the formation of multicore morphologies, which are not

commonly encountered in PISA studies. Based on these observations, it is anticipated that the PISA of graft copolymers conducted through *grafting from* polymerisations may generally be dictated by chain entanglements if the backbone retains Gaussian behaviour and is sufficiently long. These findings are expected to differ significantly from the PISA behaviour of rigid, densely grafted polymers, which remains unexplored and is an intriguing subject for future studies. Despite chain entanglements being a well-known characteristic of polymers, it is generally not used for an advantage in polymer self-assembly. They could, however, provide a useful tool for preparing new functional materials such as the gel-like particle clusters which appear an intriguing subject for a rheological study. Furthermore, the multicore particle morphologies could make for an interesting alternative for conventional micelles in encapsulation and release studies. With this in mind, we have successfully re-designed the presented system for aqueous media, thus expanding the scope of potential applications. The synthetic route used in this study may be simplified into a one-pot protocol by constructing the functionalised backbone via copolymerisation of the stabilising monomer with a CTA-functional monomer (an inimer). This strategy circumvents the need for purification steps, therefore making the synthesis better suited for large-scale processes.

Finally, the performance of graft copolymer lubricants was assessed in non-polar solvents to gain insight into the role of grafting density and architectural details, and to evaluate their suitability for use as oil additives. While the reduction in grafting density and the positioning of the polar linear segment were found to have a large impact on the solution behaviour (i.e., micellisation) of the polymers, friction tests showed very little difference between the various polymers. The intricate interplay between the flexible and insoluble linear segment and the steric bulk of the grafted segments was identified as a key factor in governing micellisation and surface adsorption. Careful consideration of the observed relationships between polymer architecture and solvent/adsorption characteristics should allow the preparation of next-generation additives which readily adsorb to metal, forming a thick protective lubricating film. Given the considerable number of studies and patents involving aqueous bottlebrush polymer lubricants, publications involving oil-soluble lubricants may be expected to emerge soon and to provide further guidance for their design. Further work is needed to assess their performance under different operating conditions, the durability of the compounds, and the nature of any degradation

products. In particular, the degradation (as well as undesirable odour and colour) of RAFT agents is often of concern. While end-group removal could be used to eliminate the issue, it may not be a commercially viable approach due to its added cost. Although controlled radical polymerisation technologies are used industrially, the current price of RAFT agents greatly exceeds that of monomers; therefore, preparation of lubricants in this way may not be cost-effective. In-house technology for synthesising RAFT agents on a large scale, such as Lubrizol's production of CTA-1, could possibly mitigate this issue. Nonetheless, RAFT and MADIX have been suggested to be especially promising for use in industrial processes due to their polymerisation protocols being practically the same as those of free radical polymerisations with an added transfer agent, and their wide range of compatible vinyl monomers, chain-end functionalities, and reaction conditions.